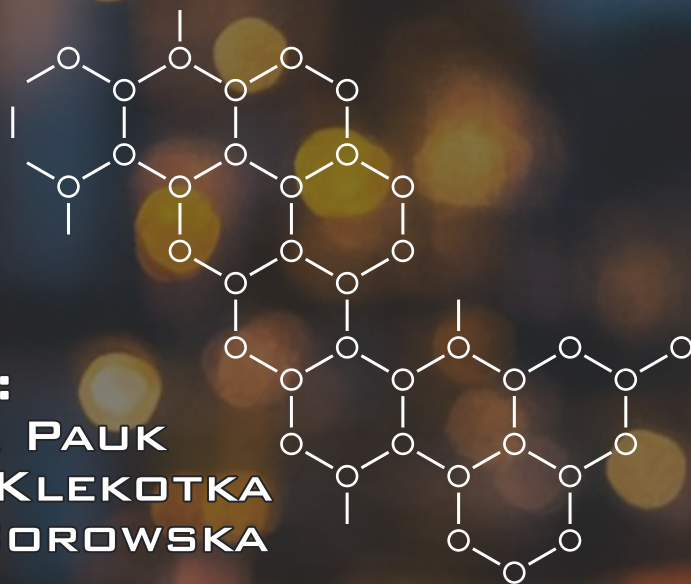


# RECENT DEVELOPMENTS IN BIOMEDICAL ENGINEERING

EDITORS:  
JOLANTA PAUK  
MARCIN KLEKOTKA  
MARTA BOROWSKA



# **RECENT DEVELOPMENTS IN BIOMEDICAL ENGINEERING**

Editors

Jolanta Pauk, Marcin Klekotka, Marta Borowska



**Politechnika  
Białostocka**

OFICyna WYDAWNICZA POLITECHNIKI BIAŁOSTOCKIEJ  
BIAŁYSTOK 2024

Reviewers:  
Prof. Kristina Daunoravičienė  
Prof. Koos Jaap van Zwieten

Science editor in the discipline of biomedical engineering:  
Prof. Jan Ryszard Dąbrowski, PhD, DSc

Copy editor:  
Aniela Staszewska, Edyta Chrzanowska

DTP & cover of a book:  
Marcin Dominów

Cover photo:  
TungArt7, [https://pixabay.com/pl/illustrations/  
budowa-pracownik-in%C5%BCynier-kask-8941880](https://pixabay.com/pl/illustrations/budowa-pracownik-in%C5%BCynier-kask-8941880)

© Copyright by Politechnika Białostocka, Białystok 2024

ISBN 978-83-68077-36-0  
ISBN 978-83-68077-37-7 (e-Book)  
DOI: 10.24427/978-83-68077-37-7



Ministry of Science and Higher Education  
Republic of Poland



**Doskonała  
Nauka**

Project co-financed by state funds,  
awarded by the Minister of Education and Science  
under the program "Excellent Science II – Support for Scientific Conferences".



The publication is available on license Creative Commons Recognition of authorship  
– Non-commercial use – Without dependent works 4.0 (CC BY-NC-ND 4.0)

Full license content available

on the site [creativecommons.org/licenses/by-nc-nd/4.0/legalcode.pl](https://creativecommons.org/licenses/by-nc-nd/4.0/legalcode.pl).

The publication is available on the Internet  
on the site of the Publishing House of Białystok University of Technology.

Print: Print Profit sp. z o.o

---

Publishing House of Białystok University of Technology  
Wiejska 45C, 15-351 Białystok  
e-mail: [oficyna.wydawnicza@pb.edu.pl](mailto:oficyna.wydawnicza@pb.edu.pl)  
[www.pb.edu.pl](http://www.pb.edu.pl)

# Content

Preface .....	5
Pressure-relieving silicone orthopedic insole made by 3D printing <i>Łukasz Bolesta, Eliza Romańczuk-Ruszek, Bogna Sztorch, Robert Eedward Przekop</i> .....	9
System for lung X-Ray image analysis using machine learning algorithms <i>Aleksandra Chilimonik, Anna Kasperczuk, Małgorzata Zdrodowska, Agnieszka Dardzińska-Głębocka</i> .....	27
Automatic mechanical diagnostic using deep learning methods <i>Agnieszka Dardzińska-Głębocka, Anna Kasperczuk, Jakub Dąbrowski</i> .....	41
Application supporting the interpretation of laboratory test results <i>Julia Kiryluk, Marta Borowska</i> .....	51
Artificial intelligence in neuroimaging of cerebral aneurysms – theoretical study <i>Żaneta Anna Mierzejewska</i> .....	65
Utilization of the spin-coating method to produce elastic composites for applications in biomedical engineering <i>Joanna Mystkowska, Anna Powojaska, Jakub Ławrynówicz</i> .....	83
Assessment of the wettability of PDMS and denture acrylic polymer by oral gels <i>Joanna Niewęglowska, Dawid Łysik, Joanna Mystkowska</i> .....	103
Mechanical properties of polylactide-based composites with iron powder additions – experimental and numerical evaluation <i>Dominika Nowińska, Eliza Romańczuk-Ruszek, Zbigniew Oksiuta</i> .....	115
Design of an ankle joint orthosis for people with extensive sweating <i>Mateusz Perzan, Anna Falkowska</i> .....	125
Influence of the femoral neck-shaft and anteversion angles on the loadings acting in the musculoskeletal system during walking <i>Justyna Skubich, Szczepan Piszczatowski</i> .....	141
Key factors in bone marrow transplant outcomes: statistical insights <i>Vanessa Stabla, Małgorzata Zdrodowska, Anna Kasperczuk, Agnieszka Dardzińska-Głębocka</i> .....	159



The importance of rotational exercise programs in the treatment of a patient with autism spectrum disorder in specialized facilities – a case report <i>Jolanta Grażyna Zuzda, Olga Jauer-Niworowska, Agata Śladewska, Michał Roman, Arkadiusz Niedziółka</i> .....	173
List of tables .....	187
List of figures.....	189

# Preface

This monograph is designed to present the recent developments in the field of biomedical engineering. The contents of the monograph present some of the research problems that are currently explored within the field of biomaterials, biomechanics, and artificial intelligence. A total of 12 chapters presented here are focused on various topics ranging from biomechanics to artificial intelligence applications in various fields.

In “*Pressure-relieving silicone orthopedic insole made by 3D printing*” the authors present the concept of a silicone orthopedic insole in which various structures and degrees of filling are used. As a result, they proved that the dynamic viscosity of silicone affects the 3D printing parameters. The proposed solution shows great potential to speed up the printing process, and the 75% honeycomb geometry fill achieves the highest stress values.

In “*System for lung X-ray image analysis using machine learning algorithms*” authors developed a system for analyzing lung X-ray images using machine learning techniques, with particular emphasis on the convolutional neural network (CNN) model. Results showed the effectiveness of the system in automatically analyzing lung X-ray images, confirming its potential as a tool to support the diagnostic process.

In “*Automatic mechanical diagnostics using deep learning methods*” the authors created a classification model using deep learning methods to classify healthy, COVID-19 and viral influenza patients based on chest X-ray images. The results demonstrated aptitude in detecting the COVID and Healthy class, achieving 71% and 81% precision, respectively. Unfortunately, the level of classification accuracy of the Influenza class is a big minus for this type of model.

In “*Application supporting the interpretation of laboratory test results*” authors proposed a new web application supporting the interpretation of laboratory test results such as blood counts, urine tests, and the levels of individual vitamins in the body. The results demonstrate a valuable contribution to the development of tools supporting laboratory diagnostics and improving the preparation of patients for medical consultations.

In “*Neuroimaging in the detection of cerebral aneurysms*” the author presents the state of the art in neuroimaging in detecting cerebral aneurysms and suggests that artificial intelligence can be applied.

In “*Utilization of the spin-coating method to produce elastic composites for applications in biomedical engineering*” authors investigated research on the use of the spin-coating method for the production of flexible composite materials. The results proved

that the spin-coating parameters affected the thickness and roughness of the composites, while they had no significant effect on the density and contact angle of tested composites.

In *“Assessment of the wettability of PDMS and denture acrylic polymer by oral gels”* the authors aimed to assess the wettability of prosthetic acrylic and PDMS surfaces by oral mucin-based gels enriched with polysaccharides such as k-carrageenan, acacia gum, carob gum, and xanthan gum. The results demonstrated the advisability of using additives in gels. It was observed that with increasing storage time of the preparations (0, 1, 3, 7 days), the average contact angle increased, and for both tested surfaces: PDMS and acrylic surfaces were the highest on the 7<sup>th</sup> day.

The study *“Mechanical properties of polylactide-based composites with iron powder additions – experimental and numerical evaluation”* aims to check the mechanical properties of the samples, and on their basis, samples were modeled for numerical tests. The results showed that samples with the addition of iron nanopowder have better properties than iron powder. Moreover, poor adhesion of metal particles to the polymer was visible.

In *“Design of an ankle joint orthosis for people with extensive sweating”* the authors' aim was the design of an ankle orthosis designed for people with excessive sweating. The developed test results made it possible to determine the effect of hyperhidrosis on the strength properties of the tested samples. They also made it possible to design an optimal ankle orthosis design.

In *“Influence of the femoral neck-shaft and anteversion angles on the loadings acting in the musculoskeletal system during walking”* the authors explored the influence of FNS and FA on muscle forces and joint reaction forces during walking. Four musculoskeletal models with a variable geometry of the femoral bone were taken into consideration. The greatest changes in active muscle forces were observed in the case of muscles with their attachments located on the proximal part of the femur. On the other hand, in the case of the hip and knee joint reaction force, the greatest differences between the results obtained using particular models were noticeable both in the values of local extrema and at the time of their occurrence.

The paper *“Key factors in bone marrow transplant outcomes: statistical insights”* examined critical factors affecting bone marrow transplant outcomes, focusing on the effect of increased doses of CD34+ cells/kg on patients' overall survival time and quality of life without inducing adverse events. The findings of this study underscored the complex interplay between various factors and the success of bone marrow transplantation (BMT). One of the key insights was the pivotal role of CD34+ cell dosage in the graft which appears to significantly influence the overall survival times of patients without introducing adverse effects that could diminish their quality of life.

In *“The importance of rotational exercise programs in the treatment of a patient with autism spectrum disorder (ASD) in specialized facilities and in rural areas – a case report”* the authors aimed to present the new program of rotational movement exercises

(PR) in the therapy of a child with ASD. The scientific justification for linking the program of rotational movement exercises (PR) with the cognitive and emotional development of a child with ASD was indicated.

We hope the readers find the monograph to be a captivating journey into the scientific world, where they immerse themselves in the themes explored within its pages.



# Pressure-relieving silicone orthopedic insole made by 3D printing

*Łukasz Bolesta<sup>1,2</sup>, Eliza Romańczuk-Ruszek<sup>1\*</sup>,  
Bogna Sztorch<sup>3</sup>, Robert Edward Przekop<sup>3</sup>*

*<sup>1</sup> Faculty of Mechanical Engineering, Institute of Biomedical Engineering,  
Białystok University of Technology, Wiejska 45C, 15-351 Białystok, Poland*

*<sup>2</sup> University of Medical Science in Białystok (WSMed),  
Krakowska 9 Street, 15-875 Białystok, Poland*

*<sup>3</sup> Centre for Advanced Technologies, Adam Mickiewicz University in Poznan,  
Uniwersytetu Poznańskiego 10 Street, 61-614 Poznan, Poland*

*lukasz.bolesta.108801@student.pb.edu.pl, \*e.romanczuk@pb.edu.pl,  
bogna.sztorch@amu.edu.pl, rprzekop@amu.edu.pl*

**Abstract:** Silicone orthopedic insoles are becoming more popular due to their unique features, such as effective correction and comfort of use. This work presents the concept of a silicone orthopedic insole in which various structures and degrees of filling are used. Additionally, the designed insert was obtained by 3D printing from two silicones with different rheological properties. The 3D printed insoles were subjected to a static compression test and their quality was examined using confocal microscopy. The results indicate that the dynamic viscosity of silicone affects the 3D printing parameters, i.e. the pressure of the extruded material and the printing speed. Moreover, the filling geometry and its percentage of filling influence the compressive strength. Silicone with a lower dynamic viscosity speeds up the printing process, and the 75% honeycomb geometry fill achieves the highest stress values.

**Keywords:** Insole, 3D printing, DIW method, Silicone, Mechanical properties

## 1. Introduction

Shoe insoles have been used for many decades to correct structural deformities and load distribution in areas of the foot that are subjected to excessive pressure. In 1865, a breakthrough was made in the field of foot orthopaedics when Everett H. Dunbar of Bridgewater, Massachusetts, introduced the first insoles designed

to minimise pain. This was pioneered by placing leather ‘insoles’ between the insole and the sole of the shoe. This innovative step was directed at providing additional support to the arch of the foot, resulting in significant relief of pain and discomfort associated with orthopedic problems [1–5].

Modern technology is revolutionizing many fields, including orthopedics. Traditional methods of manufacturing orthotics are slowly giving way to innovative solutions such as the use of computer numerically controlled (CNC) machine tools or 3D printing, particularly the FDM method. These methods not only speed up the production process, but also enable orthotics to be precisely tailored to individual patients’ needs. Both of these technologies are used to produce orthopedic insoles. The CNC method has gained enormous popularity in many fields, including orthopedics. The capability of CNC equipment makes it possible to achieve complex shapes. This allows orthotics to be tailored to each patient’s biomechanical requirements. The manufacturing process of orthotics using the CNC method is largely automated, allowing for faster and more efficient production of orthotics while reducing the waiting time for the finished product [6-9]. The CNC method was an innovation compared to traditionally produced insoles. However, with the development of 3D printing, the possibility of using this technology to produce orthopedic insoles was noticed. 3D printing allows for individualization of the design and a faster manufacturing process [5–8].

3D printing using fused deposition modelling (FDM) is one of the most common incremental manufacturing processes [10]. In a study by Uday Kumar Jonnala et al.[11] an innovative method for designing orthotics was proposed, using a mesh structure whose manufacture was based on incremental manufacturing methods, particularly FDM technology. The application of this method took place in the context of orthopedic insole design, which helped to reduce the cost of manufacturing custom orthotics. The design of the orthopedic insole used a gyro lattice structure, which is a 100% density fill type TPMS structure, and the printing material was soft PLA. In order to customise the design and production of the orthotics, it was necessary to use CAD tools, allowing full use of incremental manufacturing technology. This technique not only helps to reduce the time required for design, but is also economically viable. With this approach, orthopedic insoles can be efficiently adapted to individual patient requirements, while reducing production costs. The developed design methodology can be applied to different types of footwear and has a high market potential for people with comparable needs. Using this method, the patient achieves a high level of personalisation. This study focuses on the design and production of orthotic insoles, but does not consider clinical effectiveness or end-user comfort [11].

As noted earlier, the most commonly used 3D printing technology is FDM. However, it has limitations in terms of the materials from which the inserts can be made. One of the newest 3D printing methods is Direct Ink Writing (DIW), which allows to print elements from semi-liquid materials. Direct Ink Writing (DIW, direct ink writing) is a technology based on extruding material through a nozzle without heating it. The extrusion of the material is carried out by the movement

of a piston pushing the extruded material. Two mechanisms are mainly used to push the piston: a screw and a pressure mechanism. A schematic of the method described is shown in Fig. 1. The aim of this technology is to produce parts by extruding concentrated slurries that are formulated from the main material and additives to achieve the desired viscoelastic properties. The relationship between the ink rheology and the various printing parameters in the DIW method is crucial to achieve the intended shapes of parts with the desired physical and mechanical properties [12–17].

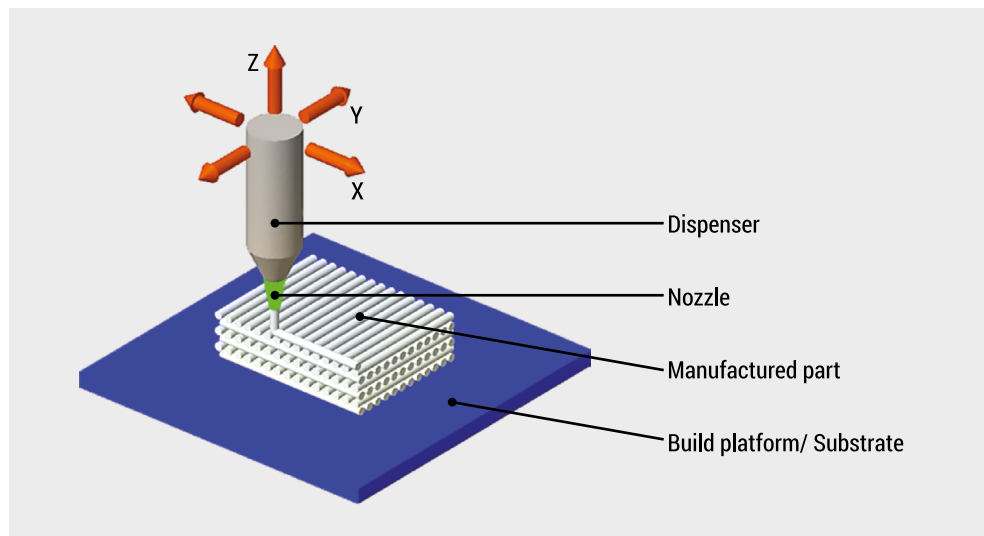


FIG. 1. Schematic of printing using DIW technology [17]

In this work, 3D printing technology using the DIW method was used to produce an orthopedic relief insole. The work focused on analyzing the influence of material rheology on the printing process and the quality of the insole.

## 2. Materials and methods

The concept behind the developed orthotic is to create a universal orthotic shape that would not only meet medical standards, but also provide patients with maximum comfort and improved quality of life during gait. The whole process started with an analysis of commercially available orthotics, design and manufacturing technology. Key aspects included ergonomics, foot biomechanics, structural durability, and effectiveness in correcting various gait disorders. Based on the dimensions of the commercial orthotic insoles, a concept of the in-house model was developed in CAD software – SOLIDWORKS CAD 3D (Fig. 2, 3).





FIG. 2. 3D model created in SOLIDWORKS CAD

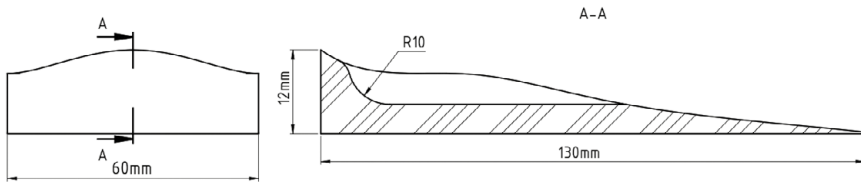


FIG. 3. Dimensions of an orthopedic insole

The proposed orthotic concept allows the user to customise different orthotic filling structures for the designated area in Fig. 4 – highlighted in red. With this concept, the user has the flexibility to choose the structure and the degree of filling, allowing the orthotics to be tailored to individual needs and preferences. This solution ensures that the orthotic insole can be personalised, which is key to dealing effectively with different foot health problems.



FIG. 4. Orthotics insole area subjected to filling modification with different structures and degrees of filling

Three types of infill were assumed: rectangular, honeycomb, triangular, and different degrees of infill: 50%, 75% and 100% (Table 1), in order to test the influence of the type and degree of filling on the properties of the resulting orthotic insole.

TABLE 1. Type and degree of filling of the orthopedic insole used in the study

Type of filling	Degree of infill [%]
Rectangular	50; 75
Honeycomb	50; 75
Triangular	50; 75
Full	100

The orthotic was printed from two different types of silicone: [3-(N, N-di-methylamino) propyl] trimethoxysilane (denoted as silicone A), and a medical silicone based on polysiloxanes (denoted as silicone B).

The orthopedic silicone insoles were printed on the F-NIS 23151 3D printer from Sygnis S.A. The printer is based on DIW (Direct Ink Writing) technology, which allows printing from semi-liquid materials, e.g. silicones or single-component pastes, e.g. gypsum. During printing, a 55 ml cartridge and a 0.63 mm nozzle were used. The height of the applied layers was 0.3 mm. For the printing, the parameters listed in Table 2 were used. The printing parameters were chosen based on previous test trials on the materials to eliminate inefficient settings and ensure optimal quality and efficiency of the process. Simplify 3D software provided by the printer manufacturer was used to print the orthotics, which enabled efficient preparation of the model for printing.

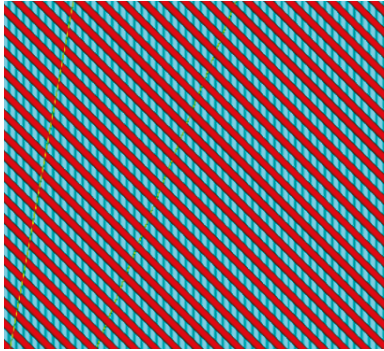
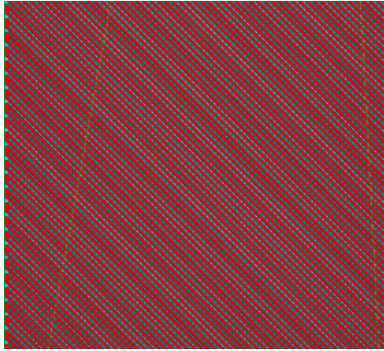
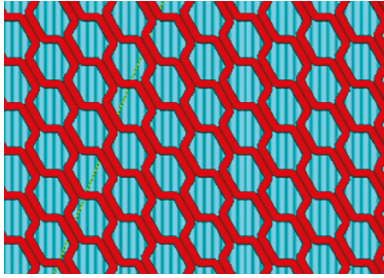
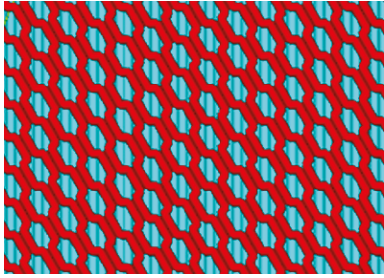
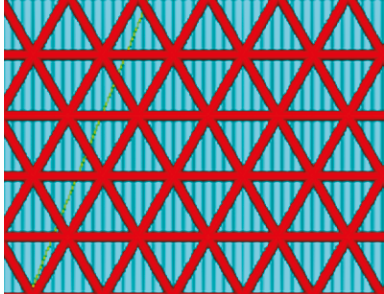
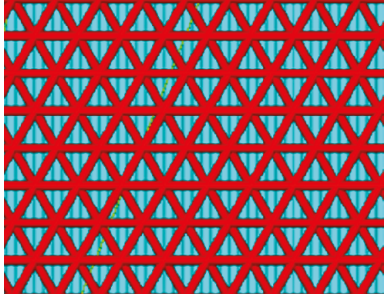
TABLE 2. Printing parameters for silicones

Type of silicone	Parameter	Type of filling		
		Rectangular	Honeycomb	Triangles
<b>A</b>	Printing speed [mm/s]	0.4	0.3	0.3
	Pressure [MPa]	0.90	0.80	0.8
<b>B</b>	Printing speed [mm/s]	0.6	0.5	0.5
	Pressure [MPa]	0.110	0.100	0.100

The printing process was carried out using adjusted printing parameters, i.e. printing speed and air pressure, which depended on the type of silicone used. The introduction of variable printing parameters during the process is adapted to the properties of the specific silicone and, in the case of polysiloxane-based silicone, the possibility to increase the printing speed is an important aspect. As a result, the printing of the insert can take place in a shorter time, which is important for applications requiring fast and precise printing.

Different fill levels have been adopted: 50%, 75% and 100% for each silicone. The 100%-filled inserts acted as a reference sample for the printed inserts with varying fill levels, as the commonly used commercial silicone inserts are characterised by 100% fill. Table 3 shows images of the different degrees of filling and the type of filling.

TABLE 3. Comparison of the degree of infill for different types of infill

Type of filling	50%	75%
<b>Rectangular</b>		
<b>Honeycomb</b>		
<b>Triangles</b>		

During the layered printing process of the rectilinear infill, a technique was used to apply successive layers at 90 degrees to the previous layer in order to achieve a uniform and optimal distribution of material. A representation of this process is illustrated in Figure 5. This strategy aims to increase the stability and uniformity of the infill structure, resulting in improved mechanical strength and properties of the final article.

The rheological testing of the silicones was carried out on a Haake RheoStress 6000 rheometer in a plate-to-plate system, where the silicone under test was placed directly onto a 21°C plate. Three measurements containing 1 ml each of the test silicone ([3-(N,N-dimethylamino)propyl]trimethoxysilane and polysiloxane-based silicone) were carried out for each silicone. The samples were tested over a period of 100 seconds.

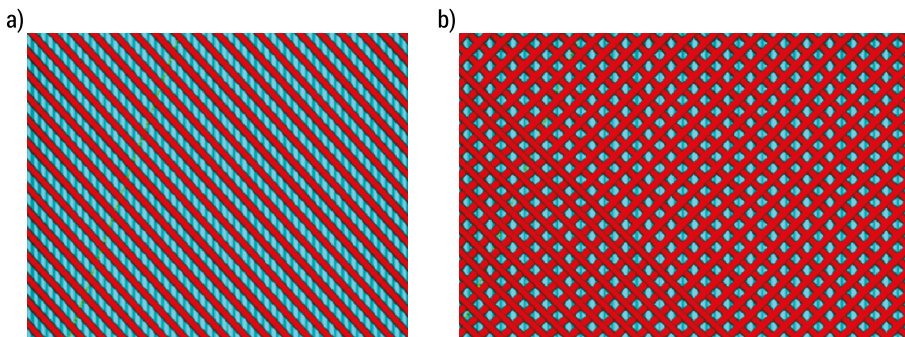


FIG. 5. Layering method for rectilinear infill: (a) first layer; (b) second layer applied at 90°

The compressive strength test was carried out using a Zwick Roell Z010 on 15x15 mm cylindrical specimens. The dimensions of the test specimens were chosen to prevent it from buckling under load, which can significantly affect the results.

The specimens were subjected to a static compression test with a speed of 10mm/second and an initial force of 1N. During the experiment, the specimen was subjected to compression along the main vertical axis. Before proceeding to the actual tests, seven test trials were carried out for each silicone. One test for each variant shown in Table 1 to determine the threshold of significant deformation. The deformation threshold for the test materials was assumed to be 60%. The specimens for the static compression test were characterized by the same structure and degree of filling used in the inserts. Two types of silicone were used. The type and degree of filling are described in Table 1. On the basis of the tests carried out, the stress  $\sigma$  and strain  $\epsilon$  of the material were calculated and the stress-strain relationship curves were plotted.

The printed insoles were subjected to microscopic observation on an Olympus OLS 4000 LEXT laser confocal microscope. The microscopic observation allowed the quality of the printed insole filling to be checked. When the LEXT OLS4000 microscope is operated in confocal mode, an image is generated based on the reflection of light from a specific focus plane. The benefits of confocal microscopy include the ability to produce high contrast images, the reduction of interference associated with focusing in different planes, and the ability to analyse three-dimensional structures.

### 3. Results and discussion

Testing of the rheological properties of the silicones used made it possible to determine the influence of rheology on printing parameters and print quality. After analysing the test results, significant differences were observed between the results obtained for the two types of silicone. The dynamic viscosity shown in Figure 6 for silicone A starts at 3234.83 Pa·s and decreases to a value of 500 Pa·s at a shear rate of 10 [1/s]. For silicone B (Figure 7), the initial dynamic viscosity value reaches 639.02 Pa·s

and drops to a value of 100 Pa·s at a shear rate of 20 [1/s]. Table 4 shows an averaged summary of the maximum and minimum dynamic viscosity values obtained in the test carried out for both silicones.

TABLE 4. Averaged maximum and minimum dynamic viscosity values obtained in the test for silicone A and B (source: own elaboration)

Dynamic viscosity value	A	B
Maximum [Pas]	3234.83±20.12	639.02±6.12
Minimum [Pas]	105.46±1.25	44.21±1.24

Based on the graphs shown in Figures 6 and 7 and the data in Table 4, it was noted that silicone A has 5 times higher dynamic viscosity than silicone B, which alters the parameters when printing orthotics. The lower dynamic viscosity of silicone B allowed for a shorter printing time for the orthotics compared to silicone A. It was noted that the differences in the rheology of the silicones tested significantly affected both printing time and printing pressure. In the work by Wei et al [18], the influence of rheology on the quality of DIW printing was analyzed. This work showed that the rheology of materials has a significant impact on the quality and speed of printing, which was noticed in this work. Additionally, Wei's work analyzed the influence of the chemical composition of materials. This analysis shows that the composition of the material used and its cross-linking time have a significant impact on the quality of prints, but also on the ability of the printed object to maintain its shape and the weight of subsequent layers. A similar conclusion can be seen based on the results presented in this paper.

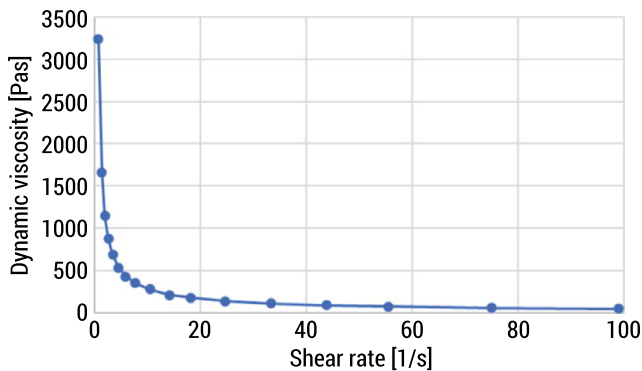


FIG. 6. Plot of dynamic viscosity versus shear rate for silicone A

In this study, a static compression test was carried out for all types and degrees of filling. A static compression test was chosen for the study because silicone insoles are subjected to pressure during use. Table 5 and Table 6 show the average compressive strength ( $R_c$ ) values, which served as the basic data for creating comparison charts

for the different sample types and for analysing the  $R_c$  values. The 100% infill, which achieved a stress of 3.18 MPa, provided a benchmark for the other cases. The closest to this was the variant with a honeycomb infill of 75%. This result suggests that a certain reduction in the degree of filling slightly affects the achieved stress, which may be an important aspect from the point of view of efficiency and production costs. In contrast, the lowest stress value was obtained for the triangular infill variant at 50%. This observed reduction in the stress value may be due to the smaller amount of material, which in turn affects the mechanical properties. When comparing the values for silicone B shown in Figure 9, the 100% infill achieved a strength of 2.05 MPa, which provides a reference value for comparison. The closest to this result was the variant with a triangular filling of 75%, suggesting that reducing the degree of filling slightly affects the strength obtained. In contrast, the lowest strength value was obtained for the triangularly filled variant at 50%, similar to the silicone A.

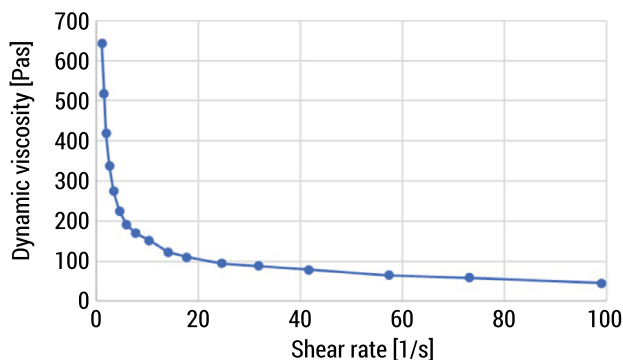


FIG. 7. Plot of dynamic viscosity versus shear rate for silicone B

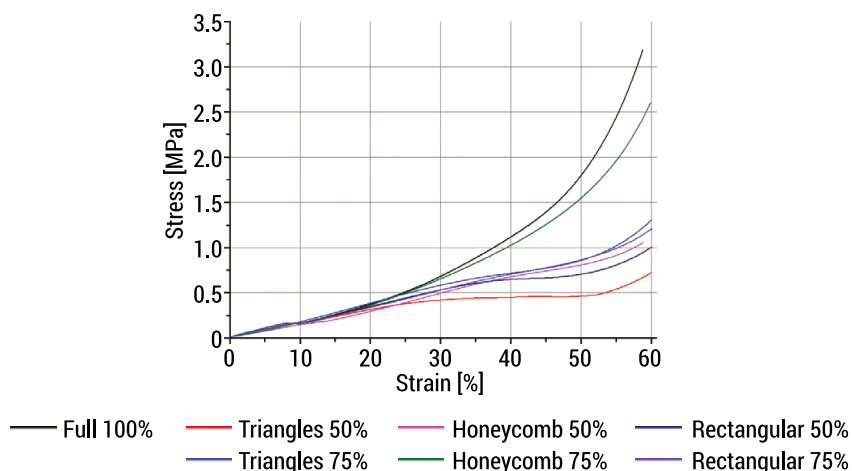


FIG. 8. Stress-strain relationship for similar values of average  $R_c$  of silicone A

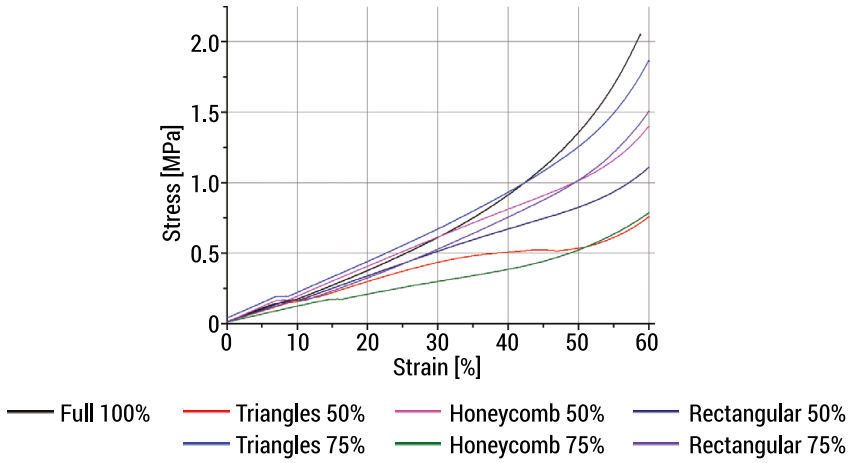


FIG. 9. Stress-strain relationship for similar values of average  $R_c$  of silicone B

TABLE 5. Medium  $R_c$  values of silicone A for different filling types and their filling grades

Type of silicone	Silicone A						
Type of filling	Rectangular		Honeycomb		Triangles		Full
Degree of infill [%]	50	75	50	75	50	75	100
Compressive strength ( $R_c$ ) [MPa]	1.01±0.01	1.21±0.02	1.06±0.01	2.59±0.04	0.72±0.01	1.30±0.03	3.18±0.07

TABLE 6. Medium  $R_c$  values of silicone B for different filling types and their filling grades

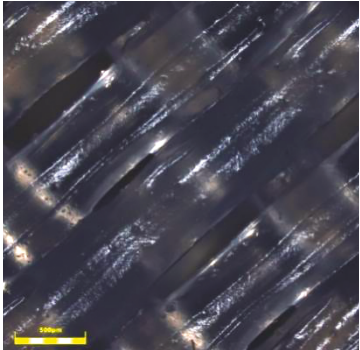
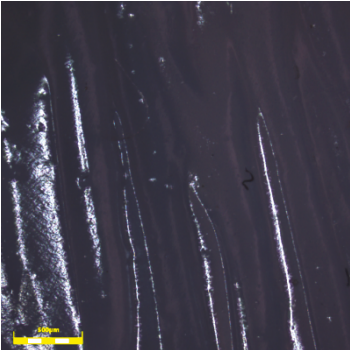
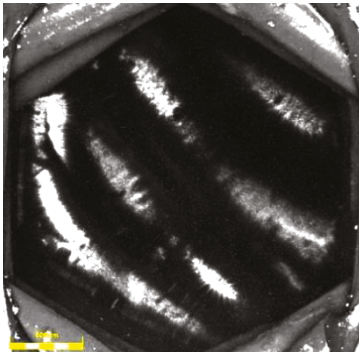
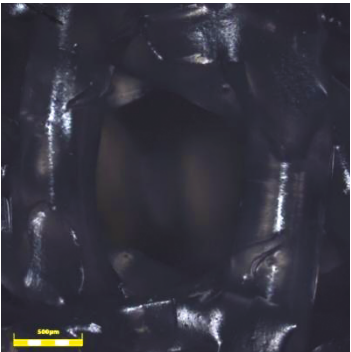
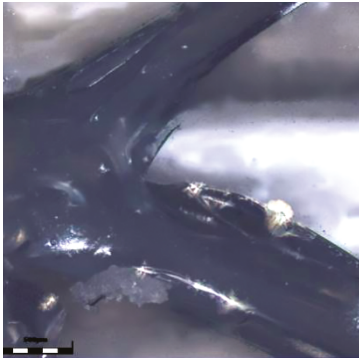
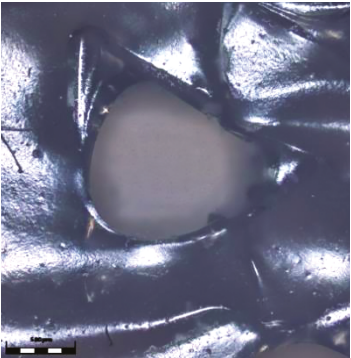
Type of silicone	Silicone B						
Type of filling	Rectangular		Honeycomb		Triangles		Full
Degree of infill [%]	50	75	50	75	50	75	100
Compressive strength ( $R_c$ ) [MPa]	1.11±0.02	1.51±0.04	0.79±0.01	1.87±0.03	0.76±0.01	1.40±0.04	2.05±0.06

The microscope images obtained are summarised in Table 7 for silicone A and in Table 8 for silicone B. During the microscopic observations, it was observed that the structure with 50% infill showed larger geometric details compared to the structure with 75% infill. This may be due to differences in the amount of material used for printing and the effect of the degree of filling on the overall



form of the structure. In addition, it is an important fact that the cross-linked structure retains its original shape and did not deform, demonstrating the effectiveness of the cross-linking process in maintaining the intended form of the structure.

TABLE 7. Magnification of the structures obtained after printing for silicone A

Type of filling	50%	75%
Rectangular		
Honeycomb		
Triangles		



During the printing process, the triangle angles were assumed to be  $60^\circ$ . Subsequently, the triangle angle was measured during microscopic observation, confirming that the results obtained were consistent with the initial assumptions. Figure 10 shows the measurement of the triangle angle, confirming that the printing process was correct and in line with the theoretical assumptions.

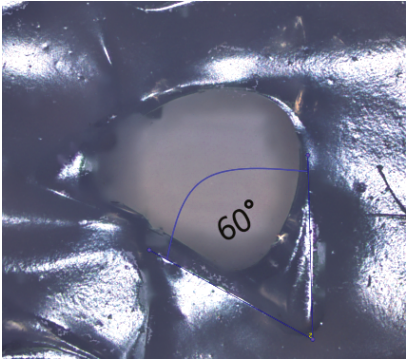
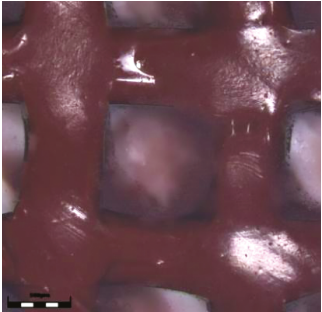
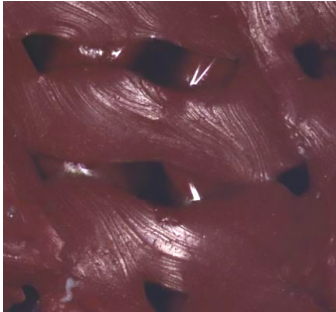
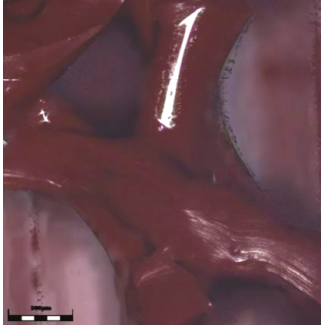
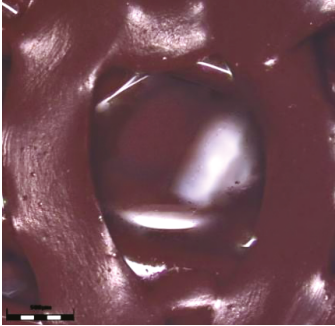
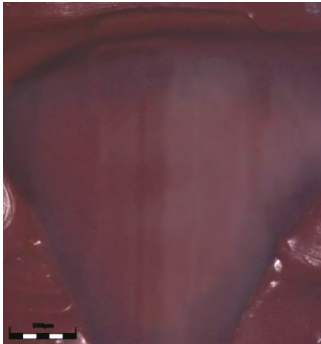
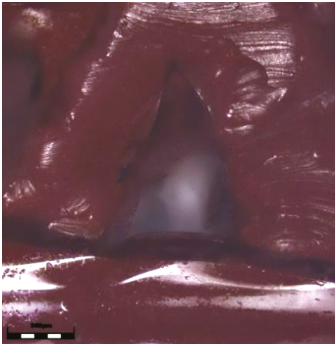


FIG. 10. Angle measurement for triangular infill

The better quality of the structures obtained (Table 8) in the case of silicone B can be related to its distinctive color (red). Silicone A, which was used, was colorless, which affected the detail of the visible structures, compared to silicone B with its distinct color. The color of the material can affect the contrast and visibility of detail during microscopic observation, which can be crucial for analysing the geometry and quality of the structure. It is also worth considering that differences in the visibility of structures may be due not only to the color of the material, but also to other optical properties such as transparency, gloss or light absorption. Therefore, the presence of color in a material can affect the effectiveness of microscopic observation and the interpretation of results.

TABLE 8. Magnification of the obtained structures after printing for silicone B

Type of filling	50%	75%
Rectangular		

Type of filling	50%	75%
Honeycomb		
Triangles		

During the printing process, a nozzle with a diameter of 0.63 mm was used. After microscopic observation, the width of the layers is 0.5 mm (Fig. 11). This indicates the existence of material shrinkage during the crosslinking process, especially in the context of the filling structure. It is noteworthy that despite the crosslinking process, the width of the inserted insole did not change, suggesting that the shrinkage of the material on the outside of the insole will not reduce the size of the insole for a given size of the structure.

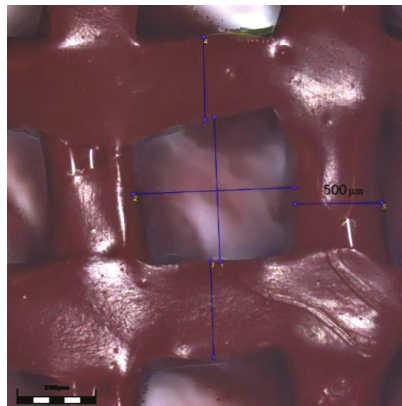


FIG. 11. Measurement of the width of the obtained layer

The orthotics shown in Figures 12 were printed from type A silicone, characterized by a smooth and transparent structure, and represent an innovative solution in the field of orthopedic products. Their unique flexibility and softness make them an ideal material for use in the production of orthotics, especially in the context of orthopedic prosthetics. The transparent structure of silicone makes it possible to observe the shape of the filling, which is crucial in the process of customizing orthotics. The use of Type A silicone insoles pushes the boundaries of conventional solutions, while offering comfort and effective support for different areas of the foot. In the case of insoles made of silicone B, the internal structure is not possible due to the color of the silicone used, as shown in Figure 13 a. Only after removing the top layer (1 print path), which shields the internal structure, can we observe its internal shape, shown in Figure 13 b.

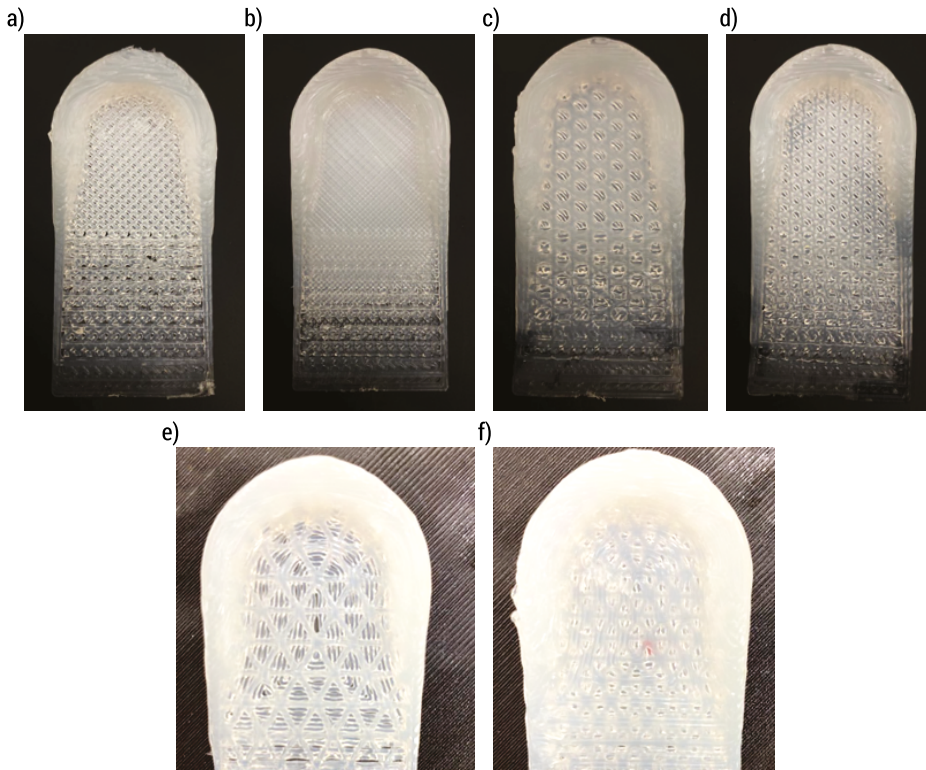


FIG. 12. Orthotic insole printed from silicone A with: a) rectilinear shape filling and 50% degree of infill, b) rectilinear shape filling and 75% degree of infill, c) honeycomb filling and 50% degree of infill, d) honeycomb filling and 75% degree of infill, e) triangular shape filling and 50% degree of infill, f) triangular shape filling and 75% degree of infill

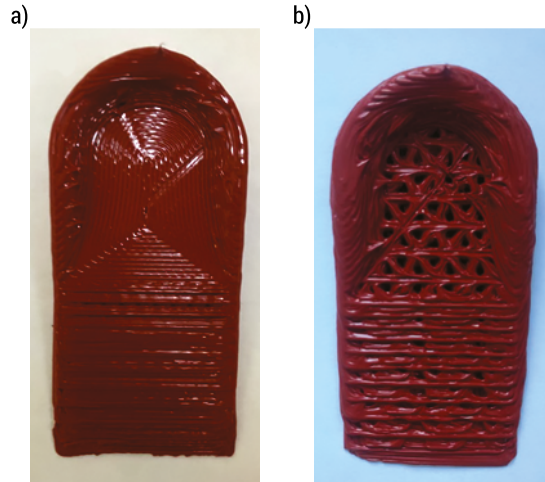


FIG. 13. Orthotic insole printed from silicone B: a) with triangular shape filling and filling degree of 75%, b) with triangular shape filling and filling degree of 50%

The results presented in this paper indicate that the mechanical properties are influenced by both the rheology of the printed material and the type and degree of filling. Similar conclusions were presented in the work of Farkas et al. [19] in which the influence of the direction (different layer angles: 0°, 45° and 90°) and the thickness of the printing layer on the tensile and compressive properties of the dental material were analyzed. Research has shown that both the direction and thickness of the printing layer affect the mechanical properties.

## 4. Conclusion

The orthotic was developed with a variety of structures in relief areas to provide optimal support and comfort for the patient. The use of 3D printing allows the creation of personalized orthotic solutions, tailored to the individual needs of each patient. The dynamic viscosity of the silicone material affects the 3D printing parameters (speed, pressure). For silicone with a lower dynamic value, a higher 3D printing speed and lower pressure were used. An important factor affecting the mechanical properties of such an insole is the variety of densities and types of filling, which has a significant impact on its resistance to compression. Moreover, silicone with a higher dynamic viscosity is characterized by higher mechanical properties compared to silicone with a lower dynamic viscosity. This makes it possible to precisely tailor the insole to the specific pathology the patient is facing. Despite the even distribution of traces in the printing process, imperfections in materials such as silicone can occur in the form of air bubbles, which may require further technological improvements to eliminate.

## References

1. Brown C., Clinical Advantage: Making Your Own Temporary Foot Orthosis. *Orthopaedic Physical Therapy Practice*, 2014, 26(3), 204–207.
2. Domínguez-Morales M.J., Luna-Perejón F., Miró-Amarante L., Hernández-Velázquez M., Sevillano-Ramos J.L., Smart Footwear Insole for Recognition of Foot Pronation and Supination Using Neural Networks. *Applied Sciences*, 2019, 9(19), 3970.
3. Nigg B.M., Herzog W., Read L.J., Effect of viscoelastic shoe insoles on vertical impact forces in heel-toe running. *The American Journal of Sports Medicine*, 1988, 16(1), 70–76.
4. Crabtree P., Dhokia V.G., Newman S.T., Ansell M.P., Manufacturing methodology for personalised symptom-specific sports insoles. *Robotics and Computer-Integrated Manufacturing*, 2009, 25(6), 972–979.
5. Anthony A.A., Anggoro P.W., Jamari J., Bayuseno A.P., Advanced Manufacturing Process of Orthotic Shoe Insoles Using A New Material Based on the Taguchi Methodology. *Proceedings of 2<sup>nd</sup> Borobudur International Symposium on Science and Technology (BIS-STE 2020)*, 2021, 203, 372–380.
6. ICONIC – Materials for the production of insoles, <https://sklep.iconic.pl/produkty/materialy-do-produkcji-wkladek> (access: 26.01.2024).
7. Yick K.L., Tse C.Y., The use of textiles and materials for orthopedic footwear insoles. In: *Handbook of Footwear Design and Manufacture*, ed. A. Luximon, Woodhead Publishing 2021, 361–388.
8. Mendes A.A.M.T., Silva H.J. de A., Costa A.R.A., Pinheiro Y.T., de Lins C.A.A., de Souza M.C., Main types of insoles described in the literature and their applicability for musculoskeletal disorders of the lower limbs: A systematic review of clinical studies. *Journal of Bodywork and Movement Therapies*, 2020, 24(4), 29–36.
9. Anggoro P.W., Anghony A.A., Tauviquirrahman M., Jamari J., Bayuseno A.P., Reverse innovative design and manufacturing strategy for optimizing production time of customized orthotic insoles with CNC milling. *Journal of Physics: Conference Series*, 2020, 1517(1).
10. Alizadeh-Osgouei M., Li Y., Vahid A., Ataee A., Wen C., High strength porous PLA gyroid scaffolds manufactured via fused deposition modeling for tissue-engineering applications. *Smart Materials in Medicine*, 2021, 2, 15–25.
11. Jonnala U.K., Sankineni R., Kumar Y.R., Design and development of fused deposition modeling (FDM) 3D-Printed Orthotic Insole by using gyroid structure. *Journal of the Mechanical Behavior of Biomedical Materials*, 2023, 145, 106005.
12. Zhou L.Y. et al., Multimaterial 3D Printing of Highly Stretchable Silicone Elastomers. *ACS Applied Materials & Interfaces*, 2019, 11(26), 23573–23583.
13. Tagliaferri S., Panagiotopoulos A., Mattevi C., Direct ink writing of energy materials. *Materials Advances*, 2021, 2, 540.
14. Lewis J.A., Smay J.E., Stuecker J., Cesarano J., Direct Ink Writing of Three-Dimensional Ceramic Structures. *Journal of the American Ceramic Society*, 2006, 89(12), 3599–3609.
15. Kim F. et al., Direct ink writing of three-dimensional thermoelectric microarchitectures. *Nature Electronics*, 2021, 4(8), 579–587.
16. del-Mazo-Barbara L., Ginebra M.P., Rheological characterisation of ceramic inks for 3D direct ink writing: A review. *Journal of the European Ceramics Society*, 2021, 41(16), 18–33.
17. Khan S.A., Lazoglu I., Development of additively manufacturable and electrically conductive graphite-polymer composites. *Progress in Additive Manufacturing*, 2020, 5(2), 153–162.

18. Wei P., Cipriani C., Hsieh C.M, Kamani K., Rogers S., Pentzer E., Go with the flow: Rheological requirements for direct ink write printability. *Journal of Applied Physics*, 2023, 134(10), 100701.
19. Farkas A.Z., Galatanu S.V., Nagib R., The Influence of Printing Layer Thickness and Orientation on the Mechanical Properties of DLP 3D-Printed Dental Resin. *Polymers* (Basel), 2023, 15(5), 1113.



# System for lung X-Ray image analysis using machine learning algorithms

*Aleksandra Chilimonik<sup>1</sup>, Anna Kasperczuk<sup>1\*</sup>,  
Małgorzata Zdrodowska<sup>1</sup>, Agnieszka Dardzińska-Głębocka<sup>2</sup>*

*<sup>1</sup> Faculty of Mechanical Engineering, Institute of Biomedical Engineering,  
Białystok University of Technology, Wiejska 45C, 15-351 Białystok, Poland*

*<sup>2</sup> Faculty of Mechanical Engineering, Institute of Mechanical Engineering,  
Białystok University of Technology, Wiejska 45C, 15-351 Białystok, Poland*

*aleksandra.chilimonik.108806@student.pb.edu.pl, \*a.kasperczuk@pb.edu.pl,  
m.zdrodowska@pb.edu.pl, a.dardzinska@pb.edu.pl*

**Abstract:** This chapter focuses on the development of a system for analyzing lung X-ray images using machine learning techniques, with particular emphasis on the convolutional neural network (CNN) model. The main goal was to build an effective diagnostic tool that supports the identification of various pulmonary diseases. The scope of the work includes a review of basic radiological imaging techniques, analysis and evaluation of existing methods for analyzing X-ray images, and detailed development and implementation of the CNN model. Tests conducted on real medical data demonstrated the effectiveness of the system in automatically analyzing lung X-ray images, confirming its potential as a tool to support the diagnostic process. The results of the study indicate significant opportunities for further development of the system. This work underscores how the integration of machine learning and medical image analysis can improve the quality and efficiency of diagnostic imaging, offering valuable support for physicians' therapeutic decision-making.

**Keywords:** Machine learning, Knowledge mining, X-ray image analysis

## 1. Introduction

The COVID-19 pandemic, caused by the SARS-CoV-2 virus, has led to an unprecedented health and economic crisis. While the diagnosis of SARS-CoV-2 infection is primarily microbiological, imaging techniques play a crucial role in supporting diagnosis, classifying disease severity, guiding treatment, detecting complications,



and assessing treatment response. As highlighted in the study by Chamorro et al., chest X-rays, whether performed in conventional radiology departments or using portable units, are the first-line imaging examination due to their wide availability and cost-effectiveness (“Radiologic diagnosis of patients with COVID-19”). Computed tomography (CT) of the chest is more sensitive than conventional chest X-rays, enabling the identification of complications beyond lung involvement and suggesting alternative diagnoses. The most common radiologic findings in COVID-19 include air-space opacities (consolidations and/or ground-glass opacities), typically bilateral, peripheral, and predominantly located in the lower lung fields [1].

X-ray images are one of the most widely used imaging tests in medicine. They allow a quick and non-invasive assessment of the condition of chest organs. However, the correct interpretation of X-ray images often requires a high level of knowledge and experience on the part of the physician, which can be a limiting factor in situations where a quick and accurate diagnosis is needed. The amount of imaging data in today’s medical environment continues to grow, creating the need for new, more optimal methods of image interpretation. In addition, X-ray images can be subject to artifacts or distortions, making them difficult to evaluate.

Therefore, there is a need to develop a system that, using machine learning algorithms, would be able to automatically analyze lung X-ray images and detect various abnormalities in them. Such a system could significantly improve the quality and efficiency of diagnostic imaging, as well as assist doctors in making therapeutic decisions.

Visual inspection of X-ray images is a fundamental step in radiological diagnostics, where an experienced radiologist evaluates the image to identify features characteristic of various medical conditions. This method involves analyzing images to detect abnormalities such as changes in tissue density, the presence of foreign bodies, bone fractures, and other anomalies. It is often complemented by additional diagnostic methods, including those that utilize machine learning [2].

Segmentation aims to divide the image into regions characterized by uniform properties or belonging to specific objects within the image. This process involves indexing, which assigns identifiers to individual objects [3]. There are three main types of segmentation methods [4]:

- Thresholding: Separates objects from the background based on a set intensity level.
- Region-based methods: Group pixels based on their similarity.
- Edge-based methods: Rely on detecting intensity changes to delineate object boundaries.
- In the context of X-ray images, filters are commonly used to enhance contrast and extract details of anatomical structures, as well as to reduce noise that can distort the image.

Texture in medical images refers to patterns of pixel intensity that can contain information about tissue structure. Texture analysis focuses on extracting features that describe these patterns at different scales and directions. This technique aims

to extract information to understand and characterize differences between image regions [5]. The primary approach to texture analysis includes statistical methods that examine pixel intensity distributions and their statistics [6]:

- Histogram Analysis: Studies the distribution of pixel intensities to extract texture features.
- Gray-Level Co-occurrence Matrices (GLCM): Analyze texture by assessing how often different combinations of pixel intensities occur together.

Other techniques, such as model-based methods including fractal analysis, allow for evaluating texture complexity. In X-ray images, these methods can identify structural tissue changes characteristic of specific medical conditions. The application of machine learning, particularly deep learning, opens new possibilities in texture analysis. Neural networks, especially convolutional neural networks (CNNs), can be trained to recognize subtle texture patterns in X-ray images, significantly improving diagnostic accuracy [7].

Radiomics is a method that extracts a large number of features from medical images using data-characterization algorithms. Unlike other image analysis methods like segmentation or texture analysis, radiomics takes a comprehensive approach, focusing on extracting a vast amount of quantitative features from medical images. This includes not only texture but also shape, intensity, and multidimensional patterns. Radiomics can identify subtle patterns in images that may not be visible to the human eye but can indicate specific disease characteristics, such as tumor aggressiveness or treatment response [8, 9].

Most recent radiomics studies use manual feature extraction techniques, such as texture analysis, followed by classical machine learning classifiers like random forests or support vector machines. There are several differences between these methods and CNNs. First, CNNs do not require manual feature extraction. Second, CNN architectures do not necessarily need expert segmentation of tumors or organs. Third, CNNs require much larger datasets due to millions of parameters involved in training, making them more computationally intensive and needing graphical processing units (GPUs) for model training [10, 11].

Convolutional neural networks (CNNs), used in image data processing, mimic the mechanisms of animal visual systems. They operate by applying filters or kernels to create feature maps from visual input data, processing them similarly to how the animal visual cortex responds to seen images. In animal brains, individual neurons are sensitive to limited areas of the visual field, and their connections form a comprehensive image. In CNNs, each feature map represents a fragment of complex visual information [12].

The many hidden layers in deep neural networks enable them to interpret more complex patterns than traditional convolutional models. These different layers learn various aspects of the data. For example, with image inputs, the initial layers may interpret basic features like pixel brightness, while later layers detect more complex features like shapes or edges used to identify objects in the image. Increasing

the number of layers allows the network to extract more abstract or complex features from the input data. In other words, the more layers a network has, the better it can recognize and analyze deeper, more intricate patterns and features in the input data [13].

In the context of X-ray images, deep neural networks function similarly. The initial layers focus on detecting basic features like contrasts and textures. Subsequent layers learn to recognize more complex patterns, such as specific tissue structures or signs of pathology. This way, deep networks can effectively analyze X-ray images, identifying subtle diagnostic features that may be invisible to the human eye [14].

In summary, the literature indicates a rapid advancement in the use of advanced machine learning techniques, particularly deep learning models, for more accurate and efficient X-ray image analysis. However, there remains a need for further development of algorithms to improve their effectiveness, given the relative novelty of techniques like CNNs.

The purpose of this work is to develop a tool for analyzing lung X-ray images using a system based on machine learning algorithms, which would be an effective diagnostic tool to help identify lung diseases.

## 2. Lung disease classification program

### 2.1. System assumptions

The built system uses convolutional neural networks (CNN) to analyze chest X-ray images, with the aim of diagnosing whether a given case is COVID-19, pneumonia, or the patient's health condition.

The development of the system consisted of building a CNN model that would be able to correctly diagnose lung X-rays in terms of the diseases being studied.

COVID-19 and pneumonia require different treatment protocols. A quick and precise diagnosis can ensure that patients receive the right therapy. For example, treatment of COVID-19 may require specific antiviral agents, isolation, and contact tracing, while bacterial pneumonia is often treated with antibiotics [15].

Both of these diseases may show some similarities, such as the presence of infiltrative lesions and inflammatory clusters, which presents a diagnostic challenge. The introduction of a convolutional network (CNN) model can significantly help differentiate between COVID-19 and other forms of pneumonia based on X-rays. CNNs are particularly effective at image analysis due to their ability to detect complex patterns and features in visual data [2]. The tool is designed to support the diagnostic process, minimize the time needed for accurate diagnosis and reduce the risk of misdiagnosis.

An important consideration in the interpretation of lung X-rays, especially when identifying ground-glass opacities (GGO), is ensuring accurate differentiation between various conditions that present similar radiological features. This is highlighted in the work of Van Dalfsen and Delsing, who emphasize that not all GGO patterns are indicative of COVID-19 (“Niet elke matglasafwijking duidt op COVID-19”). Their study presents cases where initial diagnoses based on GGO were revised after further testing revealed alternative causes such as *Pneumocystis jiroveci* pneumonia or autoimmune pneumonitis. Incorporating these insights into our analysis underscores the necessity of a comprehensive approach in the development of machine learning models for lung X-ray analysis. Our system aims to integrate such nuanced understanding, thereby enhancing its diagnostic accuracy and utility in clinical settings. By referencing relevant literature, we ensure that our diagnostic tool not only identifies GGOs but also supports differential diagnosis, improving overall patient outcomes [16].

## 2.2. Analysis and preparation of image data

The first step before proceeding with the construction of the convolutional network (CNN) model was to collect, prepare and analyze the data that will be used later for training, validation and testing of the model. X-rays were taken with signs of pneumonia, with symptoms of COVID-19 and with healthy lungs with no signs of disease.

The data used in this study come from anonymous collections made publicly available on the Kaggle platform [14, 17–19].

The data was taken from several datasets to increase their diversity in order to create a more efficient model that will be better able to generalize and recognize patterns on new data from different sources.

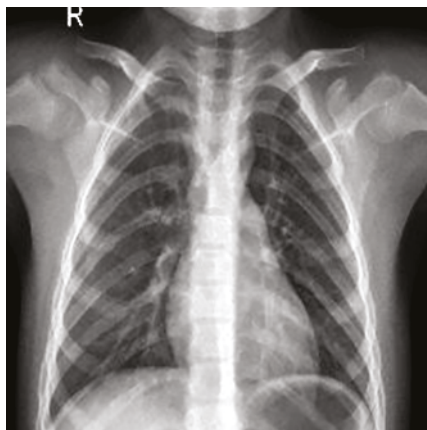


FIG. 1. Sample X-ray image without signs of disease [17]

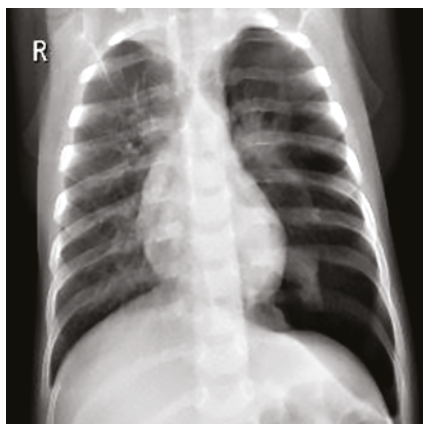


FIG. 2. Sample X-ray image of pneumonia [18]

In the next part, the data sets prepared in this way can be used to build a list of images and labels and to group them. Image paths were combined with the corresponding labels to build a dataset that includes image paths and their corresponding classification labels (0 – healthy, 1 – pneumonia, 2 – COVID-19).

**Healthy:** Chest X-rays of healthy patients. The lungs appear to be clear with no apparent abnormalities such as significant shading, spots, or abnormal structures [20].

**Pneumonia:** X-ray images of patients with pneumonia. Certain areas of shading or consolidation that are characteristic of pneumonia can be observed in the images [21].

**COVID-19:** X-ray images of patients with confirmed COVID-19. They are characterized by more scattered “milky glass” patterns, as well as other irregularities, which are indicative of viral pneumonia caused by SARS-CoV-2 [15].

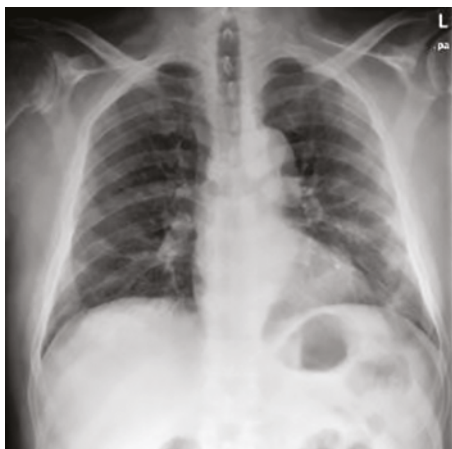


FIG. 3. Sample X-ray image of COVID-19 [4]

Each image must be properly processed before being uploaded to the CNN model. For this purpose, a `process_data` function is defined that reads the image, converts it to grayscale, normalizes the pixel values, and resizes each image to a format (244x244 pixels). They are then converted into an array, which will allow the algorithm to read the data from the images.

Each of the collections contains 244-by-244-pixel images in a single-channel, i.e. converted to grayscale. The training set consisted of 3075 X-ray images, the test set consisted of 711 images, and the validation set consisted of 693 images. Labels used in a “one-hot” format, which made it possible to evaluate the model on data that was not used during the training process.

TABLE 1. Dataset dimensions used in the CNN model: Number of samples and image dimensions for training, test, and validation, along with their corresponding class label counts

Dataset	The shape of the data	Shape Labels
Data Training	(3075. 244. 244. 1)	(3075. 3)
Test data	(711. 244. 244. 1)	(711. 3)
Data validation	(693. 244. 244. 1)	(693. 3)

## 2.3. Building and training of the CNN model

Properly prepared data was used in the next step to train the convolutional neural network model. The model chosen for this purpose is a sequential model from the Tensorflow Keras library, which is a special library for Python. The choice of this model was a compromise between its simple implementation and the lack of the need for a large computing power of a computer, and the ability to detect complex features in the lung X-rays used.

The programming structure of the CNN model is as follows:

```
model1 = Sequential([
Conv2D(16, (3, 3), activation = 'relu', input_shape = (244, 244, 1)),
MaxPooling2D(2, 2),
Conv2D(32, (3, 3), activation = 'relu'),
MaxPooling2D(2, 2),
Conv2D(64, (3, 3), activation = 'relu'),
MaxPooling2D(2, 2), Flatten(),
Dense(128, activation = 'relu', kernel_regularizer = l2(0.001)), Dropout(0.55),
Dense(3, activation = 'softmax')
```

A summary of the architecture of the model, which was later used to train the model, is presented in the form of a table. Individual layers, the shape of the data and the number of parameters to be learned are highlighted.

TABLE 2. Summary of the Sequential CNN Model

Layer	Shape	Parameters to learn
conv2d	242. 242. 16	16
max_pooling2d	121. 121. 16	0
conv2d_1	119. 119. 32	4640
max_pooling2d_1	59. 59. 32	0
max_pooling2d_2	57. 57. 64	18496
flatten	50176	0
dense	128	6422656
dropout	128	0
dense_1	3	387

- First Convolutional Layer (Conv2D): It consists of 16 filters of  $3 \times 3$  size and expects an input of  $244 \times 244$  pixels in grayscale. This layer allowed us to capture the general features of the image and reduced computational complexity. It contained 160 parameters for learning.
- First Layer MaxPooling (MaxPooling2D): Reduced the dimensionality of the data by taking the maximum of a  $2 \times 2$  window and moving it by 2 pixels. It didn't have the parameters to learn.
- Second Convolutional Layer (Conv2D): Consisting of 32 filters of  $3 \times 3$  size, it allowed to catch more complex and detailed features of the images. It contained 4640 parameters for learning.
- Second MaxPooling Layer (MaxPooling2D): Like the first MaxPooling layer, it reduced the spatial dimensions of the image, limiting the number of parameters and calculations in the network.
- Third Convolutional Layer (Conv2D): Made up of 64  $3 \times 3$  filters. This layer further enhanced the model's ability to detect complex features in the data. It contains 18 496 parameters.
- Third layer MaxPooling (MaxPooling2D): Continued the process of reducing the dimensionality of images.
- Flatten: Converted multidimensional data from previous layers into a one-dimensional array, preparing it for processing by dense layers.
- Dense Layer: The first dense layer with 128 neurons and L2 regularization, which helped prevent the model from being overtrained by penalizing high weights. It contained 6 422 656 parameters.
- Dropout layer: A 55% rejection rate is applied, counteracts overlearning by randomly shutting down some neurons in the training process. It didn't have the parameters to learn.

- **Output Layer (Dense):** A final dense layer with 3 neurons, using softmax activation to classify images into three categories: healthy, pneumonia, and COVID-19. It contained 387 parameters.

In summary, the CNN model that was designed consisted of several sequentially arranged layers designed to pick up features from chest X-rays and classify them into three categories: lung health, pneumonia, and COVID-19.

Before implementing the data into training, the next step was to increase the diversity of training data by using augmentation. For this purpose, ImageDataGenerator, a function from Tensorflow, was used. The transformations used are insignificant, they consist of: rotations, vertical and horizontal shifts, horizontal flipping of images.

TABLE 3. Convolutional neural network training results

Epoch	Loss	Accuracy	Val_loss	Val_accuracy
1	1.34	0.2812	0.3401	0.8604
2	0.8214	0.8338	0.3689	0.8878
3	0.4311	0.8723	0.3265	0.9156
4	0.4119	0.8825	0.2996	0.9328
5	0.3746	0.8865	0.2760	0.9328
6	0.3631	0.9007	0.2726	0.9270
7	0.3511	0.8952	0.2706	0.9399
8	0.3507	0.8967	0.2541	0.9313
9	0.3427	0.8999	0.2470	0.9428
10	0.3314	0.9031	0.2305	0.9371
11	0.3272	0.9052	0.2268	0.9442
12	0.3203	0.9080	0.2304	0.9413
13	0.3130	0.9105	0.2277	0.9428
14	0.3177	0.9083	0.2119	0.9449
15	0.3021	0.9135	0.2106	0.9456
16	0.2878	0.9202	0.3144	0.8856
17	0.2895	0.9188	0.2233	0.9399
18	0.2947	0.9180	0.2147	0.9528

In the table above is presented the performance of the program during the training of the neural network model and the results of this process, showing the improvement of accuracy and reduction of loss as the training progresses using the 'early stopping' technique after 18 epochs. The results consist of parameters such as:

- The model was trained over 18 epochs, which means that the training dataset was used to update the model weights 18 times.



- Loss values on the training set start at 1.34 in the first epoch and steadily decrease to 0.2947 in the 18<sup>th</sup> epoch, suggesting that the model is increasingly adapting to the training data.
- The accuracy of the model on the training set starts at 0.2812 in the first epoch and increases to 0.9180 in the 18<sup>th</sup> epoch, indicating that the model's ability to correctly classify X-ray images is gradually improving.
- Losses on the validation set (val\_loss) initially decrease, reaching a low value of 0.2147 in the last epoch, but small fluctuations are noticeable, which may indicate little variation in the fit of the model to the validation set.
- The validation accuracy (val\_accuracy) improves significantly and reaches 0.9528 in epoch 18, indicating the high generalizability of the model to new data.
- An early stopping mechanism was used to avoid the risk of overtraining the model; Training was terminated after 18 epochs, as no significant improvement was observed on the validation set for subsequent epochs.
- Summarizing the above results, it can be concluded that:
- The model seems to learn well, which indicates that the training process was effective, which is confirmed by the increase in training and validation accuracy.
- The high validation accuracy compared to the training accuracy means that the model has good generalization capabilities.

The training of the CNN model in the form of a graph is as follows:

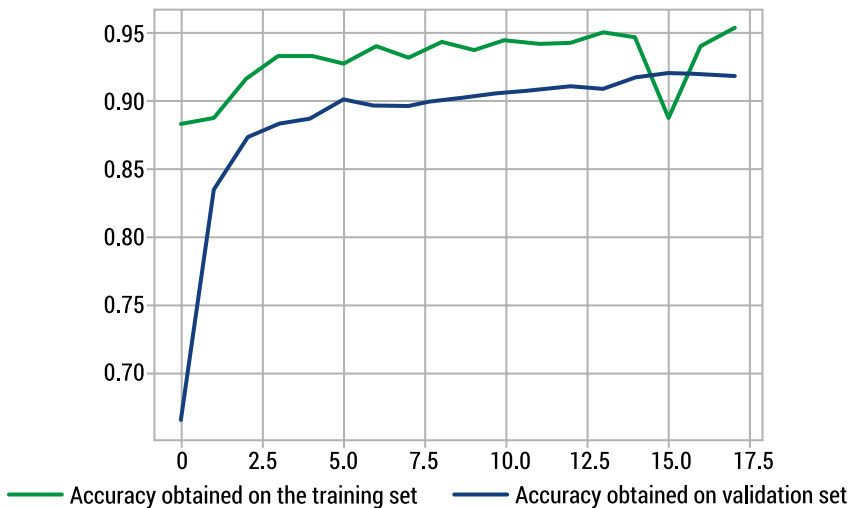


FIG. 4. Accuracy obtained on the training and validation dataset

The results indicate effective model learning, which is visible in the form of increasing accuracy on the training and validation sets.

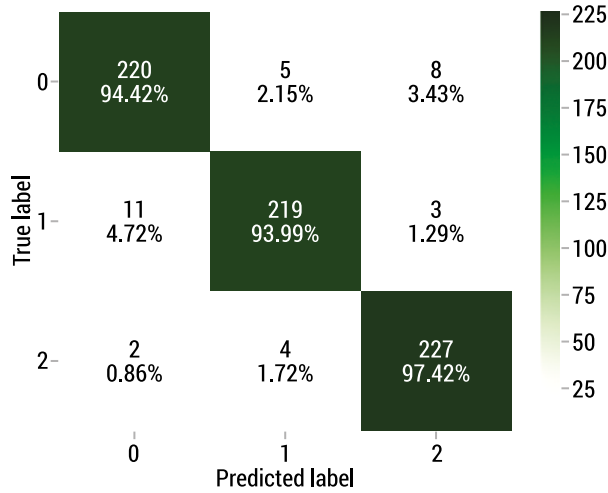


FIG. 5. A confusion matrix showing errors and evaluating the performance of the classification model

The confusion matrix above provides information about true and predicted classification labels. The labels are, in order: 0 for healthy, 1 for pneumonia, and 2 for COVID-19. The description of the confusion matrix analysis is as follows:

- Class 0 (Healthy): The model correctly classified 220 cases as healthy, accounting for 94.42% of all cases in this category. It has been reported that 5 healthy cases have been incorrectly classified as pneumonia and 8 as COVID-19.
- Class 1 (Pneumonia): The model identifies cases of pneumonia with high efficiency, with an accuracy of 93.99%, correctly classifying 219 cases. However, 11 healthy cases were misinterpreted as pneumonia, and 3 cases of COVID-19 were also assigned to this category.
- Class 2 (COVID-19): Here, the model shows the highest classification precision among all classes, with 227 correctly classified COVID-19 cases, resulting in a 97.42% success rate. Only 2 healthy cases and 4 cases of pneumonia were erroneously attributed to COVID-19.

In general, high percentages on the diagonal of the matrix indicate that the model has high accuracy in classification for all three classes. It can be seen that the model tends to be better at recognizing COVID-19 cases, and it is most difficult to distinguish between healthy and pneumonia patients. A small number of classification errors (false positives and false negatives) is indicative of good model performance. A trained model is not perfect and sometimes gets it wrong.

The following are the results of a classification model in which the operation of the built CNN model was tested on a test set to see how well the model generalizes on the new data:

- Accuracy: About 95.28%, which means that the model correctly classified about 95.28% of the samples.

- Sensitivity: Also around 95.28%, suggesting that the model has a high ability to correctly identify all available positive cases.
- Accuracy: A value of approximately 95.28%, indicating a high percentage of correctly positive predictions relative to all positive predictions.
- F1 Score: Around 95.27%, the harmonic mean of sensitivity and precision, indicating a good balance between both of these metrics.
- ROC AUC: About 99.16%, which means that the model differentiates very well between classes – the higher the value, the better the model’s ability to distinguish between different classes.

These results show that the model performs very well across all KPIs, with an exceptional score for ROC AUC, suggesting that the model is particularly effective at distinguishing between different classes.

### 3. Summary and conclusion

The CNN model achieved significant accuracy in classifying lung X-ray images into categories: healthy, pneumonia, COVID-19. This model achieved 92% accuracy in the classification of radiographs, with a sensitivity of 95% and a precision of 95%, which proves its effectiveness in recognizing the lung health conditions studied.

As a result of the conducted research and analysis, it has been shown that CNNs show significant efficiency in the process of recognizing and analyzing X-ray images of the lungs. Their ability to accurately detect subtle diagnostic features in X-ray images, as demonstrated by real-world testing, highlights the potential of these technologies to advance novel diagnostic methods. The use of convolutional networks in the analysis of radiological images can significantly contribute to improving the quality and accuracy of medical diagnostics, offering support in clinical decision-making and increasing the efficiency of detection of pulmonary diseases.

The results of this study, although not perfect, indicate the potential use of convolutional neural networks in the analysis of X-ray images of the lungs. Improving this model would have the potential to enable its practical use by medical professionals in the future. Today, although the use of advanced machine learning technologies is being explored in medicine, there is still room for innovation and the development of more effective diagnostic tools. The program can be improved by adding the following:

- The inclusion of additional categories of lung diseases in the model would increase its clinical applicability.
- Experimenting with more complex network architectures – could further improve the accuracy and sensitivity of the model.
- Using an extended set of training data, including images with a variety of characteristics, can improve the model’s ability to generalize.

- Conducting clinical trials in real medical conditions would allow for the assessment of the practical effectiveness of the model.
- Consultations with specialists would make it possible to verify the results of the model's classification, which would increase its reliability and precision.

Further work on the optimisation of the presented system may contribute to the expansion of available diagnostic methods, offering new perspectives in the field of diagnostic imaging.

## Acknowledgment

This work is supported by the Ministry of Science and Higher Education of Poland under research projects WZ/WM-IIB/2/2024.

## References

1. Martínez Chamorro E., Díez Tascón A., Ibáñez Sanz L., Ossaba Vélez S., Borruel Nacenta S., Radiologic diagnosis of patients with COVID-19. *Radiologi'a*, 2021, 63(1), 56–73.
2. Waite S. et al., Analysis of Perceptual Expertise in Radiology – Current Knowledge and a New Perspective. *Frontiers in Human Neuroscience*, 2019, 13, 213.
3. Stańpor K., Metody klasyfikacji obiektów w wizji komputerowej. PWN, Warszawa 2011.
4. Mustafa W.A., Salleh N.M., Idrus S.Z.S., Jamlos M.A., Rohani M., Overview of Segmentation X-Ray Medical Images Using Image Processing Technique. *Journal of Physics: Conference Series*, 2020, 1529(4), 042017.
5. Shafi A., Padha D., Medical Image Segmentation: A Review of Recent Techniques, Advancements and a Comprehensive Comparison. *International Journal of Computer Sciences and Engineering*, 2019, 7(7), 114–124.
6. Khaksar Ghalati M., Nunes A., Ferreira H., Serranho P., Bernardes R., Texture Analysis and Its Applications in Biomedical Imaging: A Survey. *IEEE Reviews in Biomedical Engineering*, 2022, 15, 222–246.
7. Bharodiya A.K., Gonsai A.M., An Improved Edge Detection Algorithm for X-Ray Images Based on the Statistical Range. *Heliyon*, 2019, 5(10), e02743.
8. Yip S.S., Aerts H.J., Applications and limitations of radiomics. *Physics in Medicine & Biology*, 2016, 61(13), 150–66.
9. Timmeren J., Cester D., Tanadini-Lang S., Alkadhi H., Baessler B., Radiomics in medical imaging – “how-to” guide and critical reflection. *Insights Imaging*, 2020, 11(1), 91.
10. Lambin P. et al., Radiomics: extracting more information from medical images using advanced feature analysis. *European Journal of Cancer*, 2012, 48(4), 441–446.
11. Yamashita R., Nishio M., Do R.K.G., Togashi K., Convolutional neural networks: an overview and application in radiology. *Insights Imaging*, 2018, 9, 611–629.
12. Mocz V., Jeong S.K., Chun M., Xu Y., Multiple Visual Objects are Represented Differently in the Human Brain and Convolutional Neural Networks. *Scientific Reports*, 2023, 13, 9088.
13. Benbrahim B., Hachimi H., Amine A., Deep Convolutional Neural Network with TensorFlow and Keras to Classify Skin Cancer Images. *Scalable Computing Practice and Experience*, 2020, 21(3), 379–390.
14. Litjens G. et al., A survey on deep learning in medical image analysis. *Medical Image Analysis*, 2017, 42, 60–88.

15. Sánchez-Oro R., Torres Nuez J., Martínez-Sanz G., Radiological findings for diagnosis of SARS-CoV-2 pneumonia (COVID-19). *Medicina Clínica* (English Edition), 2020, 155(1), 36–40.
16. Dalfsen M.T. van, Delsing C.E., Niet elke matglasafwijking duidt op COVID-19. *Ned Tijdschr Geneesk*, 2021, 165, d5488
17. <https://www.kaggle.com/datasets/paultimothymooney/chest-xray-pneumonia> (access 12.09.2024).
18. <https://www.kaggle.com/datasets/pranavraikokte/covid19-image-dataset> (access: 12.09.2024).
19. <https://www.kaggle.com/datasets/prashant268/chest-xray-covid19-pneumonia> (access: 12.09.2024).
20. Hou J., Gao T., Explainable DCNN based chest X-ray image analysis and classification for COVID-19 pneumonia detection. *Scientific Reports*, 2021, 11, 19003.
21. <https://swiphealth.com/konsolidacja-pluc-oznaki-objawy-i-przyczyny> (access: 12.09.2024).

# Automatic mechanical diagnostics using deep learning methods

*Agnieszka Dardzińska-Głębocka<sup>1</sup>, Anna Kaspercuk<sup>2\*</sup>, Jakub Dąbrowski<sup>1</sup>*

*<sup>1</sup> Faculty of Mechanical Engineering, Institute of Mechanical Engineering, Białystok University of Technology, Wiejska 45C, 15-351 Białystok, Poland*

*<sup>2</sup> Faculty of Mechanical Engineering, Institute of Biomedical Engineering, Białystok University of Technology, Wiejska 45C, 15-351 Białystok, Poland*

*a.dardzinska@pb.edu.pl, \*a.kaspercuk@pb.edu.pl*

**Abstract:** The main goal of this work is to create a classification model using deep learning methods, to classify healthy, COVID-19 and viral influenza patients based on chest X-ray images. Two models were created, one used manual feature extraction based on texture features and the other performed feature extraction automatically in one of the network layers. Both models used an eight-layer artificial neural network for classification. The obtained models were then compared with each other. A window-based classification application was created based on the model that achieved higher accuracy. Deep learning methods used to create disease classifiers can significantly speed up and facilitate the diagnostic process.

**Keywords:** Automatic diagnosis, Deep learning, Chest X-ray, Disease classification

## 1. Introduction

Due to the constant proliferation of collected data, the need to quickly analyze large amounts of information has arisen. This challenge is met by methods of data mining, which enable the extraction of new knowledge from seemingly unrelated data. Among the most popular mining methods we can include association analysis, classification, textual data analysis or clustering [1–3].

The human brain contains a huge network of neurons, responsible for performing many computationally demanding operations such as face recognition and speech. Such advanced operations are made possible by the effective use of the multilayered nature of the neural network. The human brain is made up of more than 100 billion interconnected neurons, each of which uses biochemical reactions to receive, process and transmit information [4].

Artificial neural networks are information analysis and processing systems based on the actions of human brain neurons. Individual artificial neurons can reflect the basic characteristics of neurons found in the human brain. The basic element from which an artificial neural network is built is an artificial neuron, which is a simplified model of a biological neuron found in the brain [5, 6].

Individual artificial neurons are combined in layers to form an artificial neural network. There are many different types of artificial neural networks, one of which is a unidirectional neural network, that is, one where the flow of each signal takes place in the direction from the input, through hidden layers (if any), to the output. We can distinguish several types of unidirectional networks, these include multilayer perceptrons, regression networks, radial networks and probabilistic networks [7].

The multilayer perceptron (MLP, or MultilayerPerceptron), which is one of the most popular and widely used types of unidirectional networks, consists of an input layer, one or two hidden layers, an output layer, and is a representation of a neural network in advance. All neurons from one layer are fully connected to the neurons of neighboring layers. These connections represent weights, or the importance parameter of each connection. Each weight carries information about the relationship between the problem and its solution [7]. The number of neurons in the input layers and output layers depends on the problem currently being solved. Typically, the number of neurons in the input layer is equal to the number of independent variables of the currently analyzed model, while the number of neurons in the output layer is determined by the number of dependent variables. The number of the hidden layer can be defined as half of the sum of the number of neurons of the input and output layers, although we can get the best results when it comes to selecting the number of neurons of the hidden layer by choosing it empirically [7].

A very important aspect of a good neural network is its ability to generalize, that is, to solve cases similar to those on which it has been taught, but not identical. It is important to avoid situations in which the network becomes overlearned. Overlearning occurs when the network has been taught for too long and depends too much on the learning data for its predictions, thus paying too much attention to features that only characterize the learning data set, which are not always universal for subsequent cases [7].

Using interconnected layers of neural networks, we have a variation of machine learning called deep learning, which is the process of learning high-level representations from a variety of data. The data required for deep learning can take on a structured and unstructured nature. In the case of structured data, we use artificial intelligence algorithms to perform binary class predictions (for example, whether the required state has been achieved – 1 or not achieved – 0), where each individual feature of the data contains a piece of information about the observation, teaching the created model of how individual features interact with the final classification result. Unstructured data refers to any data that is not naturally arranged and structured into individual features, such as images, audio or text. A deep learning

model can learn how to extract high-level features on its own, directly from unstructured data [8].

Deep learning encompasses a class of models that attempt to learn particular deep features of the input data in a hierarchical manner using networks typically consisting of more than three layers. This type of network is initiated by unsupervised learning and then corrected in a supervised manner. Models based on deep learning can extract increasingly complex features at higher levels of layers, so they provide better approximations than shallow models (consisting of fewer than 3 layers) [9].

Since networks based on deep learning consist of multiple layers of hidden neural networks, the term deep learning is almost synonymous with deep neural networks. Keep in mind that any system that uses multiple hidden layers to learn high-level output data representations is a form of deep learning (including, for example, deep belief networks or Boltzmann machines). Each layer of a deep neural network is connected to the previous layer by a set of weights. The most common of the layers is the dense layer, which directly connects all units in the layer to each unit of the previous layer. The final output layer is the result of the process of going through all the hidden layers, the network then generates a set of numbers which is the probability that the original input belongs to one of the  $n$  categories. As with the operation of an artificial neuron, individual weights are used to teach the entire network. During the learning process, data is sent through the network and the resulting output is compared with the input state. The resulting error is propagated backwards and during this process the network adjusts the weights accordingly to improve the prediction as much as possible. During the learning process, each unit acquires the ability to identify a specific function. Deep networks can consist of any number of intermediate and hidden layers [9].

A popular solution for creating classifiers is to use deep learning, which eliminates the need for manual feature extraction. The sentence is taken over by one of the many layers of the created network. Much of the literature related to deep learning-based classifiers uses pretrained models (pretrained models), which work well for image identification, for example. Such models include, for example, AlexNet, GoogleNet and DenseNet201. The works performed [10, 11] a comparative analysis for different types of trained models used to classify cases of influenza-associated pneumonia and COVID-19. The study used AlexNet, GoogleNet, and SqueezeNet models to classify lung X-ray images of patients with covid and non-covid pneumonia. The results of all models were similar to each other, for two classes reaching about 98% accuracy. In contrast, for multi-class matching (three classes), the percentage of correct classification decreased to about 96%. In the paper "Classification of the COVID-19 infected patients using DenseNet201-based deep transfer learning" [12], the authors used the trained DenseNet201 model to classify patients with covidian pneumonia. Computed tomography images of both sick and healthy subjects were used as input data. The model created with them classified one of two classes with an accuracy of 97% for the validation set and 96.25% for the test set [13, 14].



## 2. Materials and methods

Lung X-ray images of patients from three groups were analyzed: subjects – those with COVID-19 pneumonia, those with influenza pneumonia, and healthy subjects. The images were downloaded from medical data repositories hosted on Kaggle [15, 16]. The images were divided into three classes – COVID (covid pneumonia), GRYPA (influenza pneumonia), HEALTHY (healthy person), each class containing 60 images. The number of photos is relatively small, due to limited access to public repositories containing photos of patients after covid pneumonia. MATLAB R2021a was used to process the photos and create the models.

The next step, after separating the images into different classes, was to perform preprocessing. For this purpose, the following operations were performed [17]:

- Cropping the area of interest. Cropping the area of interest is essential to eliminate the influence of unnecessary regions, such as parts of the neck or shoulders, and to remove any markings on the X-ray images. After cropping, the patient's lung area should cover as much of the image as possible.
- Scaling the images to an equal resolution. Scaling the images to an equal resolution significantly reduces the image size, which accelerates the program's operation by shortening loading times.
- Reducing noise and interference. Noise and interference reduction was performed using a filter known as Gaussian blur. For this purpose, the `imgaussfilt` function with the default parameter was applied in MATLAB R2021a.

Feature extraction was carried out using both manual and automated methods. The extracted features were used to build classifiers based on deep learning methods. The models were evaluated based on measures of the quality of their fit [18].

Using the `graycoprops` function, a gray level co-occurrence matrix (GLCM) was created from which the values of contrast, correlation, energy and homogeneity parameters were obtained. Using appropriate MATLAB functions, additional parameters such as mean, median, standard deviation, mean squared, variance, entropy, fashion, kurtosis, skewness, L1 norm and L2 norm were obtained. All the obtained parameters are based on the shades of gray present in the analyzed images. Table 1 shows some of the parameters obtained for the images of patients with covid inflammatory pneumonia.

TABLE 1. Examples of parameters of extracted image features

<b>Contrast</b>	<b>0.115</b>	<b>0.093</b>	<b>0.071</b>	<b>0.061</b>	<b>0.069</b>
Correlation	0.939	0.969	0.979	0.986	0.975
Energy	0.226	0.196	0.179	0.190	0.261
Homogeneity	0.942	0.954	0.964	0.970	0.966
Mean	109.766	143.951	132.446	153.937	139.160

<b>Contrast</b>	<b>0.115</b>	<b>0.093</b>	<b>0.071</b>	<b>0.061</b>	<b>0.069</b>
Median	108	149	133	160	154
Deviation std.	29.595	38.183	40.545	47.397	34.833
Mean squared	15.969	15.969	15.969	15.969	15.969
Variance	875.858	1457.954	1643.887	2246.479	1213.307
Entropy	11.371	11.370	11.358	11.355	11.372
Fashion	84	188	127	209	170
Kurtosis	2.082	2.312	2.188	2.194	3.076
Skewness	0.197	-0.433	-0.175	-0.503	-1.097
L1 norm	9878972	12955552	11920183	13854302	12524411
L2 norm	4790.616	4790.598	4790.610	4790.616	4790.616

Based on the created parameter database, a deep learning-based model was developed. The data used to create the model was divided as follows: 80% of the data was allocated to the training set, and 20% to the validation set. The created network consists of 8 layers. The selection of appropriate layers and their parameters was carried out experimentally, based on literature and online sources [12,13,14]. The layers used to create the network in this work are:

- Input Layer (in MATLAB – imageInputLayer): Responsible for loading images with a specified resolution of 300x300 pixels.
- Dense Layer with 50 neurons (in MATLAB – fullyConnectedLayer): A layer that connects all neurons and compares the obtained weights.
- Dense Layer with 30 neurons:
- Convolutional Layer (in MATLAB – convolution2dLayer): A layer responsible for the convolutional type of neural network, acting as a filter to detect the most important features.
- Dense Layer with 3 neurons: A layer with a size corresponding to the number of estimated classes.
- SoftMax Layer (in MATLAB – softmaxLayer): A layer responsible for normalizing the obtained features to parameters that can be interpreted as probabilities.
- Output Layer (in MATLAB – classificationLayer): A layer responsible for classification.

The training parameters of the network are as follows:

- Solver: sgdm
- Initial Learning Rate: 0.0003
- Validation Frequency: 5
- Maximum Number of Epochs: 10
- Mini-Batch Size: 10
- Data Shuffling: After each epoch
- Regularization Method: l2norm

In addition to the model based on manual feature extraction, automatic feature extraction was also utilized. With this approach, the manual feature extraction process using the previously discussed algorithm is not necessary. For a model using automatic extraction of image features, Deep Network Designer, implemented in Matlab, was used along with the Deep Learning Toolbox. Deep Network Designer allows a simple and intuitive way to create a model based on deep neural networks, in which the model detects image features automatically from the images provided to it. As in the case of creating a model with manual feature extraction, three classes of lung X-ray images – COVID, Influenza and Healthy – were used to create the new model. The created model, like the previous one, consists of eight layers. A diagram of the model in Deep Network Designer's graphical interface is shown in Figure 1.

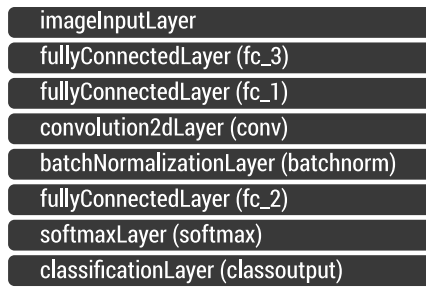


FIG. 1. Diagram of the model with automatic feature extraction

### 3. Results

Analyzing the obtained values of the coefficients, we are able to conclude that the obtained model performs well in detecting the COVID and Healthy class, achieving 71% and 81% precision, respectively. Problems with classification appear with the Influenza class. In this case, the model achieved only 50% precision and sensitivity, making the classification of this class almost random. The overall classification accuracy for the test set was 80%, which is a good result, unfortunately, the level of classification accuracy of the Influenza class is a big minus for this type of model (tab. 2).

TABLE 2. Table of model quality coefficients with manual feature extraction

	COVID	Flu	Healthy
Sensitivity	1	0.5	0.9
Specificity	0.8	1	0.9
Precision	0.71	0.5	0.81
Accuracy of test set	0.8 = 80%		
Validation accuracy	0.64 = 64%		

The model based on automatic feature extraction achieved 83% accuracy for the test set. The COVID class had the highest sensitivity value, while the Healthy class had the lowest. The average precision value for this type of model was about 83%, a much higher result than for the model with manual feature extraction. Each class achieved a specificity value of about 90% or more, indicating very good attribution of the lack of occurrence of the classes in question (tab. 3).

TABLE 3. Table of quality coefficients of the model with automatic feature extraction

	<b>COVID</b>	<b>Flu</b>	<b>Healthy</b>
Sensitivity	1	0.8	0.7
Specificity	0.89	0.95	0.9
Precision	0.83	0.88	0.77
Accuracy of test set	0.83 = 83%		
Validation accuracy	0.97 = 97%		

Due to the better performance of the quality parameters of the model with automatic feature extraction, this type of model was used to create a window application. This type of application provides a quick and intuitive way to perform batch analysis of images. This application allows, after uploading the X-ray images, to make the assignment of the patient to the correct group.

## 4. Summary and conclusion

The purpose of this study was to create a classification model that, using deep learning methods, facilitates the process of diagnosing COVID-19 and influenza patients. Artificial neural networks and deep learning represent modern techniques of data analysis, providing the possibility to create models that allow the performance of classifications with high accuracy and support the work of doctors, diagnosticians and researchers. In the present study, two classification models were created, differing from each other in the method of extracting features obtained during X-ray examinations.

Despite the small number of images used to create the models, both the model with both manual and automatic feature extraction did its job, classifying cases of COVID-19 infection, influenza and healthy individuals. The manual model, which used image texture features as input, achieved a validation accuracy of 64% in the training process. Despite the rather low accuracy percentage for the learning data, this type of model achieved 80% accuracy for the test set data. The COVID class achieved a sensitivity coefficient value of 1, indicating very good prediction of this class compared to others [6, 8]. The Healthy class represented a similar level, obtaining a similar sensitivity value and the highest precision value among the three classes

for this model – 0.81. Of the three classes predicted by the model with manual feature extraction, the Influenza class showed the lowest values of sensitivity and precision parameters, but it is worth noting that the level of specificity for this class was the highest – the Influenza class was not mistakenly attributed to other classes. By removing the influenza class, we can expect a relatively accurate predictive model for two classes, COVID and Healthy. The procedure of reducing the classes could also positively increase the percentage of model accuracy on both the learning and testing sets. The development time for this type of model was very short, so it is flexible and provides the opportunity to make corrections without having to wait a long time to rebuild the model.

The second type of model – with automatic feature extraction, carried out directly by the input layer of the artificial neural network – showed higher accuracy values. The validation accuracy, obtained on the learning set, increased by 33%, while for the test set, the result was similar at 83% accuracy. The large increase in validation accuracy may be one sign of overfitting [6], and can be remedied by increasing the number of images used to create the model. The model with automatic feature extraction had similar levels of quality coefficients for all three classes. As with the previous model, the COVID class achieved a sensitivity value of 1, and the level of specificity and precision also improved. The prediction of the Influenza class improved significantly, with a slight decrease in the specificity parameter by 0.05, we managed to increase the level of sensitivity for this class from 0.5 to 0.8, and precision from 0.5 to 0.88. At the cost of a significantly more accurate classification of the Influenza class, the sensitivity and precision values for the Healthy class decreased. Finally, the values of quality coefficients for the model with automatic feature extraction were more optimal than those obtained for the model with manual extraction, and thus it was used to create a windowed classifier application. Compared to other popularly used COVID-19 and Influenza classifiers [12, 13, 14], the classifier created within the framework of the present work achieved similar, although slightly lower, results. In order to obtain higher values for the quality parameters of the models created in this work and their classification accuracy, it would be necessary to have access to a large number of X-ray images that can be used to better teach the network.

The created classification application can be expanded by diagnosing additional diseases, such as pneumonia caused by bacterial influenza. The use of models based on deep learning can positively impact disease diagnosis. With such solutions and applications based on them, diagnosis can be significantly accelerated and facilitated. Classification applications can find use in narrowing down diagnoses, helping novice doctors gain experience in diagnosis, as well as speeding up the work of research teams.

## Acknowledgment

Research was performed as a part of projects MB/WM/3/2021 and financed with use of funds for science of MNiSW.

## References

1. Dardzińska-Głębocka A., Kasperczuk A., Comparative Evaluation of the Different Data Mining Techniques Used for the Medical Database. *Acta Mechanica et Automatica*, 2016, 10, 233–238.
2. Dardzińska-Głębocka A., Kasperczuk A., Automatic system for IBD diagnosis. *Procedia Computer Science*, 2021, 192, 2863–2870.
3. Dardzińska-Głębocka A., Zdrodowska M., Analysis children with disabilities self-care problems based on selected data mining techniques. *Procedia Computer Science*, 2021, 192, 2854–2862.
4. Abraham A., Artificial Neural Networks, Handbook of Measuring System Design. Wiley, London 2005.
5. Derlatka M., Borowska M., Ensemble of Heterogeneous Base Classifiers for Human Gait Recognition. *Sensors*, 2023, 23, 1–19.
6. Tadeusiewicz R., Szaleniec M., Leksykon sieci neuronowych. Wydawnictwo Fundacji „Projekt Nauka”, Wrocław 2015.
7. Park Y.S., Lek S., Artificial Neural Networks: Multilayer Perceptron for Ecological Modeling. *Ecological Model Types*, 2016, 28, 123–138.
8. Foster D., Generative Deep Learning. O'Reilly, Sebastopol 2019.
9. Chen Y., Lin Z., Zhao X., Wang G., Gu Y., Deep Learning-Based Classification of Hyperspectral Data. *IEEE Journal of Selected Topics in Applied Earth Observations and Remote Sensing*, 2014, 7(6), 2094–2107.
10. Roopa H., Asha T., Feature Extraction of Chest X-ray Images and Analysis Using PCA and kPCA. *International Journal of Electrical and Computer Engineering*, 2018, 8(5), 3392–3398.
11. Hasan M.S., An application of pre-trained CNN for image classification. *20<sup>th</sup> International Conference of Computer and Information Technology*, 2017.
12. Jaiswal A., Gianchandani N., Singhm D., Kumar V., Kaur M., Classification of the COVID-19 infected patients using DenseNet201 based deep transfer learning. *Journal of Biomolecular Structure and Dynamics*, 2020, 39(15), 5682–5689.
13. Pham T.D., Classification of COVID-19 chest X-rays with deep learning: new models or fine tuning?. *Health Information Science System*, 2021, 9(1), 2.
14. Ibrahim A.U., Ozsoz M., Serte S., Al-Turjman F., Yakoi P.S., Pneumonia Classification Using Deep Learning from Chest X-ray Images During COVID-19. *Cognitive Computation*, 2021, 1–13.
15. Chest X-rays – Pneumonia Detection, [www.kaggle.com/wilhelmberghammer/chest-xrays-pneumonia-detection](https://www.kaggle.com/wilhelmberghammer/chest-xrays-pneumonia-detection) (access: 10.05.2023).
16. COVID-19 Chest X-ray Image Dataset, [www.kaggle.com/alifrahman/covid19-chest-xray-image-dataset](https://www.kaggle.com/alifrahman/covid19-chest-xray-image-dataset) (access: 10.05.2023).
17. Chen T.J., Chuang K.S., Chang J.H., Shiao Y.H., Chuang C.C., A Blurring Index for Medical Images. *Journal of Digital Imaging*, 2006, 19(2), 118–125.
18. Stojanović M., Apostolović M.A., Stojanovic D., Milosević Z., Topalović A., Lakusić V.M., Golubovic M., Understanding sensitivity, Specificity and predictive values. *Vojnosanitetsky pregled Military-medical and pharmaceutical review*, 2014, 71(11), 1062–1065.



# Application supporting the interpretation of laboratory test results

*Julia Kiryluk<sup>1</sup>, Marta Borowska<sup>1\*</sup>*

*<sup>1</sup> Faculty of Mechanical Engineering, Institute of Biomedical Engineering,  
Białystok University of Technology, Wiejska 45C, 15-351 Białystok, Poland*

*julia.kiryluk.108966@student.pb.edu.pl, \*m.borowska@pb.edu.pl*

**Abstract:** The following article concerns the subject of laboratory diagnostics and its most important part, which is the analysis of test results and the identification of diseases. The developed web application supporting the interpretation of laboratory test results is described, focusing on blood counts, urine tests and the levels of individual vitamins in the body. By reviewing the professional literature, it was possible to determine the correct reference ranges of all examined parameters characterizing individual studies. Diseases and transient health conditions that could be identified based on abnormal results were then classified. After reviewing the IT solutions available on the market, the design assumptions of the application being developed were determined, characterizing its new functionalities and capabilities. As part of the practical part, algorithms were developed for the interpretation of test results: blood count, general urine test and the level of selected vitamins. To implement the application, tools for creating web applications were used, i.e. HTML, CSS and JavaScript. In order to check the correct operation, validation tests of all HTML and CSS files were performed, and then an online survey was conducted, which was addressed to a group of potential future users to assess the usability and functionality of the developed solution. The results of this work may constitute a valuable contribution to the development of tools supporting laboratory diagnostics and improving the preparation of patients for medical consultations.

**Keywords:** laboratory tests, advisory system, interpretation of laboratory test results, blood count, urine test

## 1. Introduction

The development of technology and new discoveries in medicine have resulted in the creation of various IT solutions supporting the analysis and interpretation of laboratory test results. Emerging applications and computer programs support and improve the work of doctors and medical staff.



The introduction of new information technologies into laboratory diagnostics contributes to improving the efficiency, precision and safety of diagnostic processes. However, despite many available applications supporting laboratory diagnostics, patients still do not commonly use them after testing. This may be related to the availability of tools that are too complicated to use by people without medical education or unintuitive in the case of elderly people.

The application supporting the interpretation of laboratory tests aims to improve the analysis of results in order to easily and quickly identify existing diseases, ailments or temporary health conditions. Thanks to this interpretation, when coming to a doctor's visit, the patient will be able to present the history of the same diseases in the family circle. Additionally, when verifying test results, the application is intended to inform about a critical health condition and the need to immediately consult a doctor.

Web applications available on the market supporting the interpretation of results do not offer analysis of urine test results and vitamin levels, which are so important to consume appropriately nowadays, when food is highly processed and low in minerals and vitamins. Therefore, an application that offers various types of tests seems to be necessary, including the most popular ones: blood count and urine test, as well as others – frequently performed, and at the same time free, easy to use and a web application, i.e. it does not require space in the computer's memory or mobile phone, only Internet access.

## 2. Analysis of laboratory test results

The first laboratory test discussed is a complete blood count, the normal reference ranges of which are presented in Table 1. It is worth noting that the parameters related to red blood cells (RBC, HGB and HCT) differ in norms depending on gender, because monthly menstruation results in a total reduced number of erythrocytes in women's peripheral blood.

Based on individual blood parameters, and more precisely their increased or decreased values, it is possible to identify many diseases or the patient's temporary health condition. As a result of the analysis, it is possible to detect not only diseases closely related to hematology, such as anemia or polycythemia, because the morphological examination also provides information about the condition of the entire body, e.g. dehydration, tissue or bone marrow damage, but also various stages of pregnancy. Temporary health conditions detected by blood counts include stress, physical exertion, intense vomiting and heavy bleeding.

TABLE 1. Blood count reference ranges [1, 2]

	Reference ranges	
	Women	Men
RBC	3.5–5.2 mln/ $\mu$ l	4.2–5.4 mln/ $\mu$ l
WBC	4000–10 000/ $\mu$ l	
HGB	12–16 g/dl (7.5–9.9 mmol/l)	14–18 g/dl (8.7–11.2 mmol/l)
HCT	37–47%	40–54%
MCV	80–103 fl	
MCH	24–35 pg	
MCHC	32–36 g/dl	
PLT	150 000–400 000/ $\mu$ l	

Another test whose normal reference ranges and properties are presented in Table 2 is a general urine test.

TABLE 2. Reference ranges and urine properties [1,3]

	Reference ranges/properties
Color	straw yellow
Clarity	clear, slightly opalescent
pH	approximately 6.0 (4.5–8.0)
Specific gravity	1016–1022 g/l
Protein	0
Glucose	0
Ketone	0
Bilirubin	0
Urobilinogen	small amount (0.5–1 mg/dL)
Nitrites	0
Urine sediment	Red blood cells (0–2), white blood cells (0–5), crystals – occasionally

The most common abnormality in the color of urine is dehydration, when the color changes from straw yellow to orange or even red. Another parameter is urine transparency, where an abnormality is defined as its turbidity. This may be caused by the presence of bacteria, leukocytes, yeast, as well as an increased amount of mucus, urates and phosphates. An incorrect pH reaction may be the result of various diseases as well as the use of diets with increased amounts, e.g. of protein, meat or vegetables. In the case of decreased weight, it is concluded that the ability of the kidneys to dilute and concentrate urine has been impaired, and the presence of protein may indicate kidney disease, heart defects and urinary tract abnormalities. In the presence of glucose, diabetes or damage to the kidney tubules is suspected, and in the presence of ketone

compounds – starvation, fever and diabetes. The appearance of bilirubin and increased urobilinogen levels in urine may indicate liver disease or jaundice, and the presence of nitrites is characteristic of urinary tract infections [1, 3].

The last analyzed test is the determination of the level of individual vitamins, the correct reference ranges of which are presented in Table 3.

TABLE 3. Reference ranges of selected vitamins in the body [4–9]

Vitamin	Reference ranges
A	< 0.1 mg/l – serious deficiency < 0.2 mg/l – deficiency, supplementation recommended 0.3–0.7 mg/l – normal level > 1.2 mg/l – toxic amount
B <sub>1</sub> (thiamine)	> 49 µg/l – normal level
B <sub>2</sub> (riboflavin)	136–470 µg/l – normal level
B <sub>6</sub>	8.7–27.2 µg/l – normal level
B <sub>9</sub> (folic acid)	0–3 ng/ml – clinical deficiency 3–5 ng/ml – deficiency 6–20 ng/ml – normal level
B <sub>12</sub> (cobalamin)	< 200 pg/ml – deficiency 200–400 pg/ml – insufficient values > 400 pg/ml – normal level
C	4.6–14.9 mg/l – normal level
D	0–10 ng/ml – deep deficit 10–20 ng/ml – deficit 20–30 ng/ml – deficiency 30–50 ng/ml – normal level 50–100 ng/ml – excess >100 ng/ml – toxic amount
E	5–18 mg/l – normal level

A list of probable diseases that may occur in the case of hypovitaminosis or hypervitaminosis of selected vitamins is presented in Table 4.

TABLE 4. Consequences of deficiency and excess of selected vitamins [4–9]

Vitamin	Consequences of deficiency	The consequences of excess
A	vision disorders, keratosis and peeling of the epidermis, reduced immunity, growth inhibition	liver enlargement, irritability, headache, changes in bone structure, skin changes
B <sub>1</sub> (thiamine)	neurological disorders, cardiovascular disorders, beriberi disease	muscle tremors, heart palpitations

Vitamin	Consequences of deficiency	The consequences of excess
B <sub>2</sub> (riboflavin)	exfoliation of the epidermis, inflammation of the tongue, redness of the conjunctiva, dysfunctions of the nervous system	itching, numbness in limbs
B <sub>6</sub>	stomatitis, seborrheic dermatitis, eczema, anemia	pyridoxine addiction, neuropathy syndrome
B <sub>9</sub> (folic acid)	atherosclerosis, depression, dementia, anemia	damage to the nervous system, disorders of the digestive system
B <sub>12</sub> (cobalamin)	neuropathy, myelopathy, anemia, neuropsychiatric disorders	liver diseases, malignant and hematological tumors, kidney failure
C	weakness, fatigue, bleeding gums, reduced physical capacity	gastrointestinal disorders, formation of kidney stones
D	bone mineralization disorder (children – rickets, adults – osteomalacia, osteoporosis)	hypercalciuria, hypercalcemia
E	skeletal myopathy, retinopathy, ataxia, impaired immune response	contact dermatitis, allergic lesions, weakening of the effect of vitamin K

In order to avoid the effects of vitamin deficiencies, you should eat a varied diet rich in such products so that no vitamin is missing. Table 5 presents the sources of selected vitamins.

TABLE 5. The most common sources of selected vitamins in food [4–10]

Vitamin	Sources of vitamins in food
A	dairy products, fatty fish, eggs, carrots, green leafy vegetables, liver
B <sub>1</sub> (thiamine)	yeast, liver, dairy products, eggs, whole grain products, nuts, buckwheat and millet, white beans, red lentils, soy, peas
B <sub>2</sub> (riboflavin)	dairy products, eggs, whole grain products, rice, mushrooms, liver, green leafy vegetables, nuts, legumes, sesame, pumpkin and sunflower seeds
B <sub>6</sub>	whole grains, white meat, dairy products, eggs, fish, peanuts, legumes, leafy vegetables
B <sub>9</sub> (folic acid)	green vegetables, legumes, oranges, asparagus, beans, whole grains, yeast, eggs
B <sub>12</sub> (cobalamin)	yeast, meat, offal: liver and kidneys, fish, dairy products, eggs
C	berries and citrus fruits, green vegetables, radishes, peppers, red peppers
D	fatty fish, dairy products, eggs
E	vegetable oils, nuts and seeds

### 3. Application design

Based on a review of the literature and IT solutions available on the market for research analysis, design assumptions for a web application that would respond to the gap in the market were developed.

The designed web application should meet the following assumptions:

- topics: interpretation of laboratory test results,
- application development technology: HTML, CSS and JavaScript,
- subpages: 1 – *Home page with menu*, 2 – *Selection of results analysis*, 3 – *Blood count analysis*, 4 – *Urinalysis analysis*, 5 – *Vitamin analysis*, 6 – *Vitamins knowledge base*, 7 – *Diseases knowledge base* (go to the login panel), 8 – *Login*, 9 – *Target disease knowledge base*,
- users: adults, including patients and doctors, as well as medical students,
- analysis of test results: blood count, urine and levels of vitamins A, B<sub>1</sub>, B<sub>2</sub>, B<sub>6</sub>, B<sub>9</sub>, B<sub>12</sub>, C, D and E,
- disease knowledge base consisting of the name of the disease and its description (diagnosis, types, causes, symptoms),
- access to the disease knowledge base only for doctors – secured with a login panel,
- vitamin knowledge base consisting of the name of the vitamin, its most important role in the body, the health condition in which it is particularly advisable to take a given vitamin and the source of its occurrence in food,
- ability to search for diseases/vitamins in individual databases.

### 4. Application implementation

To implement the web application, Brackets software was used, which is a text editor created for web designers and front-end programmers [11]. Its distinguishing feature among other editors is the live preview of the document being created. The software enables the use of HTML (HyperText Markup Language) and JavaScript languages as well as CSS style sheets (Cascading Style Sheets).

The structure of individual subpages of the application was described using HTML, giving some elements special importance, e.g. header or hyperlink. The use of CSS allowed us to characterize the final graphic layout of the application interface, including the arrangement of photos, text parameters and the appearance of tables. The JavaScript language made it possible to describe all interactions, in the case of this application it was primarily the process of interpreting the result, displaying a detailed analysis and logging in to the doctor's account.

The most important function of the developed application is the analysis of the results of selected laboratory tests. By selecting the *Results Analysis* subpage from the menu, the user is redirected to the selection panel for the study

he is interested in. If one test is selected, the user is redirected to the appropriate subpage, while if no or several tests are selected, the message “Please select one test for analysis” is displayed.


After selecting the blood count analysis, the relevant subpage displays the most important information about the test, a message that the application does not replace consultation with a doctor, and then a table with empty fields for entering your test results (Fig. 1).

LabAnalysis

Blood count result analysis

Blood count involves determining the level of blood components, such as red blood cells - erythrocytes, white blood cells - leukocytes, platelets - thrombocytes, hematocrit and hemoglobin. The result of this test informs about the condition of the circulatory system and all organs in the body.

**Remember!**  
The analysis obtained in this application does not replace a medical consultation. However, it allows you to properly prepare for the visit by reviewing your family's disease history and informs you about health and life-threatening conditions.



Below, enter the values of individual parameters from the laboratory test result. Pay special attention to the units.

Sex

☐ Woman ☐ Man

Blood count parameters

Parameter	Description	Reference range	Value
RCB	erythrocytes - number of red blood cells	Women: 3.5 - 5.2 min/jl Men: 4.2 - 5.4 min/jl	<div>e.g. 4.5</div> min/jl
WBC	leukocytes - the number of white blood cells	4 000 - 10 000/jl	<div></div> /jl
HGB	hemoglobin concentration	Women: 12 - 16 g/dl Men: 14 - 18 g/dl	<div></div> g/dl
HCT	hematocrit - concentration of blood cell volume in plasma	Women: 37 - 47% Men: 40 - 54%	<div></div> %
MCV	average red blood cell volume	80 - 103 fl	<div></div> fl
MCH	average weight of hemoglobin in a blood cell	24 - 35 pg	<div></div> pg
MCHC	average concentration of hemoglobin in blood cells	32 - 36 g/dl	<div></div> g/dl
PLT	platelet count	150 000 - 400 000/jl	<div></div> /jl

SHOW RESULT

FIG. 1. Blood count analysis subpage

After entering all the values, the result is displayed, containing the detected abnormalities and diseases that may occur with such results (Fig. 2).

BLOOD MORPHOLOGY ANALYSIS RESULT:

Abnormalities detected:

low erythrocyte count  
high leukocyte count  
low level of mean red blood cell volume  
low platelet count

Probable ailments or diseases:

anemia, leukocytosis, leukemia, thrombocytopenia

FIG. 2. Example of a blood count analysis result

If any of the fields are not completed, intentionally or accidentally, a message is displayed on the screen asking the user to enter all the necessary data for analysis.

If a urinalysis is selected, in order to obtain an interpretation, in addition to completing the values, the user must select appropriate data from drop-down lists to accurately characterize the urine parameters. After entering all the values,

a result is displayed containing the detected abnormalities and diseases that may occur with such results. In some cases, in addition to listing abnormalities and predicted diseases, a message is displayed regarding life-threatening results, e.g. hematuria (Fig. 3).

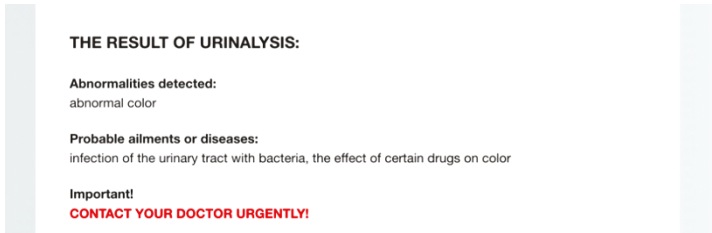


FIG. 3. Example of a urine analysis result with an important message

The last option for selecting a test for analysis is the vitamin level (Fig. 4). The user selects the vitamin he is interested in from the drop-down list, enters the value and after pressing the button, he receives information about the result.

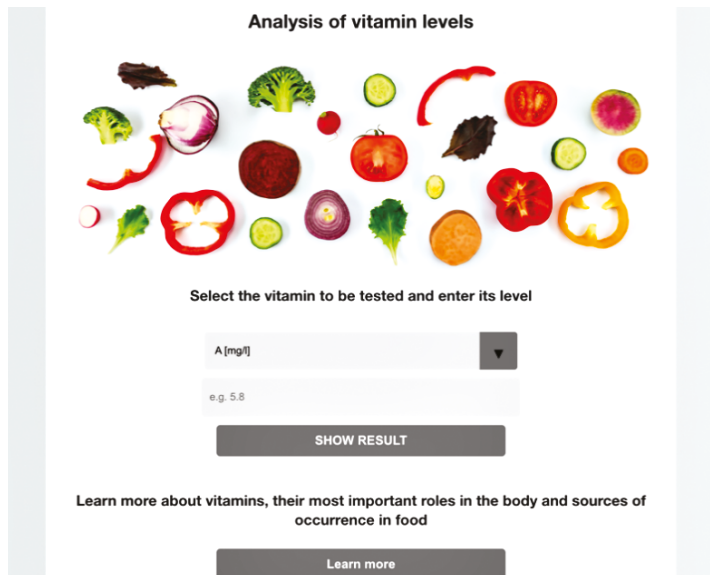


FIG. 4. Subpage *Analysis of vitamin levels*

As a result of the analysis, the user receives information about the vitamin level (“DEFICTION”, “NORMAL”, “EXCESS”), the consequences of deficiency or excess and, only in the case of deficiency, a list of products that are a healthy source of a given vitamin (Fig. 5).

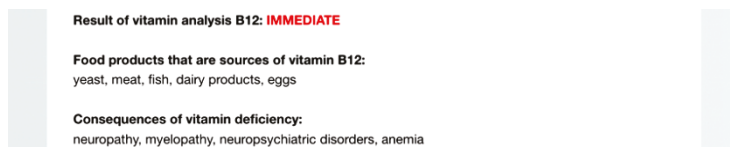


FIG. 5. Example result of the analysis of vitamin B12 level

By clicking the button under the vitamin level analysis or by selecting the last item from the menu, the user goes to the Knowledge Base of vitamins, which describes the most important roles in the body, health conditions in which supplementation of these vitamins is recommended, and sources in food (Fig. 6).

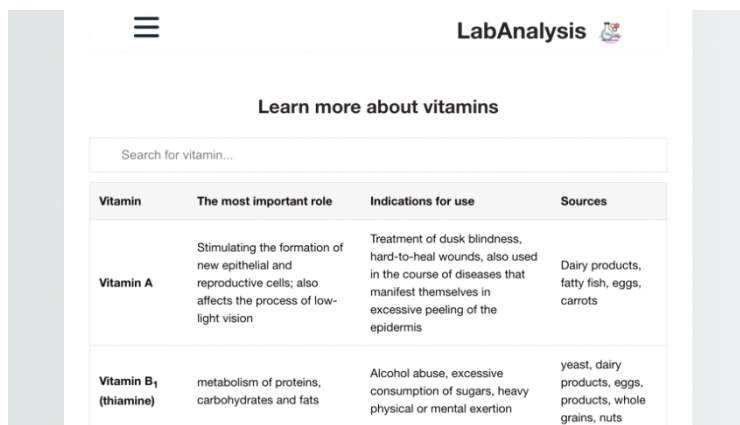


FIG. 6. *Vitamins knowledge base* subpage

After selecting the *Diseases knowledge base* option from the menu, the user is first redirected to the Login subpage with the doctor’s account login panel. A function written in JavaScript is responsible for handling the clicking of the “Log in” button. Login details have been saved in the program code, making it impossible to create a new account yourself. Therefore, any changes can only be made by the programmer or a person with access to the source code.

If the correct data is entered, the user is redirected to the subpage with the Target *Disease knowledge base*, which contains various diseases with their descriptions, causes and symptoms. This tool supports doctors and medical students, allowing them to quickly find and recall all the necessary information.



# 5. Application testing

As part of testing the web application, the correct display was checked in the three most popular web browsers in the world, i.e. Google Chrome, Safari and Microsoft Edge, as well as on a mobile device – a mobile phone. The web application was displayed and worked properly in all tested web browsers.

Then, code validation was performed for all HTML files creating the application structure and CSS files. Validation was carried out on the W3C website [12–13], and no errors were found as a result of the tests.

The last stage of testing the application was an online survey containing 15 questions, which was completed by 40 people, including 26 women and 14 men. The youngest person testing the application was 18 years old and the oldest was 58 years old. The average age was 30 years, while the age of the people differed from the average age by an average of 12.51 years (Table 6).

TABLE 6. Statistics on the age of people testing the application

Variable	Number of respondents	Average	Minimum	Maximum	Standard deviation
age	40.00	30.00	18.00	58.00	12.51

The high value of the standard deviation proves that the group was very diverse in age, which is also visible in the histogram (Fig. 7).

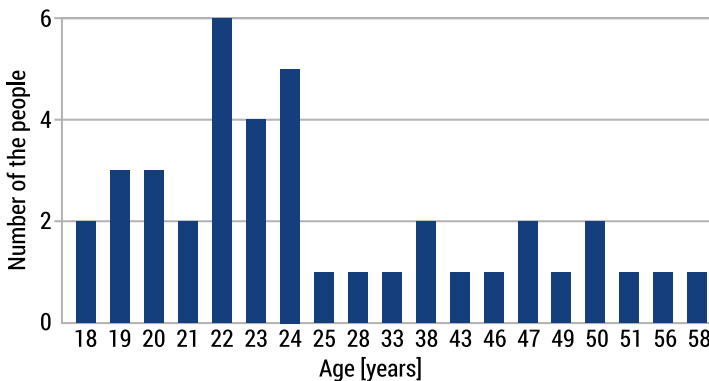


FIG. 7. Histogram regarding the age of respondents

Almost half of the respondents had higher education (17 people – 42.5%), the second largest group were people with secondary education (13 people – 32.5%), while the fewest respondents had only completed primary school (2 people – 5%) and secondary school. industry (1 person – 2.5%). The education of the respondents is presented in a pie chart (Fig. 8).

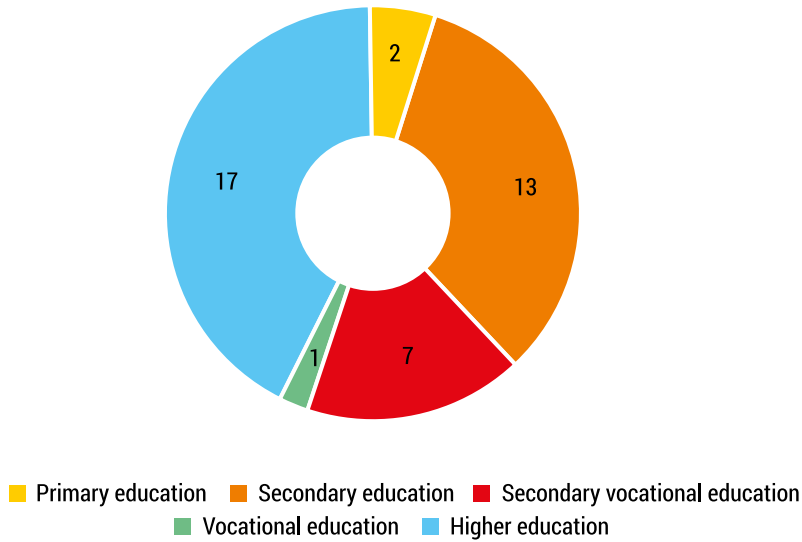


FIG. 8. Pie chart regarding the education of respondents

Then, respondents answered questions related to the appearance and use of the application. For each of them, you had to choose one of 5 answers: *Definitely yes*, *Yes*, *Neutral*, *No* or *Definitely not*. The summary of responses is presented in pie charts (Fig. 9).

The vast majority of respondents answered positively to all the above questions by selecting *Definitely yes* or *Yes*. Most answers were *Definitely yes* to the question about the intuitiveness of the interface (29 people – 72.5%) and to the question about the simplicity of obtaining an analysis of the selected study (28 people – 70%).

However, the answers to the question “*Would you use such an application?*” provide optimistic feedback, as many as 90% of respondents declared that they would use this type of tool.

The next question concerned the possibility of developing the application in the future. The respondents suggested the following directions of development: “*I would add a parameter memory option*”, “*Adding more vitamins in the database*”, “*I would increase the number of parameters available to check blood count*”, “*Suggestions of additional tests after displaying the reasons*”, “*Selection of tests such as sodium level, potassium etc.*” and “*I would add vitamin correlation, i.e. what not to combine multi-vitamin supplementation with.*”

It should be noted that many people liked the current version of the application and gave the following answers: “*Everything works correctly and the actions are intuitive*”, “*It’s good*”, “*It’s good enough*”, “*I have no objections*” and “*No I have no complaints about the application.*”

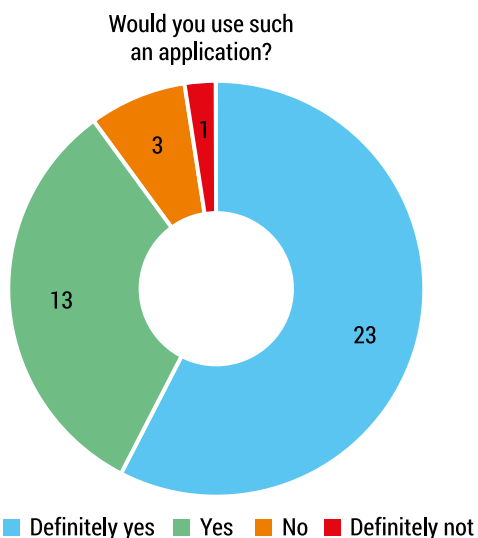
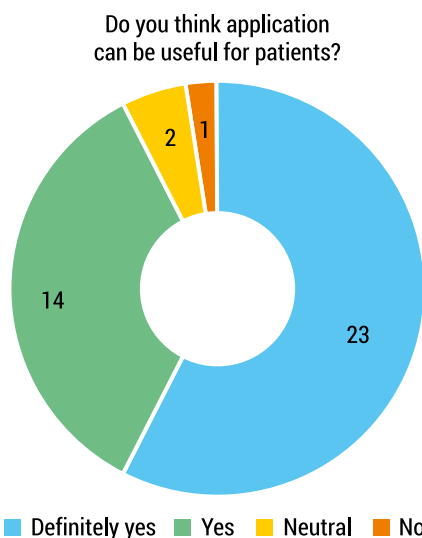
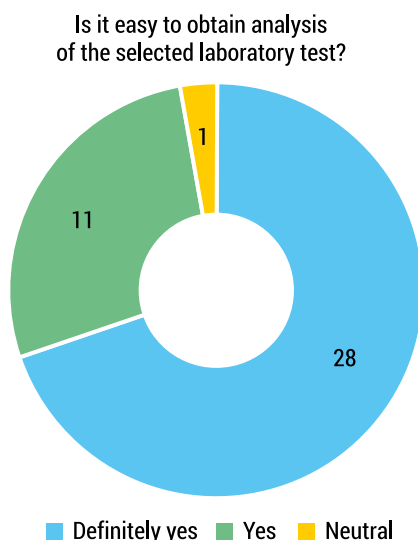
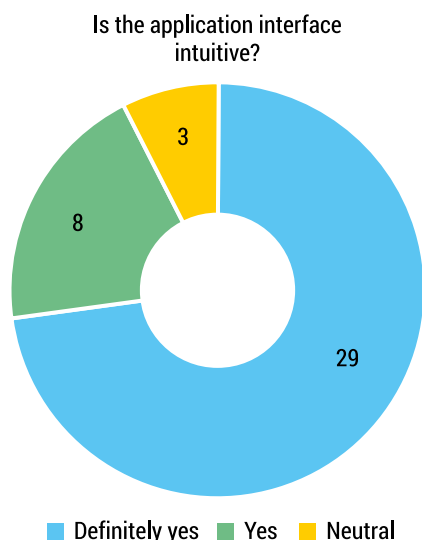


FIG. 9. Answers to questions regarding application evaluation

At the end of the survey there was a question addressed only to doctors or future doctors, as it related to the prospects of using such an application in their daily work. Two respondents answered:

- “Yes. It could be a good and handy tool for work, where you can quickly check or recall the potential causes of specific diseases causing abnormalities in laboratory results.”

- *“I think it’s definitely a useful app. In a doctor’s normal life, various patients come to him, so the application, which intuitively suggests what to do, will greatly facilitate work and help in everyday diagnoses.”*

## 6. Conclusions

The article emphasizes the importance of IT support in laboratory diagnostics, and more specifically in the interpretation of test results. Despite the widespread use of ordering and performing laboratory tests, the process of interpreting the results remains a key challenge for medical staff.

The application, which has been developed, aims to help patients better prepare for a doctor’s visit by self-monitoring their health. Detected probable diseases will allow the patient to delve deeper into his treatment history, as well as seek information from his immediate family about the occurrence of certain diseases. Then, during a visit to the doctor, he will pay special attention to particular diseases suffered in the past, because there is a likelihood of their recurrence or, in the case of a family, the likelihood of heredity. Therefore, there is a greater chance of diagnosing the disease in its early stage, which is associated with more effective treatment.

Additionally, during the analysis of the result, the application identifies values characteristic of a threat to health or life and informs the patient about it with a message about the need for immediate medical consultation. This solution minimizes the risk of health deterioration that could occur as a result of postponing the visit even for a few days.

The application offers analysis of urine tests and vitamin levels with food suggestions, which are distinctive functionalities compared to other applications. In addition, based on an online survey, it is noticeable that the application is already meeting the needs of users, and 90% of those surveyed said they would use such a tool. Two doctors and future doctors responded that the app could support their daily work in making diagnoses and checking and recalling potential causes of selected disease entities.

## References

1. Solnica B., Dembińska-Kieć A., Jerzy N., Diagnostyka laboratoryjna z elementami biochemii klinicznej. Edra Urban & Partner, Wrocław 2022.
2. Wrotek K., Interpretacja wyników badań. Helion, Gliwice 2007.
3. Szutowicz A., Raszeja-Specht A., Diagnostyka Laboratoryjna. Gdański Uniwersytet Medyczny, Gdańsk 2009.
4. Jarosz M., Rychlik E., Stoś K., Charzewska J., Normy żywienia dla populacji Polski i ich zastosowanie. Narodowy Instytut Zdrowia Publicznego–Państwowy Zakład Higieny, Warszawa 2020.
5. Gorczyca M., Zejc A., Chemia leków. Wydawnictwo Lekarskie PZWL, Warszawa 2019.

6. Albahrani A.A., Greaves R.F., Fat-soluble vitamins: clinical indications and current challenges for chromatographic measurement. *The Clinical Biochemist Reviews*, 2016, 37(1), 27–47.
7. Kołodziejczyk A., Naturalne związki organiczne. Wydawnictwo Naukowe PWN, Warszawa 2023.
8. Almohanna H.M., Ahmed A.A., Tsatalis J.P., Tosti A., The role of vitamins and minerals in hair loss: a review. *Dermatology and Therapy*, 2019, 9(1), 51–70.
9. European Food Safety Authority (EFSA), *Dietary reference values for nutrients summary report*, 2017, 14(12).
10. Pałasz M., Petzke E., Leksykon witamin i minerałów. Wydawnictwo SBM, Warszawa 2019.
11. Brackets, <https://brackets.io> (access: 24.01.2024).
12. HTML file validator, <https://validator.w3.org/nu/> (access: 27.01.2024).
13. CSS file validator, <https://jigsaw.w3.org/css-validator/> (access: 27.01.2024).

# Artificial intelligence in neuroimaging of cerebral aneurysms – theoretical study

*Żaneta Anna Mierzejewska<sup>1\*</sup>*

<sup>1</sup> *Faculty of Mechanical Engineering, Institute of Biomedical Engineering, Białystok University of Technology, Wiejska 45C, 15-351 Białystok, Poland, \*a.mierzejewska@pb.edu.pl*

**Abstract:** An aneurysm is a significant, pathological dilatation of a blood vessel associated with excessive weakening of the wall of an artery or, less often, a vein. Most often, aneurysms are congenital, but they can also cause long-term atherosclerosis or hypertension. Although a ruptured aneurysm is a life-threatening condition, the vast majority of brain aneurysms do not cause any symptoms. Such aneurysms are increasingly detected during the diagnosis of ailments not related in any way to the presence of an aneurysm – dilated pupil, drooping eyelid or double vision. The causes of brain aneurysms are unknown, but a number of factors that can increase the risk of their appearance, enlargement and rupture have already been identified. Brain aneurysms occur more often in adults than in children and more often in women than in men. Additionally, identified factors include nicotine addiction and uncontrolled high blood pressure (hypertension). Rarely, aneurysms may be one of the components of genetically determined diseases. If an aneurysm is suspected or a subarachnoid hemorrhage occurs, the basic diagnostic test is Computed Tomography Angiography (AngioCT) and Magnetic Resonance Angiography (AngioMR). Those are a non-invasive diagnostic methods used to assess blood vessels, which combines the advantages of CT or MRI and traditional angiography. Artificial intelligence is playing an increasingly important role in medicine, including in the detection of brain aneurysms. AI-based techniques, especially machine learning and deep learning, are being used to analyze medical images to identify and classify aneurysms with a precision much higher than the discerning human eye can achieve.

**Keywords:** Cerebral aneurysms, Subarachnoid hemorrhage, Computed tomography angiography, AngioCT, AI-based techniques

## 1. Introduction

A cerebral aneurysm, referred to in medical literature as an intracranial aneurysm or cerebrovascular aneurysm, is a disease of the arteries of the brain. It is a widening or bulging of the wall of a blood vessel, which usually occurs as a result

of weakening to the vessel wall. Blood flowing under pressure pushes the weakened part of the artery out, this bulge gradually increases in size and leads to damage to the artery wall (Fig. 1) [1–3]. When blood flows from a ruptured artery into the space between the brain and the membrane covering the brain – called the arachnoid mater – it is defined as a subarachnoid hemorrhage [4]. Blood may also flow directly into the brain tissue, forming an intracerebral hematoma, or into the ventricles of the brain, forming an intraventricular hematoma [5].

One theory says that the cause of a brain aneurysm is a congenital abnormality in the structure of the cerebral arteries, which means that there are fewer muscle and elastic fibers in the bifurcation of the artery. A cerebral aneurysm most often occurs at the point of bifurcation of arteries into distal branches or at the point of departure of individual arteries [3, 7–9]. In 85% of cases aneurysms are located in the anterior part of the cerebral arterial circle (Willis). Most of them are formed on the so-called anterior communicating artery (35%), followed by the middle cerebral artery (20%), the bifurcation of the carotid artery (8–12%), the distal part of the anterior cerebral artery (3–5%), anterior choroidal artery (3%) and ophthalmic artery (2%) [10].

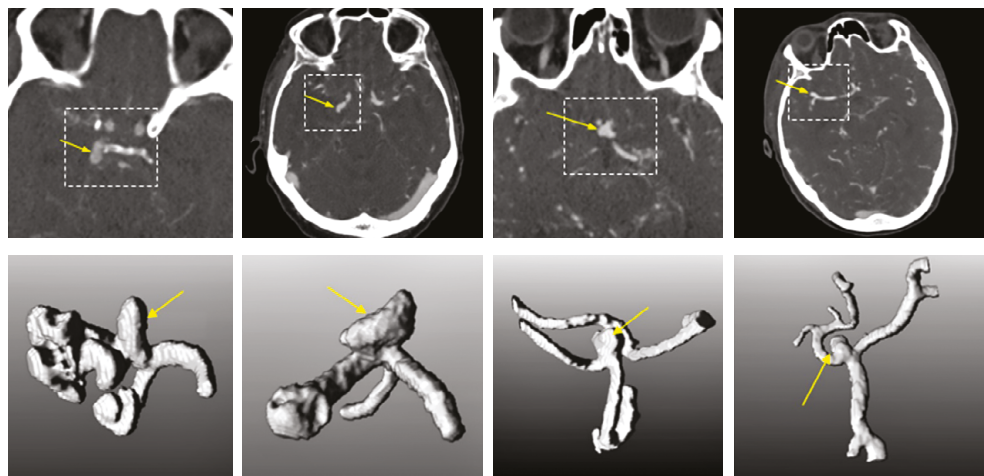


FIG. 1. Four examples of cerebral aneurysm [6]

This location means that cerebral aneurysms, especially small ones, can be easily missed in standard diagnostic imaging, which leads to delays in their detection and treatment. In response to these challenges, there is growing interest in the use of artificial intelligence (AI) in the diagnosis of brain aneurysms.

## 2. Materials and methods

the literature study was based on full versions of English-language scientific articles published in the last decade. To search for articles, numerous databases of scientific publications, including: Scopus, CORE, PubMedCentral (PMC) and GoogleScholar, as well as websites of journals publishing articles in the field of biomedical engineering and medicine were used. The main emphasis was placed on organizing knowledge about brain aneurysms, their causes, specificity, classification and finally symptoms, diagnosis and treatment. At the same time, based on a few publications, an attempt to indicate how artificial intelligence can contribute to improving diagnostics in the field of detecting brain aneurysms was made.

## 3. Results

When analyzing the cause of changes, aneurysms are distinguished: true, pseudoaneurysm and dissecting. A true aneurysm is most often the result of congenital disorders in the structure of blood vessel walls. Its occurrence may also be influenced by trauma or inflammation in the body. A pseudoaneurysm occurs when the continuity of the artery is interrupted and a hematoma develops, which is eventually surrounded by body tissues. This change resembles an aneurysm, but by definition it is not a typical aneurysm, hence the name pseudoaneurysm. The third type of change is the so-called dissecting aneurysm. It occurs as a result of a rupture of the intima, which is usually caused by congenital defects or hypertension. Aneurysms can also be differentiated according to their location, e.g. thoracic aortic aneurysm, abdominal aortic aneurysm, cerebral aneurysm [11–13].

Aneurysms can also be divided according to the shape of the lesion. There are two types: saccular aneurysms – constituting approximately 80% of all aneurysms and fusiform aneurysms – occurring much less frequently (Fig. 2). Saccular aneurysms consist of a neck and a sac, similar in shape to a ball. The width of the aneurysm neck is important when planning the type of procedure, because a wide neck may cause the springs used to close its lumen (embolization) to fall out, which may cause the vessel to close, resulting in an ischemic stroke. The wall of a saccular aneurysm is usually thin, however, as patients age, atherosclerotic lesions appear and grow in the aneurysm wall. Thrombuses form in the lumen of the aneurysm, located near the wall or blocking its lumen. Over time, in the process of organization, clots transform into fibrous connective tissue, and the aneurysm then looks like a nodular formation [14, 15].

Fusiform aneurysms are located primarily in the basilar and middle cerebral arteries, unlike saccular aneurysms, which are typically located where the arteries divide. They are usually caused by atherosclerotic changes. Therefore, they occur mainly in people of advanced age, although they may also appear in young people



after arterial inflammation or connective tissue diseases [17]. In such cases, the aneurysm wall usually does not contain an internal elastic membrane, and the intima-media becomes atrophied and fibrotic. Spindle cell aneurysms rarely cause subarachnoid hemorrhages. In turn, clots are more likely to form in their lumen. Thrombosis of basilar artery fusiform aneurysms may lead to ischemic stroke in the brainstem and/or cerebellum. Large aneurysms of this artery may, in turn, compress the brain stem and cause symptoms (so-called brain stem syndromes) [18].

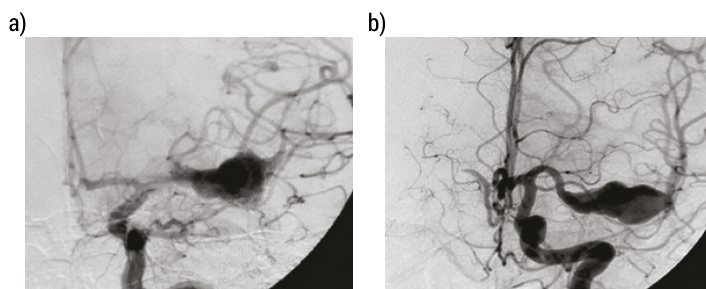


FIG. 2. Saccular(a) and fusiform (b) aneurysm [16]

The incidence of cerebral aneurysms is not precisely known. According to various studies, it is estimated that they occur in 0.2–7.9% of the population. Most of them, 88%, are revealed by subarachnoid hemorrhage, 8% show symptoms of a brain tumor, and 4% are detected accidentally. Aneurysms occur more often in women than in men and, according to various sources, the ratio is approximately 1.8:1. A slightly higher incidence of aneurysms was also found in first- and second-degree relatives of people who had subarachnoid hemorrhage (SAH). Some researchers have detected various chromosomal loci (e.g. polymorphisms of 19 different single nucleotides on chromosomes 9, 8 and 4) that could be associated with a higher likelihood of aneurysms, but so far no specific gene has been found to be responsible for this increased risk. The peak incidence of aneurysm rupture occurs at the age of 55–60 (only about 20% of aneurysms rupture in people between 15–45 years of age, and about 2% of aneurysms occur in people under 18 years of age) [3, 19–22].

The statistics are very ambiguous because in many cases a brain aneurysm is detected too late or not at all. Currently, thanks to brain imaging methods, it is possible to detect aneurysms in many people who were not even aware of the risks associated with it. Diagnostics are therefore of particular importance.

### 3.1. Causes of aneurysms and their symptoms

The causes of brain aneurysm include primarily congenital abnormalities of the arterial wall structure and atherosclerosis, during which the so-called atherosclerotic plaques, made of cholesterol particles. This condition promotes aneurysms and directly

threatens health, posing the risk of stroke or heart attack. Sometimes brain aneurysms occur as a result of inflammatory changes in the artery wall. This usually happens because the vessel lumen is blocked by an infected clot. Such aneurysms are called septic aneurysms. In addition to the deficit in the structure of the intima and the elastic intima of the vessel, there are also: all developmental abnormalities located in the area of the cerebral arterial circle, chronic obstructive pulmonary disease, Marfan syndrome (a genetic disease of connective tissue affecting the functioning of the cardiovascular, skeletal and visual systems), inflammation of artery walls, diabetic angiopathy, polycystic kidney disease, nicotine addiction and alcohol and/or drug abuse, head injuries and hereditary factors. However, the most common cause of aneurysm rupture is increased blood pressure [23,24].

In the case of large-sized brain aneurysms or their critical location, patients may experience symptoms such as headaches, which, when intense, may cause loss of consciousness, dizziness, and drooping eyelids (so-called ptosis). The disease may cause visual disturbances, including double or blurred vision, as well as enlargement of one pupil. In severe cases, brain aneurysms are accompanied by difficulties in speaking, loss of balance, short-term memory problems, convulsions, hemiparesis, and impaired consciousness. However, a brain aneurysm does not always rupture and then the disease is asymptomatic or accompanied by non-specific symptoms [25].

Most often, however, the disease is revealed only when the aneurysm bursts. Hemorrhage occurs and is counteracted by the body's defense mechanisms (clot formation, artery spasm, etc.). Thanks to these mechanisms, the hemorrhage may be minor. In general, there is a relationship between the amount of extravasated blood and the patient's condition. The first symptom of an aneurysm rupture is a sudden, very severe headache, which may be accompanied by nausea and vomiting. In more severe cases, there are: disturbances in the level of consciousness of the head up to complete loss of consciousness, neurological symptoms – for example, stiff neck, paresis of the limbs and others [26, 27].

Hemorrhage causing extravasation of a larger amount of blood leads to death due to respiratory and circulatory disorders. The neurological condition after subarachnoid hemorrhage resulting from a ruptured aneurysm is assessed on the Fischer or Hunt-Hess scale. After the first hemorrhage, the patient is at risk of another hemorrhage, which may occur after several hours or days [4]. Hemorrhage from an intracranial aneurysm is a life-threatening condition. For this reason, it is necessary to urgently perform appropriate imaging tests (computer tomography with contrast agent, cerebral arteriography) to detect the site of bleeding. When an intracranial aneurysm is detected, treatment is necessary by turning off the blood supply to the aneurysm, but patients in a serious condition are not operated on urgently, as urgent surgery in such a condition is difficult due to cerebral edema [28].

In the case of subarachnoid or intracerebral hemorrhage or hemorrhage into the ventricular system of the brain, the symptoms are similar to those described above, however, the patient's condition is more severe, consciousness disorders and neurological symptoms are more frequent and more pronounced. Intracerebral

hemorrhage causes the formation of an intracerebral hematoma, which in turn leads to an increase in intracranial pressure that is unfavorable for the patient. This condition may require urgent surgical treatment, which involves removing the hematoma and closing the source of bleeding [29, 30].

Aneurysm rupture is the most common cause of subarachnoid hemorrhage (approximately 80% of SAH is caused by aneurysm rupture). How dangerous this situation is, is demonstrated by the fact that 10–15% of these sick people die before help arrives. Of those who go to hospital, 46% die within the next 30 days regardless of treatment. In turn, among patients who survive the primary hemorrhage and, due to various reasons, do not undergo embolization or surgical treatment, the most common cause of death is repeated hemorrhage. The risk of its occurrence in the first 2 weeks after the first hemorrhage is approximately 15–20%. Of the patients who survive hemorrhage, approximately 30% have severe, irreversible neurological damage, and over 66% never regain full mobility [31–34].

## 3.2. Diagnosis

Diagnosis of brain aneurysms that do not cause clinical symptoms involves performing computed tomography angiography (commonly CT angiography; Fig. 3) or magnetic resonance angiography (MR angiography; Fig. 4). Although the «gold standard» is still an angiographic examination with contrast administered through a catheter inserted into the vessel. It is an invasive examination and should not be performed in the absence of obvious indications. Local complications resulting from the insertion of a catheter into a vessel are estimated at ~5%, the overall incidence of neurological complications is ~1%, and permanent neurological deficits are ~0.5% [35]. In some patients, especially when the results of CT or MRI angiogram do not allow us to clearly determine whether the patient has an aneurysm, traditional subtraction angiography of cerebral vessels is performed, which is the most accurate method of examination.

The main role of blood vessels is to supply cells with blood with oxygen and nutrients necessary for the proper functioning of tissues – as well as to collect unnecessary metabolic products that should be removed from the body. Disruption of this mechanism may be particularly severe in the case of veins and arteries located in the head, which “serve” the brain, eyes and other key organs located in this area. When there is a suspicion that the symptoms reported by the patient may be caused by, for example, a blood clot, atherosclerotic narrowing of a vessel or its improper development, it is usually necessary not only to confirm such assumptions, but also to precisely locate the abnormality in order to undertake effective therapy [36]. A simple, cheap and widely available vascular imaging test, such as Doppler ultrasound, is unfortunately not applicable when the problem occurs inside the skull, because the ultrasound waves used in this procedure are unable to penetrate the bone structures [37]. That is why angiography is used.

The examination of blood vessels using a computed tomography scan is called CT angiography. “Angiography” was created by combining two Greek words “angeion” and “graphein”. The first of them literally means “vessel”, and the second “to draw, to plot”. So it’s hard to imagine a better name for this test that allows us to show our blood vessels. It is worth adding that in angiography we distinguish venography – imaging of veins and arteriography – imaging of arteries [38, 39].

Traditional head angiography involves delivering a special substance called contrast to a selected blood vessel and performing an X-ray. The contrast strongly absorbs X-ray radiation, so the arteries and veins filled with it become clearly visible on the X-ray. The contrast agent (also known as contrast agent) is delivered to a specific place through a long catheter placed in the bloodstream through a small incision made under anesthesia. In the case of imaging the vessels of the head, it often runs from the femoral artery to the carotid arteries, where the transported contrast is released. It is not very pleasant and carries a high risk of complications resulting from infection – which is why this method is now being abandoned [40].

Its place is taken by modern technology, which is spiral computed tomography. X-rays are also used here, but instead of just one or a few x-rays, a whole series of x-rays are created, taken in many different planes and at different angles. These photos are then overlaid and digitally processed to create highly detailed, two- and three-dimensional models of the scanned areas [41, 42]. Advanced software now allows imaging of vascular structures with an accuracy of 1 mm. It is to this that the study owes the adjective “computed” in its name. The word “spiral” comes from the trajectory of the lamps emitting radiation and the detectors located in front of them, which collect this radiation after it passes through the tissues. Lamps and detectors move in a circle inside the circular casing of the tomograph (i.e. the device used to perform tomography), while a special table with the patient lying on it slowly slides into the opening of the machine. As a result, the mentioned X-ray images are taken in a spiral [43].

The moment when a selected part of the body is x-rayed must be precisely timed with the moment when the shading substance reaches this area. This is why in classic angiography, contrast is introduced through a catheter. Tomography, however, allows it to be administered through a cannula inserted at the beginning of the examination, using an automatic syringe, which is much more convenient and significantly reduces the risk of complications. Scanning starts after a few or a dozen or so seconds and lasts about the same time. The entire procedure, including preparing the patient and providing him with appropriate instructions, takes from several minutes to a maximum of half an hour [40, 41].

In the case of CT angiography, CT images are collected in the arterial phase of flow, after contrast administration (Fig. 3). This method allows visualization of aneurysms 2–3 mm in size with a sensitivity estimated at 77–97% and a specificity of 87–100%. CT angiography can be used to perform periodic follow-up examinations in patients after endovascular embolization procedures, after procedures with partial exclusion of the aneurysm from the circulation using vascular clips, as well as in patients treated conservatively [44]. The scanning itself is not noticeable

in any way, but the administration of contrast – apart from the discomfort associated with the insertion of the cannula – can cause quite unpleasant allergic reactions. In extremely rare cases, it can even be life-threatening, which is why after a head angiogram the patient should remain in the medical facility for several dozen minutes so that its staff can intervene immediately if necessary. Iodine-based contrast agents used in head CT angiogram also place an additional burden on the kidneys, and sometimes their use results in a deterioration of the condition of patients suffering from thyroid diseases. We must also not forget about the harmful effects of X-ray radiation on the DNA of cells. Due to this, the test should not be performed too often, especially in children and the elderly, and pregnant women should not undergo it at all [46].

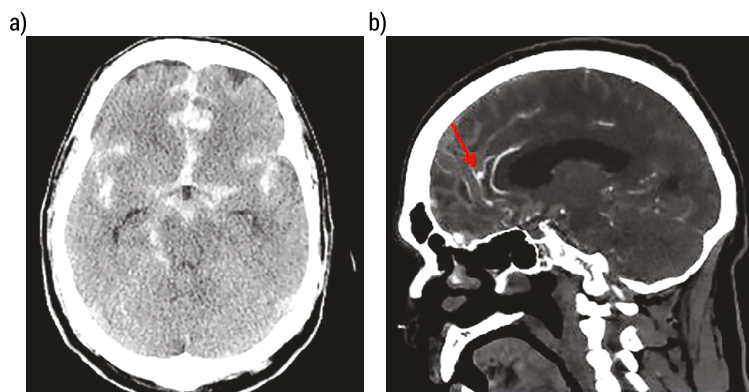


FIG. 3. Head CT (A) demonstrates angioCT (B) showing a 5-mm ruptured aneurysm (arrow) [45]

An innovative diagnostic method that allows for a comprehensive assessment of the condition of the brain's blood vessels is Magnetic Resonance Angiography (angioMR; Fig. 4). During this examination, precise images of the intracranial arteries are obtained, which allows for a complete analysis of blood circulation within the brain [47]. Unlike classic angiography that uses X-ray radiation, MRI angiogram eliminates the potential risk of radiation. This patient-safe method is based on the use of a strong magnetic field and radio waves, which do not have a harmful effect on the human body. Depending on the indications, the examination can be performed without the use of contrast; the use of a contrast substance increases the precision of imaging and allows the characterization of some changes [48]. The magnetic resonance technique uses the properties of hydrogen atoms that are present in the cells of the human body. Thanks to the magnetic field, they emit waves recorded by MRI equipment and are transformed into an extremely precise image thanks to which the specialist performing the examination can see the internal structures of a given area. It sometimes happens that an angiogram requires intravenous administration of a contrast agent. Importantly, unlike X-ray radiation, magnetic resonance imaging of the head does not have any harmful ionizing effects on the tissues [49].

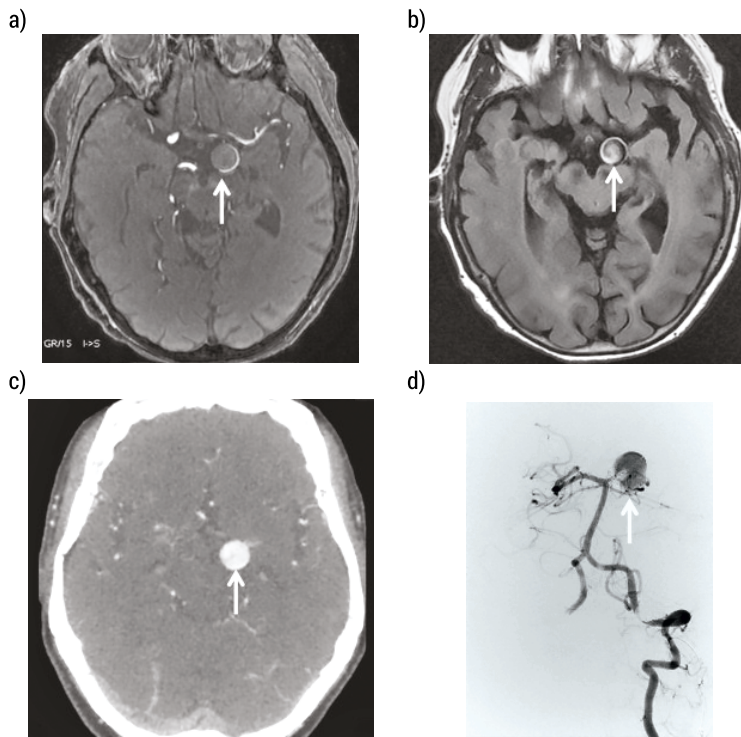


FIG. 4. Defective visualization of the aneurysmal sac in real time angioMR [50]

### 3.3. Treatment of brain aneurysms

The traditional method of treating a ruptured aneurysm is to perform a pterional craniotomy. This is a type of neurosurgical procedure that uses a temporal-frontal approach to the brain (the name “pterional” refers to the pterygoid process of the temporal bone). This is a frequently used surgical approach for brain surgery because it provides access to many important areas, such as the primary cerebral arteries and anatomical structures located around the base of the skull. This allows the aneurysm to be dissected and closed from the outside with a titanium clip (Fig. 5).

It is an invasive method, but it gives practically 100 percent success and certainty of cure. The disadvantages of this method are: the risk of ischemic changes in the place where the spatulas are placed, the risk of damage and, consequently, the closure of small, microscopic vessels – perforators, which reach the deep structures of the brain and, as a result, the appearance of transient or non-transient neurological deficits, the risk of fluid flow, the development of wound infection and, as a result – meningitis or encephalitis [51].

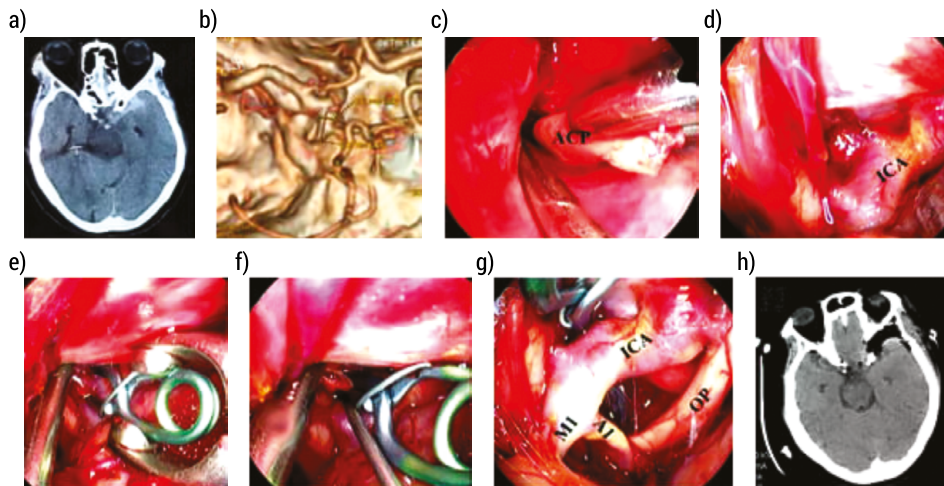


FIG. 5. An unruptured MCA aneurysm was clipped via the traditional pterional approach under the neuroendoscope. (A) Pre-operative CT scan showed no SAH or hematoma in the brain. (B) Pre-operative CTA scan showed a saccular aneurysm at the left MCA bifurcation. (C) A sylvian fissure was sharply dissected under neuroendoscope. (D) Aneurysm and the branches of MCA were exposed under the neuroendoscope. (E) MCA was clipped temporarily. (F) Aneurysm was clipped under the neuroendoscope and temporary clip was removed. (G) Postoperative CT scan showing no hematoma and damage in the brain. (H) Postoperative CTA scan showed that aneurysm was clipped completely and the MCA and its branches were preserved [52]

If there are contraindications to applying a clip, two other methods are used – trapping and wrapping. Trapping involves completely separating the aneurysm from the blood circulation by blocking the blood flowing through the aneurysm. This is achieved by placing a clamp on the artery at both the front and back ends of the aneurysm, which prevents blood from flowing into the aneurysm. When an aneurysm is closed, it stops growing and may even shrink, reducing the risk of rupture over time. Wrapping, on the other hand, involves wrapping the aneurysm with a material that indirectly blocks blood flow to the aneurysm. The most commonly used materials are special fabrics or foils. After wrapping the aneurysm, the patient's tissue forms scar tissue around the aneurysm, which leads to its closure. Although this technique does not directly block blood flow, over time it leads to the closure of the aneurysm and reduces the risk of rupture [53, 54].

Aneurysm embolization (Fig. 6) is an invasive procedure that involves injecting embolization material into the aneurysm to close it or reduce the risk of rupture. This is a frequently used method of treating brain aneurysms, especially when the aneurysm is difficult to access for surgery or when there are risks associated with traditional surgery [55]. The procedure begins with inserting a catheter through the skin into a blood vessel, most often via the femoral or carotid artery. The catheter is guided by imaging such as fluoroscopy or angiography. A thin catheter is inserted through the catheter into the aneurysm. Then, the embolization material, most often



in the form of microscopic catheters, coils or medical glue, is injected into the interior of the aneurysm. This material inhibits the inflow of blood into the aneurysm sac, and secondly, it causes clotting of the blood that had previously flowed there, which in turn leads to the formation of a clot filling the aneurysm sac. After some time, the clot grows completely and becomes covered with endothelium, which restores the original structure of the vessel [56–58].

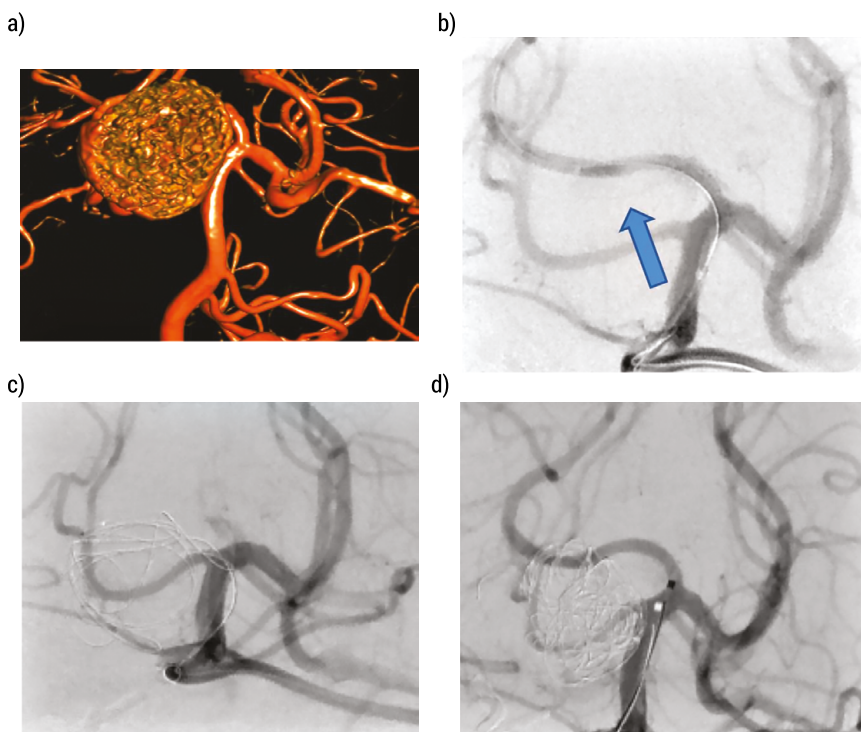


FIG. 6. Aneurysm embolization [59]

Both methods – surgical clip placement and embolization – lead to the exclusion of the aneurysm from the circulatory system. The method of treatment is decided by the medical team together with the patient; the team includes a neurosurgeon and an interventional (procedure) radiologist. When choosing one of the two methods of treatment described above, the medical team takes into account many factors, such as the location of the aneurysm, its size, shape, width of the neck and adjacent vessels, and determines the procedural risk.

The size of the aneurysm is extremely important in the course of the disease, prognosis, and the decision on planned treatment. The risk of rupture of an aneurysm with a diameter of up to 10 mm is estimated at 0–4% per year and is correspondingly higher in the case of larger aneurysms [60]. Moreover, it should be remembered that their size is not constant – aneurysms may enlarge, therefore, if a decision is made not to treat the aneurysm, it is recommended to periodically perform imaging tests



to assess its size. The risk of rupture of aneurysms measuring 10 mm or more is 1% per year, and in the case of smaller aneurysms it is lower. However, recent reports suggest that aneurysms up to 10 mm in diameter rupture more often than originally thought [61]. This has led to a change in the approach to the treatment of unruptured intracranial aneurysms – now it is recommended to treat them when their diameter exceeds 7 mm. In the case of surgical treatment of aneurysms, the risk of perioperative and post-operative complications increases with the size of the aneurysm and is the lowest for those up to 5 mm (2.3%), for aneurysms ranging from 6 to 15 mm the risk is 6.8%, while the highest is in the case of aneurysms 16–25 mm (14%) [62].

## 4. The use of artificial intelligence in neuroimaging

The problem of brain aneurysms affects approximately 5% of Polish society, i.e. every 20<sup>th</sup> person in our country lives with an intracranial aneurysm. The annual incidence of this disease varies depending on the country and ranges from 2 cases per 100,000 in China to 22.5 per 100,000 in Finland. They occur more often in women and most often are detected in the fifth decade of life [63]. The emergence of changes is facilitated by, among others, hypertension, smoking and regular alcohol abuse. In people predisposed to aneurysm formation, the blood vessel appears normal, but in some places, it has a thinner wall, which begins to bulge with age. Most patients do not know about this because most aneurysms do not burst or bleed. Despite progress in endovascular and neurosurgical techniques, approximately 60% of people die almost immediately after its rupture. This proves how serious a threat to health and life a brain aneurysm is [64]. Although there are effective endovascular techniques that can protect the dilated vessel (reducing the risk of rupture), to get to this stage, the aneurysm must first be detected. This is where artificial intelligence can come in handy.

Solutions based on artificial intelligence technology are currently widely used in various areas of medicine and health care. One of the key areas is diagnostic imaging – one of the most important methods of obtaining information about the patient's condition. Thanks to technologies such as X-rays, magnetic resonance imaging, ultrasound or computed tomography, it is possible to recognize pathological changes in the body without the need for surgical intervention, and artificial intelligence is able to further improve the imaging diagnostics process [65]. Photos of anatomical structures require analysis by qualified personnel, from technicians to radiologists and surgeons. The volume of these analyses is massive, and the huge amount of work and staff shortages in the health service mean that the waiting time for tests and image descriptions is often several weeks or even months. Advanced algorithms and AI systems however can analyze vast amounts of medical data, including medical images, laboratory test results, and clinical data. This makes it possible to diagnose many diseases faster and more accurately, including cancer, heart disease and neurological diseases [66]. Examples of solutions in which artificial intelligence has been implemented in imaging

diagnostics include numerous lung examinations after COVID-19 [67], examination of fractures and orthopedic injuries [68] or examination of skin lesions for the diagnosis of melanoma [69]. Computer programs using machine learning can help detect even the smallest pathological changes, which increases the chances of early diagnosis and effective treatment, therefore the use of artificial intelligence will be more and more common, also in the diagnosis of brain aneurysms.

The conclusions of a study conducted by a South Korean team of researchers have just been published in the official journal of the European Society of Radiology [70]. They report that thanks to the use of so-called deep learning, artificial intelligence is able to independently analyze the examination of cerebral arteries and identify an aneurysm there. The discussed algorithm was prepared on the basis of available images of cerebral arteries obtained from magnetic resonance imaging. This is the first study of this kind that aims to reliably assess the accuracy of an AI algorithm. The algorithm successfully classified the lesion as an aneurysm in 92–98% of cases, where the human assessment reaches approximately 89%.

A retrospective study on the detection of cerebral aneurysm in computed tomography imaging was conducted by a team of scientists from leading medical universities in the United States. They used scans of fifty-one patients taken over a two-year period and the RAPID Aneurysm software. Artificial intelligence correctly identified sixty aneurysms – 5% more than a team of neuroradiology specialists, with an accuracy of their shape and location of 99.7% [71].

The possibilities of artificial intelligence in automatic diagnosis of aneurysms were also analyzed by Krackov et al. [72]. For this purpose, they used image analysis software installed on a smartphone and the mechanism of the convolutional network in the learning process. These tools allowed the achievement of classification accuracy above 90% in validation images, and the authors indicated that the reliability of such a study may not only improve diagnosis, but may also soon be a standard element of telemedicine.

Bizjak and Špiclin, in turn, conducted a meta-analysis of published articles that concerned the discussed issues. The criteria adopted by the authors were studies conducted using automated deep learning algorithms in the analysis of CT images. Over the last ten years, there have been only fifteen such publications, which indicates that this topic is new and the potential of using artificial intelligence in the diagnosis of aneurysms is yet untapped. Nevertheless, the authors focused on diagnostic accuracy, sensitivity of the selected method and the number of false-positive results. These parameters were assessed using the Preferred Reporting Items for Systematic Reviews and Meta-Analysis (PRISMA) guidelines and the Quality Assessment of Diagnostic Accuracy Studies 2 (QUADAS-2) tool. Their analysis of fifteen cases show that the diagnostic methods used were characterized by high sensitivity, ranging from 87 to 95% with a confidence interval from 0.83 to 0.91, but these results only concerned aneurysms whose diameter exceeded 3 mm. For smaller changes, the sensitivity of the algorithms used was only 56% [73].

## 5. Conclusion

Most aneurysms do not cause any symptoms until they rupture. Some patients may experience minor bleeding prior to rupture, and the associated headaches are not severe, but may be accompanied by nausea and vomiting, although these are rare. Although headache is a common reason for emergency care, and patients are rarely referred for detailed imaging tests, when assessing the patient's condition, it is necessary to consider the possibility of warning bleeding, which can save the patient's life.

Although the doctor's knowledge and experience as well as a correct and complete interview are crucial here, artificial intelligence is changing the face of medicine, opening new horizons in diagnosis, treatment and healthcare management.

The use of artificial intelligence in medicine brings many benefits – from shortening the diagnosis time, through adapting therapy to the individual needs of patients, to faster development of modern drugs and pharmaceuticals. In turn, in radiology, artificial intelligence combines advanced image analysis technologies based on machine learning, which allows for faster and more detailed interpretation of data. Machine learning algorithms, especially deep learning, are able to analyze MRI and CT images and automatically detect anomalies in blood vessels, supporting the classification of pathological changes based on images, which increases the accuracy of differentiating these changes and, ultimately, the correct diagnosis. Because the algorithms can precisely segment various brain structures, measure the volumes and other parameters of aneurysms, they make it possible to monitor the development of the disease and estimate the risk of aneurysm rupture or other complications.

Creating a tool to analyze large amounts of data in a short time and detect certain patterns can significantly improve the quality of health care, but it should be remembered that artificial intelligence in medicine is only of a supporting nature, and it is the doctor who makes the final decision as to further action. Although the use of AI in everyday medical practice is already at the implementation stage and more and more innovative IT solutions are available, it should be emphasized that many of them are not included in the current regulations. Therefore, in order to be the beneficiary of available technologies that are intended primarily to serve the good of the patient, it is necessary to create appropriate foundations, a favorable legal environment and ethical framework to ensure the transparency of new solutions, guarantee patient safety and enforce responsibility for decisions made on the basis of analyses carried out by artificial intelligence.

## References

1. Chalouhi N., Hoh B.L., Hasan D., Review of cerebral aneurysm formation, growth, and rupture. *Stroke*, 2013, 44(12), 3613–3622.
2. Texakalidis P. et al., Aneurysm formation, growth, and rupture: the biology and physics of cerebral aneurysms. *World Neurosurgery*, 2019, 130, 277–284.
3. Sheikh M.A.A., Shuib A.S., Mohyi M.H.H., A review of hemodynamic parameters in cerebral aneurysm. *Interdisciplinary Neurosurgery*, 2020, 22, 100716.
4. Tawk R.G. et al., Diagnosis and treatment of unruptured intracranial aneurysms and aneurysmal subarachnoid hemorrhage. *Mayo Clinic Proceedings*, 2021, 96(7), 1970–2000.
5. Oppong M.D. et al., Aneurysmal intracerebral hematoma: risk factors and surgical treatment decisions. *Clinical Neurology and Neurosurgery*, 2018, 173, 1–7.
6. Firouzian A. et al., Intracranial aneurysm segmentation in 3D CT angiography: method and quantitative validation with and without prior noise filtering. *European Journal of Radiology*, 2011, 79(2), 299–304.
7. Tang H. et al., Underlying mechanism of hemodynamics and intracranial aneurysm. *Chinese Neurosurgical Journal*, 2022, 8(2), 120–127.
8. Marbacher S., Strange F., Frösén J., Fandino J., Preclinical extracranial aneurysm models for the study and treatment of brain aneurysms: a systematic review. *Journal of Cerebral Blood Flow & Metabolism*, 2020, 40(5), 922–938.
9. Cras T.Y. et al., Determinants of the presence and size of intracranial aneurysms in the general population: the Rotterdam study. *Stroke*, 2020, 51(7), 2103–2110.
10. Feng L. et al., Anatomical variations in the Circle of Willis and the formation and rupture of intracranial aneurysms: A systematic review and meta-analysis. *Frontiers in Neurology*, 2023, 13, 1098950.
11. Gowda R., Miller T.R., Morris N.A., Atypical Aneurysms: Mycotic Aneurysms, Dissecting Aneurysms, and Pseudoaneurysms. *Cerebrovascular Disorders*, 2021, 171–187.
12. Obara H. et al., Current management strategies for visceral artery aneurysms: an overview. *Surgery Today*, 2020, 50, 38–49.
13. Yale S.H. et al., Cardiovascular Eponymic Signs: Diagnostic Skills Applied During the Physical Examination, Springer, Cham 2021, 1–45.
14. Korte J. et al., Fusiform versus Saccular Intracranial Aneurysms – Hemodynamic Evaluation of the Pre-Aneurysmal, Pathological, and Post-Interventional State. *Journal of Clinical Medicine*, 2024, 13(2), 551.
15. Rastogi V. et al., Clinical presentation, outcomes, and threshold for repair by sex in degenerative saccular vs fusiform aneurysms in the descending thoracic aorta. *Journal of Vascular Surgery*, 2023, 78(6), 1392–1401.
16. <https://radiologykey.com/aneurysms/> (access: 5.04.2024).
17. Guo Y., Song Y., Hou K., Yu, J., Intracranial fusiform and circumferential aneurysms of the main trunk: therapeutic dilemmas and prospects. *Frontiers in Neurology*, 2021, 12, 679134.
18. Hackenberg K.A., Etminan N., Neurovascular disease, diagnosis, and therapy: Brain aneurysms. *Handbook of Clinical Neurology*, 2021, 176, 121–134.
19. Inagawa T., Prevalence of cerebral aneurysms in autopsy studies: a review of the literature. *Neurosurgical Review*, 2022, 45(4), 2565–2582.
20. Caffes N. et al., Unruptured cerebral aneurysms in elderly patients: key challenges and management. *Annals of Medicine*, 2021, 53(1), 1839–1849.

21. Kaspera W. et al., Morphological and hemodynamic risk factors for middle cerebral artery aneurysm: a case-control study of 190 patients. *Scientific Reports*, 2020, 10(1), 2016.
22. Maramkandam E.B., Sudhir B.J., Kannath S.K., Patnaik B.S.V., A novel parameter for the prediction of rupture risk of cerebral aneurysms based on morphology. Proceedings of the Institution of Mechanical Engineers, Part H. *Journal of Engineering in Medicine*, 2023, 237(9), 1091–1101.
23. Fréneau M., Baron-Menguy C., Vion A.C., Loirand G., Why are women predisposed to intracranial aneurysm?. *Frontiers in Cardiovascular Medicine*, 2022, 9, 815668.
24. Fingerlin T.J. et al., Long-term aneurysm recurrence and de novo aneurysm formation after surgical treatment of unruptured intracranial aneurysms: a cohort study and systematic review. *Neurological Research*, 2020, 42(4), 338–345.
25. Moubark M. et al., Flow diverter devices in the treatment of posterior communicating artery aneurysms: mid-term clinical and radiological outcomes. *Egyptian Journal of Radiology and Nuclear Medicine*, 2020, 51, 1–9.
26. Sanchez S. et al., Morphological characteristics of brain aneurysms among age groups. *Interventional Neuroradiology*, 2023, 15910199231201520.
27. Golnari P. et al., Volumes, outcomes, and complications after surgical versus endovascular treatment of aneurysms in the United States (1993–2015): continued evolution versus steady-state after more than 2 decades of practice. *Journal of Neurosurgery*, 2020, 134(3), 848–861.
28. Neifert S.N. et al., Aneurysmal subarachnoid hemorrhage: the last decade. *Translational Stroke Research*, 2021, 12, 428–446.
29. Florez W.A. et al., Intracranial hypertension in patients with aneurysmal subarachnoid hemorrhage: a systematic review and meta-analysis. *Neurosurgical Review*, 2021, 44, 203–211.
30. Chung D.Y., Abdalkader M., Nguyen T.N., Aneurysmal subarachnoid hemorrhage. *Neurologic Clinics*, 2021, 39(2), 419–442.
31. Kanamaru H. et al., Prognostic factors varying with age in patients with aneurysmal subarachnoid hemorrhage. *Journal of Clinical Neuroscience*, 2020, 76, 118–125.
32. de Winkel J. et al., Early predictors of functional outcome in poor-grade aneurysmal subarachnoid hemorrhage: a systematic review and meta-analysis. *BMC Neurology*, 2022, 22(1), 239.
33. de Souza M.R. et al., Association between intracranial aneurysm and meningiomas: an integrative survival Analysis with identification of prognostic factors. *Clinical Neurology and Neurosurgery*, 2020, 198, 106128.
34. Al-Ageely T.A. et al., Management of brain aneurysm neck-avulsion during clipping surgery: Illustrative case and literature review. *Romanian Neurosurgery*, 2023, 164–169.
35. Chappell E.T., Moure F.C., Good M.C., Comparison of computed tomographic angiography with digital subtraction angiography in the diagnosis of cerebral aneurysms: a meta-analysis. *Neurosurgery*, 2003, 52(3), 624–631.
36. Fiederer L.D.J. et al., The role of blood vessels in high-resolution volume conductor head modeling of EEG. *NeuroImage*, 2016, 128, 193–208.
37. Schebesch K.M. et al., Doppler ultrasound measurement of blood flow volume in the extracranial internal carotid artery for evaluation of brain perfusion after aneurysmal subarachnoid hemorrhage. *Neurological Research*, 2007, 29(2), 210–214.
38. Fleischmann D. et al., Computed tomography angiography: a review and technical update. *Radiologic Clinics*, 2016, 54(1), 1–12.
39. Yang Z.L. et al., Small intracranial aneurysms: diagnostic accuracy of CT angiography. *Radiology*, 2017, 285(3), 941–952.

40. Bredahl K.K. et al., Contrast enhanced ultrasound can replace computed tomography angiography for surveillance after endovascular aortic aneurysm repair. *European Journal of Vascular and Endovascular Surgery*, 2016, 52(6), 729–734.
41. Yan J., Diagnostic value of multi-slice spiral computed tomography angiography for intracranial aneurysm. *Neurological Sciences*, 2024, 1, 1–5.
42. Yang G. et al., Application effect of multi-slice spiral CT angiography combined with MRI in the diagnosis of cerebral aneurysm. *Biotechnology and Genetic Engineering Reviews*, 2023, 1–14.
43. Hsieh J., Flohr T., Computed tomography recent history and future perspectives. *Journal of Medical Imaging*, 2021, 8(5), 052109–052109.
44. Ierardi A.M. et al., Type 2 endoleaks in endovascular aortic repair: cone beam CT and automatic vessel detection to guide the embolization. *Acta Radiologica*, 2018, 59(6), 681–687.
45. <https://practicalneurology.com/articles/2021-july-aug/case-report-cerebral-aneurysm-re-rupture> (access: 5.04.2024).
46. Park H.J. et al., Relationship between lower dose and injection speed of iodinated contrast material for CT and acute hypersensitivity reactions: an observational study. *Radiology*, 2019, 293(3), 565–572.
47. Edelman R.R., Koktzoglou I., Noncontrast MR angiography: an update. *Journal of Magnetic Resonance Imaging*, 2019, 49(2), 355–373.
48. Nagpal P., Grist T.M., MR Angiography: Contrast-Enhanced Acquisition Techniques. *Magnetic Resonance Imaging Clinics of North America*, 2023, 31(3), 493–501.
49. Ren Y. et al., Reproducibility of image-based computational models of intracranial aneurysm: a comparison between 3D rotational angiography, CT angiography and MR angiography. *Biomedical Engineering Online*, 2016, 15, 1–14.
50. Rodriguez-Régent C. et al., Non-invasive diagnosis of intracranial aneurysms. *Diagnostic and Interventional Imaging*, 2014, 95(12), 1163–1174.
51. Picinich C.M., Ruiz M.A., Mittal M.K., Waldau B., Incidence of postoperative cerebral aneurysm clip slippage: review of a consecutive case series of 115 clipped aneurysms. *World Neurosurgery*, 2022, 161, e723–e729.
52. Li Z. et al., Surgical Clipping of Intracranial Aneurysms Using a Transcranial Neuroendoscopic Approach. *Brain Sciences*, 2023, 13(11), 1544.
53. Baldoncini M. et al., Wrapping technique in fusiform aneurysms. *Neurological Sciences and Neurosurgery*, 2020, 2(1), 111.
54. Safavi-Abbasi S. et al., Techniques and outcomes of microsurgical management of ruptured and unruptured fusiform cerebral aneurysms. *Journal of Neurosurgery*, 2017, 127(6), 1353–1360.
55. Murakami T. et al., Long-term results and follow-up examinations after endovascular embolization for unruptured cerebral aneurysms. *American Journal of Neuroradiology*, 2019, 40(7), 1191–1196.
56. Cheikh A. et al., Cost of treatment of cerebral aneurysm embolization: Study of associated factors. *Neurology and Therapy*, 2016, 5, 145–154.
57. Hanel R.A. et al., Prospective study on embolization of intracranial aneurysms with the pipeline device: the PREMIER study 1 year results. *Journal of Neurointerventional Surgery*, 2020, 12(1), 62–66.
58. Feng M.T. et al., Endovascular embolization of intracranial aneurysms: to use stent (s) or not? Systematic review and meta-analysis. *World Neurosurgery*, 2016, 93, 271–278.

59. Patel A. et al., Early angiographic signs of acute thrombus formation following cerebral aneurysm treatment with the Pipeline embolization device. *Journal of NeuroInterventional Surgery*, 2017, 9(11), 1125–1130.
60. Texakalidis P. et al., Aneurysm formation, growth, and rupture: the biology and physics of cerebral aneurysms. *World Neurosurgery*, 2019, 130, 277–284.
61. Murayama Y. et al., Risk analysis of unruptured intracranial aneurysms: prospective 10-year cohort study. *Stroke*, 2016, 47(2), 365–371.
62. Malhotra A. et al., Growth and rupture risk of small unruptured intracranial aneurysms: a systematic review. *Annals of Internal Medicine*, 2017, 167(1), 26–33.
63. Śliwczyński A. et al., An analysis of the incidence and cost of intracranial aneurysm and subarachnoid haemorrhage treatment between 2013 and 2021. *International Journal of Environmental Research and Public Health*, 2023, 20(5), 3828.
64. Morel S., Bijlenga P., Kwak B.R., Intracranial aneurysm wall (in) stability – current state of knowledge and clinical perspectives. *Neurosurgical Review*, 2022, 45(2), 1233–1253.
65. Boeken T. et al., Artificial intelligence in diagnostic and interventional radiology: where are we now?. *Diagnostic and Interventional Imaging*, 2023, 104(1), 1–5.
66. Ahmad Z., Rahim S., Zubair M., Abdul-Ghafar J., Artificial intelligence (AI) in medicine, current applications and future role with special emphasis on its potential and promise in pathology: present and future impact, obstacles including costs and acceptance among pathologists, practical and philosophical considerations. A comprehensive review. *Diagnostic Pathology*, 2021, 16, 1–16.
67. Soomro T.A. et al., Artificial intelligence (AI) for medical imaging to combat coronavirus disease (COVID-19): A detailed review with direction for future research. *Artificial Intelligence Review*, 2022, 1–31.
68. Laur O., Wang B., Musculoskeletal trauma and artificial intelligence: current trends and projections. *Skeletal Radiology*, 2022, 51(2), 257–269.
69. Alsaade F.W., Aldhyani T.H., Al-Adhaileh M.H., Developing a recognition system for diagnosing melanoma skin lesions using artificial intelligence algorithms. *Computational and Mathematical Methods in Medicine*, 2021, 1–20.
70. Ueda D. et al., Deep learning for MR angiography: automated detection of cerebral aneurysms. *Radiology*, 2019, 290(1), 187–194.
71. Heit J.J. et al., RAPID Aneurysm: Artificial intelligence for unruptured cerebral aneurysm detection on CT angiography. *Journal of Stroke and Cerebrovascular Diseases*, 2022, 31(10), 106690.
72. Krackov W. et al., Artificial Intelligence Methods for Rapid Vascular Access Aneurysm Classification in Remote or In-Person Settings. *Blood Purification*, 2021, 50(4–5), 636–641.
73. Bizjak Ž., Špicli Ž., A Systematic Review of Deep-Learning Methods for Intracranial Aneurysm Detection in CT Angiography. *Biomedicines*, 2023, 11(11), 2921.

# Utilization of the spin-coating method to produce elastic composites for applications in biomedical engineering

Joanna Mystkowska<sup>1\*</sup>, Anna Powojńska<sup>1</sup>, Jakub Ławrynowicz<sup>1</sup>

<sup>1</sup> Faculty of Mechanical Engineering, Institute of Biomedical Engineering, Białystok University of Technology, Wiejska 45C, 15-351 Białystok, Poland

\*j.mystkowska@pb.edu.pl, anna.powojnska@sd.pb.edu.pl,  
jakub.lawrynowicz.107248@student.pb.edu.pl

**Abstract:** The production of elastic composites for applications in biomedical engineering is an interesting and dynamically developing issue. The presented work concerns research on the use of the spin-coating method for the production of flexible composite materials. The work contains a description of experimental methods for testing density and thickness, as well as contact angle of the composites produced by spin-coating. Research was carried out to determine the effect of the spin-coating parameters: spin speed and spin time on the properties of the produced composites. Composite materials were made with 10, 15 and 20vol% Al<sub>2</sub>O<sub>3</sub> powder filler in a silicon matrix. The composite samples were prepared at rotational speeds of 1000, 1500 and 2000 rpm and with coating times of 10, 15 and 20 seconds. The results obtained from the tests carried out made it possible to determine the influence of the process parameters on the studied properties of the composites. The paper proves that the parameters of the spin-coating process affect chosen properties of the produced composites. The density for composite with 15vol% filler was  $d = 1.52 \text{ g/cm}^3$ , and for composite with 20vol% filler was  $d = 1.65 \text{ g/cm}^3$ . The thickness of the material with 10vol% filler at 1000 rpm and 10 s was 21  $\mu\text{m}$ , while for the composite with 20vol% filler it was 60  $\mu\text{m}$ . Performed research showed that the spin-coating parameters affected thickness and roughness of the composites, while they had no significant effect on the density and contact angle of tested composites. The content of the powder filler affected the thickness of the prepared composites.

**Keywords:** Elastic composite, Spin-coating, Composite thickness, Thin films



# 1. Introduction

## 1.1. Composite materials in medical applications

One of the factors of technological development in medicine is obtaining materials with desired properties. Such possibilities are provided by, among others, design of composite materials and their modification in order to obtain a product with appropriate structural and functional properties. These materials have unique advantages over other types of materials, e.g. metals, ceramics and polymers, because appropriate modification of the chemical composition allows for controlled achievement of specific physical, chemical, mechanical and thermal properties. Composites are currently one of the most dynamically developing materials that meet the material needs of the industry [1]. The final properties of the resulting composite material depend on the individual properties of the components and their relative contents, geometry, and arrangement. Most of the composite materials consist of only two components: a matrix, which is usually a material of relatively high ductility and low fracture toughness, which surrounds a second component, often known as the reinforcement or dispersed phase. The geometry (shape and size), and the distribution (position and orientation in the matrix) of the reinforcement also determine the properties of composite.

Composite materials are used widely in medicine. Doctors are using stents in cardiology to open or prevent narrowing caused by diseases such as thrombosis in flow channels such as the heart, peripheral arteries, or veins [2]. Composite biomaterials are beginning to serve as better alternatives [2], due to the flexibility of materials in stent design, as well as their low cost, biodegradability, and wide production possibilities [3]. Cartilage can be replaced with polymer composites, such as poly[2-hydroxyethyl methacrylate] (PHEMA) reinforced with polyethylene terephthalate (PET) synthetic fibers. By appropriately changing the volume fraction of the components of this biomaterial, it is possible to obtain properties similar to those of natural cartilage [4]. Injectable hydrogels are used as artificial cartilage to reduce wear and accelerate healing [1]. Composite biomaterials made of polylactic acid (PLA), and hyaluronic acid ester (HA) are used to repair or completely replace ligaments to restore the proper functioning of affected or damaged joints [4].

One of today's challenges is the production of multifunctional smart materials. Materials' intelligence is considered in terms of detecting changes in environmental conditions, processing detected information, and making actuation by moving away from or towards the stimulus [5]. It has been shown that the external stimuli, causing sudden changes in physical properties, are diverse and include temperature, pH, solvent or ion composition, electric or magnetic field, light intensity, and the introduction of specific ions [6]. One example is flexible magnetic materials, which have recently become very popular in medical applications. The combination of magnetic and elastic properties leads to a number of interesting phenomena in response to a magnetic field. Magnetic field responsive materials can adaptively change their physical properties

under the influence of an external magnetic field [7]. Elastic, magnetic composites in biomedical engineering are made of a polymer matrix and magnetic particles, such as iron oxide ( $\text{Fe}_2\text{O}_3$ ), neodymium-iron-boron (NdFeB) titanium dioxide ( $\text{TiO}_2$ ), titanium carbide (TiC) and titanium nitride (TiN) [8]. Homogenous distribution of particles in the composite is achieved by separating the particles by polymer chains of the matrix [9]. Thanks to their good mechanical and magnetic properties, these composites are often used in medicine [10]. Enormous deformation effects, high elasticity, anisotropic elastic and swelling properties, and fast response to magnetic fields open up new possibilities for the use of such materials in various applications. Since the magnetic field is a convenient stimulus from the point of view of signal control, magnetoelastic materials are promising due to their elastic properties that can be controlled in real time [9]. The magnetic composites made of elastic rods can be controlled by an external magnetic field to perform surgical tasks. Such rods require neither wires nor other bulky mechanisms that are problematic in small anatomical areas. However, current control systems for magnetic bodies are large and expensive [11]. Microrobots, with their dimensions (from a few millimeters to a few micrometers), offer promising prospects for medical development. They are used in minimally invasive surgeries, tissue scaffolds, the control of single cells in bioengineering, and drug delivery in a non-invasive way. Millimeter-sized magnetoelastic robots were developed to move inside and on the surface of liquids, or on solid surfaces. They also have the ability to overcome obstacles and move through tight tunnels. These materials enable the transfer of substances to specific locations [12]. However, taking into account the desired biocompatible properties of materials for medical applications, there is often a need for surface modification of such materials. One of the methods of surface modification is the spin-coating method.

## 1.2. Spin-coating as a manufacturing method

The spin-coating method is used to deposit uniform and thin coatings on a flat substrate. It is commonly used in micro-manufacturing, especially where coatings with a thickness of less than 10 nm are required. Spin-coating is used to apply a variety of materials such as photoresistors, insulators, organic semiconductors, or nanomaterials [13, 14]. There are four main stages during the spin-coating process:

- a) **Dosing step** – consists of a dispensing in which the fluid is deposited on the surface. Two common dispensing methods are: static dispensing and dynamic dispensing. Static dispensing involves depositing a small volume (1 to 10  $\text{cm}^3$ ) of fluid at or near the center of the substrate. Higher viscosity or larger substrates typically require a larger volume of liquid to ensure full coverage of the substrate. Dynamic dispensing is the process of substrate rotating at a low speed (around 500 rotations per minute (rpm)) [15]. This serves to spread the liquid over the substrate and may result in less wastage of resin material [16];

- b) **Substrate acceleration stage** – the process of intense pushing of fluid from the plate surface by rotation. Due to the initial fluid thickness, spiral vortices may appear at this stage. The plate reaches the desired speed, and the fluid is thin enough that the viscous shear resistance balances the rotational accelerations [17]. Centrifugation speeds range from 1500 to 6000 rpm, depending on the properties of the fluid and the substrate [16];
- c) The stage during which the **substrate rotates** at a constant speed and the viscous forces of the fluid determine its dilution – the dilution of the fluid is generally quite uniform, although for solutions containing volatile solvents, interference color “swirling” can often be observed. Edge effects are often visible because the fluid flows uniformly outward but must form droplets at the edge in order to be ejected [18];
- d) The stage of **spinning the substrate** at a constant speed and evaporating the solvent, which determines the thinning of the coating – the thickness of the fluid reaches a point where viscous effects allow only a small amount of fluid flow. At this point, the evaporation of any volatile solvents will become the dominant process. The coating is effectively “gelling” because once the solvents are removed, the viscosity of the remaining solution will increase [18]. Once the spin is stopped, many applications require heat treating or “baking” the coating, as in the case of “spin-on-glass” or sol-gel coatings.

Steps C and D describe two processes that must occur simultaneously (viscous flow and evaporation). However, at the engineering level, viscous flow effects dominate early, while evaporation effects dominate later [16]. The spin-coating process is controlled by several operating parameters of the spin coater: the spin speed, the acceleration with which the assumed rotational speed is achieved and the time during which the sample is in the spinning stage.

Spin speed is one of the most important factors in spin-coating. The substrate speed affects the degree of radial (centrifugal) force applied to the liquid resin, as well as the characteristic turbulence of the air directly above it. In particular, the high-speed centrifugation step generally defines the final coating thickness. Relatively small changes of  $\pm 50$  rpm at this stage can result in a thickness change of 10% [15]. As the resin dries, the viscosity increases until the radial force of the spinning process can no longer move the resin significantly across the surface. At this point, the coating thickness will not decrease significantly with increasing centrifugation time [19]. Improper selection of these parameters can result in defects of the coating. They can cause the risk of infection, corrosion, allergic reactions, which may cause a serious health risk. Any contaminant particles that enter the coating solution can cause flow defects called *comets*. The particle adheres to the surface of the substrate and the flow of fluid around each obstruction causes a streak that radiates outward. Using a lid during coating is one way to reduce those particles, but the presence of the lid modifies the solvent evaporation that occurs during coating. Some *coaters*

are built with active air circulation and ventilation. Particles derived from the coating solution can be reduced using submicron syringe filters at the liquid dispensing stage [20]. *Fringes* are radially oriented lines of change in coating thickness. Usually, these are fairly smooth changes in thickness with spacing or periodicity in the range of about 50–200  $\mu\text{m}$ . Their orientation corresponds to the direction of the main fluid flow. Early evaporation of light solvents may enrich the surface layer with water and/or other less volatile substances. If the surface tension of this coating is greater than that of the output solution, then there is instability. Higher surface tension causes material to be drawn in at regular intervals, and the spaces in between are more susceptible to evaporation [16, 20]. The chuck sign patterns can be created by thermal “communication” between the solution on top of the plate and the metal vacuum holder. Therefore, the thermal conductivity of the substrate material is very important as the thermal driving force – mainly evaporative cooling, but it can also be caused by temperature differences between the solution and the substrate and the fixture. Silicon wafers, due to their higher thermal conductivity, usually have smaller thickness differences compared to glass or plastic [19]. The edges of the substrate are always problematic areas, for several reasons. Firstly, the effects of surface tension make it difficult for the radially flowing solution to detach from the plate. In this way, a small “droplet” of liquid can remain attached around the perimeter and result in thicker coatings in this edge zone. Secondly, if the substrates are not exactly circular, and especially if they are square or rectangular, then the airflow over the protruding parts (corners) will be disturbed. While the flow may still be laminar, it will have a different flow history and will usually result in uneven coating thickness in these corner areas [16].

Compliance with all the rules of proper coating by centrifugation and elimination of external factors that may affect the process which allows to achieve repeatable results without significant material loss. Coatings applied with this method are widely used in the production of medical tools and equipment. In recent years, the spin-coating method has often been the base for research into techniques to produce ultra-thin coatings. The importance of this method can be seen by observing literature reports from around the world on the production of innovative materials for use in various applications, including biomedical engineering. It can be concluded that research is being conducted in terms of the possibility of using this method to produce innovative elastic dressing materials, materials containing active agents supporting tissue regeneration and preventing infections, and elastic diagnostic sensors. On the other hand, there is a noticeable lack of research on the influence of the parameters of the spin-coating process on the properties of the obtained coatings. Hence, in this paper the influence of spin-coating parameters on the properties of silicon-based composite reinforced with  $\text{Al}_2\text{O}_3$  particles was evaluated.

## 2. Materials and methods

### 2.1. Materials preparation

The subject of the research are silicon-based composites with the addition of aluminum oxide powder. The following chemicals were used to produce materials:

- Ecoflex™ 00-20 Part A silicon elastomer base (Kauposil, Poland),
- Ecoflex™ 00-20 Part B elastomer hardener (Kauposil, Poland),
- particles of aluminium oxide  $\text{Al}_2\text{O}_3$  (Chempur, Poland).

Ecoflex™ silicon was mixed in a volume ratio of 1A:1B. Low viscosity ensures easy mixing and venting. According to the manufacturer's description, cured rubber is soft, durable and stretchy, stretching many times to its original size without tearing and rebounding to its original shape. These elastomers were tested by the manufacturer in accordance with the ISO 10993-10 standard and were classified as safe in contact with the skin. The material has a density of  $d = 1.07 \text{ g/cm}^3$ , a Shore A hardness ranging from 0 to 20 ShA and a tensile strength of  $\sigma = 1.10 \text{ MPa}$ .

The second ingredient of the composite,  $\text{Al}_2\text{O}_3$  particles used as the composites' reinforcement are in the form of a white powder, having a relative density of  $d = 3.94 \text{ g/cm}^3$ , a particle size  $d_{50}$  of 2 to 5  $\mu\text{m}$  and a pH value at level 7.3 at 20°C. The melting point of this chemical substance is approximately 2050°C.

First, the required masses of the composite components in three variants and one control variant (pure Ecoflex elastomer) were calculated. The composites with 10, 15 and 20<sub>vol</sub>% of reinforcement were prepared according to the composition given in Table 1.

TABLE 1. The composition of materials

Symbol	Material	Ecoflex™ Part A [g]	Ecoflex™ Part B [g]	$\text{Al}_2\text{O}_3$ [g]
A	Ecoflex	4.280	4.280	–
B	Ecoflex+10 <sub>vol</sub> % $\text{Al}_2\text{O}_3$	3.852	3.852	3.152
C	Ecoflex+15 <sub>vol</sub> % $\text{Al}_2\text{O}_3$	3.638	3.638	4.728
D	Ecoflex+20 <sub>vol</sub> % $\text{Al}_2\text{O}_3$	3.424	3.424	6.304

Based on the calculations, the ingredients were mixed together, maintaining the order given by the manufacturer of Ecoflex™ silicones. At first, part A and part B of the elastomer in ratio 1:1 were mixed thoroughly for 5 minutes. Then, the proper amount of reinforcement was added. The composites solutions were thoroughly hand mixed using a spoon to create a uniform liquid mass. Once all the material variants were made, they were subjected to a spin-coating process. To carry out this stage, a POLOS SPIN150i spin-coater (SPS International, The Netherlands) with two vacuum pumps (Fig. 1), and Petri dishes were used.



FIG. 1. Spin-coater with vacuum pumps

The 0.5 ml of liquid composite was applied to the center of the Petri dish, as is shown in Fig. 2a. The sample prepared in this way was placed in a vacuum holder, and after switching on the first pump, was fixed in by a vacuum created under the surface of the pan. The program was started, starting to spread the material over the surface with certain parameters. The composites were made using nine different combinations of parameters. The spin speeds of 1000, 1500 and 2000 rpm were used. The coating times of 10, 15 and 20 s were applied. Those two variables were combined with each other, resulting in process parameters.

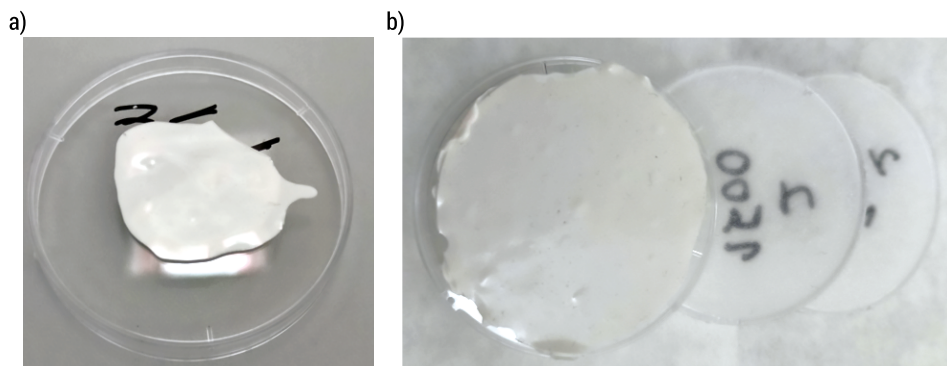


FIG. 2. Liquid composite (a) applied to a Petri dish and (b) composites obtained by using the spin-coating method

When the process was completed, the chamber was opened, and the sample removed (Fig. 2b). Then, the resulting composite samples were left at room temperature for at least 24 h to fully cross-link and harden the composites.

## 2.2. Density measurements

Density ( $\rho$ ) measurements of the produced materials were carried out using the hydrostatic method of density measurements based on Archimedes' law. The volume of a material can be determined by comparing its mass in air with the mass immersed in a liquid of known density, most commonly in a distilled water [21]. The density of material is calculated according to Equation (1):

$$\rho_a = \frac{m_1}{m_1 - m_2} \cdot \rho_l \quad (1)$$

where:

$\rho_a$  – density of the sample,

$m_1$  – sample mass in the air,

$m_2$  – sample mass in the liquid,

$\rho_l$  – density of the liquid used in the test.

To measure density of composite materials using hydrostatic method, an analytical balance (Mettler Toledo, USA) was used with the included hydrostatic density measurement kit.

## 2.3. Water contact angle

The contact angle ( $\Theta$ ) is defined as the angle between the tangent to the surface of the droplet placed on the solid and the point where the three phases meet: solid, liquid and gas (Fig. 3). The contact angle determines how well the liquid spreads over the surface. The value of this angle depends on the physical properties of the liquid, the type of substrate and the conditions of the environment [22].

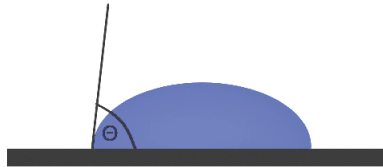


FIG. 3. Contact angle  $\Theta$  on the droplet applied to the surface

At the point of contact between the droplet and the surface, three boundaries must be taken into account: the liquid, the surface and the surrounding atmosphere. In order to obtain the droplets' equilibrium, all the forces acting at the point of contact of the boundaries must balance each other, which can be described by Equation (2):

$$\gamma_{sg} = \gamma_{sl} + \gamma_{lg} \cos \Theta \quad (2)$$

where:

$\gamma$  – surface tension at the interface,

s – solid,

l – liquid,

g – gas or second liquid.

The surface tension of the liquid-atmosphere is  $\gamma_{lg}$ , hence Equation (3):

$$\cos \Theta = \frac{\gamma_{sg} - \gamma_{sl}}{\gamma_{lg}} \quad (3)$$

Therefore, if the angle  $\Theta$  is in the range from  $0^\circ$  to  $90^\circ$ , a solid is well wettable by the liquid, so it has a hydrophilic surface. If the angle  $\Theta$  is between  $90^\circ$  and  $180^\circ$ , a solid is poorly wettable by the liquid, so it has a hydrophobic surface. If the angle  $\Theta$  is greater than  $180^\circ$ , there is a complete lack of wetting of the surface. When a particular surface is easily wetted by a particular liquid, it is called hydrophilic. On the contrary, surfaces that do not have this ability are referred to as hydrophobic [22]. A water contact angle was measured using a contact angle goniometer (Ossila, UK). During the test a 5  $\mu$ l of deionized water droplet was applied on the surface of prepared composites.

## 2.4. Thickness test

To measure the thickness (h) of the obtained composite, a paint meter (Prodig-tech, Poland) and a metal plate were used. The thickness of the composite was measured by applying a piece of the composite to a metal plate constituting the base. The device was then switched on and applied with a probe to the material to be tested. Based on the ultrasound produced, the device calculates the travel time of the ultrasound at a known speed for a given wave coming from the probe to the metal plate and then back to the sensor in the probe.

## 2.5. Surface roughness

Profilometric measurements provide information on many useful parameters for assessing the surface of the tested materials. The research focused on the roughness values of the resulting composites. To carry out these measurements, a focused laser beam measurement was used. The confocal laser measuring microscope



(LEXT OLS4000, Olympus, Japan) was used to carry out profilometric measurements. Surface analysis was possible after scanning with white or laser light. After preliminary processing of the obtained image (straightening the image of the sample surface), it was possible to perform linear roughness (Ra) measurements. It was possible using 5 lines superimposed on the image in selected places (Fig. 4a). Then, by using microscope software, the linear roughness measurements were performed. Surface roughness (Sa) was also analyzed. Three areas of 300 by 300 pixels were selected in the saved image, which resulted in the analysis of a real area of  $200 \mu\text{m}^2$  (Fig. 4b).

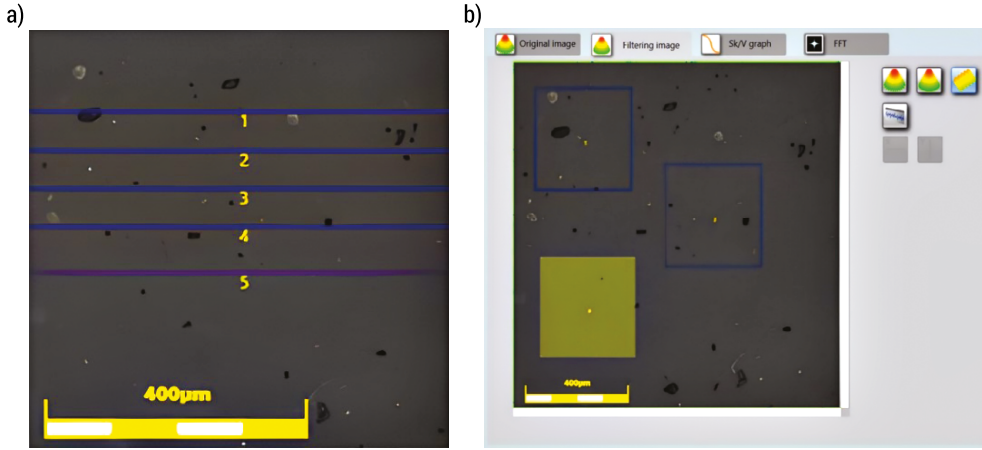


FIG. 4. Designated lines of linear roughness measurements (a), and areas of surface roughness measurements (b)

## 3. Results and discussion

### 3.1. Density

In the case of determining the density of materials, their theoretical value was first calculated, and then experimental measurements were made. At the beginning, theoretical density values ( $\rho$ ) of composites calculated on the basis of data from manufacturers were determined. They are as follows:

- $\rho_B = (0.90 \cdot 1.07 \text{ g/cm}^3) + (0.10 \cdot 3.94 \text{ g/cm}^3) = 1.36 \text{ g/cm}^3$
- $\rho_C = (0.85 \cdot 1.07 \text{ g/cm}^3) + (0.15 \cdot 3.94 \text{ g/cm}^3) = 1.50 \text{ g/cm}^3$
- $\rho_D = (0.80 \cdot 1.07 \text{ g/cm}^3) + (0.20 \cdot 3.94 \text{ g/cm}^3) = 1.64 \text{ g/cm}^3$

The first tested sample was composite B, for which the experimentally obtained density was  $\rho \sim 1.00 \text{ g/cm}^3$ , which is lower in comparison to the theoretically calculated material. This was caused by the formation of air bubbles in the composite structure.

This problem was observed mainly for samples of composite B. Thus, the results of density measurements for this composite were omitted. In the case of C and D composites, no formation of air bubbles was observed in their structure. The Table 2 presents data of the density of the tested composites.

As it is observed in Table 2, the density of composites for both C and D materials is similar to the theoretical values. The differences are only a few %, which is acceptable for the used manufacturing method. In some cases, as in the case of processes carried out at 2000 rpm, a decrease in density can be observed as the process time increases. The lowest density for composite C is  $\rho = 1.47 \text{ g/cm}^3$  and was obtained at the following parameters of spin-coating: 1500 rpm and 10 s. The highest density value for C composite,  $\rho = 1.58 \text{ g/cm}^3$  was obtained at the following parameters: 2000 rpm and 15 s. In the case of composite D, the lowest density of  $\rho = 1.57 \text{ g/cm}^3$  was recorded by the parameters: 1500 rpm and 20 s. The highest measured density of the D composite is  $\rho = 1.72 \text{ g/cm}^3$ , achieved at 2000 rpm and 10 s.

TABLE 2. The density of C and D composites

Sample	Spin speed [rpm]	Spin time [s]	Density, $\rho$ [g/cm <sup>3</sup> ]
C	1000	10	1.47
		15	1.55
		20	1.47
	1500	10	1.45
		15	1.54
		20	1.47
	2000	10	1.57
		15	1.58
		20	1.55
D	1000	10	1.61
		15	1.68
		20	1.66
	1500	10	1.69
		15	1.64
		20	1.57
	2000	10	1.72
		15	1.69
		20	1.64

The measured density for the vast majority of the tested composite samples was very similar to the calculated theoretical value of the density of the produced composites. The average density value for composites with 15<sub>vol</sub>% filler was  $1.52 \text{ g/cm}^3$ , while for the composite with 20<sub>vol</sub>% filler, it was  $1.65 \text{ g/cm}^3$ . Both of these values are

comparable to the theoretical values. In the case of 15 of the 18 samples tested, the difference between the measured and calculated density value was less than 5% of the total value, of which the difference was less than 3% for 11 samples. A difference of more than 5% between the theoretical and measured values was shown by only 2 samples, none of which exceeded 6%. It means that proposed spin-coating parameters were selected properly. However, there is no dependency in the results on the speed or time of the spin-coating process. Taking into account the values given for higher concentrations in the literature and comparing them with the results obtained in this experiment, it turns out that there is a linear relationship between the density and percentage concentration of alumina. The obtained values correlate with those presented by Liang et al., when considering this linear relationship [23].

## 3.2. Water contact angle

The results of the water contact angle tests for prepared composites B-D are presented in Fig. 5. Since the water contact angle for all measured samples is higher than  $90^\circ$ , it can be concluded that the surface of these samples is hydrophobic. For composite B, it is not possible to find a constant trend of changes in the value of this parameter for this material. It can be noticed that the discrepancies in the value of the angle between samples with different coating times increased with increasing spin speeds for this composite.

The values of the contact angle  $\Theta$  for composites prepared at 1000 rpm do not differ much from each other and they are of  $110\text{--}113^\circ$ . The maximum difference between the composites is  $2.32^\circ$ . Although these values are slightly higher with a longer coating time, it is not possible to find a significant influence of this parameter on the contact angle value for this composite. The maximum difference between the results of the contact angle at 1500 rpm is  $5.28^\circ$ . The discrepancy between the results at 2000 rpm increased to  $8.90^\circ$ , which may indicate that as the spin speed increased, the resulting composite coatings were more susceptible to larger deviations of the measured parameter. The lowest value  $\Theta = 105.4^\circ$  obtained for composite B was for samples spin-coated for 2000 rpm for 10 s.

In the case of C composite samples, it is not possible to find a constant trend of changes in the value of the contact angle with the increase of the spin speed for the tested materials. The highest differences in the angle  $\Theta$  between samples with different spin speeds occurred in the coated sample for 10 s ( $\Theta \sim 104\text{--}111^\circ$ ) and the smallest in the coated sample for 15 s ( $\Theta \sim 111\text{--}114^\circ$ ). The contact angle values increase with increasing the coating time, and the maximum difference between the measurements was  $2.94^\circ$ , so the increase in the  $\Theta$  angle value was 2.65%. The increase in the value of this angle at the speed of 2000 rpm was  $12.17^\circ$ , which gives an increase in the contact angle by 11.73%.

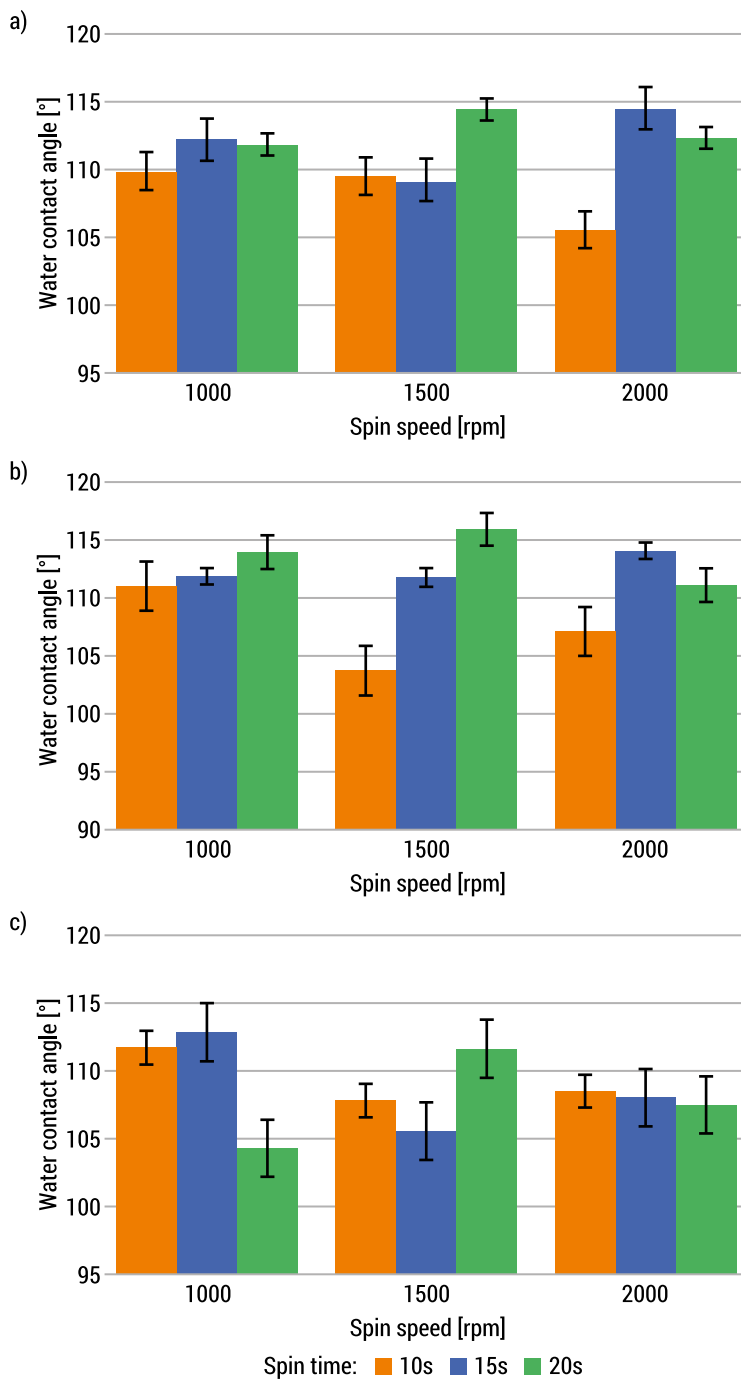


FIG. 5. Contact angle values for composites (a) B, (b) C, and (c) D with varying spin speed and spin time

On the basis of the obtained results for D composites, it is not possible to state a constant tendency of changes in the contact angle with increasing the spin speed. For samples coated for 10 s, the discrepancy of the contact angle values is  $3.93^\circ$ , for coated samples for 15 and 20 s, the discrepancies are very similar and are  $7.24^\circ$  and  $7.27^\circ$  respectively. The highest value of the contact angle was achieved for the samples coated for 10 and 15 s at a speed of 1000 rpm ( $\Theta \sim 112\text{--}113^\circ$ ), in the case of a sample coated for 20 s, the highest value of the angle  $\Theta = 111^\circ$  was measured at the spin speed of 1500 rpm. The low value was observed for a sample prepared using 1000 rpm for 20 s, where  $\Theta = 104^\circ$ . The values obtained in the study are similar to the literature data, where the contact angle of pure PDMS is about  $\Theta = 125^\circ$  in the publications of Alzahid et al. and Ruben et al. [24, 25], where the contact angle was about  $\Theta = 107^\circ$ . The value of the wetting angle decreases after surface modification or modification of the chemical composition.

It is not possible to clearly state the influence of the coating speed or time on the value of this angle. The coating parameters do not affect the contact angle value. The measurement results for individual composites and the layers made of them were noticeably different from each other by up to 10% in individual cases. Therefore, further research is necessary to confirm this thesis.

### 3.3. Thickness results

The results of thickness ( $h$ ) measurements were compared for B and D composites containing 10 or 20<sub>vol</sub>% reinforcement. In both cases, as can be seen in Fig. 6, the thickness of the composite decreased both with increasing rotational speed and increasing coating time. In the case of composite B coated for 10 s, the thickness of the produced coating decreased from  $h = 21\text{ }\mu\text{m}$  at 1000 rpm, through  $h = 16.5\text{ }\mu\text{m}$  at 1500 rpm, up to  $h = 11.5\text{ }\mu\text{m}$  at 2000 rpm. It gives the decrease of 76.09% of the composite thickness as the spin speed increased by 500 rpm, and after increasing it by another 500 rpm, this value decreased to 53.75% of the composite thickness. For composite B coated for 15 s, the layer thickness changed from  $h = 17.5\text{ }\mu\text{m}$  for 1000 rpm to  $h = 7.5\text{ }\mu\text{m}$  for 2000 rpm. For the composite coated for 20 s, the decrease in thickness when increasing the speed by 500 rpm from  $h = 13\text{ }\mu\text{m}$ , through  $h = 9.5\text{ }\mu\text{m}$ , up to  $h = 5\text{ }\mu\text{m}$ , was observed. As can be seen, the lowest changes in coating thickness occurred at the lowest rotational speed, and the largest changes were recorded at the highest rotational speed. On the other hand, if we compare the effect of coating time on the thickness of the composite with the effect of the spin speed on this value, it can be concluded from the data for B composites that the increase in rotational speed has a greater effect on these changes.

A decrease in the thickness of the composite D can be observed while increasing the spin speed as well as increasing the coating time. As the spin speed increases from 1000 to 1500 rpm, a fairly even level of thickness reduction can be observed (from  $h = 60 \mu\text{m}$  to  $h = 37 \mu\text{m}$  for 10 s). A very large drop in thickness occurred between the lowest and highest rotational speeds for all coating times and amounted to almost 85% for the composite coated for 15 s (from  $h = 48 \mu\text{m}$  to  $h = 7 \mu\text{m}$ ). The decrease in the thickness value of the D coated composite for 20 s is less than that of the coated composite for 15 s due to the achievement of a thickness of less than  $10 \mu\text{m}$ , below which the rate of decrease decreases with uniformly increasing rotational speed. By increasing the coating time twice, it is not possible to achieve as much change in coating thickness as with a double increase in rotational speed. Again, this shows a greater impact of spin speed compared to coating time.

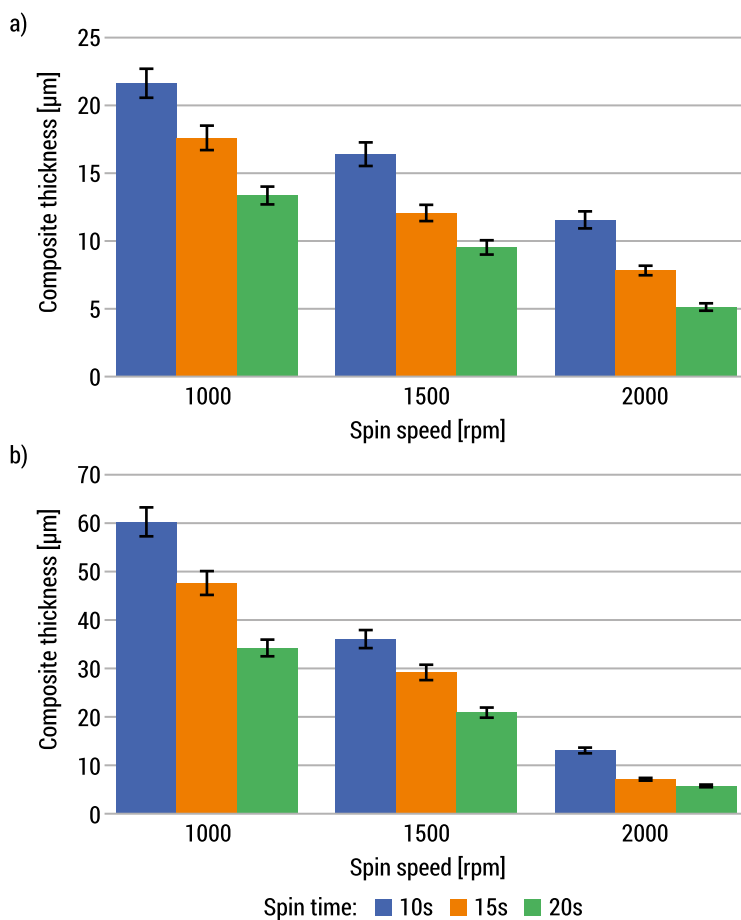


FIG. 6. The thickness of the composites containing (a) 10vol% (b) 20vol%  $\text{Al}_2\text{O}_3$  particles

The comparison of both composites, B and D, show that the thickness of material B is around 3 times lower than the material D when prepared using 1000 rpm. However, in the case of composites made at 2000 rpm, the differences in the thickness of composites B and D are not so significant. The addition of  $\text{Al}_2\text{O}_3$  particles to PDMS results in lower viscosity and thus lower thickness of the samples. With the same parameters, the thickness of the PDMS from the literature is 100–150  $\mu\text{m}$  [26].

Using the spin-coating method it is possible to obtain the composites with the thickness of 10–60  $\mu\text{m}$ , what is really promising in the case of manufacturing new materials for biomedical engineering.

To sum up, on the basis of the results obtained, it can be concluded that both the coating speed and the coating time have a significant impact on the obtained thickness of the obtained layers, but the rotational speed has a noticeably greater impact on the obtained results. It was noticed that the composites' thickness was the lowest for the longest coating time and the highest spin speed. With a subsequent increase in spin speed, no such large changes in thickness would be observed, as described in the discussion of these results. For these composites, such a limit is probably in the range of 3–5  $\mu\text{m}$ , but more research would have to be carried out to confirm this thesis.

### 3.4. Surface roughness

Two parameters were considered in the analysis of surface roughness:  $R_a$  (the arithmetic mean deviation of the profile from the base plane), which is one of the ways of defining linear roughness, and  $S_a$  (the arithmetic mean deviation of the height of surface irregularities from the reference plane), which concerns the surface roughness. The results for linear roughness are presented in Fig. 7.

It can be observed that in the case of material C, the roughness increased with increasing speed, from  $R_a = 0.03 \mu\text{m}$  to  $R_a = 0.06 \mu\text{m}$  for a process lasting 10 s. Similar changes were noticed for longer process durations, e.g. for 15 s,  $R_a$  from 0.07  $\mu\text{m}$  for 1000 rpm to 0.16  $\mu\text{m}$  for 1500 rpm was obtained. The rotational speed also influenced the roughness. The parameter  $R_a = 0.07 \mu\text{m}$  at 1000 rpm and 20 s changed to  $R_a = 0.14 \mu\text{m}$  at 2000 rpm and 20 s. No similar relationship was noticed for material D. The linear roughness, regardless of the process parameters (spin and speed time), ranged from 0.03 to 0.07  $\mu\text{m}$ . The linear roughness was relatively higher for the material containing less filler.

In Fig. 8. the results for surface roughness for two chosen materials are presented. For this parameter, the results are different from linear roughness. For composite C, it was observed that the higher the spin speed, the higher the roughness. For 15 s, surface roughness was of  $S_a = 0.22 \mu\text{m}$  for 1000 rpm and  $S_a = 0.39 \mu\text{m}$  for 2000 rpm. The lowest roughness value  $S_a = 0.15 \mu\text{m}$  was obtained at 1500 rpm and 10 s. The highest roughness value was  $S_a = 0.39 \mu\text{m}$  for 2000 rpm and 15 s. There

was no relationship in surface roughness results connected to spin time. In the case of composite D, higher rotational speed also resulted in higher surface roughness. In the case of processes lasting 15 s, the roughness obtained was  $S_a = 0.31 \mu\text{m}$  at 1000 rpm,  $S_a = 0.38 \mu\text{m}$  at 1500 rpm and  $S_a = 0.56 \mu\text{m}$  at 2000 rpm. Similar dependencies were observed for other spin times. It can be concluded that the longer the spin time, the higher the roughness is. For the process at 1500 rpm, the roughness changed from  $S_a = 0.25 \mu\text{m}$  to  $0.45 \mu\text{m}$ .

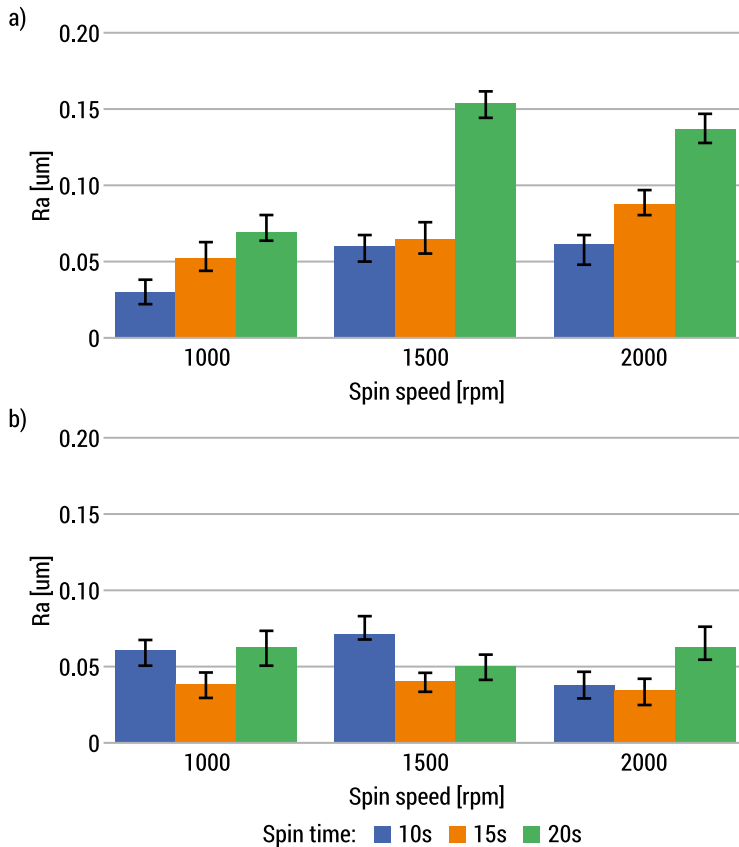


FIG. 7. Linear roughness of (a) C and (b) D composite materials

The surface roughness of composite D was twice as high as the roughness of composite C. For example, for 1500 rpm and 20 s,  $S_a$  for C sample was of  $0.26 \mu\text{m}$ , and for D sample  $S_a = 0.45 \mu\text{m}$ . The higher filler content in the composite resulted in greater surface roughness. Moreover, the higher rotational speed resulted in higher surface roughness. This may be related to the phenomenon of separation of individual powder particles during the spin-coating process.



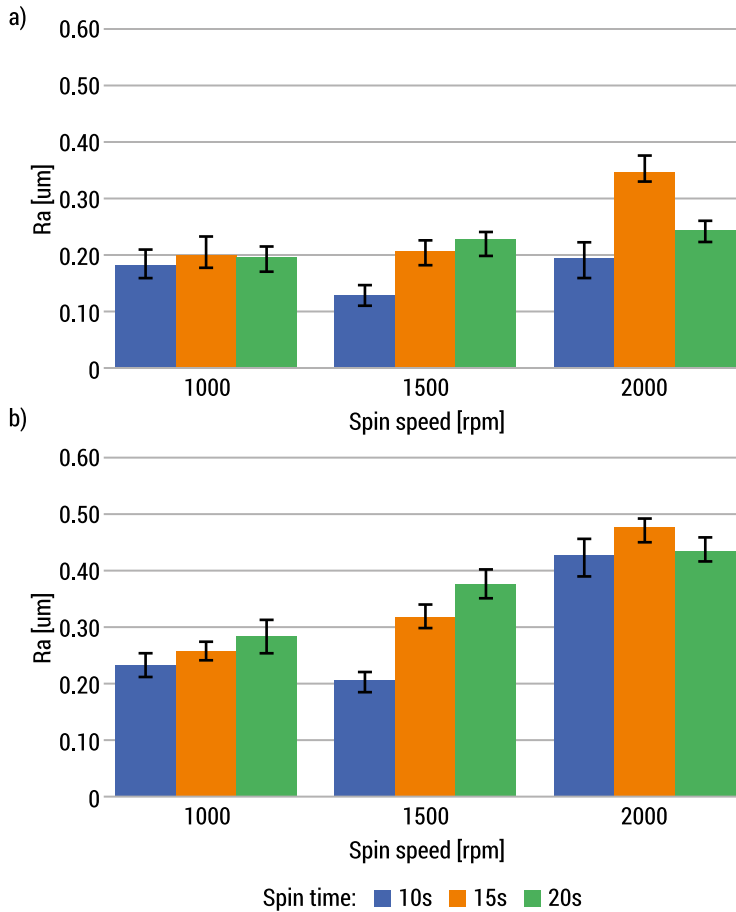


FIG. 8. Surface roughness of (a) C and (b) D composite materials

## 4. Conclusions

The spin-coating method makes it possible to produce thin flat composites. The entire process is controlled by two basic parameters: the coating speed expressed in rpm of the coated substrate and the time of the coating process. In order to determine the influence of these parameters on the properties of the produced composites, measurements of density, coating thickness, contact angle of the produced composites were used in this study. On the basis of the results obtained in the conducted work, the following conclusions can be formulated:

- increasing the speed and time of spin-coating does not affect the density of the coated composites,
- increasing the speed and time of spin-coating significantly affects the thickness of the obtained composite coatings,

- the change of process parameters does not affect the contact angle values,
- the increased content of powder filler in the tested composite resulted in an increase in the thickness of the coating, in the case of other studies the effect of the increased reinforcement content on the obtained results was not observed,
- an increase in the coating speed and time resulted in an increase in both the linear and surface roughness, while these parameters were influenced also by the formation of defects on the surface of the composites at higher coating process parameters. All obtained composites, regardless of the content of powder filler and coating parameters, were characterized by a hydrophobic surface.

The parameters of the spin-coating process have a significant impact on properties such as coating thickness, but do not affect density changes and contact angle values. This makes it possible to obtain coatings with strictly defined properties that allow them to be used in specialized methods of modification of surface layers of medical devices and for the production of materials used in tissue engineering for the regeneration and repair of skin tissues. The planned and conducted research allows for the development of innovative methods for the production of thin coatings or composites for biomedical engineering applications. These tests are in line with the current trends of research aimed at developing new techniques for obtaining modern elastic composite materials. However, further research is needed to extend the experimental analysis of the developed composites using the spin-coating method.

## References

1. Egbo M.K., A fundamental review on composite materials and some of their applications in biomedical engineering. *Journal of King Saud University – Engineering Sciences*, 2021, 33, 557–568.
2. Serruys P.W., Kutryk M.J.B., Ong A.T.L., Coronary-Artery Stents. *New England Journal of Medicine*, 2006, 354, 483–495.
3. Erne P., Schier M., Resink T.J., The Road to Bioabsorbable Stents: Reaching Clinical Reality?. *Cardiovascular and Interventional Radiology*, 2006, 29, 11–16.
4. Salernitano E., Migliaresi C., Composite Materials for Biomedical Applications: A Review. *Journal of Applied Biomaterials and Biomechanics*, 2003, 1, 3–18.
5. Yokoyama M., Biorelated polymers and gels: controlled release and applications in biomedical engineering. Academic Press, Boston 1998.
6. DeRossi D., Kajiwarra K., Osada Y., Yamauchi A., Polymer Gels. Springer, New York, 1991.
7. Filipcsei G., Csetneki I., Szilágyi A., Zrínyi M., Magnetic Field-Responsive Smart Polymer Composites. Springer, Berlin 2007, 137–189.
8. Mystkowska J., Powojńska A., Łysik D., Niewęgłowska J., Cañón Bermúdez G.S., Mystkowski A., Makarov D., The Effect of Physiological Incubation on the Properties of Elastic Magnetic Composites for Soft Biomedical Sensors. *Sensors*, 2021, 21, 1–20.
9. Powojńska A., Niewęgłowska J., Suska S., Cavadas A., Mystkowska J., Chemical stability assessment of soft magnetic composites for biomedical applications. *Engineering of Biomaterials / Inżynieria Biomateriałów*, 2022, 164, 2–8.

10. Pawlaczyk M., Schroeder G., Hybrydowe nanomateriały magnetyczne. *Cursiva*, Kostrzyn, 2017.
11. Kratchman L.B., Bruns T.L., Abbott J.J., Webster R.J., Guiding Elastic Rods with a Robot-Manipulated Magnet for Medical Applications. *IEEE Transactions on Robotics*, 2017, 33, 227–233.
12. Hu W., Lum G.Z., Mastrangeli M., Sitti M., Small-scale soft-bodied robot with multimodal locomotion. *Nature*, 2018, 554, 81–85.
13. Cesarz-Andraczke K., Kania A., Pałka K., Eksperymentalne stanowisko do zastosowań inżynierii powierzchni stopów Mg wykorzystujące metodę spin-coating. *LAB Laboratoria. Aparatura. Badania*, 2019, 6, 6–10.
14. Hanaor D., Trianni G., Sorrell C., Morphology and photocatalytic activity of highly oriented mixed phase titanium dioxide thin film. *Surface and Coatings Technology*, 2011, 205, 855–874.
15. Hellstrom S.L., Basic Models of Spin-coating. Stanford University, 2007.
16. Tyona M.D., A theoretical study on spin-coating technique. *Advances in Materials Research*, 2013, 2, 195–208.
17. Mitzi D.B., Kosbar L.L., Murray C.E., Copel M., Afzali A., High-mobility ultrathin semiconducting films prepared by spin-coating. *Nature*, 2004, 428, 299–303.
18. Meyerhofer D., Characteristics of resist films produced by spinning. *Journal of Applied Physics*, 1978, 49, 3993–3997.
19. Peeters T., Remoortere B.V., Parameters of the spin-coating process. *Applied Sciences*, 2008, 234–239.
20. Birnie D.P., Spin-coating: Art and Science. Chemical Solution Deposition of Functional Oxide Thin Films. Springer, Cham 2013, 263–274.
21. Davidson S., Perkin M., An investigation of density determination methods for porous materials. small samples and particulates. *Measurement*, 2013, 5(46), 1766–1770.
22. Huhtamäki T., Tian X., Korhonen J.T., Ras R.H.A., Surface-wetting characterization using contact-angle measurements. *Nature Protocols*, 2018, 13, 1521–1538.
23. Liang W., Li T., Zhou X., Ge X., Chen X. et al. Globular Flower-Like Reduced Graphene Oxide Design for Enhancing Thermally Conductive Properties of Silicone-Based Spherical Alumina Composites. *Nanomaterials*, 2020, 10, 544.
24. Alzahid Y.A. et al., Functionalisation of Polydimethylsiloxane (PDMS) – Microfluidic Devices coated with Rock Minerals. *Scientific Reports*, 2018, 8(1), 15518.
25. Ruben B. et al., Oxygen plasma treatments of polydimethylsiloxane surfaces: effect of the atomic oxygen on capillary flow in the microchannels. *Micro Nano Letters*, 2017, 12, 754–757.
26. Lee H.K., Chang S.L., Yoon E., A Flexible Polymer Tactile Sensor: Fabrication and Modular Expandability for Large Area Deployment. *Journal of Microelectromechanical Systems*, 2007, 15, 1681–1686.

# Assessment of the wettability of PDMS and denture acrylic polymer by oral gels

Joanna Niewęglowska<sup>1\*</sup>, Dawid Łysik<sup>1</sup>, Joanna Mystkowska<sup>1</sup>

<sup>1</sup> Faculty of Mechanical Engineering, Institute of Biomedical Engineering,  
Białystok University of Technology, Wiejska 45C, 15-351 Białystok, Poland

\*joanna.nieweglowska@sd.pb.edu.pl, d.lysik@pb.edu.pl, j.mystkowska@pb.edu.pl

**Abstract:** Surface wettability plays a crucial role in evaluating implant biomaterials, especially for oral cavity applications, where several surface phenomena, as adsorption of saliva components and microorganism adhesion occur. This also includes oral gels, which can partially perform saliva functions and are in contact with dentures or orthodontic appliances. The main goal of our research was to determine the suitability of selected preparations with mucoadhesive properties in the context of their wetting properties. This study assesses the wettability of prosthetic acrylic and PDMS surfaces by oral mucin-based gels enriched with polysaccharides such as k-carrageenan, acacia gum, carob gum, and xanthan gum. The average contact angles for the tested gel formulations in contact with denture acrylic polymer were slightly higher in comparison to the results obtained for PDMS surface. The study also analyzes the effect of 7-days incubation of these gels on their contact angle while testing on dental materials. Average contact angle generally increased from day 0 ( $\theta \sim 30\text{-}40^\circ$ ) to day 7 ( $\theta \sim 50\text{-}60^\circ$ ) for all the tested preparations using PDMS material.

**Keywords:** Wettability, Contact angle, Hydrogel, Mucin, Polysaccharides, Dental materials

## 1. Introduction

The properties of polymeric materials depend largely on the properties of the surface. The top layer, which has a different structure from the core of the material, performs various functions and is exposed to multiple factors depending on the product's intended use [1]. Numerous studies are being conducted between the top layers of multiple materials, also for biomaterials used in the oral cavity to check their interaction with oral fluids/gels. It should be pointed out that in the group of gels, various functions of hydrogels have been developed over the last few decades. The properties

of hydrogels formulations depend on their components and the functions resulted from their polymer networks. Research on hydrogels using the characteristic functions of specific polymer networks has increased over the last decade. Hydrogels, belonging to a class of cross-linked polymeric materials, are an excellent example of continuous technological development that increases social benefits while motivating and stimulating scientists to further research. These gels show promising application prospects in tissue engineering [2], drug delivery systems [3], or as lubricating agents that minimize both friction and wear [4].

Hydrogel is a three-dimensional structure composed of hydrophilic polymer chains cross-linked by physical, chemical, or polymerization methods. Hydrogels are characterized by the ability to retain large amounts of water in their structure. This property occurs due to the use of surface tension and the capillary force of the liquid. Water absorption into the hydrogel depends on many factors, including gel functional group, water level, and cross-linking network density in hydrogel [5, 6]. Due to the broad spectrum of hydrogel properties, i.e., biocompatibility, biofunctionality, environmental friendliness, and the ease of their chemical and physical modification, they are a material undergoing intensive development [7]. The gel finds applications and is an improvement of the latest hydrogel technology. In terms of materials and process, it becomes inventive and fits specific applications [8–10]. The use of topical drug carriers in the oral cavity is problematic due to their rapid elimination from the site of administration due to insufficient adhesion to the mucous membrane and washing out through saliva, especially when eating food [11].

## 1.1. Hydrogel drug delivery systems

Compared to other biomaterials, hydrogels are characterized by high water content and plasticity and have physical properties similar to natural tissue. Currently, drugs with controlled release of the active substance, formulations with directed release of the active substance and bioadhesive drug carriers, are obtained based on hydrogels [12]. A system with controlled release of the drug substance (DDS – Drug Delivery System) reduces the need for frequent drug administration, significantly increasing the safety of therapy. The purpose of developing DDS is to maintain a constant concentration of the pharmaceutically active substance in the blood. During DDS development, the key issue is the matrix selection in which the active substance is suspended [13]. Another requirement for DDS is releasing the drug into a specific place. Drug formulations based on hydrogel matrices are administered, among others, orally in adhesive gels and dressings [14]. Oral administration of medications is one of the most convenient and comfortable ways. Hydrogels administered orally can deliver the active substance to target sites [15].

By using bioadhesive gels, it is possible to extend the contact time of the drug carrier with the mucous membrane and maintain the achieved therapeutic concentration

of the substance in the tissues. Various bioadhesive polymers are used to produce hydrogels with a prolonged effect on the oral mucosa in the treatment of mucosal inflammation, fungal infections, viral infections or cancer [16–18]. Watanabe et al. obtained a hydrogel consisting of natural gums, i.e. xanthan gum and locust bean gum (carob gum/carob gum/galactomannan), from which they obtained a drug release system [15]. Locust bean gum is a galactomannan that is soluble in both cold and hot water. When heated to 80 °C, it forms pseudoplastic solutions with increased viscosity. In combination with xanthan gum, it is characterized by thickening, stabilizing and gelling properties [19, 20].

The evaluation of surface wettability in oral applications, particularly regarding interactions with dental materials is of great significance in the case of oral gels. Proteins and bacteria tend to adhere to slightly hydrophobic or hydrophilic surfaces, while less adhesion is observed when both properties are higher. Therefore, the anti-fouling effect can be achieved by changing the wettability of the teeth or the surface of the material by increasing the hydrophobicity or hydrophilicity. Many biological antifouling phenomena in nature are based on specific wettability [21]. Surface properties play a particularly important role in mucoadhesive drug delivery systems. In these preparations, the adsorption of the polymer matrix on the mucosa is limited by the wetting and swelling process of the polymer structure. Thus, the performance of mucoadhesive drug delivery systems made of polymeric materials depends on many factors such as contact angle, surface free energy, and water absorption rate [22, 23].

The wettable surfaces of natural prompt design of biomimetic oral materials covered or mixed with super wettable materials to prevent adhesion. It is believed that these new methods could provide promising directions for oral antimicrobial practice, improving antimicrobial efficacy.

## 1.2. Surface engineering

Material properties are a complex issue, and they depend not only on the base material but also on the top layer of a given product. All properties result from the material's structure parameters at each level, starting from properties at the atomic level and ending with its microstructure. Due to the wide range of material properties, their types have been specified. They are classified according to the following categories: mechanical, physical (e.g. thermal, electrical, magnetic, optical, acoustic), chemical, and biological properties. From the point of view of thermodynamics, the surface is defined as the boundary between phases – the boundary surface, in a state of thermodynamic equilibrium in the body system. Solid-gas surface affects neighboring phases (boundary phases). Entropy and mass may be exchanged between the surface and the surrounding phases. The boundary surface created from homogeneous phases influences the state of these phases, and is active, so can influence

the development of their properties [24]. Surface engineering has developed many measurement methods for advanced material testing. Materials engineering deals with the study of the relationship between the structure of a material and its properties. In contrast, surface engineering focuses on issues related to the external area of the material. The science of material surfaces is based on research on their structure, production, modification processes, and degradation of microstructure components [25].

The interactions between the surface of the implant material and the biological environment *in vitro* or *in vivo* are related to the properties of the material's surface layer, the most important of which are those relating to topography, wettability, chemical composition, and surface energy. For biomaterials, the Surface Free Energy (SFE) can assess the degree of interaction between the material and a living organism. Surfaces characterized by high surface energy, protein adsorption, and cell adhesion are suitable. The opposite phenomenon occurs for materials with a low surface energy. For surfaces with high surface energy at the cell-solid (tissue-implant) interface, there is a lower probability of adhesion to the solid surface than the sum of surface energies between the cell-liquid and solid phases. However, it should be emphasized that highly hydrophilic surfaces (characterized by very high SFE), such as hydrogels or methacrylates, do not support adhesion. The process of cell adhesion is complicated and determined by many factors, not only the surface mentioned above energy, but it can be a pretty straightforward indicator giving us preliminary information about cell adhesion. It can also be a measure of the chemical and biological resistance of the material surface to biodegradation [26–27].

The contact angle of materials is an indicator of the wetting properties of the materials' surface. High wettability (hydrophilicity) occurs at a low contact angle, which is below 90°. However, low wettability (hydrophobicity) is observed at a contact angle above 90°. Depending on the measurement method used, there are several types of contact angles in the literature. One type of angle is the static/extreme contact angle, also called Young's angle. Static testing of the contact angle value involves placing a drop of the measuring liquid on the tested surface using a measuring needle and immediately taking the measurement. The angle between a solid and a liquid drop can be determined based on the shape of the drop (Young–Laplace equation). Another tangential method is the method that is carried out at the point of contact between the liquid and the material surface. The contact angle of a liquid droplet is measured at time intervals and is related to the wettability of the material. This is the angle at which a drop of liquid forms after a certain period of contact with the surface of the material. The measurement of wettability using this method is time-dependent. Its value changes from the maximum value (static contact angle) at the beginning of the test after applying the drop ( $t = 0$  s) to the minimum value, after which the angle does not change. This is the equilibrium contact angle or Young's angle, often called the extreme contact angle. The static contact angle is part of the basic equations of capillary theory. This angle is used when analyzing the wettability of solids [28].

The second type of research details the dynamic contact angle. This method distinguishes between a rising and falling angle. When testing the dynamic angle, the measuring needle is brought closer to the material surface so that the drop contacts the surface. When dispensing liquid, the needle is in the drop. As the drop spreads on the surface of the material, its volume increases. During the examination, the so-called rising angle. The next stage is sucking out the liquid from the drops. This, in turn, causes the drops to flow backward. This creates a descending angle. Both types of angles are used to determine the wettability of a surface. Typically, the descending angle is smaller than the ascending angle. In the case of a falling angle, the surface of a solid body is characterized by higher values of surface tension and surface free energy. If the contact angle is  $0^\circ$ , the liquid spreads across the surface. It is assumed that when the contact angle is in the range of  $0-90^\circ$ , the surface has good wetting properties. For a contact angle of  $90-180^\circ$ , the surface is characterized by hydrophobic properties. However, a surface contact angle greater than  $150^\circ$  indicates the material's superhydrophobicity. At an angle of  $180^\circ$  the surface is completely non-wettable. If the angle is between  $45^\circ$  and  $90^\circ$ , the droplet penetration will depend on the structure and roughness of the surface (i.e. the height, width and distance of the protrusions on the rough surface). It is assumed that if the roughness value  $Ra < 0.5 \mu\text{m}$ , the impact of the roughness on the contact angle is insignificant [29, 30].

This study aimed to determine the wettability of various gel preparations on two surfaces imitating the properties of oral surfaces. The research was carried out on a silicone surface (PDMS) imitating body tissue and a dental acrylic surface imitating the surface of a prosthetic restoration used in the oral cavity. Additionally, the influence of polysaccharides gels incubation for 7 days in  $37^\circ\text{C}$  on a surface contact angle was assessed. The method used to determine the surface wettability of materials based on static/extreme contact angle measurements is essential due to the ease of carrying out measurements and the high accuracy of the obtained results, and is also one of the primary methods used for surface characterization.

## 2. Materials and methods

### 2.1. Polysaccharides based gels

The mucin/polysaccharide mixtures dissolved in phosphate buffered solution (PBS), which composition is presented in Table 1, were tested. The basic solution was prepared based on our previous research [31, 32] and contains 2wt.% mucin, 2wt.% xylitol, 1wt.% guar gum, and 0,5wt.% xanthan gum. As functional modifiers, the total 1wt% of selected gums, as acacia (A), locust bean (B), and k-carrageenan (C) with various percentage concentrations were used. All reagents were purchased from Sigma Chemical Co. USA.



Many polysaccharides have found wide application due to their ability to create highly viscous solutions and gelation. Galactomannans and carrageenans are the two types of hydrocolloids most commonly used. In mixtures of some galactomannans with K-carrageenan, synergistic interactions between these polysaccharides were observed, which allowed obtaining products with new functional properties [33].

Carrageenans are linear polymers composed of digalactose residues that can be linked to other compounds [34, 35]. The most common and used fractions are kappa I and II (k), iota (i) and lambda (a). K-Carrageenan is built from galactose 4-sulfate [36].

Galactomannans are polysaccharides with a main chain composed of mannose, which is incompletely and irregularly substituted at galactose [20]. Naturally occurring galactomannans include locust bean gum (MCS), obtained from the seeds of *Ceratonia siliqua*, and guar gum (GG) produced from the seeds of *Cyamopsis tetragonolobus*. These are non-gelling, neutral hydrocolloids whose solutions are characterized by high viscosity and relatively high stability over a wide pH range [37].

Due to the fact that locust bean gum creates elastic gels in combination with K-carrageenan, these ingredients were used to prepare the compositions of the tested preparations. Other configurations were introduced to examine the properties of gels obtained from various mixtures. All preparations were incubated at physiological temperature for 1, 3, and 7 days. The control sample was a non-incubated mixture.

TABLE 1. Composition of prepared gels

Preparation	Base composition [wt.%]	Polysaccharide content [wt.%]		
		Gum acacia	Locust bean Gum	K-carrageen
Control	PBS + 2wt.% mucin II + 2wt.% Xylitol  +1wt.% Guar gum +0.5wt.% Xanthan Gum	–	–	–
1A		1	–	–
1B		–	1	–
1C		–	–	1
0.5A 0.5B		0.5	0.5	–
0.5B 0.5C		–	0.5	0.5
0.5A 0.5C		0.5	–	0.5
1/3 ABC		0.33	0.33	0.33

## 2.2. Wettability test stand

For prepared gels, the contact angle tests were performed using a goniometer. Research was made in accordance with the standard PN-93/C-89438 “Foils and boards – Determination of wettability” [38]. Wettability was determined using a wetting angle goniometer (Ossila, Sheffield, UK), shown in Fig.1.

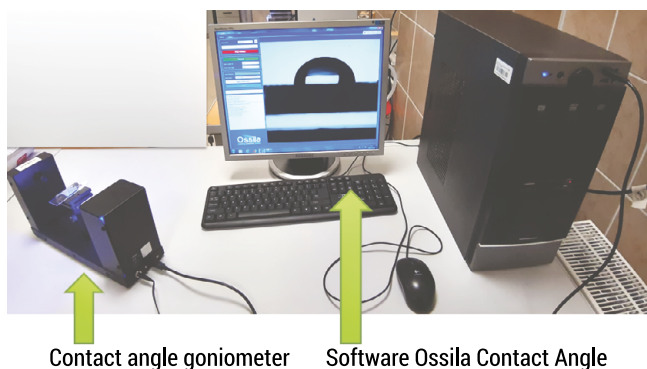


FIG. 1. Contact angle goniometer (Ossila, Sheffield, Great Britain)

The contact angles of gels were tested for two different surfaces, simulating oral cavity conditions. The one test was performed between a 10  $\mu\text{l}$  drop of a prepared gel, and the surface of Sylgard 184 PDMS silicone (Dow Corning, USA) imitating oral mucosa. The second part of the experiment included test of the contact angle between a 10  $\mu\text{l}$  drop of prepared gel and the surface of dental acrylic, imitating the surface of a prosthetic restoration used in the oral cavity. The angle measurement was repeated three times for each condition. The software uses the tangential method for measurements. The test was carried out in constant humidity conditions and at a temperature of  $21^{\circ}\text{C} \pm 1$  on the reference surface.

### 3. Results and discussion

The value of contact angle describes the hydrophilicity or hydrophobicity properties of the analyzed materials. The material is hydrophilic if the contact angle is less than  $90^{\circ}$ . Conversely, the tested material is hydrophobic when the contact angle value exceeds  $90^{\circ}$  [39, 40].

Based on the obtained data, some graphs were prepared (Fig. 2 and Fig. 3) showing the average contact angle for PDMS and acrylic materials in contact with prepared gels just after preparation and after their incubation for 1, 3, and 7 days. Three samples of each gel preparation were tested for each time interval.

Analysis of the contact angle for PDMS surface (Fig. 2) shows that the average contact angle generally increased from day 0 to day 7 for all the tested preparations. The initial contact angle was in the range of  $\theta = 35\text{--}53^{\circ}$  depending on the material and was the lowest for the 0.5B0.5C sample and for the control sample. After 7 days, the contact angle was in the range of  $\theta = 57\text{--}60^{\circ}$ . The highest contact angle ( $\theta = 60^{\circ}$ ) occurred after the 7<sup>th</sup> day of incubation and was observed for the 1A and 0.5A0.5B gels preparations, while the lowest angles ( $\theta = 30^{\circ}$  and  $\theta = 35^{\circ}$ ) were observed for 0.5B0.5C and for the control sample, respectively.

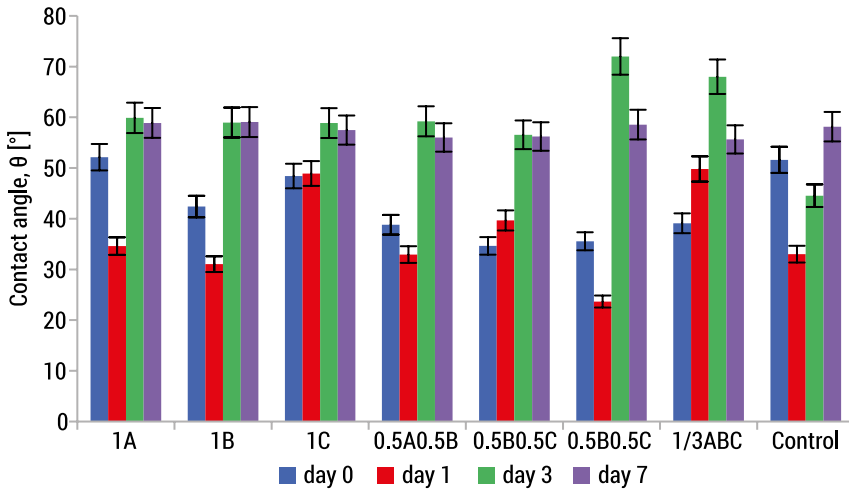


FIG. 2. Contact angle for prepared gels in contact with PDMS material

It was also observed that for all solutions, the mean contact angles did not show any significant differences between the gels, as they remained at a similar level. We can only observe slight deviations, which is the effect of the chemical composition of gels preparations. Generally, the contact angle of the tested preparations is less than 90°, meaning that the gels have good wetting properties in contact with PDMS, simulating oral mucosa. An additional important observation was the slight differences in the contact angle values obtained for 3 and 7 days from the moment of preparation, which may indicate the stability of the obtained compositions.

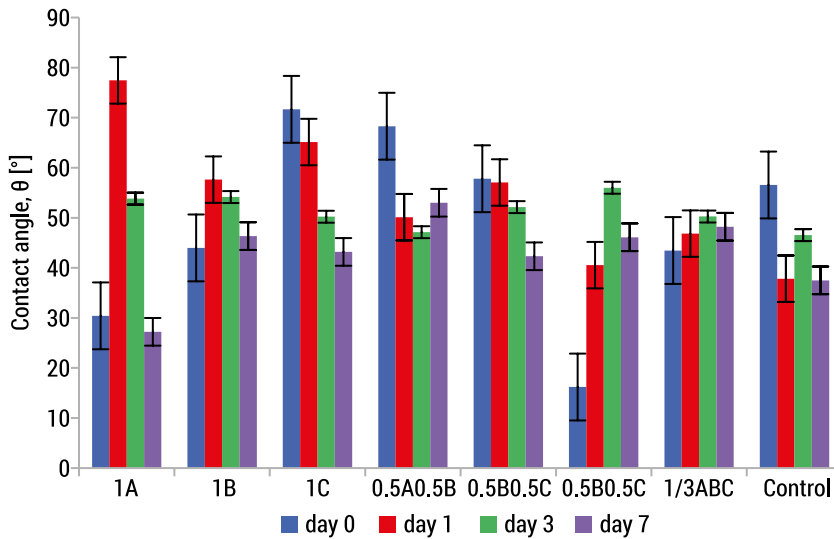


FIG. 3. Contact angle for prepared gels in contact with denture acrylic polymer

The average contact angles for the tested gel formulations in contact with denture acrylic polymer (Fig. 3) were slightly higher in comparison to the results obtained for the PDMS surface. This graph shows that the lowest contact angles ( $\theta = 15^\circ$ ,  $\theta = 30^\circ$ ) were observed respectively for the 0.5A0.5C and 1A gels on day 0, and the highest ( $\theta = 60-78^\circ$ ) were observed on days 1 and 3 for 1A, 1B, 1C and 0.5A05B preparations.

Based on the observed data, it can be concluded that the contact angle is influenced by various factors, such as the physical properties of the tested liquids, the substrate material (whether PDMS or acrylic), and the surrounding atmospheric conditions. As a result, wettability is a material property that significantly affects its behavior when in contact with liquids. The selection of an appropriate composition of a mucoadhesive gel's formulation, depends on the one hand, on the site of administration since the mucus of different mucosal tissues is characterized by various compositions and pH values, and on the other hand, it depends on the desired rate of drug release. The results presented in this paper demonstrated that the employment of suitable materials can help create an optimal mucoadhesive drug delivery system.

## 4. Conclusions

Biocompatible and naturally available polysaccharides materials are an alternative to synthetic materials. Biocompatible hydrogels can replace current drug carriers and become new, cost-effective drug delivery systems. Mucin-based gels are composed of polymer chains connected at selected points, thus creating a three-dimensional cross-linked structure. The properties and wettability of mucin-based gels can be modified by different concentrations of gums in the formulations. The conducted research demonstrated the advisability of using additives in gels.

It was observed that with increasing storage time of the preparations (0, 1, 3, 7 days), the average contact angle increased, and for both tested surfaces: PDMS and acrylic surfaces was the highest on the 7<sup>th</sup> day. The proposed methodology can be an easily accessible method of preliminary assessment of the material from the point of view of cell adhesion ability and the progress of the degradation process. All tested gels were characterized by hydrophilic properties.

The impact of the gels' incubation and the progress of their degradation process can be assessed by measuring changes in the contact angle. However, it requires correlating changes in the contact angle with other factors such as physicochemical properties (pH, conductivity, etc.), rheological and mechanical properties. The obtained results may lead to further research on the development of mucin-based materials with synthetic gums for oral biomedical engineering applications. Wettability materials with their unique physicochemical and anti-adhesion mechanisms will become an increasing area for oral antimicrobial practice and provide a new direction for solving drug resistance.

## Acknowledgment

This scientific work was realized in the frame of works, No. WI/WM- IIB/3/2023 and WI/WM-IIB/9/2023 and financed from research funds of the Ministry of Education and Science, Poland.

## References

1. Żenkiewicz M., Adhezja i modyfikowanie warstwy wierzchniej tworzyw wielko-cząsteczkowych. Wydawnictwo Naukowo-Techniczne, Warszawa 2000.
2. Aizawa Y., Owen S.C., Shoichet M.S., Polymers used to influence cell fate in 3D geometry: new trends. *Progress in Polymer Science*, 2012, 37, 645–658.
3. Qiu Y., Park K., Environment-sensitive hydrogels for drug delivery. *Advanced Drug Delivery Reviews*, 2001, 53, 321–339.
4. Sotres J., Arnebrant T., Experimental investigations of biological lubrication at the nanoscale: the cases of synovial joints and the oral cavity. *Lubricants*, 2013, 1(4), 102–131.
5. Lim L.S., Rosli N.A., Ahmad I., Lazim A.M., Amin M.C.I.M., Synthesis and swelling behavior of pH-sensitive semi-IPN superabsorbent hydrogels based on poly(acrylic acid) reinforced with cellulose nanocrystals. *Nanomaterials*, 2017, 7, 1–13.
6. Mahmud M., Daik R., Adam Z., Influence of poly(ethylene glycol) on the characteristics of g radiation-crosslinked poly(vinyl pyrrolidone)-low molecular weight chitosan network hydrogels. *Sains Malays*, 2018, 47(6), 1189–1197.
7. Yom-Tov O., Seliktar D., Bainco-Peled H., PEG-thiol based hydrogels with controllable properties. *European Polymer Journal*, 2016, 74, 1–12.
8. Wu D., Xu J., Chen Y., Y.M., Wang Q., Gum Arabic: a promising candidate for the construction of physical hydrogel exhibiting highly stretchable, self-healing and tensility reinforcing performance. *Carbohydrate Polymers*, 2018, 181, 167–174.
9. Sun N., Wang T., Yan X., Self-assembled supermolecular hydrogel based on hydroxyethyl cellulose: Formation, in vitro release and bacteriostasis application. *Carbohydrate Polymers*, 2017, 172, 49–59.
10. Gorgieva S., Kokol V., Synthesis and application of new temperature-responsive hydrogels based on carboxymethyl and hydroxyethyl cellulose derivatives for the functional finishing of cotton knitwear. *Carbohydrate Polymers*, 2011, 85(3), 664–673.
11. Junginger H.E., Mucoadhesive hydrogels. *Pharmazeutische Industrie*, 1991, 53, 11, 1056–1065.
12. Pluta J., Karolewicz B., Hydrożele: właściwości i zastosowanie w technologii postaci leku. I. Charakterystyka hydrożeli. *Polimery w Medycynie*, 34(2), 1–31.
13. Budnicka M., Gadomska-Gajadur A., Ruskowski P., Synoradzki L., Polimery biodegradowalne w leczeniu gruźlicy. Cz. I. Epidemiologia, terapia i metody leczenia. *Polimery*, 2017, 63, 711–719.
14. Subramanian D.A., Langer R., Traverso, G., Mucus interaction to improve gastrointestinal retention and pharmacokinetics of orally administered nano-drug delivery systems. *Journal of Nanobiotechnology*, 2022, 20(1), 1–23.
15. Watanabe K., Yakou S., Takayama K., Machida Y., Isowa K., Nagai, T., Investigation on rectal absorption of indomethacin from sustained-release hydrogel suppositories prepared with water-soluble dietary fibers, xanthan gum and locust bean gum. *Biological and Pharmaceutical Bulletin*, 1993, 16(4), 391–394.

16. Zou L., Cheng M., Hu K., Feng J., Tu, L., Vesicular drug delivery systems for oral absorption enhancement. *Chinese Chemical Letters*, 2023, 109129.
17. Nakamura K., Kinoshita E., Hatakeyama T., Hatakeyama H., TMA measurement of swelling behavior of polysaccharide hydrogels. *Thermochimica Acta*, 2000, 352–353, 171–176.
18. Remuñán-López C., Portero A., Vila-Jato J. L., Alonso M.J., Design and evaluation of chitosan/ethylcellulose mucoadhesive bilayered devices for buccal drug delivery. *Journal of Controlled Release*, 1998, 55(2), 143–152.
19. Phillips G.O., Williams P.A., Handbook of Hydrocolloids. Elsevier, Woodhead Publishing Limited, London 2009.
20. Nasar-Abbas S.M., Huma Z., Vu T., Khan M.K., Esbenshade H., Jayasena V., Carob Kibble, A Bioactive-Rich Food Ingredient. *Comprehensive Reviews in Food Science and Food Safety*, 2016, 15(1), 63–72.
21. Liu X., Peng L., Meng J., Zhu Z., Han B., Wang, S., Protein-mediated anti-adhesion surface against oral bacteria. *Nanoscale*, 2018, 10(6), 2711–2714.
22. Salamat-Miller N., Chittchang M., Johnston T.P., The use of mucoadhesive polymers in buccal drug delivery. *Advanced Drug Delivery Reviews*, 2005, 57(11), 1666–1691.
23. Andrews G.P., Laverty T.P., Jones D.S., Mucoadhesive polymeric platforms for controlled drug delivery. *European Journal of Pharmaceutics and Biopharmaceutics*, 2009, 71(3), 505–518.
24. Łaskawiec J., Inżynieria powierzchni. Wydawnictwo Politechniki Śląskiej, Gliwice 1997.
25. Blicharski M., Inżynieria powierzchni. Cz. II. Wydawnictwo Naukowe PWN, Warszawa 2021.
26. Goddard J.M., Hotchkiss J.H., Polymer surface modification for the attachment of bioactive compounds. *Progress in Polymer Science*, 2007, 32, 698–725.
27. Xu L.C., Effect of surface wettability and contact time on protein adhesion to biomaterial surfaces. *Biomaterials*, 2007, 28, 3273–3283.
28. Kim M.S., Khang G., Lee H.B., Gradient polymer surfaces for biomedical applications. *Progress in Polymer Science*, 2008, 33(1), 138–164.
29. Podgórski A., Sosnowski T., Metoda wyznaczania napięcia międzyfazowego i kąta zwilżania przez pomiar zanurzenia cząstki kulistej na powierzchni międzyfazowej. I. Analiza teoretyczna. *Prace Wydziału Inżynierii Chemicznej i Procesowej Politechniki Warszawskiej*, 2000, 26(1), 35–52.
30. Liber-Kneć A., Łagan S., Zastosowanie pomiarów kąta zwilżania i swobodnej energii powierzchniowej do charakterystyki powierzchni polimerów wykorzystywanych w medycynie. *Polymers in Medicine*, 2014, 44(1), 29–37.
31. Łysik D., Niemirowicz-Laskowska K., Bucki R., Tokajuk G., Mystkowska J., Artificial saliva: challenges and future perspectives for the treatment of xerostomia. *International Journal of Molecular Sciences*, 2019, 20(13), 3199.
32. Mystkowska J., Łysik D., Klekotka M., Effect of Saliva and Mucin-Based Saliva Substitutes on Fretting Processes of 316 Austenitic Stainless Steel. *Metals*, 2019, 9(2), 178.
33. Gustaw W., Mleko S., Glibowski P., Synergistyczne interakcje występujące pomiędzy polisacharydami w ich mieszaninach. *Żywność. Nauka. Technologia. Jakość*, 2001, 3(28), 5–15.
34. Russo Spena S., Grizzuti N., Tammaro D., Linking processing parameters and rheology to optimize additive manufacturing of k-carrageenan gel systems. *Gels*, 2022, 8(8), 493.
35. Łaskawiec J., Inżynieria powierzchni. Wydawnictwo Politechniki Śląskiej, Gliwice 1997.
36. Ridaut M.J. Garza S., Brownsey G.J., Morris V.J., Mixed iota-kappa carrageenan gels. *International Journal of Biological Macromolecules*, 1996, 18, 5–8.

37. Manion O., Malia C., Launay B., Cuvelier G., Hill S., Hardling S., Mitchell J., Xanthan/locust bean interactions at room temperature. *Carbohydrate Polymers*, 1992, 19, 91–97.
38. PN-93/C-89438: Tworzywa sztuczne – Folie i płyty – Oznaczanie zwilżalności.
39. Zhao T., Jiang L., Contact angle measurement of natural materials. *Colloids and Surfaces B Biointerfaces*, 2018, 161, 324–330.
40. Akbari R., Antonini C., Contact angle measurements: From existing methods to an open-source tool. *Advances in Colloid and Interface Science*, 2021, 294, 102470.

# Mechanical properties of polylactide-based composites with iron powder additions – experimental and numerical evaluation

*Dominika Nowińska<sup>1\*</sup>, Eliza Romańczuk-Ruszek<sup>1</sup>, Zbigniew Oksiuta<sup>1</sup>*

*<sup>1</sup> Faculty of Mechanical Engineering, Institute of Biomedical Engineering,  
Białystok University of Technology, Wiejska 45C, 15-351 Białystok, Poland*

*\*dominika.nowinska@sd.pb.edu.pl, e.romanczuk@pb.edu.pl, z.oksiuta@pd.edu.pl*

**Abstract:** Composite samples were made based on polylactide with the addition of iron powder and iron nanopowder with contents ranging from 0.1% (for nanoFe) to 10% (for Fe). The tests were carried out to check the mechanical properties of the samples, and on their basis, samples were modeled for numerical tests. Strength charts from experimental and numerical tests were compared. Photos of the materials were also taken using a scanning microscope. Samples with the addition of iron nanopowder have better properties than iron powder. Poor adhesion of metal particles to the polymer is visible. An attempt was made to numerically model the material properties of the composites. It was considered that, in the linear range of the material, the results from the experimental tests were in agreement with the numerical results.

**Keywords:** Polylactide, Iron powder, Mechanical properties, Composite materials

## 1. Introduction

Polylactide (PLA) has emerged as a promising biodegradable polymer due to its renewable origin, biocompatibility, and eco-friendliness. However, its inherent limitations, such as brittleness and low mechanical strength, have led to the development of PLA-based composites. PLA-based composites are materials that consist of PLA as the matrix and various reinforcing agents, such as natural fibers, nanofillers, or other biodegradable polymers. PLA-based biodegradable composites offer numerous advantages over pure PLA, including enhanced mechanical properties, improved thermal stability, and reduced environmental impact. However, several challenges and limitations must be addressed to fully realize their potential. By employing various strategies,



such as surface modification, blending with other polymers, and using advanced processing techniques, the challenges associated with PLA-based composites can be overcome. As a result, PLA-based composites have a wide range of applications in various industries, making them a promising alternative to traditional petroleum-based polymers [1–4].

Poly(lactide) (PLA) is a biodegradable polyester polymer that is produced from renewable resources, such as corn or other carbohydrate sources [4]. It is a thermoplastic polymer obtained through the saccharification and fermentation of starch, making it an environmentally interesting biopolymer [3]. PLA possesses exclusive qualities, such as good transparency, processability, glossy appearance, and high rigidity. However, it also has some shortcomings, including brittleness and a high rate of crystallization [2]. Poly(lactide) has a density of 1.25 g/cm<sup>3</sup> for the amorphous form, 1.36 g/cm<sup>3</sup> for the crystalline form, 1.36 g/cm<sup>3</sup> for L-lactide and 1.33 g/cm<sup>3</sup> for meso-lactide [5,6]. Tensile strength for amorphous PLA is reported as 39–59 MPa, elongation at break as ~6%, elastic modulus 3500 MPa, Poisson's ratio 0.36, Young modulus 1280 MPa, and Yield strength 70 MPa [6, 7]. The melting temperature ( $T_m$ ) is 165°C, and the glass transition temperature ( $T_g$ ) is about 55°C [6, 8].

Composites based on poly(lactide) have found diverse applications in the field of medicine, particularly in tissue engineering, regenerative medicine, and biomedical engineering. These composites offer suitable physicochemical properties, biocompatibility, and biodegradability, making them ideal for various medical applications [9]. Thanks to its biodegradability, subsequent operations are unnecessary to remove the implant. This also improves the patient's recovery rate and reduces healthcare costs. The biocompatibility of poly(lactide) limits the body's immune response because it decomposes into lactic acids and short oligomers that are metabolized by the body [10, 11]. Additionally, PLA-based composites are considered entirely bio-based materials with promising biodegradability and mechanical properties, making them suitable for use in sustainable medical products [1, 3]. The use of PLA-based composites in medicine is attributed to their ability to replace traditional petrochemical-based polymers, addressing environmental concerns and offering biodegradable alternatives for medical devices and implants. Furthermore, the unique properties of PLA, such as good transparency, processability, and high rigidity, make it a versatile material for medical applications. PLA-based composites have emerged as valuable materials for various medical applications, offering biocompatibility, biodegradability, and promising mechanical properties. The ongoing research and development in this field continues to expand the potential use of PLA composites in medicine [12].

The aim of this study was to check the effect of the addition of iron and nano-iron particles with different percentages on the mechanical properties of PLA composites. Furthermore, numerical tests were conducted in order to corroborate the experimental findings. The construction of an appropriate numerical model of the material will also permit further numerical analyses to be carried out with a view to determining the most appropriate location for the material's application.

## 2. Materials and methods

### 2.1. Materials preparation

Six different compositions of composites based on polylactide with different iron powder and nanopowder additions were made:

- Polylactide (99%), iron powder (1%) – PLA + 1% Fe
- Polylactide (95%), iron powder (5%) – PLA + 5% Fe
- Polylactide (90%), iron powder (10%) – PLA + 10% Fe
- Polylactide (99%), iron nanopowder (1%) – PLA + 1% nanoFe
- Polylactide (99.5%), iron nanopowder (1%) – PLA + 0.5% nanoFe
- Polylactide (99.9%), iron nanopowder (1%) – PLA + 0.1% nanoFe

PLA polymer (Ingeo 2003 D) was mixed with iron and nano-iron powder until the final concentration was 1%, 5%, 10% for iron (45  $\mu\text{m}$ ) and 1%, 0.5%, 0.1% for nano-iron (60–80 nm). The mixing process was carried out at room temperature by direct manual mixing of granules and powders. The prepared mixtures were extruded using an EHP 25Eline laboratory extruder (Zamak Mercator, Skawina, Poland). The main parameters of the process were as follows: the temperature of the hopper zone was 50°C, the temperature of the supply zone was 170°C, the temperature of the compression zone was 180°C, and the temperature of the dispensing zone was 180°C. The extruder head temperature was 175°C, and the extrusion speed was set at 5% of the maximum machine speed. After extrusion, flat samples with a thickness of 2.5 mm were obtained, from which shapes suitable for tensile tests were cut out. The dimensions of the sample are shown in Fig. 1.

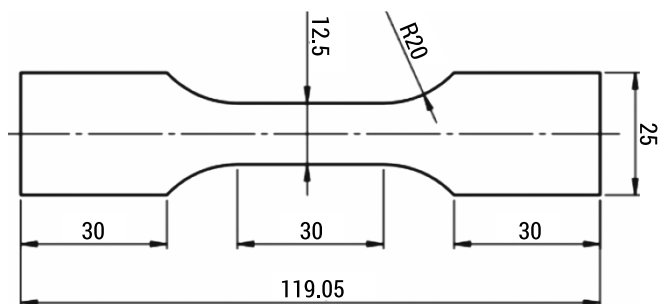


FIG. 1. Tensile specimen dimensions

### 2.2. Experimental tests

A Shore durometer (type D) was used to measure the hardness of the composites. Ten measurements were performed for each sample. Tensile tests were carried out with the MTS 858 Mini Bionix testing machine with a constant cross-head

displacement rate of 2 mm/min at room temperature. The tensile testing setup is shown in Fig. 2. Three to five tensile specimens were tested. A scanning electron microscope (SEM 3000, Hitachi, Japan) was used to observe the surface of composite materials.

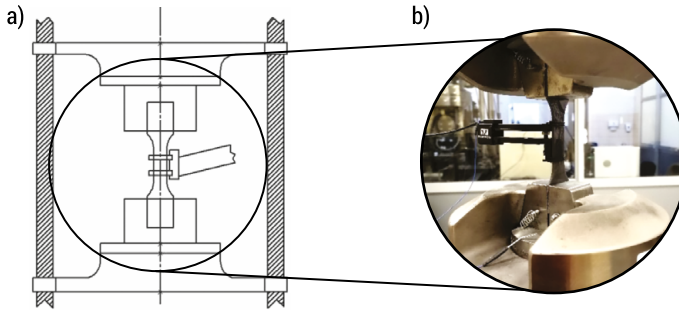


FIG. 2. Tensile test setup: a) visualization and b) a real test

### 2.3. Numerical tests

Numerical tests were conducted using an Ansys Workbench 2018 R1 (Ansys, Inc., Canonsburg, USA). The CAD model of the sample was prepared in SolidWorks 2023 software (Dassault Systèmes S.A., Vélizy-Villacoublay, France). The model was imported into Ansys Workbench software. In the Engineering Data module, material properties obtained from experimental tests were set. The research was performed in the Static Structural module. The mesh was made of tetrahedrons with an element size of 0.1 mm. Ultimately, there were 42,542 finite elements and 72,400 nodes. The boundary conditions were fixed supports in the place where the handle holding the sample is located and displacement on the other side of the sample. The mesh and boundary conditions are shown in Fig. 3.

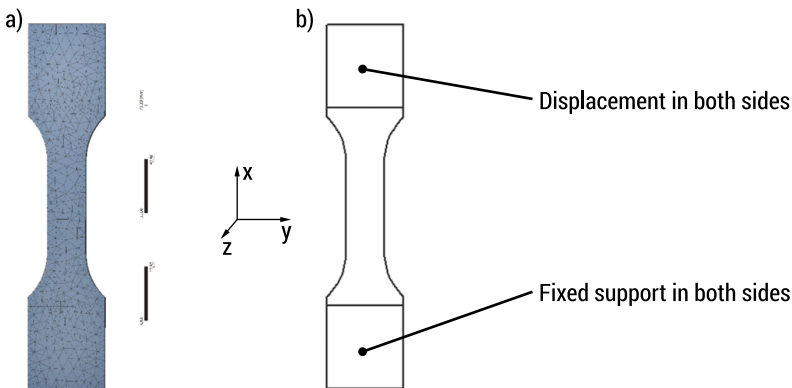


FIG. 3. Prepare for numerical tests: a) model with mesh; b) boundary conditions

## 3. Results

### 3.1. Experimental tests results

Table 1 presents the results of tensile strength tests of the tested composites. When comparing the tensile strength values for a sample made of pure PLA and samples with the addition of iron powder (1.0, 5.0, and 10 wt.%) and iron nanopowder with 0.1, 0.5, and 1.0 wt.%, in general, a decrease in the tensile parameters can be seen, however with one exception of PLA+1.0% nano-Fe. The tensile strength of the composite with 1% nano iron powder is almost twice as high compared to the composite with 1% iron. The obtained results indicate that the size of the powder particles affects the mechanical properties. As for the Young's modulus value for the composites made, these values are slightly higher for materials with the addition of iron nanopowder. These values are comparable to the young modulus of pure PLA.

TABLE 1. Tensile test results of the composite materials

Material	Tensile strength [MPa]	Strain $\varepsilon$ [%]	Young Modulus E [MPa]
PLA 100%	36.0 $\pm$ 2.5	1.03 $\pm$ 0.2	3610
PLA+10% Fe	29.5 $\pm$ 2.1	0.97 $\pm$ 0.10	3320 $\pm$ 150
PLA+5% Fe	26.3 $\pm$ 2.6	0.78 $\pm$ 0.08	3610 $\pm$ 186
PLA+1% Fe	23.1 $\pm$ 1.5	1.12 $\pm$ 0.05	3120 $\pm$ 104
PLA+ 1% nano-Fe	40.6 $\pm$ 0.8	1.45 $\pm$ 0.08	3665 $\pm$ 170
PLA+0.5% nano-Fe	34.5 $\pm$ 1.2	1.00 $\pm$ 0.10	3680 $\pm$ 125
PLA+0.1% nano-Fe	32.6 $\pm$ 0.7	1.03 $\pm$ 0.06	3590 $\pm$ 210

The hardness of the materials is in the range of 65–73°Sh with some reverse tendencies (Table 2). Composites with the addition of iron powder seem harder than those to which nanopowder was added. The hardness decreases as the percentage of powder decreases. The density of made materials is higher or the same as that of pure PLA. The composite with 1% iron powder has the highest density, and the lowest density is the material with 0.1% iron nanopowder.

TABLE 2. Hardness and density values of the tested composite materials

Material	PLA+10% Fe	PLA+ 5% Fe	PLA+1% Fe	PLA+1% nanoFe	PLA+ 0.5% nanoFe	PLA+0.1% nanoFe
Hardness [°Sh]	73.3 $\pm$ 0.94	67.30 $\pm$ 1.86	66.30 $\pm$ 2.21	64.80 $\pm$ 1.28	65.10 $\pm$ 1.20	67.20 $\pm$ 1.76
Density [g/cm <sup>3</sup> ]	1.31	1.62	1.90	1.30	1.27	1.25

In the images taken by SEM (Fig. 4), iron, and nano-iron particles can be observed, and in some cases clusters of particles. Iron particles are very clearly visible in the photos presented. One can notice visible differences in their quantity depending on their percentage in the composite. A weak association of iron particles and nano-iron with polylactide can be seen. Empty spaces between the particles and the polylactide are also visible. This most likely indicates poor adhesion of metallic particles to the polymer and influences the mechanical properties of the composite materials.

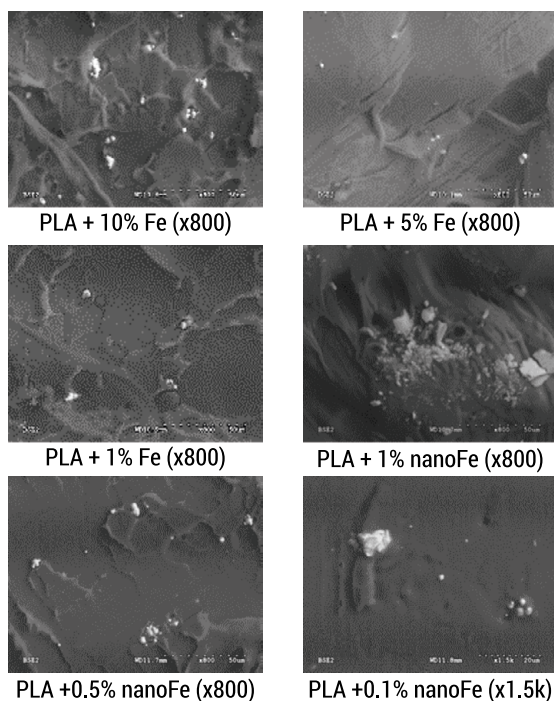


FIG. 4. SEM observations of the composite materials

## 3.2. Numerical simulations

Numerical tests were performed and the results are presented in this section. An equivalent (von Mises) stress test was performed, simulating the conditions prevailing during the tensile test. Based on the results shown in Figure 5, an identical stress distribution can be seen, decreasing in the direction of sample narrowing. The highest stresses ( $\sim 36$  MPa) were observed for the composite sample with the addition of 1% iron nanopowder and the lowest ( $\sim 18$  MPa) for the material with the addition of 5% iron powder.

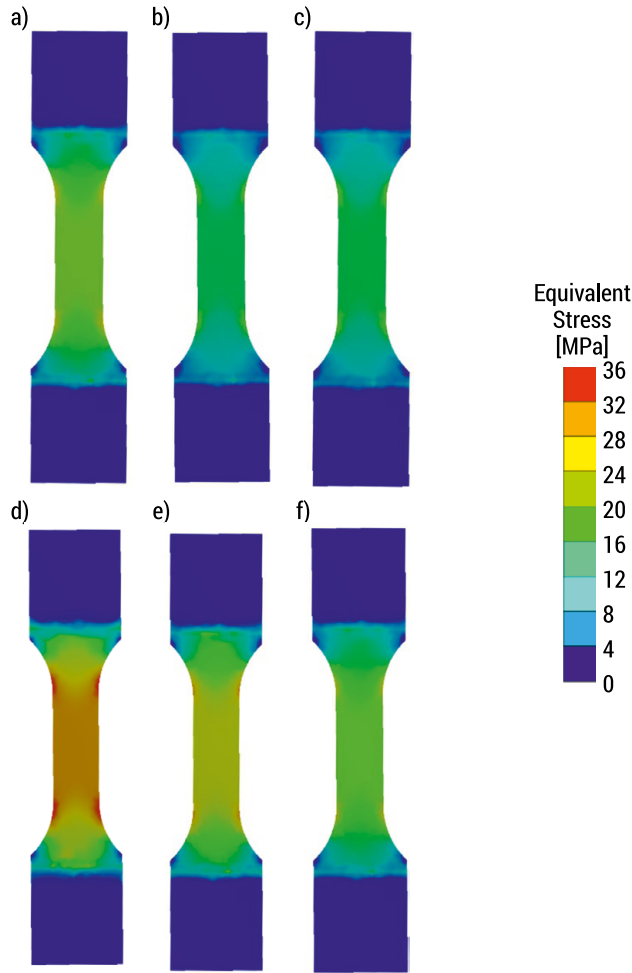


FIG. 5. Equivalent (von-Mises) stress maps for samples: a) PLA + 10% Fe; b) PLA + 5% Fe; c) PLA + 1% Fe; d) PLA + 1% nanoFe; e) PLA + 0.5% nanoFe; f) PLA + 0.1% nanoFe

### 3.3. Comparison of the experimental and numerical results

Based on the experimental and numerical results, stress-strain diagrams were prepared, which were then compared for materials with the addition of iron powder (Fig. 6a) and with the addition of iron nanopowder (Fig. 6b). At first glance, it is visible that stress-strain charts for numerical studies have more straight-line characteristics than those for experimental studies. The initial slope of the graphs is very similar, as well as their length. It can be noticed that for materials with the addition of nanoFe, these graphs overlap because they are almost identical. It can be seen that the highest stress

value was achieved by the composite with the addition of 1% iron nanopowder (both in the case of numerical and experimental tests).

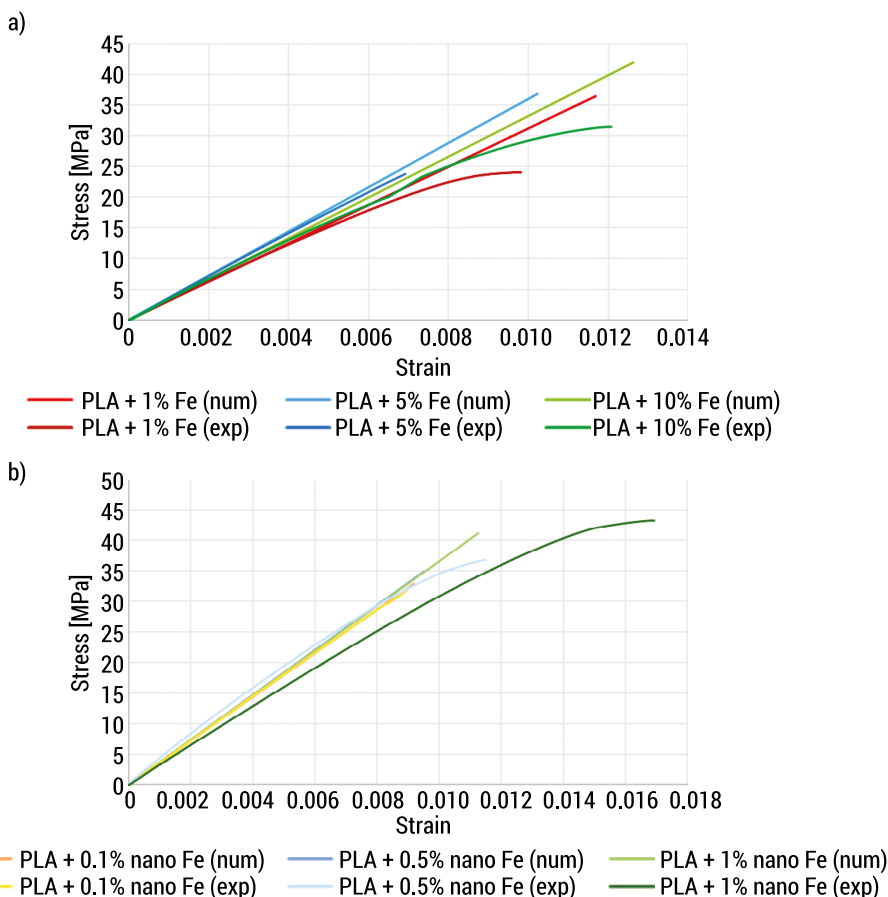


FIG. 6. Stress-strain comparison charts for numerical and experimental study: a) for composites based on PLA with iron powder additions; for composites based on PLA with iron nanopowder additions

## 4. Discussion

In the field of medical materials, there is a continued and intensifying search for materials that are more effective and have superior mechanical and biological properties. This opens up the possibility of modifications to known and used materials, with a particular focus on biodegradable materials [13]. One such material is polylactide, which is promising due to its production from non-toxic, renewable raw materials. PLA and its composites are employed in the medical field for a range of small implants,

threads, and drug-delivery mechanisms [15, 16]. However, it has the significant disadvantage of brittleness and often too long or too short biodegradation times. These properties can be enhanced through the incorporation of additives [17]. In the present study, iron powders and nano-iron were employed as fillers. Comparable mechanical properties can be observed for the proposed fillers in the absence of nanoFe, but the addition of 1% nanoFe results in superior mechanical properties. The incorporation of iron powder with a particle size of 45  $\mu\text{m}$  resulted in a reduction in the strength of polylactide.

The scanning electron microscope (SEM) images demonstrate the presence of gaps between the metal particles and the polylactide matrix. This may be attributed to the inadequate adhesion of the polymer to the metal particles. It is probable that the incorporation of an appropriate linking agent between the two phases will result in a significant enhancement of the mechanical properties of the final composite in comparison to its absence. It is of paramount importance that this ingredient is biocompatible and suitable for use in the human body.

An attempt was made to map the material properties of the fabricated composites in numerical testing software. This was conducted to ascertain the viability of undertaking further material studies utilizing numerical analysis. It was observed that the properties of the modeled material and the fabricated material exhibited a similar trend in the linear range of the material. In order to obtain more accurate numerical results, it will be necessary to model the material in the linear-elastic range. This will permit the potential utilisation of the material for diverse tissue reconstructions to be evaluated without the necessity of fabricating an implant and conducting experimental studies, which are considerably more challenging to arrange.

## 5. Conclusions

The incorporation of an iron particle filler does not enhance the mechanical properties of polylactide. The incorporation of nano-iron particles into polylactide does not result in a deterioration of its mechanical properties. In fact, at a concentration of 1% by weight, the mechanical properties of the polylactide are enhanced.

The SEM microscope images demonstrated poor adhesion of the iron particles and nano-gelase to the polylactide. This can be improved by adding a suitable ingredient to the material to bond the two phases.

The material model for the numerical analyses corresponds to the properties of the fabricated composites in the linear range of the material. In order to obtain more accurate results from the numerical analyses, it will be necessary to model the properties in the linear-elastic range. This will permit the assessment of the suitability of the material for use in a variety of implants or medical devices in terms of its mechanical strength. This will facilitate the identification of potential applications for the composite.



## References

1. Trivedi A.K., Gupta M.K., Singh H., PLA Based Biocomposites for Sustainable Products: A Review. *Advanced Industrial and Engineering Polymer Research*, 2023, 6(3), 382–395.
2. Sahayaraj A.F., Muthukrishnan M., Kumar R.P., Ramesh M., Kannan M., PLA based bio composite reinforced with natural fibers – Review. *IOP Conference Series: Materials Science and Engineering*, 2021, 1145(1), 012069.
3. Li X., Lin Y., Liu M., Meng L., Li C., A review of research and application of polylactic acid composites. *Journal of Applied Polymer Science*, 2023, 140(7), e53477.
4. Wu Y., Gao X., Wu J., Zhou T., Nguyen T.T., Wang Y., Biodegradable polylactic acid and its composites: Characteristics, processing, and sustainable applications in sports. *Polymers*, 2023, 15(14), 3096.
5. Farah S., Anderson D.G., Langer R., Physical and mechanical properties of PLA, and their functions in widespread applications – A comprehensive review. *Advanced Drug Delivery Reviews*, 2016, 107, 367–392.
6. Auras R., Harte B., Selke S., An overview of polylactides as packaging materials. *Macromolecular Bioscience*, 2004, 4(9), 835–864.
7. PLA (96:4 L:D ratio content) produced by NatureWorks Co., technical data sheet, Available from: [www.natureworksllc.com](http://www.natureworksllc.com).
8. Mehta R., Kumar V., Bhunia H., Upadhyay S.N., Synthesis of poly (lactic acid): a review. *Journal of Macromolecular Science, Part C: Polymer Reviews*, 2005, 45(4), 325–349.
9. Casalini T., Rossi F., Castrovinci A., Perale G., A perspective on polylactic acid-based polymers use for nanoparticles synthesis and applications. *Frontiers in Bioengineering and Biotechnology*, 2019, 7, 259.
10. DeStefano V., Khan S., Tabada A., Applications of PLA in modern medicine. *Engineered Regeneration*, 2020, 1, 76–87.
11. Taib N.A.A.B., Rahman M.R., Huda D., Kuok K.K., Hamdan S., Bakri M.K.B., Khan A., A review on poly lactic acid (PLA) as a biodegradable polymer. *Polymer Bulletin*, 2023, 80(2), 1179–1213.
12. Liu S., Qin S., He M., Zhou D., Qin Q., Wang H., Current applications of poly (lactic acid) composites in tissue engineering and drug delivery. *Composites Part B: Engineering*, 2020, 199, 108238.
13. Park S.B., Lih E., Park K.S., Joung Y.K., Han D.K., Biopolymer-based functional composites for medical applications. *Progress in Polymer Science*, 2017, 68, 77–105.
14. Jamshidian M., Tehrany E.A., Imran M., Jacquot M., Desobry S., Poly-lactic acid: production, applications, nanocomposites, and release studies. *Comprehensive Reviews in Food Science and Food Safety*, 2010, 9(5), 552–571.
15. Lasprilla A.J., Martinez G.A., Lunelli B.H., Jardini A.L., Maciel Filho R., Poly-lactic acid synthesis for application in biomedical devices – A review. *Biotechnology Advances*, 2012, 30(1), 321–328.
16. Avérous L., Polylactic acid: synthesis, properties and applications. In: Monomers, polymers and composites from renewable resources, eds. M.N. Belgacem, A. Gandini, Elsevier, Oxford 2008, 433–450.
17. Bergström J.S., Hayman D., An overview of mechanical properties and material modeling of polylactide (PLA) for medical applications. *Annals of Biomedical Engineering*, 2017, 44, 330–340.

# Design of an ankle joint orthosis for people with extensive sweating

*Mateusz Perzan<sup>1</sup>, Anna Falkowska<sup>1\*</sup>*

*<sup>1</sup> Faculty of Mechanical Engineering, Institute of Mechanical Engineering,  
Bialystok University of Technology, Wiejska 45C, 15-351 Bialystok, Poland*

*mateusz.perzan@gmail.com, \*a.falkowska@pb.edu.pl*

**Abstract:** The purpose of this study is the design of an ankle orthosis designed for people with excessive sweating. Considering the available solutions of these types of stabilizers, and taking into account the problem of hyperhidrosis, a device tailored to the anatomical structure of the patient was designed, keeping an appropriate level of ventilation and moisture absorption. A solution was proposed in the form of a personalized ankle orthosis, manufactured from biodegradable polylactide, using 3D printing. The design of the orthosis assumes an incomplete (hexagonal) arrangement of the structure. Therefore, experimental strength tests were carried out on PLA specimens produced by the FDM method with different degrees of density of the hexagonal structure. The tested samples were subjected to temporary exposure in an environment mimicking excessive sweating (0.9% NaCl solution). The developed test results made it possible to determine the effect of hyperhidrosis on the strength properties of the tested samples. They also made it possible to design an optimal ankle orthosis design.

**Keywords:** Ankle orthosis, Rehabilitation, 3D printing, Durability properties, Orthopedics

## 1. Introduction

Injuries to the ankle joint are some of the most common injuries to which athletes in particular are exposed. During physical activities, accidents often occur, which usually turn out to be minor injuries. However, more advanced sprains can lead to several weeks of immobilisation and hospital rehabilitation, which does not guarantee full recovery.

In the recovery process, ankle orthoses play a key role in the field of orthopaedics, offering the necessary support and bracing in the face of numerous conditions.

However, it is important to bear in mind that a certain group of people have a specific physiology, which can include increased sweating. Excessive sweating has a number of potential consequences including skin irritation, general discomfort and even the risk of infection. This is particularly exacerbated by contact with ankle brace components, which are not necessarily made of natural materials. Current solutions, in the form of special insoles or cooling preparations, do not always meet expectations, especially in terms of adequate stabilisation and effectiveness in wicking away moisture.

The current market for orthopedic products including ankle orthoses requires solutions that guarantee good heat exchange. This issue is crucial for those suffering from excessive sweating, also known as hyperhidrosis. This condition, according to reported data, occurs in as many as 17% of surveyed teenagers, and general statistics show that ever-increasing problems with excessive sweat production occur in 2–3% of the entire population. In addition, the results of the study show that about 30% of those surveyed struggle with hyperhidrosis of the hands and feet. Given the very high prevalence of the aforementioned ailment and the complexity of its causes, a multifaceted approach is required, including the appropriate adjustment of products for patients, in order to effectively manage the condition and improve their quality of life [1–5].

On the basis of consumer feedback, there is a need for an innovative ankle brace that, in addition to its stabilising function, should regulate excessive perspiration, thus increasing user comfort. In addition, it is important that the orthosis is adjusted to take into account the specific anatomical structure of the patient's foot. An excellent solution may be the use of 3D printing technology. This makes it possible to obtain the desired shape and size without a lengthy technological process.

## 1.1. Structure and functioning of the ankle joint

The ankle joint, also known as the ankle and knee joint, connects the tibia, fibula and ankle bones, among others. It is one of the most stressed joints in the human body, playing a key role in maintaining balance, base stability and acting as a shock absorber during walking, running and other movements. Its structure allows flexion, extension, adduction and inversion movements, as well as rotation of the foot. It is extremely important for the proper functioning of the musculoskeletal system, and disorders in its area can lead to numerous conditions and injuries [6]. The general structure of the joint, including the ankle, is shown in Figure 1.

Injuries to the ankle joint are quite common, mainly among young people and especially those with an active lifestyle. However, they only account for about 6 % of all injuries [8].

During physical exertion, such as during sports competitions, the foot and ankle absorb enormous loads. The ankle, as a weight-bearing joint, can be subjected to various forces, reaching a pressure equivalent to up to six times the athlete's body weight.

Depending on the type of sport practised, the load transferred to the ankle joint can lead to fractures, damage or ligament ruptures, which are associated with long-term recovery [7].

From the literature data analysed, it appears that the most common injury to the ankle and knee joint is a sprain. It is the result of 14 to 33 % of all sports activity accidents and is closely related to the collateral ligaments, resulting in damage to part of the joint capsule (Fig. 1), the ankle-scapular ligament and the calcaneofibular ligament. Lateral sprain occurs as a result of the inversion mechanism, i.e. a situation in which the foot positions itself on the lateral edge. This causes damage to the ligamentous structures and the joint capsule. In contrast, tibiofemoral torsion results from the dorsiflexion mechanism of the foot. However, analysing the information available in scientific publications, in the majority of cases these injuries are not serious and only about 33% of them require temporary stabilisation [8].

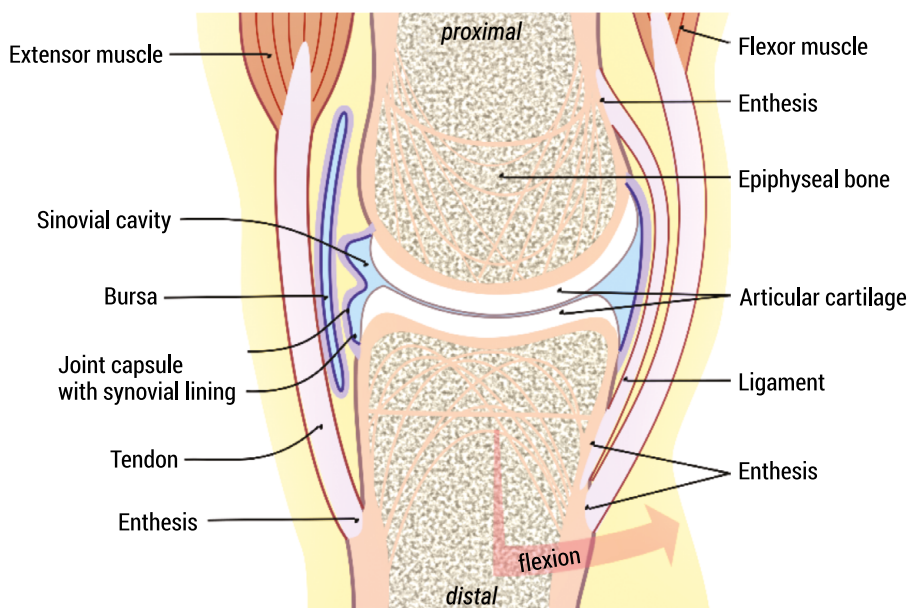


FIG. 1. General structure of the joint [9]

Excessive sweating (hyperhidrosis), is a condition that develops irrespective of age, gender and race and often leads to a reduced quality of life. It is associated with an impairment of the sweat gland system, located in the epithelial tissue of the body [5].

Depending on the cause, hyperhidrosis can be divided into primary and secondary (influence of comorbidities, medication, stress). Taking into account the degree of body involvement in the condition, hyperhidrosis can be limited – relating to individual skin surfaces or generalised – affecting the whole body. The vast majority (90%) of cases are primary hyperhidrosis, limited to certain areas of the body [5].

## 1.2. Functions of the orthosis

The purpose of the stabiliser, used mainly for sprains or fractures of the ankle joint, is to reduce the load and stabilise the area, aiming to improve mobility. It is also intended to counteract increasing pain, which occurs when the body transfers weight to the foot and is exacerbated when walking. The stabiliser protects the structures from further damage, creating favourable regenerative conditions [10].

In the orthosis, the ankle joint remains in the correct position after a sprain both in static situations, e.g. sitting, standing, and dynamic situations, i.e. during movement. The brace prevents instability of the joint, which is a major cause of recurrent injury, ligament damage and even bone displacement. The stabiliser also reduces the appearance of swelling and keeps the skin in good condition, thus guaranteeing proper blood and lymph flow [10].

External support of the ankle joint is repeatedly used both in the post-traumatic recovery of ligaments and in the prevention of first and recurrent dislocations. This significantly reduces the incidence of ankle joint injury. The choice of technique in which the stabiliser is made depends mainly on the individual patient's preference, and the effectiveness of the stabiliser depends on the design used and the properties of the materials from which it is made. The use of external support during an injury is a good way to prevent ankle sprains. Bracing performed has been shown to reduce the risk of ankle sprain in 50–70% of people who have previously experienced a similar injury. Stabilisation has been shown to be more effective than neuromuscular training, reducing the incidence of ankle injuries by 47%. This effectiveness was also confirmed by other studies. Studies were presented that analysed Numbers-Needed-to-Treat (NNT) to determine the effectiveness of orthoses and taping. A significantly lower ratio of NNT patients was observed with the use of bracing compared to the use of taping [11]. Another publication found that athletes who used stabilisers (either as a result of an injury or as a preventive measure) had a 64% reduction in the risk of sprain [12].

## 2. Design of an ankle orthosis

Fused Deposition Modelling (FDM) is a 3D printing method in which raw material, otherwise known as filament, is typically heated to a liquid state and then extruded through the nozzle of a 3D printer. The nozzle head has the ability to move in three degrees of freedom (DoF) to deposit the extruded polymer on the heating table according to instructions in G-code form. The principle of the FDM process is illustrated in Figure 2. The filament is fed continuously through the extruder and spool of the 3D printer via two rollers rotating in opposite directions. The material is applied to the heating table layer by layer until the required shape and size is achieved. During the layering process, the printer nozzle moves back and forth according to the spatial

coordinates of the 3D CAD model (from which the corresponding G-code is created). Sometimes, in 3D printer systems using the FDM technique, multiple extrusion nozzles are used to apply the polymer, particularly when components with heterogeneous compositions are required to be created. Typically, the quality and application performance of the filament is highly dependent on its thermoplastic properties, as well as the heating capabilities of the printer. One of the most commonly used materials with the FDM method is PLA – a polylactide [13].

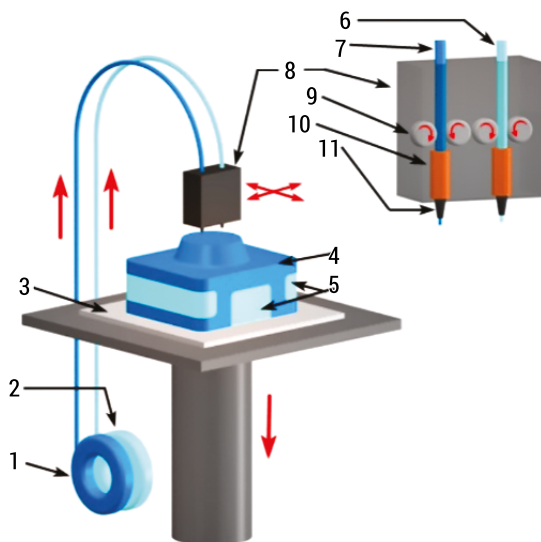


FIG. 2. Principle of 3D printing process using FDM technique (1 – spool of main filament, 2 – spool of auxiliary filament, 3 – heating table, 4 – component created, 5 – support elements of the component, 6 – auxiliary filament, 7 – main filament, 8 – extruder, 9 – guide rollers, 10 – liquefying guide, 11 – nozzle) [14]

The most commonly used polymers for the production of filaments are poly(acrylonitrile-co-butadiene-co-styrene) (ABS) and polylactic acid/polylactide (PLA). Considering the biodegradability, biocompatibility and thermoplastic renewability of polyester, together with its excellent mechanical strength and processability, PLA clearly leads over ABS [15]. Currently a fashionable and aliphatic polymer, PLA is derived from renewable resources such as sugar cane, maize and cassava. In addition, it requires low energy consumption and produces minimal greenhouse gases during the production process. Combining all the aforementioned characteristics together, and also highlighting the fact that it is an environmentally friendly material with antibacterial properties, makes it a promising polymer for sustainable products [14].

Currently, manufacturers are placing great emphasis on realising the potential of biodegradable raw materials. The interest in these building materials is driven by a combination of environmental responsibility, market pressures, numerous regulations, economic benefits and innovation [16, 17].

# 2.1. Structural and technological assumptions of the developed orthosis

## 2.1.1. The purpose of the project

One of the first issues to be determined when creating the design brief is the target group of the product. The present solution concerns a patient weighing approximately 70 kg, who has suffered an ankle and shin joint injury in the form of a sprain and ligament tear, while also suffering from hyperhidrosis. The aforementioned case requires immobilisation and support during the recovery period, as well as ensuring appropriate sweat management.

Personalisation turns out to be the best solution, so the stabiliser should be properly adapted to the size and circumference of the ankle, as too small may cause unnecessary pressure, while too large will not provide proper support. Thus, it is assumed that the design should fit into the shoe. As mentioned earlier, a good solution is to use 3D printing. This is a multi-step process, described in the Figure 3.

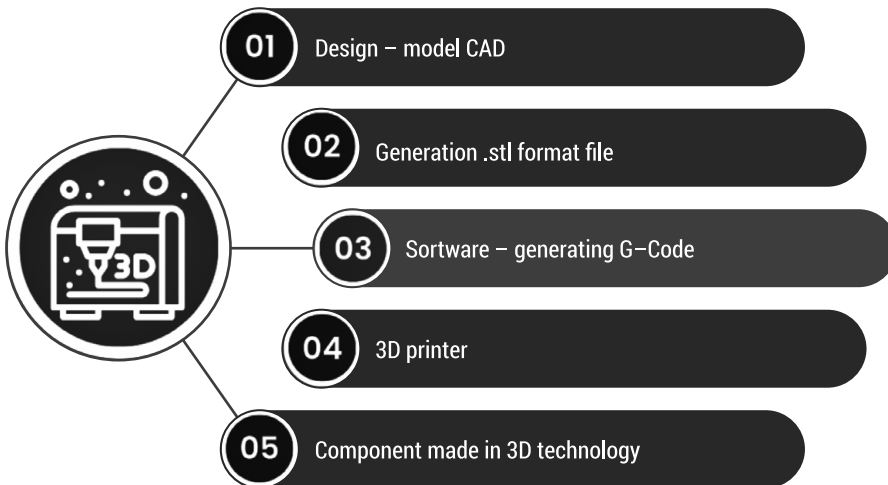


FIG. 3. 3D printing process

Therefore, one of the first stages of its creation is a 3D scan of the patient's leg, on the basis of which, using the appropriate software, the stabiliser is designed from scratch. Such a solution makes it possible to adapt the product to the anatomy of the future user and to take into account the indicated aspects influencing the comfort of wearing it even for a long period of time, which is impossible in the case of universal orthopedic braces.

An important consideration is ease of donning and doffing so that the product is easy to handle, especially if the orthosis will be donned and doffed repeatedly. This is extremely important for people with excessive sweating, as it enables the required

level of hygiene to be maintained. Excessive sweating will be counteracted by using a perforated structure in key areas of the orthosis to increase airflow and reduce the unpleasant effects of this ailment.

In terms of environmental awareness and responsibility, the use of biodegradable materials that decompose in a way that is less harmful to the environment is a step towards sustainable production. Polylactide (PLA) is proving to be a good choice as a filament for use in incremental manufacturing, as it fits into the application palette of many industries, including medicine.

In order to develop an appropriate spatial structure for the orthosis to allow adequate ventilation, especially in the context of excessive sweating, strength testing of different structures should be carried out. The choice of the target structure will allow a good balance between strength and usability of the orthosis.

## 2.2. Experimental tests

The solution concerns the use of PLA as the building material. Therefore, samples with a hexagonal structure with 30% and 50% filling were subjected to strength analysis. Beforehand, they were placed in an environment that mimicked body fluids – in an aqueous NaCl 0.9% solution (saline) for a period of 2 to 8 weeks.

In order to carry out strength tests on the structures used in the orthosis design, it was essential to print the corresponding samples using the FDM method. The 3D printing process consisted of several steps, namely: creating a CAD model of the specimen, generating a file in .STL extension and obtaining a G-code programme that the 3D printer was able to read.

The study was designed to determine the effect of an environment of increased perspiration on the degradation rate of the material (PLA), as well as the infill density of the model – an ankle orthosis – on the prevailing environment. The change in mechanical properties was recorded through monotonic tensile testing of the PLA and analysis of the results.

### 2.2.1. Results of the experimental tests

Considering the data presented in Table 1, it was undoubtedly considered correct to conclude that the PLA material undergoes a slight degradation process as a result of being in a humid environment, which alters its characteristic strength parameters. As the residence time in solution increases, the strength parameters decrease in value, becoming more given to the forces acting on them. This is an extremely important issue, especially for the design and planning of products using PLA material as raw material for construction.

Analysing the averaged stress-strain relationship curves shown in Figure 4, the greatest difference was observed between samples with honeycomb filling



and a density of 30%, which were not placed in saline solution and after two weeks' exposure. There was a noticeable decrease in tensile strength (from 13 MPa to 11.1 MPa), as well as an increase in strain (from approximately 4.7% to 5.5%). Considering all the averaged tensile curves, no significant differences were noticed, e.g. with regard to the parameter  $R_m$  (tensile strength). Of course, it should be noted that discrepancies in values between samples residing in solution for different lengths of time do occur, but by analysing the degradation process it can be concluded that initially the polymer structure reacts rapidly to the environment, after which it enters a stage where further reactions slowly occur.

TABLE 1. Summary of the obtained parameters of PLA material as a result of monotonic tensile test

	Density of filling 30%									Density of filling 50%					
	Duration of exposure in saline solution														
	0 weeks		2 weeks		4 weeks		6 weeks		8 weeks		0 weeks		8 weeks		
E [MPa]	868.37	863.5	816.59	838.4	903.79	846.1	827.73	813.6	859.69	847.4	1079	1060.3	1018.4	1023.1	
	873.93		862.84		796.45		809.25		858.51		1043.8		992.04		
	848.20		835.87		838.15		803.96		824		1058.2		1059		
$\varepsilon$ [%]	3.8	4.7	4.4	5.4	5.7	5.0	6.1	6.9	4.4	5.5	3	4.3	5.1	5.4	
	4.1		5.7		4.3		7		5.9		4.1		5.5		
	6.1		6.1		5.1		7.5		6.1		5.8		5.6		
R <sub>u</sub> [MPa]	12.09	12.3	9.06	9.2	8.73	9.3	10.06	10.0	9.66	9.6	13.73	14.1	9.47	9.9	
	12.26		9.14		9.88		9.68		9.48		14.2		10.08		
	12.40		9.25		9.2		10.32		9.78		14.4		10.17		
R <sub>0.2</sub> [MPa]	12.69	12.8	10.54	10.6	10.67	10.6	10.76	10.7	10.81	10.7	14.11	14.1	10.71	11.1	
	12.85		10.53		10.59		10.48		10.77		10.79		14.09		11.04
	12.83		10.59		10.62		10.77		10.51		14.07		11.56		
R <sub>m</sub> [MPa]	13.01	13.0	10.97	10.7	10.91	10.9	11.04	11.0	11.24	11.1	14.81	14.8	12.43	11.9	
	13.02		10.65		10.87		11.01		11.14		14.78		11.85		
	12.86		10.62		10.78		10.83		11.02		14.76		11.38		

For specimens with a fill density of 50%, two tests were performed – for specimens that were placed in salt solution for 8 weeks and specimens that were not exposed to environmental influences. In Figure 5, a perfectly visible changing characteristic of PLA material properties was observed. As a result of the high humidity environment, there was a significant decrease in average tensile strength (from 14.8 MPa to 11.9 MPa), breaking stress (from 14.1 MPa to 9.9 MPa), as well as Young's modulus, causing an increase in the degree of plasticity of the sample.

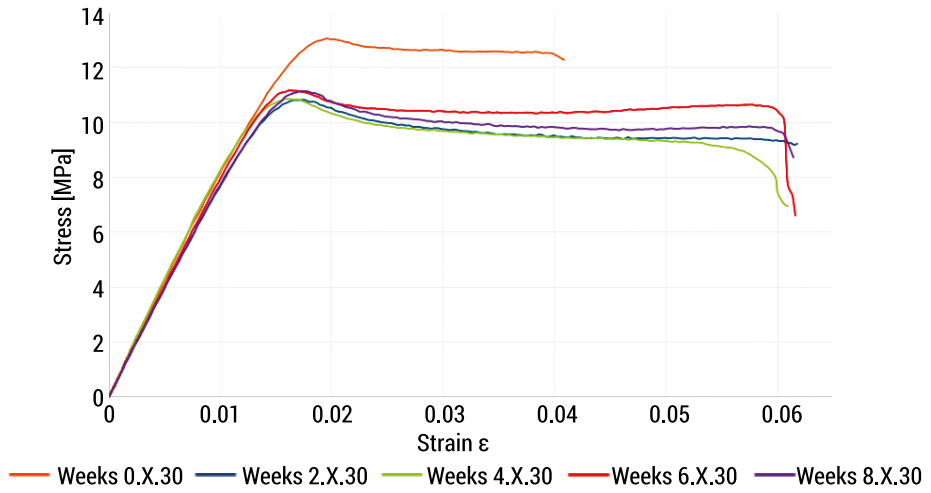


FIG. 4. Summary of tensile plots of honeycomb-filled PLA specimens with a density of 30%

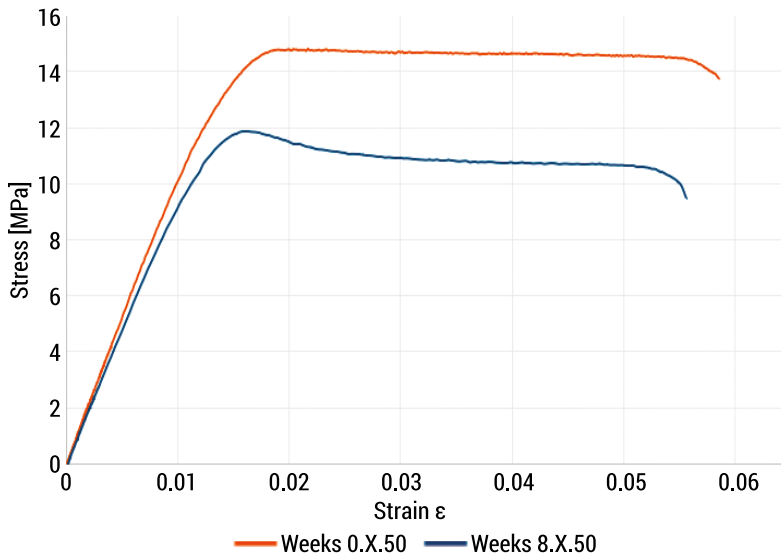


FIG. 5. Summary of tensile plots of honeycomb-filled PLA specimens with a density of 50%

In Figures 6 and 7, the graphs focus mainly on the changes observed in the application of different filling densities. According to the graphs, in both cases an increase in filling from 30% to 50% resulted in a material that is more resistant to degradation processes, which is confirmed by the strength parameters of the samples.

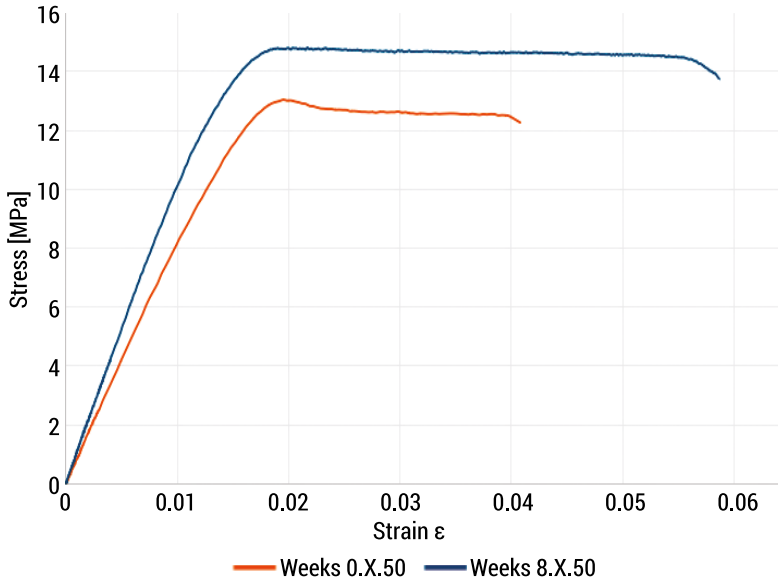


FIG. 6. Summary of tensile plots of PLA samples with honeycomb filling and 30% and 50% density, without exposure in saline solution

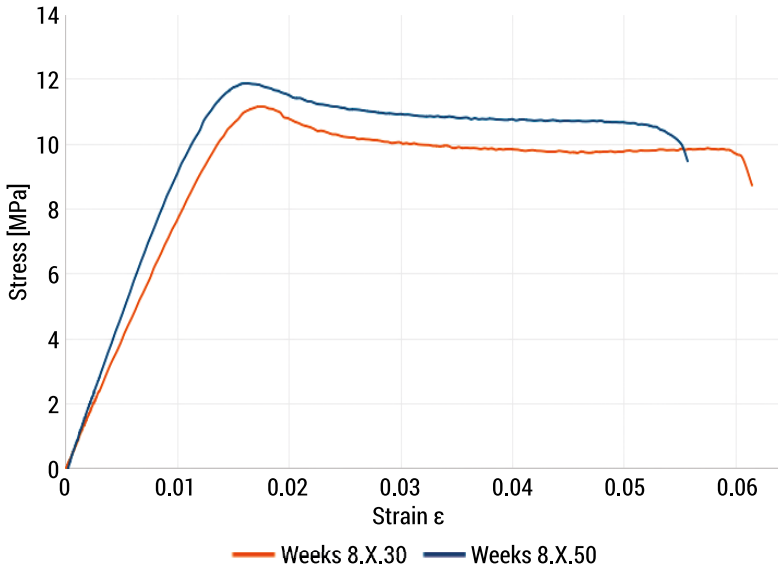


FIG. 7. Summary of tensile plots of PLA samples with honeycomb filling and 30% and 50% density, after 8-week exposure in saline solution

After the strength tests, it can be concluded that monotonic tensile tests of samples produced by 3D printing prove to be essential for assessing the strength of the material used, as well as the quality of the creation method applied. This is important in the fields of engineering and manufacturing, providing high-quality products.

## 2.3. Final design solution

The first step in the process of designing the ankle orthosis model was to select the appropriate software and acquire a 3D scan of the patient's leg in .STL format. The leg scan used for this project was obtained from the GrabCAD online platform, which contains thousands of models from various disciplines in its libraries. The use of the scan enabled the work to be optimised and a high-quality model to be selected, meeting the standards for the realisation of a medical device project. The Autodesk Fusion 360 environment, into which the aforementioned scan was imported, was chosen to create the orthosis model (Fig. 8).

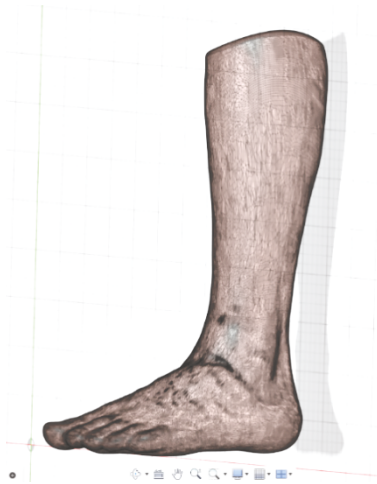


FIG. 8. Patient leg scan in Autodesk Fusion 360

The next step was to position the model in the immediate vicinity of the centre of the coordinate system, which provided optimal possibilities for the reference points of the shapes forming the mesh. Using a shape in the form of a sphere, the grid area of the orthosis being created was circled. This solution allowed the beginning and end of the structure to be determined according to the size and anatomical structure of the foot.

Based on the shape, an initial model of the mesh adjacent directly to the skin was generated. The resulting mesh contains detailed geometry information, enabling accurate mapping. (Fig. 9).

In the next stage, the correctness of the mesh was assessed and numerous corrections made to the appropriate degree of adhesion. This resulted in the creation of a basis for further design stages. The advanced features of Autodesk Fusion 360 allowed the newly generated shape meshes to be significantly modified, while retaining key details. The mesh of the orthosis was subjected to localised rescaling and moved away from the surface of the ankle joint area to maintain comfort. In addition, attention should be paid to the implementation of the insertion and removal solution, as shown

in Figure 10. A special open space in the design of the orthosis was designed to allow the user, who has suffered an ankle injury, to insert the stabiliser by positioning the foot. Such a solution will provide the user with the possibility of avoiding excessive movement of the joint and handling with reduced pain. The edges of the designed orthosis have been appropriately rounded and profiled so that they do not cause unnecessary rubbing, especially during the process of fitting.

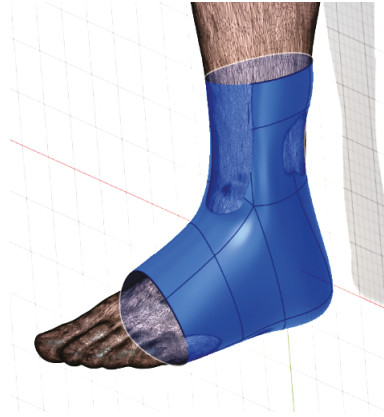


FIG. 9. Optimized patient foot grid

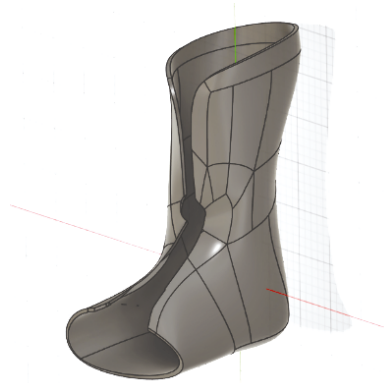


FIG. 10. Developed solid mesh of the ankle orthosis

The next stage was to prepare the solid for optimisation processes. Individual elements of the model determined to be critical – located in the area of the ankle and shin joint – were deprived of the possibility to change their shape. The automated modelling function in the Autodesk Fusion 360 environment allows for the generation of alternative design forms, which sometimes result in significant changes to the geometry of the base object. For this reason, some of the surfaces of the solid were declared immobile to ensure that the AI-corrected design could be obtained without changing the most important parts of the design (Fig. 11).

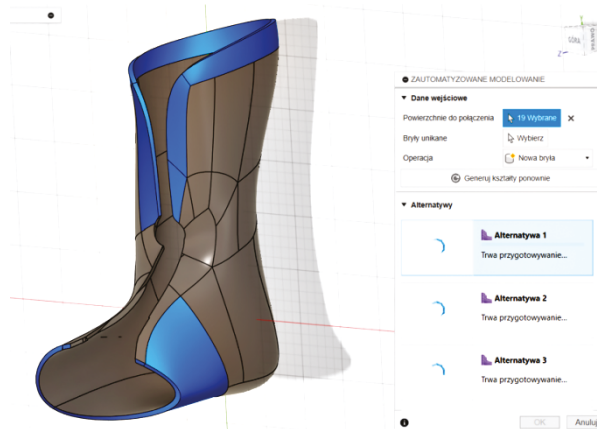


FIG. 11. Use of automated modeling functions

Once the optimisation process of the stabiliser body had been attempted, it was perforated due to the design goal of obtaining a model designed for people with excessive sweating. The perforations made not only had a positive effect on reducing the weight of the product, thus increasing comfort, but also improved heat transfer properties. The use of this technique means that heat and moisture is better dissipated, making the foot sweat less. When analysing where the perforations were to be located and how large the holes could be, the critical elements under most stress were taken into account. The final result in the form of a finished model of the ankle brace is shown in Figure 12.

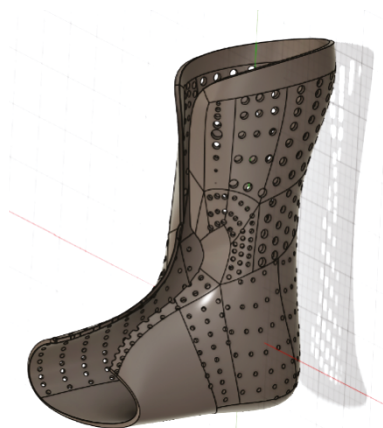


FIG. 12. Final model of ankle and knee joint orthosis

The final stage of the project was to properly prepare the model file exported in .STL format, in order to obtain a high quality print. PrusaSlicer was the software used to analyse the printout parameters and to show how the supports were applied.

In Figure 13, a model of the orthosis in the preparation process is presented. According to the data obtained, an orthosis with a wall thickness of 4 mm and an infill density of 30% would weigh 178.28g, hence it is possible to insert the affected leg into a shoe. The target object in the form of the printed stabiliser was marked in orange, while the support elements were marked in green. The software allowed a preview of the print including layers, parameter control, support generation and optimisation, as well as G-code generation.

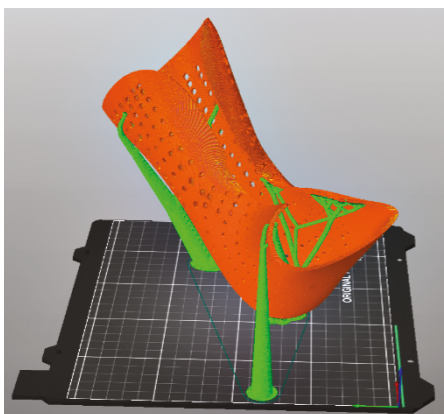


FIG. 13. Ankle joint orthosis model in PrusaSlicer

### 3. Summary and discussion

An ankle brace is a special type of support used when faced with the need to stabilise the ankle and knee joint as a result of an injury. Depending on whether it is a sprain, fracture or chronic ailment, these medical devices provide the required degree of immobilisation or restriction of part of the movement. They help to reduce pain and swelling and provide excellent added value to the treatment and rehabilitation process.

Designing an ankle brace model proved to be a more challenging task than initially anticipated. To finalise the project, the work had to be divided into stages. This involved defining the target group and thus developing the design guidelines for a personalised orthosis. In this case, it was extremely important to follow the zero waste trend, so a biodegradable polylactide was chosen. An important aspect was to print specimens of a certain type and density and carry out strength tests. An additional element was the temporary exposure of the printed samples in saline solution. This was to imitate the problem of excessive sweating in the context of PLA degradation. The results

obtained allowed the optimal variant of the orthosis design to be taken. The final design was developed in the next step, in which the various construction stages were presented.

The developed design and the conducted strength tests allowed the following conclusions:

1. Better strength properties were registered for the samples with 50% fill, both in long-term exposure in NaCl solution (8 weeks) and without it. Long-term exposure to an environment that imitates excessive sweating causes a decrease in strength properties, which is related to PLA degradation. However, the greatest decrease in strength parameters is recorded quite quickly (already after 2 weeks). In the following weeks, the reduction in these parameters is not significant.
2. The manufacture of a personalized, perforated ankle brace with an openwork design not only allows the brace to be adapted to the patient's anatomy, but also to offset the negative effects resulting from excessive sweating. An additional advantage is the low weight of the stabiliser, which increases comfort during its use.
3. The design of the orthosis, which is fully adapted to the patient's anatomy and additionally provides the desired degree of stabilisation and ventilation, can be obtained using the appropriate software (Autodesk Fusion 360). The tools used in the programme allow the required machining and modification of the mesh during design.

## References

1. Onikijuk A., Nadmierne pocenie się – jak pozbyć się wstydlivego problemu?, *Czytelnia Zdrowia*, 2021, [www.cefarm24.pl/czytelnia/porady-okolozdrowotne/nadmierne-pocenie-sie-przyczyny/](http://www.cefarm24.pl/czytelnia/porady-okolozdrowotne/nadmierne-pocenie-sie-przyczyny/) (access: 3.06.2024).
2. Kupczyńska D., Nadpotliwość – przyczyny i metody leczenia, 2019, [www.arseestetica.pl/blog/nadpotliwosc-przyczyny-i-metody-leczenia/](http://www.arseestetica.pl/blog/nadpotliwosc-przyczyny-i-metody-leczenia/) (access: 3.06.2024).
3. Doolittle J. et al., Hyperhidrosis: An Update on Prevalence and Severity in the United States. *Archives of Dermatological Research*, 2016, 308(10), 743–749.
4. Styczeń P., Wstydlivy problem. *Uroda i Medycyna*, 2016, 1(10).
5. Jabłonowska O., Woźniacka A., Dzikowska-Bartkowiak B., Hyperhidrosis: causes and treatment options. *Dermatology Review*, 2020, 107(3), 246–256.
6. Budowa stawów stopy. *Dlatawow.pl* – wszystko o twoich stawach. <https://dlatawow.pl/budowa-stawow-stopy/> (access: 3.06.2024).
7. Jelinek J.A., Porter D.A., Management of Unstable Ankle Fractures and Syndesmosis Injuries in Athletes. *Foot and Ankle Clinics*, 2009, 14(2), 277–298.
8. Pedrycz A., Frąckiewicz M., Cichacz B., Siermontowski P., Urazy w obrębie stawu skokowego. Diagnostyka, profilaktyka, leczenie operacyjne. *Journal of Polish Hyperbaric Medicine and Technology Society*, 2014, 4(49).
9. [https://en.wikipedia.org/wiki/Joint\\_capsule](https://en.wikipedia.org/wiki/Joint_capsule).
10. Jak wybrać ortezę i stabilizator stawu skokowego? Sklep weron.pl. <https://weron.pl/wiedza/wpis/37-jak-wybrac-orteze-i-stabilizator-stawu-skokowego.html> (access: 3.06.2024).



11. Walasek M., Jakie są trendy i kluczowe wyzwania w postprodukcji 3D? 3D.edu.pl 2023. <https://3d.edu.pl/jakie-sa-trendy-i-kluczowe-wyzwania-w-postprodukcji-3d/> (access: 3.06.2024).
12. Bellows R., Wong C.K., The effect of bracing and balance training on ankle sprain incidence among athletes: a systematic review with meta-analysis. *International Journal of Sports Physical Therapy*, 2018, 13(3), 379–388.
13. Mwema F.M., Akinlabi E.T., Basics of Fused Deposition Modelling (FDM). *Fused Deposition Modeling*, 2020, 1–15.
14. Mendricky R., Accuracy analysis of additive technique for parts manufacturing. *MM Science Journal*, 2016, 2016(5), 1502–1508.
15. Liu W., Zhou J., Ma Y., Wang J., Xu J., Fabrication of PLA Filaments and its Printable Performance. *IOP Conference Series: Materials Science and Engineering*, 2017, 275, 012033.
16. Song J.H., Murphy R.J., Narayan R., Davies G.B.H., Biodegradable and compostable packaging an alternative to conventional plastics. *Philosophical Transactions of the Royal Society of London. Series B*, 2011, 366(1572), 1781–1782.
17. De Bie F., Gobius G., Ravard M., Scola P., Veras R., Stay in the cycle Rethinking recycling with PLA bioplastics. <https://www.totalenergies-corbion.com/media/xy4a3pcj/stay-in-the-cycle-whitepaper-about-pla-recycling-totalenergies-corbion.pdf> (access: 3.06.2024).

# Influence of the femoral neck-shaft and anteversion angles on the loadings acting in the musculoskeletal system during walking

Justyna Skubich<sup>1\*</sup>, Szczepan Piszczatowski<sup>1</sup>

<sup>1</sup> Faculty of Mechanical Engineering, Institute of Biomedical Engineering,  
Białystok University of Technology, Wiejska 45C, 15-351 Białystok, Poland

\*j.skubich@pb.edu.pl, s.piszczatowski@pb.edu.pl

**Abstract:** Bone deformities of the femur, e.g. increased or decreased femoral neck-shaft angle (FNS) and improper femoral anteversion angle (FA), can lead to altered loadings acting in the musculoskeletal system and pathological gait patterns. The aim of this study was to investigate the influence of FNS and FA on muscle forces and joint reaction forces during walking. Four musculoskeletal models with a variable geometry of the femoral bone were taken into consideration. The greatest changes in active muscle forces were observed in the case of muscles with their attachments located on the proximal part of the femur. On the other hand, in the case of the hip and knee joint reaction force, the greatest differences between the results obtained using particular models were noticeable both in the values of local extrema and in the time of their occurrence. Understanding of the influence of femoral deformities (FNS and FA) on loading occurring in the musculoskeletal system can help in assessing the biomechanics of the lower limb and designing appropriate interventions for individuals with altered femoral anatomy.

**Keywords:** Femoral neck-shaft angle, Femoral anteversion angle, Muscle forces, Joint reaction forces, AnyBody

## 1. Introduction

Musculoskeletal simulations have been used in biomechanical analysis, allowing the estimation of muscle and joint reaction forces among both healthy people and subjects with musculoskeletal disorders [1–5]. Various software and different models of the musculoskeletal system are used to determine these parameters. The two most commonly used musculoskeletal modeling systems are OpenSim [6] and AnyBody

Modeling System [7]. While OpenSim is a free open-source modeling and simulation framework, AnyBody is a commercial software. It is very important that the standard model available in the AnyBody system is constantly developed and updated by the program creators.

The femoral neck-shaft angle (FNS) and femoral anteversion angle (FA) are two important anatomical parameters of the femur that can significantly influence the loadings acting in the musculoskeletal system during walking. The femoral neck-shaft angle (FNS) refers to the angle between the neck and the shaft of the femur, which can vary among individuals. Similarly, the femoral anteversion (FA) refers to the torsion of the femoral head and neck in relation to the femoral shaft, indicating the degree of twist between the proximal and distal parts of the femur on the transverse plane [8, 9]. FA goes through substantial development during growth with a change from 30° at birth, decreasing to 15° in adulthood [8], whereas the FNS decreases from 140° to 125°. FA affects the loading on the hip, such as moment arm lengths and lines of action of muscles around the joint are altered. As a consequence, improper FA causes differences in gait patterns and is a risk factor for clinical problems. Improper femoral anteversion can cause disturbances in mobility [10], differences in gait, such as in-toeing and increased hip internal rotation [11, 12], as well as associated orthopedic [13] and functional complications. De Pieri et al. [14] noticed that an improper femoral anteversion angle can affect the orientation of the hip intra-articular forces. They found significant correlations between higher femoral anteversion angle and higher medial (loaded stance phase) and anterior (swing phase) hip joint reaction forces during walking.

Abnormal structure and activity of spastic muscles in people with CP leads to bone deformities, e.g. deformation of the femoral bone [15, 16]. Under the influence of abnormal loads occurring in CP, abnormal femoral neck-shaft angle and anteversion angle are often observed. When the femoral neck-shaft angle is <125°, it is considered as coxa vara. Coxa valga (>125°) can lead to increased stress in the hip joint and a higher risk of hip dislocation [17, 18]. The anteversion angle with the correct structure of the limb is in the range 12-15° [18]. Torsion of the femoral neck of more than 15° results in excessive internal rotation of the limb in the hip joint and positioning of the foot with the toes turned inward during locomotion. However, anterior rotation lower than 12° causes excessive external rotation of the limb and external rotation of the foot [18].

Previous studies have shown that modeling of femoral anteversion is particularly important in the analysis of patients with cerebral palsy, which often is characterised by bone deformations [19–21]. Overall, the femoral neck-shaft angle and anteversion angle can influence the loadings acting in the musculoskeletal system during walking by affecting the biomechanics of the hip and knee joints.

The aim of the study was to investigate the influence of FNS and FA on muscle forces and joint reaction forces during walking. Four variants of the musculoskeletal models with various FNS and FA values were developed and used to calculate muscle forces and joint reaction forces, based on the motion capture data of participants with a typical gait pattern.

## 2. Methods

### 2.1. Data necessary for modeling

In order to obtain the data necessary for modeling, movement was recorded for a group of 20 young healthy people (10 women/10 men) in the most similar age range (i.e. 19–21 years) with similar anthropometric parameters (i.e. body height  $169.9 \pm 3.8$  cm and body weight  $65.3 \pm 4.3$  kg) and with no historical injuries or damages on the lower limbs at the time of the experiment were recruited for this study. All qualified participants walked along a 9-meter walkway with self-selected velocity at least 10 times. The research was approved by the Ethical Review Board (R-I-002/356/2017). Information about the current health condition was collected, as well as data such as gender, age and anthropometric parameters: body height, body weight, pelvic width, and the length of the right and left lower limb (length of thigh, shank and foot). Twenty-four reflective skin markers were applied to the subject's lower limb. The time-spatial trajectories of the markers were recorded using the Qualisys Motion Capture System (Qualisys AB, Gothenburg, Sweden). A set of twenty-four reflective skin markers was placed on the lower part of the body for each participant according to a modified Helen Hayes marker set [22]. Additional markers were placed on medial femoral epicondyles and medial malleoluses as well as three markers located on the foot [22]. The ground reaction forces were measured simultaneously using two force platforms (Kistler, Winterthur, Switzerland). Marker data were registered at the frequency of 118 Hz and analogue data from the force platforms at 1000 Hz. The data taken from the motion capture system were exported to a file in the .C3D format.

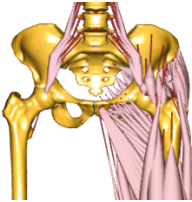
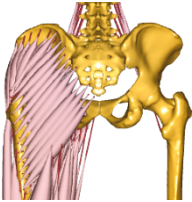

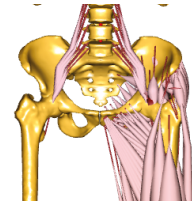
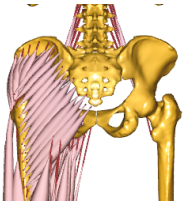

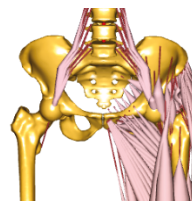
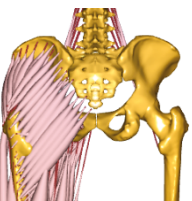

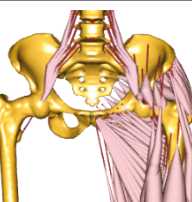
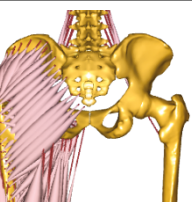

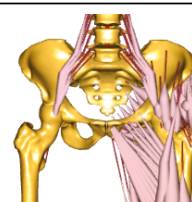
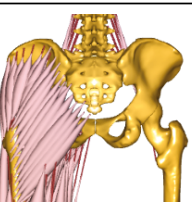

### 2.2. Musculoskeletal modeling

The concept of this study was based on the use of a model of the musculoskeletal system to evaluate selected biomechanical parameters (muscle force, joint reaction force) during walking. For analysis of the musculoskeletal system the AnyBody Modeling System was used (version 7.3, AnyBody Technology A/S, Aalborg, Denmark). An attempt was made to modify the geometric model of the femoral bone. The surface model of a standard, unscaled femoral bone available in the repository (TLEM 2.0) was exported from AnyBody software and saved as an external STL file. This bone model was characterised by a femoral neck-shaft angle equal to  $125^\circ$  and an anteversion angle equal to  $5^\circ$ . Then, the femur model was deformed in four independent ways, respectively increasing / decreasing the femoral neck-shaft angle or increasing / decreasing the anteversion angle. This way, four different geometrical models were obtained, taking into account the deformation of the femoral bone [22]:

- FNS\_150 – femoral neck-shaft angle increased to  $150^\circ$ ,
- FNS\_100 – femoral neck-shaft angle decreased to  $100^\circ$ ,

- FA\_40 – femoral anteversion angle increased to 40°,
- FA\_0 – femoral anteversion angle decreased to 0°.

TABLE 1. Effect of including deformed femoral bones in the standard model [22]

Model	Anterior view	Posterior view	Lateral view
Standard model (SM)			
FA_0			
FA_40			
FNS_100			
FNS_150			

The deformed surface geometric models of the femur allowed the determination of the data necessary to modify the models of left and right femurs, which was carried out directly in the AnyBody software using the so-called “personalised

scaling procedure”. The bone model in STL format was the basis for transformation of the standard model into the geometry of deformed bone. The following transformations were performed: linear, RBF (Radial Basis Functions) and STL. All transformations were performed based on the information contained in the research by Skubich [22], Marra et al. [23] and Andersen [24].

The deformed bone models were incorporated into the general model in the AnyBody system. After enabling the deformed femur geometry, all segments were scaled using the Length-Mass-Fat [24, 25] linear scaling procedure to adjust the bone length for each study participant.

The results obtained with the use of a standard model of the musculoskeletal system available in the repository of the AnyBody system will be compared with the results of a simulation conducted on a modified model with changed geometry of the femoral bone. The standard model and models with modified femur geometry were shown in Table 1. This way, the effect of including the deformed geometry of the right and left femur with an incorrect neck-shaft angle or anteversion angle was visualised. The bone segments were presented in anterior, posterior and lateral views. The presented summary shows the effect of the scaling procedure used in relation to the geometry of the proximal part of the femur, and allows us to observe how the lines of action of the muscles having their attachments on the femur and pelvis were changed.

After modifying the femoral anteversion angle or neck-shaft angle, changes in muscle length were observed for all actons which have their attachments on the femur and/or pelvis, i.e.: gluteus maximus, gluteus medius, gluteus minimus, tensor fascia latae, biceps femoris (long and brevis head), semitendinosus, semimembranosus, quadriceps femoris, adductor longus, adductor brevis, adductor magnus, sartorius, gastrocnemius, iliopsoas, quadratus femoris, piriformis, popliteus, plantar, obturator externus and internus, gemellus (superior and inferior). This is primarily due to the variable position of the femur in relation to the pelvis, which is partially visualised in Table 1. The change in length for particular muscles was different and depended on the used model. For example, when modifying the neck-shaft angle, the greatest changes in the length of muscle actons compared to the standard model were observed for the hip adductor muscles. The change in the anteversion angle affected primarily the change in the length of the rectus femoris and iliopsoas. In turn, in the case of the gluteus muscles, each of the introduced modifications significantly changed the length of these actons.

## 2.3. Numerical simulation processing

All numerical simulations using a previously prepared model in the AnyBody system were divided into two stages: (1) determination of kinematic parameters (inverse kinematics) and (2) determination of muscle and joint reaction forces (inverse dynamics).

For this purpose, data recorded during experimental tests were used, containing information about the current position of markers and the ground reaction forces. Data from the .C3D file was imported into the AnyBody Modelling System. Next, marker trajectories and ground reaction forces (GRF) were filtered using a second-order low-pass Butterworth filter with a cut-off frequency of 5 and 12 Hz, respectively, and used as input for an inverse dynamics analysis in the AnyBody [7, 26]. An inverse dynamics analysis, based on a third-order-polynomial muscle recruitment criterion [26–29], was performed to calculate required muscle forces, as well as joint reaction forces. All analysed parameters were determined in relation to an appropriate coordinate system, according to the International Society for Biomechanics' (ISB) recommendations [30].

Numerical simulations using a standard or modified models were performed for each research participant, for a minimum of 5 correct trials. All simulation results were normalised to 100% of the gait cycle. Additionally, the values of muscle and joint reaction forces as well as their standard deviations were normalised to body weight (%BW). The results were averaged for each participant and for the entire research group.

A comparison of the differences in muscle forces and joint reaction forces observed between the standard model (SM) and models with modified geometry of the femoral bone (FA\_0, FA\_40, FNS\_100 and FNS\_150) were quantified using the root-mean-squared differences (RMSD). Differences between analysed models were assessed using ANOVA statistical analysis (Tukey's Post-Hoc Test).

## 3. Results

### 3.1. Active muscle force

The following muscles were included in the analysis: BFL – biceps femoris long head, BFB – biceps femoris short head, ST – semitendinosus, SM – semimembranosus, GMa – gluteus maximus, GMe – gluteus medius, GMi – gluteus minimus, PM – psoas, IL – iliacus, TFL – tensor fasciae latae, TA – tibialis anterior, GA – gastrocnemius, SO – soleus, AM – adductor magnus, AB – adductor brevis, AL – adductor longus, RF – rectus femoris, VM – vastus medialis, VI – vastus intermedius, VL – vastus lateralis.

Figure 1 presents a summary of active muscle force waveforms allowing for the assessment of the influence of all variants of femur geometry modification (FA\_0, FA\_40, FNS\_100 and FNS\_150) on the loadings acting in the musculoskeletal system, in comparison with the results obtained for the standard model (SM).

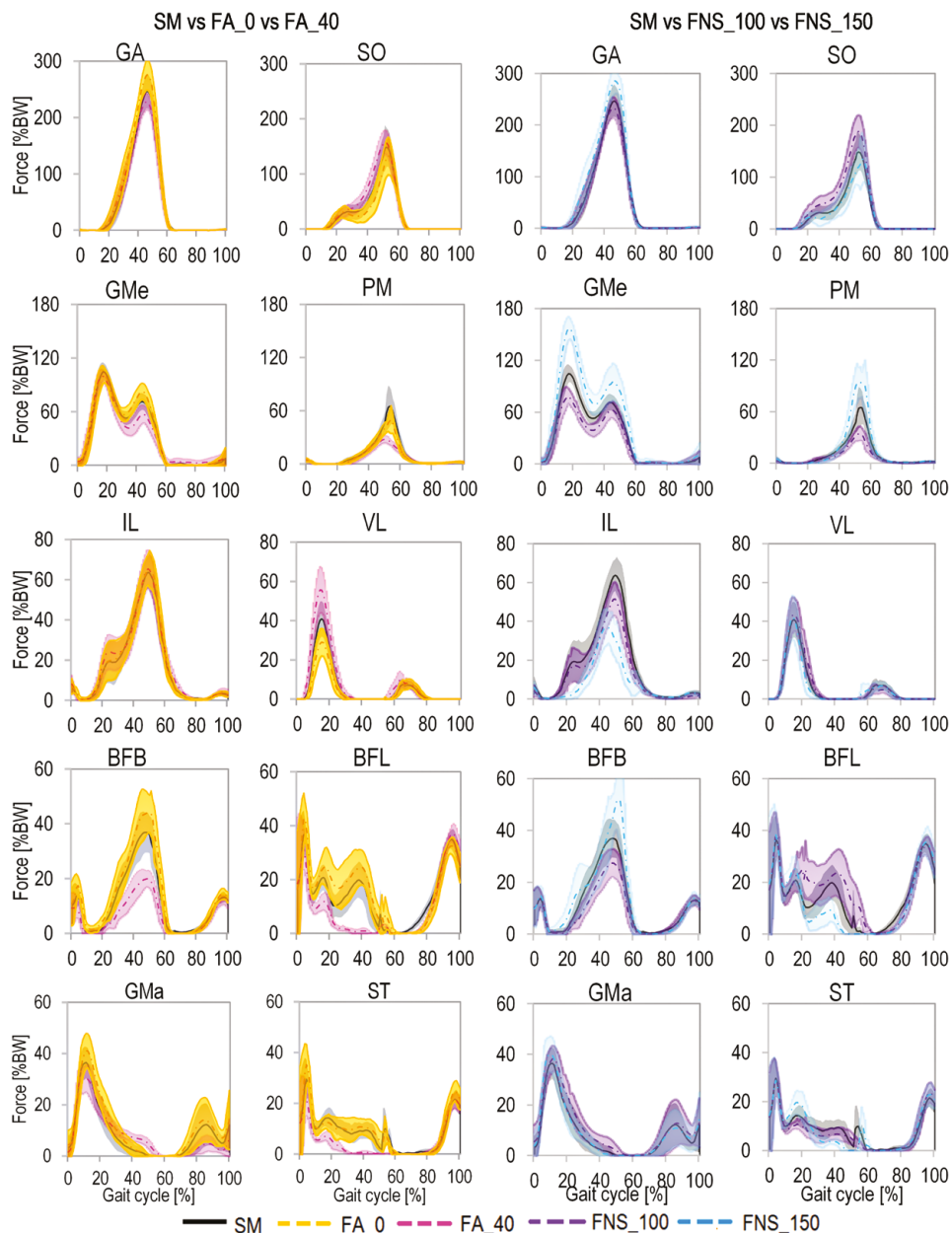


FIG. 1. Muscle active force waveforms for 20 muscles. Comparison of the results obtained for models with modified geometry of the femoral bone (FA\_0, FA\_40, FNS\_100 and FNS\_150) and the standard model (SM) (mean  $\pm$  SD)





The differences in the results of active muscle forces (Fig. 1, Fig. 2) were observed in the case of the gluteus muscles, which have attachments near the proximal part of the femur (i.e. greater trochanter). The impact of model with modified femoral neck-shaft angle (RMSD>15%BW) on GMe muscle force was higher than the impact of a model with modified femoral anteversion angle (RMSD<15%BW). The GMe in the model with an increased neck-shaft angle (FNS\_150) generated higher values of muscle force during stance phase (an increase of 70%BW in the first local maximum and 20%BW in the second local maximum) compared to the standard model (SM). Different results for this muscle were observed in the model with decreased neck-shaft angle (FNS\_100). In this case, a decrease of the muscle force of approximately 30%BW was visible during the first local maximum (approx. 20%GC). The modification of the anteversion angle mainly influenced the change in the value of the second local maximum (an increase in force by 9%BW with decreased FA (FA\_0) and a reduction in force by 21%BW with increased FA (FA\_40)). In the case of the gluteus maximus and minimus (GMa, GMi), the waveforms were similar to those obtained for the standard model. Only with an increased anteversion angle does the active force have a different waveform, this is most visible in the case of the GMi muscle. The gluteus minimus (GMi) muscle in this modification variant generates force higher than in standard models (RMSD 17%BW).

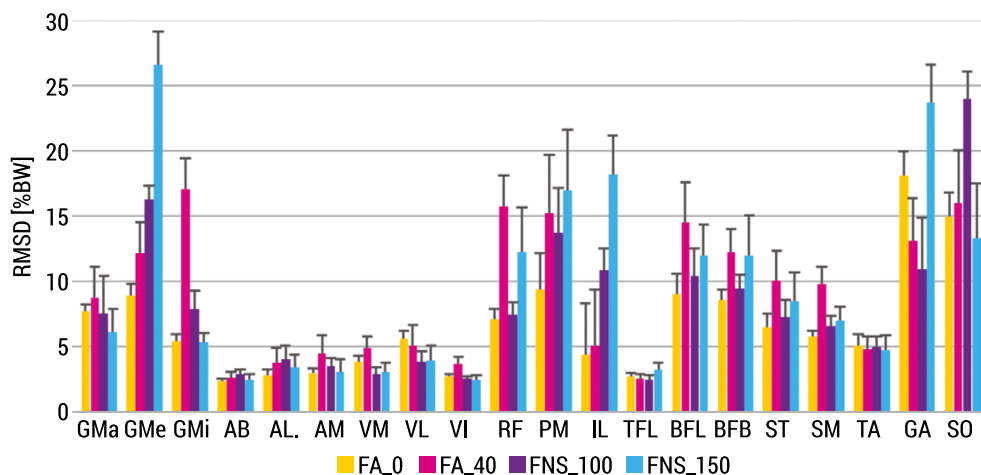


FIG. 2. Mean root-mean-square-differences (RMSD) for the comparison of muscle forces between the standard model (SM) and models with modified geometry of the femoral bone (FA\_0, FA\_40, FNS\_100 and FNS\_150). Error bars represent standard deviation

In the case of the FNS\_150 and FA\_40 models, there are differences in the work of the rectus femoris muscle, namely in both models (RMSD: 17%BW for FA\_40, 13%BW for FNS\_150), an increased muscle forces is visible for almost the entire duration of the stance phase. This is related to the changed pathway of this muscle and is a result of a different position of the femur in relation to the pelvis, resulting

of which the muscle force arms of this muscle have been shortened. Compared to the standard model, the active muscle force for the iliopsoas (PM, IL) was most changed when using model with increased the neck-shaft angle (FNS\_150; RMSD: 17%BW for PM, 18%BW for IL). Compensation between the PM and IL muscles is visible – when the muscle forces of one of them decrease, the muscle forces of the other increase at the same time.

With an increased anteversion angle (FA\_40), the activity time of the posterior thigh muscles (ST, SM, BFL, BFB) in the stance phase was shortened from 59%GC to 25-30%GC, with a simultaneous reduction in the value of muscle force. In other variants, although the muscle activity time remained almost unchanged compared to the standard model, the value of muscle force changed significantly. The decreased anteversion angle (FA\_0) resulted in an increase in force by 2-5%BW during 30-58%GC – for the SM, ST (RMSD – 7%BW) and an increase by 7-13%BW during 18-55 %GC for the BFB, BFL (RMSD – 9%BW). The decreased neck-shaft angle (FNS\_100) only resulted in an increase in the force of the BFL muscle by 7-10%BW during 18-55%GC with a simultaneous weakening of the BFB muscle by approximately 8%BW at the same time. In turn, the increased neck-shaft angle (FNS\_150) resulted primarily in an increase in the force of SM and ST muscles at the beginning of the stance phase to approximately 30% of the gait cycle. For the muscles in posterior compartment of the shank (GA and SO) only a change in the maximum values of active muscle force can be observed. It should be noted that if the value of the GA force decreases, the value of the SO force increases at the same time (FA\_0, FNS\_100).

For the remaining muscles (AB, AL, AM, VL, VM, VI, TFL, TA) the differences between the standard model (SM) and all models with modified geometry of the femoral bone were at a similar level regardless (RMSD – below 6%BW) (Fig. 2)

## 3.2. Hip and knee joint reaction forces

The changes in muscle function resulting from modifications in the geometry of the femur were reflected in the hip and knee joint reaction forces (Fig. 3, Table 2). The differences in the hip joint reaction force between analysed models were visible in the values of the first and second local maxima. An increase in the value of the proximal-distal (P\_D) component of the hip joint reaction force was observed in the case of the both models with an increased neck-shaft angle (FNS\_150) and a decreased anteversion angle (FA\_0). In the FNS\_150 both local maxima were at similar level (approx. 395 %BW;  $p < 0,05$ ). Moreover, decreased force value at the first local maximum was observed for model with a decreased neck-shaft angle (FNS\_100) by 41%BW ( $p < 0,001$ ), compared to the standard model. Differences can be noticed in the times of occurrence of both local maximum values and local minimum. In the model with a decreased neck-shaft angle, the local minimum occurred earlier in comparison to the other modified models and standard model.

TABLE 2. Statistical analysis for the hip and knee joint reaction force components (P\_D – proximal-distal; M\_L – medial-lateral; A\_P – anterior-posterior) for selected time-points (local extrema) presented in Fig. 1.3 and the level of significance of differences between results obtained for the standard model (SM) and models with modified geometry of the femoral bone (FA\_0, FA\_40, FNS\_100 and FNS\_150) ( $p < 0.05$ ; x – no statistically significant difference)

		Model	Time points		
			1	2	3
HIP	P_D	FA_0	0.014	0.019	0.01
		FA_40	x	x	x
		FNS_100	<0.001	0.012	x
		FNS_150	<0.001	0.04	x
	M_L	FA_0	x	0.03	x
		FA_40	x	<0.001	x
		FNS_100	x	<0.001	0.04
		FNS_150	0.03	<0.001	0.03
	A_P	FA_0	<0.001	<0.001	
		FA_40	<0.001	<0.001	
		FNS_100	x	x	
		FNS_150	x	x	
KNEE	P_D	FA_0	0.04	0.03	x
		FA_40	x	x	x
		FNS_100	x	x	x
		FNS_150	0.005	0.01	0.04
	M_L	FA_0	x	0.03	0.007
		FA_40	x	<0.001	x
		FNS_100	x	<0.001	0.03
		FNS_150	0.04	<0.001	0.01
	A_P	FA_0	0.04	x	<0.001
		FA_40	0.003	<0.001	<0.001
		FNS_100	x	<0.001	x
		FNS_150	x	<0.001	x

The increase in proximal-distal component of the knee joint reaction force (compared to the SM model) in the stance phase, similarly to the hip joint, is mostly visible for model with an increased neck-shaft angle (FNS\_150;  $p < 0.05$ ) and a decreased anteversion angle (FA\_0;  $p < 0.05$ ). In turn, a decrease in the value of the second local maximum of reaction force was observed (by 20%BW) in models with a decreased neck-shaft angle (FNS\_100;  $p > 0.05$ ) and an increased anteversion angle (FA\_40;  $p > 0.05$ ).

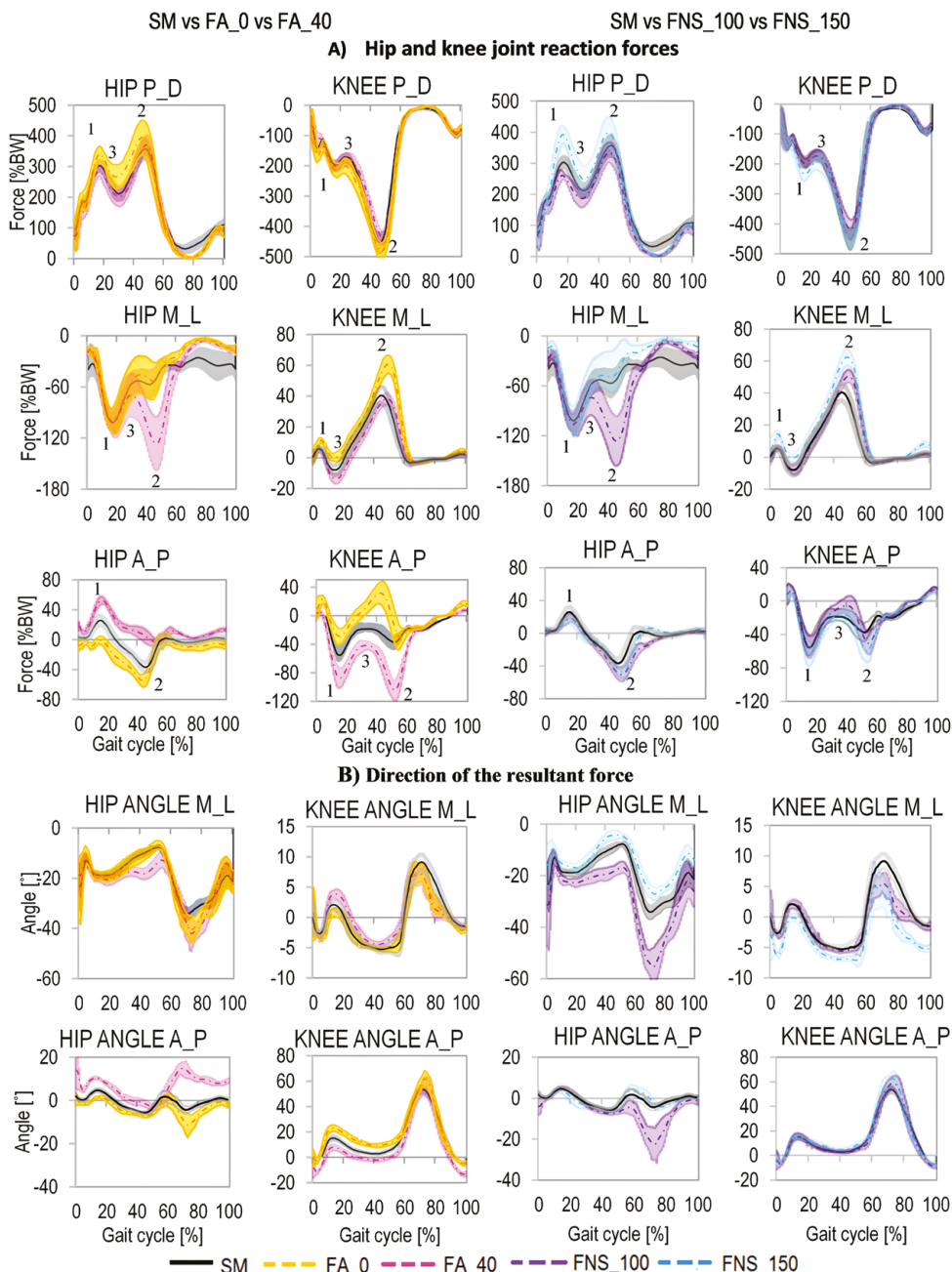


FIG. 3. Hip and knee joint reaction forces obtained using modified models (FA\_0, FA\_40, FNS\_100, FNS\_150) compared to results obtained using the standard model (SM) (mean  $\pm$  SD): A) reaction force components (P\_D – proximal-distal; M\_L – medial-lateral; A\_P – anterior-posterior) and B) angles of deviation of the force direction resultant force in the coronal (M\_L) and sagittal (A\_P) planes. The time-points at which the results were further statistically analysed are marked: 1÷3

In the case of the FA\_40 and FNS\_100 models, the time waveforms of the medial – lateral (M\_L) component in the hip joint were very similar, and the differences in values between these models were only at the level of 3-7%BW. It should be noted that the direction of the resultant hip joint reaction force also changes. Using model with an increased neck-shaft angle, the force vector was directed more vertically, while with a decreased neck-shaft angle, the medial deviation increases. Analysing the results of the anterior – posterior (A\_P) component in the hip joint, it is worth noting that a decrease in the anteversion angle (FA\_0;  $p<0.05$ ) makes the vector direction of resultant force posterior. In turn, increasing the anteversion angle (FA\_40;  $p<0.05$ ) causes the force vector to be directed anteriorly almost during the entire gait cycle.

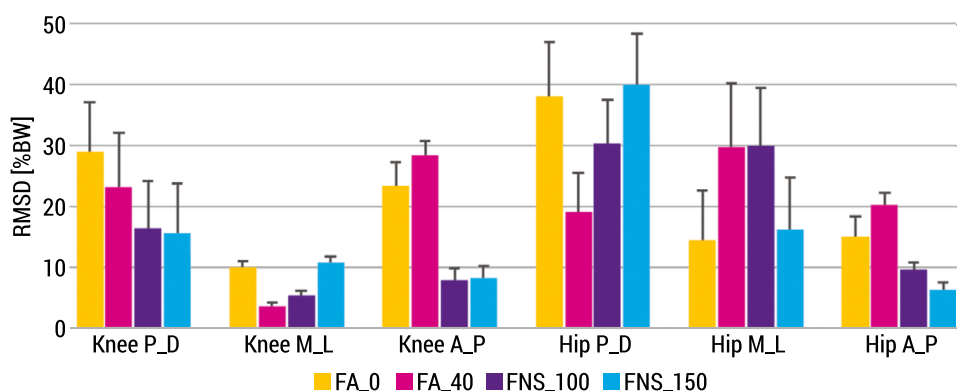


FIG. 4. Mean root-mean-square-differences (RMSD) for the comparison of joint reaction forces components (P\_D – proximal – distal; M\_L – medial – lateral; A\_P – anterior posterior) between the standard model (SM) and models with modified geometry of the femoral bone (FA\_0, FA\_40, FNS\_100 and FNS\_150). Error bars represent standard deviation

The waveform of the M\_L component of the knee joint reaction for the FA\_40 model was most similar to the SM model, while in the case of FA\_0 and FNS\_150, an increase in the reaction force (by approx. 25%BW) was visible. The greatest changes in the knee joint reaction forces were observed for the A\_P component, especially with a changed anteversion angle ( $p<0.05$ ). Increasing it (FA\_40) causes the vector to turn to the posterior side, while decreasing it (FA\_0) causes the vector to be turned to the anterior side.

In the case of the knee proximal-distal and anterior-posterior forces, the greatest changes were observed for FA\_0 (P\_D – RMSD = 28%BW; A\_P – RMSD = 24%BW) and FA\_40 (P\_D – RMSD = 23%BW; A\_P – RMSD = 27%BW) compared to SM. In turn, for the hip proximal-distal forces, these differences were greatest for FNS\_150 (RMSD = 40%BW), FA\_0 (RMSD = 38%BW) and FNS\_100 (RMSD = 30%BW). Large differences for the hip medial-lateral forces were observed between the standard model and FA\_40, FNS\_100 models (RMSD = 30%BW for both models) (Fig. 4).

## 4. Discussion

The performed numerical simulations allowed the assessment of the influence of individual modifications of the model, and thus potential changes in the structure and function of the musculoskeletal system, on the loads occurring in the system.

The greatest differences in the active muscle forces between the analysed models were observed especially in the case of muscles which have their attachments on the proximal part of the femur. This is due to the changed pathway of these muscles as a result of the different position of the femur in relation to the pelvis, resulting in which the muscle force arms were changed. Large differences were also observed for the shank muscles.

Modification of the musculoskeletal models by a changed femoral neck-shaft angle or anteversion angle led to statistically significant differences in the predicted joint reaction forces during the gait cycle in comparison to the generic baseline model, based on a cadaveric template. This finding is in agreement with previous studies [19]. It can be seen that the greatest differences in the knee joint reaction force, compared to the standard model, were visible in the waveforms of the medial-lateral and anterior-posterior components. In the case of the hip joint reaction force, the greatest differences between the results obtained using particular models were visible for both the values of local maxima and the time of their occurrence. Increased femoral anteversion leads to reduced joint load during walking, which was also confirmed in the studies by Kainz et al. [19], Alexander et al. [31], and Modenese et al. [32]. In models with an increased femoral neck-shaft angle, the muscle forces increased, which explains the increased hip joint reaction forces, which confirmed the findings of previous studies [33]. It can also be noticed that a change in the femoral neck-shaft angle affects the direction of the reaction force vector in the coronal plane (more vertical position for an increased neck-shaft angle and a more medial position for a decreased neck-shaft angle). In turn, a change in the anteversion angle mainly results in a rotation of the resultant force in the sagittal plane (in the anterior direction for an increased anteversion angle or in the posterior direction for a decreased anteversion angle), similarly to the studies by other authors [14, 19, 31, 34].

This study had the following limitations. First, at this stage of the research, the influence of only single modifications to the standard model was assessed. However, it should be understood that a given person may have more than one manifestation of pathological changes at the same time, e.g. an abnormal neck-shaft angle and anteversion angle of the femur may occur at the same time. Second, we only included motion capture data from a few healthy participants. It would be worth conducting future research for people with femoral deformities, because the pathological gait is characterised by very high variability [35]. Future research should evaluate how subject-specific gait patterns influence muscle and joint reaction forces.

## 5. Conclusion

In conclusion, we conducted numerical simulations for a musculoskeletal model and assessed the influence of four variants of the femur model modification with various FNS and FA values on muscle forces and hip and knee joint reaction forces.

Overall, the femoral neck-shaft angle and anteversion angle of the femur have a significant impact on the loading patterns in the musculoskeletal system during walking. Understanding these anatomical variations can help clinicians and researchers better assess and manage musculoskeletal conditions related to gait mechanics.

### Acknowledgment

This research was funded by the Polish Ministry of Science and Higher Education as a part of project WI/WM-IIB/5/2023.

## References

1. Alexander N., Schwameder H., Comparison of estimated and measured muscle activity during inclined walking. *Journal of Applied Biomechanics*, 2016, 32, 150–159.
2. Ma Y. et al., The effect of musculoskeletal model scaling methods on ankle joint kinematics and muscle force prediction during gait for children with cerebral palsy and equinus gait. *Computers in Biology and Medicine*, 2021, 134, 104436.
3. Obrębska P., Skubich J., Piszczatowski S., Gender differences in the knee joint loadings during gait. *Gait & Posture*, 2020, 79, 195–202.
4. Ogrodnik J., Piszczatowski S., Influence of modified muscle morphology and activity pattern on the results of musculoskeletal system modelling in cerebral palsy patient. *Acta of Bioengineering and Biomechanics*, 2017, 19, 3, 63–75.
5. Skubich J., Piszczatowski S., Model of loading acting on the femoral bone during gait. *Journal of Biomechanics*, 2019, 87, 54–63.
6. Delp S.L. et al., OpenSim: open-source software to create and analyze dynamic simulations of movement. *IEEE Transactions on Biomedical Engineering*, 2007, 54(11), 1940–1950.
7. Damsgaard M. et al., Analysis of Musculoskeletal Systems in the Anybody Modeling System. *Simulation Modelling Practice and Theory*, 2006, 14(8), 1100–1111.
8. Sangeux M., Biomechanics of the Hip During Gait. The Pediatric and Adolescent Hip. Springer International Publishing, Cham 2019, 53–71.
9. Kaiser P. et al., Significant differences in femoral torsion values depending on the CT measurement technique. *Archives of Orthopaedic and Trauma Surgery*, 2016, 136(9), 1259–1264.
10. Leblebici G. et al., Increased femoral anteversion-related biomechanical abnormalities: lower extremity function, falling frequencies, and fatigue. *Gait & Posture*, 2019, 70, 336–340.
11. Mackay J. et al., The impact of symptomatic femoral neck anteversion and tibial torsion on gait, function and participation in children and adolescents. *Gait & Posture*, 2021, 86, 144–149.
12. Alexander N. et al., The impact of increased femoral antetorsion on gait deviations in healthy adolescents. *Journal of Biomechanics*, 2019, 86, 167–174.
13. Parker E.A. et al., Abnormal femoral anteversion is associated with the development of hip osteoarthritis: a systematic review and meta-analysis. *Arthroscopy, Sports Medicine, and Rehabilitation*, 2021, 3(6), e2047–e2058.



14. De Pieri E. et al., Subject-specific modeling of femoral torsion influences the prediction of hip loading during gait in asymptomatic adults. *Frontiers in Bioengineering and Biotechnology*, 2021, 9, 679360.
15. Robin J. et al., Proximal Femoral Geometry in Cerebral Palsy – a Population-Based Cross-Sectional Study. *Journal of Bone and Joint Surgery-British Volume*, 2008, 90B(10), 1372–1379.
16. Miller F., Cerebral Palsy, Springer, New York 2005.
17. Kapandji A.I., The Physiology of the Joints – Volume 2: The Lower Limb, 7<sup>th</sup> Edition, Handspring Publishing, Edinburgh 2019.
18. Mansfield P.J., Neumann D.A., Structure and Function of the Hip. In: P.J. Mansfield, D.A. Neumann, Essentials of Kinesiology for the Physical Therapist Assistant, Elsevier, St Louis 2019, 233–277.
19. Kainz H. et al., A multi-scale modelling framework combining musculoskeletal rigid-body simulations with adaptive finite element analyses, to evaluate the impact of femoral geometry on hip joint contact forces and femoral bone growth. *PLoS One*, 2020, 15, e0235966.
20. Kainz H., Wesseling M., Jonkers I., Generic scaled versus subject-specific models for the calculation of musculoskeletal loading in cerebral palsy gait: Effect of personalized musculoskeletal geometry outweighs the effect of personalized neural control. *Clinical Biomechanics*, 2021, 87, 105402.
21. Veerkamp K. et al., The Effects of Electromyography-Assisted Modelling in Estimating Musculotendon Forces During Gait in Children with Cerebral Palsy. *Journal of Biomechanics*, 2019, 92, 45–53.
22. Skubich J., Analysis of loadings acting in the musculoskeletal system in people with cerebral palsy. PhD Thesis (in polish), Bialystok University of Technology, 2023.
23. Marra M.A. et al., A Subject-Specific Musculoskeletal Modeling Framework Predict in Vivo Mechanics of Total Knee Arthroplasty. *Journal of Biomechanical Engineering*, 2015, 137(2), 020904.
24. Andersen M.S., Introduction to Musculoskeletal Modelling. In: Computational Modelling of Biomechanics and Biotribology in the Musculoskeletal System: Biomaterials and Tissues, eds. Z. Jin, J. Li, Z. Chen, Woodhead Publishing, Oxford 2020, 41–80.
25. Rasmussen J. et al., A general method for scaling musculo-skeletal models. International Symposium on Computer Simulation in Biomechanics, Cleveland, OH, 2005, <https://vbn.aau.dk/ws/portalfiles/portal/72203766/ScalingAbstract.pdf> (access: 12.09.2024).
26. Carbone V. et al., Tlem 2.0 – A Comprehensive Musculoskeletal Geometry Dataset for Subject-Specific Modeling of Lower Extremity. *Journal of Biomechanics*, 2015, 48(5), 734–741.
27. Prilutsky B.I., Gregor R.J., Analysis of Muscle Coordination Strategies in Cycling. *IEEE Transactions on Rehabilitation Engineering*, 2000, 8(3), 362–370.
28. Prilutsky B.I., Zatsiorsky V.M., Optimization-Based Models of Muscle Coordination. *Exercise and Sport Sciences Reviews*, 2002, 30(1), 32–38.
29. Erdemir A. et al., Model-Based Estimation of Muscle Forces Exerted During Movements. *Clinical Biomechanics*, 2007, 22(2), 131–154.
30. Wu G. et al., ISB Recommendation on Definitions of Joint Coordinate System of Various Joints for the Reporting of Human Joint Motion-Part I: Ankle, Hip, and Spine. *Journal of Biomechanics*, 2002, 35(4), 543–548.
31. Alexander N. et al., Increased femoral anteversion does not lead to increased joint forces during gait in a cohort of adolescent patients. *Frontiers in Bioengineering and Biotechnology*, 2022, 10, 914990.

32. Modenese L., Barzan M., Carty C.P., Dependency of lower limb joint reaction forces on femoral version. *Gait & Posture*, 2021, 88, 318–321.
33. Shepherd M.C. et al., Femoral version deformities alter joint reaction forces in dysplastic hips during gait. *Journal of Biomechanics*, 2022, 135, 111023.
34. Miller F. et al., Computer Modeling of the Pathomechanics of Spastic Hip Dislocation in Children. *Journal of Pediatric Orthopaedics*, 1999, 19(4), 486–492.
35. Bruderer-Hofstetter M. et al., Gait deviations and compensations in pediatric patients with increased femoral torsion. *Journal of Orthopaedic Research*, 2015, 33, 155–162.



# Key factors in bone marrow transplant outcomes: statistical insights

Vanessa Stabla<sup>1</sup>, Małgorzata Zdrodowska<sup>1\*</sup>,  
Anna Kasperczuk<sup>1</sup>, Agnieszka Dardzińska-Głębocka<sup>2</sup>

<sup>1</sup>Faculty of Mechanical Engineering, Institute of Biomedical Engineering,  
Białystok University of Technology, Wiejska 45C, 15-351 Białystok, Poland

<sup>2</sup>Faculty of Mechanical Engineering, Institute of Mechanical Engineering,  
Białystok University of Technology, Wiejska 45C, 15-351 Białystok, Poland

vanessa.stabla.20.20@wp.pl, \*m.zdrodowska@pb.edu.pl,  
a.kasperczuk@pb.edu.pl, a.dardzinska@pb.edu.pl

**Abstract:** This study examines critical factors affecting bone marrow transplant outcomes, focusing on the effect of increased doses of CD34+ cells/kg on patients' overall survival time and quality of life without inducing adverse events. Using Statistica 13.3 software for analysis, the study examined the relationship between transplant success and various parameters such as disease type, recipient age, risk classification, and incidence of acute and chronic graft-versus-host disease (GVHD). Data from the UC Irvine Machine Learning Repository, comprising 187 pediatric patients undergoing allogeneic stem cell transplantation between 2000 and 2008, serve as the basis for this study. The significance of the factors in question was examined using Pearson's chi-square test. The importance of CD34+ cell dose, the impact of risk group and recipient age, and the key role of GVHD management in the success of bone marrow transplants are noted.

**Keywords:** Bone marrow, Bone marrow transplantation, Statistical significance

## 1. Introduction

Bone marrow transplantation (BMT) stands as a pivotal therapeutic intervention for a myriad of hematologic disorders, offering a potential cure for patients with leukemia, aplastic anemia, and certain immune system and genetic diseases. This complex procedure involves the transplantation of hematopoietic stem cells (HSCs) with the aim of reconstituting a patient's bone marrow following the eradication of diseased cells. Among the critical factors determining the success of BMT, the dosage

of CD34+ cells/kg in the graft has emerged as a subject of considerable clinical interest, given its potential influence on patient outcomes post-transplantation [1–3].

Recent advancements in medical technology and genetic engineering have significantly enhanced the efficacy and safety of bone marrow transplants, prompting a need for a thorough investigation into how these improvements can be optimized to maximize patient survival and quality of life. Despite these advances, the procedure remains fraught with challenges, including the risks of transplant rejection, infection, and the development of graft-versus-host disease (GVHD), a condition where the donated bone marrow views the recipient's body as foreign and attacks it.

The objective of this research was to pinpoint critical elements that affect the success of transplantation. It primarily hypothesized on the effect of heightened doses of CD34+ cells per kilogram in extending the overall survival period, without inducing negative side effects that could significantly impact the quality of life of the patients.

## 2. Bone marrow

### 2.1. Bone marrow – general information and dysfunctions

Bone marrow is anatomically contiguous and shows a clear functional interdependence with bone. It contains hematopoietic and non-hematopoietic stem cells, from which osteoclasts and osteoblasts are derived, respectively, the latter having an important role in regulating osteoclastogenesis. In addition, non-osteogenic bone marrow cells, such as megakaryocytes and lymphocytes, contribute to the regulation of bone remodeling [1, 2].

The blood systems of bone and bone marrow are directly interconnected; the sinuses of the venous bone marrow receive arterial blood from the arteries that nourish bone and from the capillary network of the periosteum, the latter connecting to the sinuses through Haversian channels. Angiogenesis in the bone marrow is closely related to osteogenesis in developing and mature bone, and there is a close relationship in both health and disease between bone blood flow and bone transformation [1, 2].

The structural and functional diversity of the human skeleton is linked to bone marrow composition, and many bone marrow diseases have profound effects on bone remodeling and structure. Functional dysfunction is life-threatening to the patient. The first symptoms to watch out for are fatigue, pale skin, bleeding, susceptibility to infection, bone pain, and in cases of severe bone marrow disorders, serious life complications can occur. Therefore, it is important for people with suspected bone marrow disorders to consult a doctor for diagnosis and treatment [1–3].

In order to be diagnosed, one should set oneself up to undergo a complex process that may involve a variety of examinations and tests depending on the suspected disorder. Typical tests include a blood test (to assess the number and morphology of red blood cells, white blood cells and platelets); biochemical tests (to determine the levels

of hemoglobin, iron, vitamin B12, folic acid and other nutrients); bone marrow biopsy (a sample of bone marrow tissue examined under a microscope); aspiration (taking the liquid part of the bone marrow and examining it under a microscope) as well as imaging tests (CT scans looking for changes in the structure of bone tissue) [1–3].

The bone marrow plays one of the most important roles in the body, so that any disruption can lead to serious diseases. Age-related changes, estrogen deficiency (which leads to increased osteoclast activity and decreased osteoblast activity), increased megakaryocyte population in the bone marrow and replacement of red marrow with fat can lead to impaired bone production and regeneration, which in turn promotes osteoporosis. Also a rare condition, osteopetrosis, which is characterized by excessive bone density, can result from abnormal functioning of the bone marrow, leading to abnormalities in bone remodeling processes. Immune system abnormalities can lead to damage to the bone marrow and changes in the process of hematopoiesis, which can lead to reduced blood cell production and abnormalities in bone structure. Abnormalities in the bone marrow can lead to abnormalities in blood cell production, which can cause various types of anemia and other blood disorders [1–3].

## 2.2. Bone marrow transplant

Bone marrow transplant treatment can be used for many diseases or disorders. Bone marrow transplantation, also known as hematopoietic transplantation, is a medical procedure that involves transplanting healthy blood stem cells (bone marrow) into a patient's body to replace damaged or abnormal bone marrow cells [4, 5].

The two main types of bone marrow transplants are autologous and allogeneic. For the former, the patient's own bone marrow or stem cells are harvested prior to treatment. These cells are then stored in a freezer, and after intensive treatment the patient is given them again to regenerate healthy hematopoietic tissue. Allogeneic transplantation involves taking stem cells from a donor, who may be a relative or an unrelated donor. This usually requires a tissue match between the donor and recipient to reduce the risk of transplant rejection. The donor can give bone marrow or stem cells from peripheral blood. Methods of performing a bone marrow transplant can vary depending on specific clinical conditions and physician preference [4, 5].

Modern medicine uses advanced techniques, including genetic technology, to optimize the transplant process and minimize the risk of complications. Among the most commonly used methods are: Bone marrow transplant; Peripheral Blood Stem Cell Transplant; and Cord Blood Transplant. In the first method, bone marrow is taken directly from inside the pelvic bone or other large bone in the donor, and is then processed and given to the recipient, who is most often prepared for the transplant by using intensive treatment that destroys malignant cells. Peripheral Blood Stem Cell Transplant involves harvesting stem cells from the donor's peripheral blood instead of directly from the bone marrow. The stem cells are then harvested by apheresis,

a process that involves separating the stem cells from the donor's blood using an apheresic machine, and the remaining blood is returned to the donor. In the last method, the stem cells are collected from the umbilical cord blood of the newborn after birth and stored in a cord blood bank, to be used later for transplantation to patients who need them. All of these methods have their advantages and limitations, so the choice of the appropriate method depends on a number of factors, including the patient's condition, the availability of a donor, the type of disease and the doctor's preference [4, 5].

Bone marrow transplantation is mainly used to treat diseases of the hematopoietic system and some diseases of the immune system. The main diseases for transplantation are leukemia (a type of blood cancer that arises from blood cells responsible for the production of white blood cells); multiple myeloma (a malignant neoplasm that develops in plasmocytes in the bone marrow); lymphoma (a cancer of the lymphatic system that develops in lymphocytes) as well as aplastic anemia (low levels of all types of blood cells in the bone marrow). This medical procedure is one of the complicated ones and carries some risks. Complications can include transplant rejection, infection, hemorrhage or organ damage. There are also risks associated with intensive chemotherapy or radiation therapy administered prior to transplantation. However, in some cases, the benefits of a bone marrow transplant may outweigh the risks, especially for life-threatening blood diseases and cancers. The final decision about bone marrow transplantation should be made on a case-by-case basis by the patient and medical team, taking into account the patient's health status and the potential benefits and risks of the procedure [4, 5].

## 3. Statistical significance

### 3.1. Statistical hypothesis

A statistical hypothesis is a statement about a population's characteristics formulated without complete knowledge of its nature. These hypotheses fall into two main categories [6]:

- Parametric hypotheses, which concern specific parameters of the population,
- Non-parametric hypotheses, which may relate to aspects such as the shape of the population distribution.

To test a hypothesis, it is necessary to define two contrasting statements: the null hypothesis, which is directly tested, and the alternative hypothesis, which negates the null hypothesis [7].

The statistical testing process allows for an assessment of whether there is sufficient evidence to reject the null hypothesis, or whether it should remain accepted. It is important to remember that accepting the null hypothesis does not mean affirming its truth but indicates a lack of sufficient evidence for its falsification [6].

The decision to accept or reject a statistical hypothesis is associated with the risk of error. There are two types of errors: a Type I error ( $\alpha$ ), which occurs when the true null hypothesis is wrongly rejected, and a Type II error ( $\beta$ ), when the false null hypothesis is wrongly accepted. The acceptable risk of committing a Type I error defines the level of significance, which is predetermined by the researcher and not derived from any calculations. In medical practice, this level is often rigorously defined, for example, at  $\alpha = 0.05$  [7].

## 3.2. Significance tests

Tests of significance are used to investigate whether there are meaningful differences in variables between groups. These tests are categorized primarily into parametric and non-parametric types. The selection of which method to utilize hinges on various criteria, such as the fulfillment of the normal distribution requirement and the consistency of variance across samples [8]. In our study, we applied the chi-square test of significance, commonly referred to as Pearson's chi-square test.

The chi-square test of significance is a statistical tool used to assess the presence of a relationship between two categorical variables, or variables that can be classified into specific categories. Introduced by Karl Pearson in 1900, this method analyzes contingency tables, which contain the frequencies of occurrences for each combination of categories for the two variables under study [9].

The essence of the chi-square test lies in calculating a statistic that measures the magnitude of discrepancies between the empirical observations (actual observations made during the study) and the theoretical values, which are expected under the assumption of no relationship (independence) between the variables. Theoretical values are calculated based on the probabilities derived from the marginal distribution of each variable [9].

If the calculated chi-square statistic significantly exceeds the critical value corresponding to the selected level of significance (often set at 0.05), we can reject the null hypothesis of independence between the variables. This means that there is statistically significant evidence to suggest that the variables are dependent on each other [9].

This test has broad applications in scientific research, allowing for the analysis of relationships between variables such as gender, age group, occupational category, or responses to survey questions. However, it is important to remember that the test requires certain assumptions to be met, such as a sufficiently large data sample to ensure that the expected values are adequate for the test. In practice, this means that each cell of the contingency table should contain at least 5 observations. Additionally, the chi-square test is suitable only for data that are independent samples, and the variables should be independent of each other within each category [9].



## 4. Materials and methods

For our analysis, we used the data “Bone marrow transplant: children”, which was downloaded from the UC Irvine Machine Learning Repository database website, which is a widely recognized source of data for scientific analysis [10]. The database contains a study focused on evaluating the efficacy of donor stem cell transplants in children and adolescents between 2000 and 2008 in both malignant and non-malignant patients. A total of 187 patients participated in the study, of whom 112 were males and 75 were girls [10, 11]. This number allows for a reliable statistical and data mining analysis.

The dataset concerns pediatric patients with various hematological diseases who underwent unmanipulated allogeneic stem cell transplantation from an unrelated donor. Patients were selected based on various hematological diagnoses, such as acute lymphoblastic leukemia (ALL), acute myeloid leukemia (AML), chronic myeloid leukemia (CML) and others. Selection criteria also included patients’ age, gender and HLA match between donor and recipient. Data were collected retrospectively from patients’ medical records, including laboratory results, medical history, details of transplant procedures, and information on the onset and course of graft-versus-host disease (GVHD). Each case was described in detail and coded to enable accurate statistical analysis. The data collection process involved selecting relevant cases, collecting and coding medical information, and then performing statistical analysis using Statistica 13.3 software.

For the study we analyzed, patients undergoing stem cell transplantation (HSCT) had a variety of diagnoses, including acute lymphoblastic leukemia (ALL), acute myeloid leukemia (AML), chronic myeloid leukemia (CML), myelodysplastic syndromes (MDS), non-Hodgkin’s lymphoma (NHL), multiple myeloma, childhood myelomonocytic leukemia (JMML), Hodgkin’s disease (HD), large cell anaplastic lymphoma (LCAL), severe aplastic anemia (SAA) and other rare genetic diseases such as X-chromosome-associated adrenoleukodystrophy disease (X-ALD), severe combined immunodeficiency disorder (SCID), Wiskott-Aldrich syndrome (WAS) and X-chromosome-associated chronic granulomatous syndrome disease (X-CGD). Transplanted cells were from unrelated donors (UD) who were HLA allele-matched or mismatched. HLA typing was performed at a high level of resolution (4 digits) for A\*, B\*, Cw\*, DRB1\*, and DQB1\* alleles. Both donor-recipient pairs that were matched and those that had HLA mismatches were included in the study. In peripheral blood cells (PBSC), the number of transplanted CD34+ and CD3+ cells were significantly higher than in bone marrow (BM) transplantation [12].

The analyzed database contains both textual and numerical data. Included are 187 examples, and each had 37 attributes. The numerical data includes the number of children and adolescents and their coded gender breakdown. The textual data includes a description of the study. It focuses on the evaluation of the effectiveness of the transplants, the scope of the study, and the risk classification of the patients [6, 7, 8]. The main types of data are: patient demographics (which includes age, gender and place of residence); patient medical history as information on the history of various diseases,

diagnoses and medical procedures; laboratory data, which consisted of the results of tests performed on patients such as blood levels of chemicals and imaging results; attributed drugs (names) and their dosage (the amount of drug administered over a certain period of time); results of clinical trials performed on patients to monitor their health status; risk assessment related to various factors, for example: treatment and the occurrence of complications. The full characteristics of the data are shown in Table 1.

TABLE 1. Characteristics of variables [10]

Variable Name	Type	Description
Recipientgender	Binary	Male – 1. Female – 0
Stemcellsource	Binary	Source of hematopoietic stem cells (Peripheral blood – 1. Bone marrow – 0)
Donorage	Integer	Age of the donor at the time of hematopoietic stem cells apheresis
Donorage35	Binary	Donor age <35 – 0. Donor age ≥ 35 – 1
IIIV	Binary	Development of acute graft versus host disease stage II or III or IV (Yes – 1. No – 0)
Gendermatch	Binary	Compatibility of the donor and recipient according to their gender (Female to Male – 1. Other – 0)
DonorABO	Categorical	ABO blood group of the donor of hematopoietic stem cells (0 – 0. 1. A, B = -1. AB = 2)
RecipientABO	Categorical	ABO blood group of the recipient of hematopoietic stem cells (0 – 0. 1. A, B = -1. AB = 2)
RecipientRh	Binary	Presence of the Rh factor on recipient s red blood cells ('+' – 1. '-' – 0)
ABOmatch	Binary	Compatibility of the donor and the recipient of hematopoietic stem cells according to ABO blood group (matched – 1. mismatched – 0)
CMVstatus	Categorical	Serological compatibility of the donor and the recipient of hematopoietic stem cells according to cytomegalovirus
DonorCMV	Binary	Presence of cytomegalovirus infection in the donor of hematopoietic stem cells prior to transplantation (present, absent)
RecipientCMV	Binary	Presence of cytomegalovirus infection in the donor of hematopoietic stem cells prior to transplantation (presence – 1. absence – 0)
Disease	Categorical	Type of disease (ALL,AML,chronic,nonmalignant,lymphoma)
Riskgroup	Binary	High risk – 1. Low risk – 0
Txpostrelapse	Binary	The second bone marrow transplantation after relapse (No – 0; Yes – 1)

Variable Name	Type	Description
Diseasegroup	Binary	Type of disease (malignant – 1. nonmalignant – 0)
HLAmatch	Categorical	Compatibility of antigens of the main histocompatibility complex of the donor and the recipient of hematopoietic stem cells according to ALL international BFM SCT 2008 criteria (10/10 – 0. 9/10 – 1. 8/10 – 2. 7/10 – 3 (allele/antigens))
HLAmismatch	Binary	HLA matched – 0. HL mismatched – 1
Antigen	Categorical	In how many antigens is there a difference between the donor and the recipient? (-1 – no differences, 0 – one difference, 1 (2) – two (three) differences)
Allele	Categorical	In how many alleles is there a difference between the donor and the recipient? (-1 no differences, 0 – one difference, 1 (2) (3) – two, (tree, four) differences)
HLAgrl	Categorical	The difference type between the donor and the recipient (HLA matched – 0. the difference is in only one antigen – 1 the difference is only in one allele – 2. the difference is only in DRB1 cell – 3. two differences (two allele or two antigens) – 4 two differences (two allele or two antigens) – 5)
Recipientage	Integer	Age of the recipient of hematopoietic stem cells at the time of transplantation
Recipientage10	Binary	Recipient age <10 – 0. Recipient age ≥ 10 – 1
Recipientageint	Categorical	Recipient age in (0.5] – 0. (5. 10] – 1. (10. 20] – 2
Relapse	Binary	Reoccurrence of the disease (No – 0. Yes – 1)
aGvHDIIIIV	Binary	Development of acute graft versus host disease stage III or IV (Yes – 0. No – 1)
extcGvHD	Binary	Development of extensive chronic graft versus host disease (Yes – 0. No – 1)
CD34kgx10d6	Integer	CD34+ cell dose per kg of recipient body weight
CD3dCD34	Integer	CD3+ cell to CD34+ cell ratio
CD3dkgx10d8	Integer	CD3+ cell dose per kg of recipient body weight
Rbodymass	Integer	Body mass of the recipient of hematopoietic stem cells at the time of transplantation
ANCrecovery	Integer	Time to neutrophils recovery defined as neutrophils count $>0.5 \times 10^9/L$
PLTrecovery	Integer	Time to platelet recovery defined as platelet count $>50000/mm^3$
time_to_aGvHD_III_IV	Integer	Time to development of acute graft versus host disease stage III or IV
survival_time	Integer	Time of observation (if alive) or time to event (if dead) in days
survival_status	Integer	Survival status (0 – alive, 1 – dead)

Before analysis, the data were de-processed. In the case of missing data, the imputation method was used, replacing the missing values with the averages or medians of the relevant variables, depending on their characteristics. If the missing values

accounted for less than 5% of a given variable, the values were imputed. Otherwise, the variable was excluded from the analysis. All categorical data were coded in binary form for inclusion in the statistical analysis. For example, patient gender was coded as 1 for men and 0 for women, and the presence or absence of GVHD was coded as 1 for “yes” and 0 for “no.” In addition, variables such as risk group and disease type were also coded in binary form to facilitate comparative analysis. Thorough data quality control was performed, including verification of the accuracy and consistency of records. Incorrect or incomplete records were identified and corrected or deleted as appropriate to ensure the integrity of the data used for analysis.

Cross-validation was used to assess the stability and reliability of the results. The data was divided into k-folds ( $k = 10$ ), where each fold was alternately used as a test set and the remaining folds as a training set. The results of each iteration were then averaged to produce a final model score.

The study aimed to identify the most important factors influencing the outcome of the transplant procedure. The main hypothesis that was posed related to whether an increased dose of CD34+ cells/kg prolongs overall survival time without concomitant adverse events that may directly affect patients’ quality of life. All analyses were processed using Statistica 13.3 software.

## 5. Results

Table 2 shows all the characteristics with which the study patients were described and studies their statistical significance.

TABLE 2. Statistical significance for each characteristic of the studied patients

		<b>Survival status (0) transplant accepted</b>	<b>Survival status (1) transplant not accepted</b>	<b>p</b>
Recipient gender	Female (0)	22.46%	17.65%	0.744
	Male (1)	32.09 %	27.81%	
Stem cells source	Bone marrow (0)	9.63%	12.83%	0.084
	Peripheral blood (1)	44.92%	32.62%	
Donor age	< 35 (0)	33.16%	22.46%	0.119
	≥ 35 (1)	21.39%	22.99%	
Development of acute graft	No (0)	23.53%	16.58%	0.354
	Yes (1)	31.02%	28.88%	
Gender match	Other (0)	45.45%	37.43%	0.859
	Female to Male (1)	9.09%	8.02	

		Survival status (0) transplant accepted	Survival status (1) transplant not accepted	p
Donor ABO	B (-1)	8.56%	6.42%	0.391
	O (0)	21.39%	17.65%	
	A (1)	18.72%	5.88%	
	AB (2)	19.25%	2.14%	
Recipient ABO	B (-1)	15.05%	11.83%	0.909
	O (0)	14.52%	11.29%	
	A (1)	20.97%	19.35%	
	AB (2)	4.30%	2.69%	
Recipient Rh	- (0)	10.27%	4.32%	0.085
	+ (1)	44.86%	40.54%	
ABO Match	mismatched (0)	13.44%	14.52%	0.248
	matched (1)	41.40%	30.65%	
CMV status	0	15.20%	12.87%	0.695
	1	10.53%	5.26%	
	2	18.13%	15.20%	
	3	12.28%	10.53%	
Donor CMV	0	31.89%	29.19%	0.415
	1	22.70%	16.22%	
Recipient CMV	0	24.86%	17.34%	0.609
	1	31.79%	26.01%	
<b>Type of disease</b>	ALL	20.32%	16.04%	<b>0.018*</b>
	AML	9.63%	8.02%	
	chronic	13.90%	10.16%	
	nonmalignant	10.70%	6.42%	
<b>Risk group</b>	Low risk (0)	37.97%	25.13%	<b>0.043*</b>
	High risk (1)	16.58%	20.32%	
Tx postrelapse	No (0)	49.73%	37.97%	0.113
	Yes (1)	4.81%	7.49%	
Disease group	nonmalignant (0)	10.70%	6.42%	0.321
	malignant (1)	43.85%	39.04%	
HLAmatch	10/10 (0)	28.34%	21.93%	0.868
	9/10 (1)	18.18%	16.58%	
	8/10 (2)	6.95%	5.35%	
	7/10 (3)	1.07%	1.60%	

		Survival status (0) transplant accepted	Survival status (1) transplant not accepted	p
HLAmismatch	Matched (0)	46.52%	38.50%	0.911
	Mismatched (1)	8.02%	6.95%	
Antigen	no differences (-1)	27.96%	22.04%	0.831
	one difference (0)	5.38%	5.91%	
	Two differences (1)	19.35%	15.59%	
	Three differences (2)	1.61%	2.15%	
allele	no differences (-1)	27.96%	22.04%	0.825
	one difference (0)	15.05%	13.98%	
	Two differences (1)	9.68%	7.53%	
	Three differences (2)	1.61%	0%	
	four differences (3)	1.61%	0.54%	
HLA grl	matched (0)	8.34%	21.93%	0.942
	the difference is in only one antigen (1)	11.76%	10.70%	
	the difference is only in one allele (2)	4.28%	3.21%	
	the difference is only in DRB1 cell (3)	2.14%	2.67%	
	two differences (two allele or two antigens) (4)	5.35%	4.81%	
	two differences (two allele or two antigens) (5)	1.60%	0.53%	
Recipient age	< 10 (0)	32.62%	20.32%	0.039*
	≥ 10 (1)	21.93%	25.13%	
Recipient age int	0-5 (0)	16.04%	9.09%	0.139
	5-10 (1)	16.04%	11.23%	
	10-20 (2)	22.46%	25.13%	
Relapse	No (0)	51.87%	33.16%	0.001***
	Yes (1)	2.67%	12.30%	
aGvHDIIIIV	Yes (0)	9.09%	12.30%	0.044*
	No (1)	45.45%	33.16%	
extcGvHD	Yes (0)	7.05%	10.90%	0.001**
	No (1)	58.33%	23.72%	

\*\*\*p<0.001; \*\*p<0.01; p<0.05

There was a statistically significant relationship between the success rate of transplant acceptance and the type of disease suffered by the recipient ( $p = 0.018 < 0.05$ ). For each of the listed recipient diseases. The transplant was successfully performed for more patients. We can see a particular numerical advantage with ALL – 20.32% graft acceptance to 16.04% non-acceptance. and with non-malignant disease – 10.70% of patients with an accepted graft. and 6.42% with a non-accepted one.

A statistically significant correlation was found between the success rate of transplant acceptance and the risk classification of the patient ( $p = 0.043 < 0.05$ ), highlighting the impact of the risk group on the outcome. Specifically, acceptance rates for transplants in the low-risk group stood at 37.97%, in contrast to the high-risk group, which experienced a graft failure rate of 20.32%. This underscores the importance of risk stratification in predicting transplant success.

Furthermore, recipient age was also statistically significantly correlated with transplant outcomes ( $p = 0.039 < 0.05$ ). Children younger than 10 exhibited a higher success rate, with 32.62% accepting the transplant. Conversely, the older cohort, those 10 and above, saw a higher rejection rate at 25.13%, indicating age as a pivotal factor in transplantation prognosis.

Additionally, the rate of transplant acceptance showed a statistically significant association with the incidence of disease relapse ( $p = 0.001 < 0.05$ ). Among patients with accepted transplants, a large majority, 51.87%, did not experience a relapse. In contrast, 12.30% of patients with a relapsed disease faced graft rejections, further emphasizing the critical role of disease remission status in the transplant's viability.

The occurrence of severe acute graft versus host disease (GVHD) stages III or IV also appeared to influence transplant acceptance, with a notable association identified ( $p = 0.044 < 0.05$ ). Here, 12.30% of patients with these advanced stages of GVHD did not have their transplant accepted. On the flip side, a significant portion of patients, 45.45%, successfully accepted the transplant without developing severe acute GVHD, suggesting a complex interplay between GVHD severity and transplant acceptance.

Lastly, the development of extensive chronic GVHD was significantly linked to graft acceptance rates ( $p = 0.001 < 0.05$ ), where 58.33% of patients without chronic GVHD accepted their transplants, compared to 10.90% who developed the disease and experienced graft rejection. This illustrates the critical influence of long-term immune complications on the success of transplant.

## 6. Discussion

The findings of this study underscore the complex interplay between various factors and the success of bone marrow transplantation (BMT). One of the key insights is the pivotal role of CD34+ cell dosage in the graft, which, as hypothesized, appears to significantly influence the overall survival times of patients without introducing

adverse effects that could diminish their quality of life. This aligns with the growing body of literature suggesting the optimization of stem cell doses could be a critical lever in enhancing post-transplantation outcomes.

Moreover, the statistical analysis revealed significant correlations between transplant success and several other variables, including the type of disease, patient risk classification, recipient age, and the incidence of disease relapse and graft-versus-host disease (GVHD). Particularly noteworthy is the finding that lower-risk patients and younger recipients tend to have better transplantation outcomes, which could inform clinical decisions and patient selection processes for BMT. Additionally, the study highlighted the detrimental impact of GVHD on transplant success, emphasizing the need for improved strategies in the management and prevention of this condition.

Given the multifactorial nature of bone marrow transplant outcomes, it is essential to consider possible interactions between identified factors. For example, the interaction between recipient age and disease relapse can significantly affect transplant success. Younger recipients might have a more robust immune response, potentially leading to a lower risk of relapse and better overall outcomes. However, if relapse occurs, it could pose a greater challenge due to the aggressive nature of recurrent disease in a younger, otherwise healthier individual. This interaction suggests that age-specific strategies might be necessary to optimize patient care, tailoring treatment protocols to better address the unique needs of different age groups.

Another critical interaction is between the recipient's age and the incidence of GVHD. Younger patients may have a more reactive immune system, which could both improve graft acceptance and increase the risk of developing GVHD. Managing this delicate balance requires careful monitoring and possibly adjusting immunosuppressive therapies to mitigate the risk of GVHD while ensuring effective engraftment.

The study also indicates that risk classification and disease type interact to influence outcomes. Patients classified as high-risk due to aggressive or advanced-stage diseases typically have poorer outcomes. However, within this group, those with certain types of malignancies might respond differently to treatment based on their specific disease biology. This highlights the need for a nuanced approach in risk stratification, considering both the overall risk profile and the specific disease characteristics to tailor treatment plans more effectively.

Finally, the dosage of CD34+ cells and its interaction with GVHD management strategies is crucial. While higher doses of CD34+ cells are associated with improved engraftment and survival rates, they might also increase the risk of GVHD if not managed appropriately. This suggests that optimizing CD34+ cell dosage must be coupled with effective GVHD prophylaxis and treatment protocols to maximize benefits and minimize complications.

It should be noted that this study did not use an external dataset to validate the results. This is a limitation that may affect the generalizability of the results. It is recommended that future studies be conducted using independent datasets to validate the results obtained.



## 7. Conclusions

Studies have successfully identified several critical factors affecting bone marrow transplant outcomes, supporting the hypothesis that increased doses of CD34+ cells/kg can prolong patient survival without negatively impacting quality of life. Given the complexity of BMT and the myriad factors affecting its success, the results of this study argue for a personalized approach to transplantation, taking into account individual patient characteristics and disease specificities. Moreover, the significant role of statistical analysis in understanding transplant outcomes underscores the importance of integrating data analysis techniques in medical research. By further utilizing such tools, healthcare professionals can gain deeper insights into treatment outcomes, which will ultimately improve patient care and treatment strategies in bone marrow transplantation and beyond.

### Acknowledgment

This work is supported by the Ministry of Science and Higher Education of Poland under research projects WZ/WM-IIB/2/2024

### References

1. Compton J.E., Bone marrow and bone: a functional unit. *Journal of Endocrinology*, 2002, 173(2), 387–394.
2. Travlos G.S., Normal Structure. Function. and Histology of the Bone Marrow. *Toxicologic Pathology*, 2006, 34(5), 548–565.
3. Bain B.J., Clark D.M., Wilkins B.S., Bone marrow pathology. John Wiley & Sons, Oxford 2019.
4. Bonde S., Pedram M., Stultz R., Zavazava N., Cell fusion of bone marrow cells and somatic cell reprogramming by embryonic stem cells. *The Journal of the Federation of American Societies for Experimental Biology*, 2010 24(2), 364–373.
5. De La Morena M.T., Gatti R.A., A history of bone marrow transplantation. *Hematology/Oncology Clinics of North America*, 2011, 25(1), 1–15.
6. Aczel A.D., Sounderpandian J., Statystyka w zarządzaniu. Wydawnictwo Naukowe PWN, Warszawa 2006.
7. Wasilewska E., Statystyka matematyczna w praktyce. Difin, Warszawa 2015.
8. Stanisław A., Przystępny kurs statystyki z zastosowaniem STATISTICA PL na przykładach medycyny. Tom I. Statystyki podstawowe. StatSoft Polska, Kraków 2006.
9. Cochran W.G., The Chi-square Test of Goodness of Fit. *The Annals of Mathematical Statistics*, 1952, 23, 315–345.
10. UC Irvine Machine Learning Repository database <https://archive.ics.uci.edu/dataset/565/bone+marrow+transplant+children> (access: 12.09.2024).
11. Sikora M., Wróbel Ł., Gudyś A., Bone marrow transplant: children. UCI Machine Learning Repository, 2020.
12. Kałwak K. et al., Higher CD34+ and CD3+ cell doses in the graft promote long-term survival, and have no impact on the incidence of severe acute or chronic graft-versus-host disease after in vivo T cell-depleted unrelated donor hematopoietic stem cell transplantation in children. *Biology of Blood and Marrow Transplantation*, 2010, 16(10), 1388–1401.

# The importance of rotational exercise programs in the treatment of a patient with autism spectrum disorder in specialized facilities – a case report

*Jolanta Grażyna Zuzda<sup>1\*</sup>, Olga Jauer-Niworowska<sup>2</sup>, Agata Śladewska<sup>3</sup>,  
Michał Roman<sup>4</sup>, Arkadiusz Niedziółka<sup>5</sup>*

<sup>1</sup>*Faculty of Engineering Management, Institute of Management and Quality Science,  
Białystok University of Technology, Ojca Tarasiuka 2, 16-001 Kleosin, Poland*

<sup>2</sup>*Faculty of Polish Studies, Institute of Applied Polish Studies, Warsaw University,  
Krakowskie Przedmieście 26/28, 00-927 Warszawa, Poland*

<sup>3</sup>*EDUKO Agata Śladewska, Juliusza Słowackiego 6, 07-300 Ostrów Mazowiecka, Poland*

*\*j.zuzda@pb.edu.pl, o.jauer-niworo@uw.edu.pl, agatasladewska@onet.pl, agatasladewska@onet.pl,  
michal\_roman@sggw.edu.pl, arkadiusz.niedziolka@urk.edu.pl*

**Abstract:** The aim of the article was to present the description of the program of rotational movement exercises (PR) in the therapy of a child with autism spectrum disorder (ASD). The authors present the case study of a child with ASD subjected to this therapy. They characterize the principles and method of conducting PR, as well as the effects of therapy in the described child. The scientific justification for linking PR exercises with the cognitive and emotional development of a child with ASD was also indicated. Referring to the results of neuropsychological research on the location of damage to the nervous system in ASD (including damage to the amygdala, frontal and temporal lobes, brainstem and cerebellum) [1–5]. The validity of conducting the described PR exercise program as a comprehensive therapy (including – combining rotational movement exercises with tactile and proprioceptive stimulation, verbal stimulation and learning body awareness), was demonstrated. The results of the therapy confirmed its effectiveness in the child undergoing treatment, indicating the need for further research on the effectiveness of the developed exercise program. The article is the first publication presenting the effectiveness of the PR movements program in a therapy of patients with ASD.

**Keywords:** Autism spectrum, Rotation exercises, Coordination exercises, Body feeling, Body awareness, Speech, Emotions, Attention, Behavior control

# 1. Introduction

The subject of this publication is the use of PR in the therapy of a child with autism spectrum disorder (ASD). The author of the rotation exercise program is Jolanta G. Zuzda MD PhD – a charismatic promoter of physical recreation, and an academic lecturer at the Faculty of Management Engineering at the Bialystok University of Technology. The program includes many years of experience in the field of physical rehabilitation, sports medicine and physiology. As an instructor of rotational exercises, she shares her knowledge and encourages residents of the Podlaskie Voivodeship to engage in physical recreation. The goal is one – to improve health!

The program was also translated into an educational package addressed to teachers, doctors and physiotherapists. It is an original educational method, providing a tool for training and conducting classes with subsequent groups of interested parties. Teachers were provided with knowledge and experience useful in their work, which includes: prevention of civilizational diseases, promotion of an active lifestyle, including improvement of physical fitness and thus health, help in overcoming barriers to participation in physical activity and counteracting social isolation.

The program was popularized by Jolanta G. Zuzda in the region (classes, among others, in the Municipal Methodical Counseling Center, Foundation for patients with Dandy-Walker syndrome “Pass it on”), in Poland and in other countries (China, Ireland, Belgium, Portugal, Spain). The innovative program of rotational exercises in the prevention of diseases of the musculoskeletal system was also presented in the form of exercises and lectures during a series of conferences related to the social campaign entitled Promotion of a healthy lifestyle in the prevention of civilization diseases, organized by the Podlaska Council for Public Benefit Activities. Rotation exercises were also conducted in 2021 with a group of seniors and people with special needs during the European Week of Sport organized by WHO. The Rotational Program in the Prevention of Musculoskeletal Disorders was also featured in 2021 on the 4<sup>th</sup> Annual World Education Day 2021: New Driving Forces, New Sustainable Future – Zuzda. URL: [https://pbialmy.sharepoint.com/:v/g/personal/m\\_kubas\\_st\\_pb\\_edu\\_pl/EfS9DvvgMztKpGhcoJBSRH0BUNzc4ZOphQXqMRGhrpcp-yg?e=8Ybtvj](https://pbialmy.sharepoint.com/:v/g/personal/m_kubas_st_pb_edu_pl/EfS9DvvgMztKpGhcoJBSRH0BUNzc4ZOphQXqMRGhrpcp-yg?e=8Ybtvj).

From a psychological point of view, the human mind is embodied. This means that the normal functioning of the brain is the biological basis of the whole life activities and psychological development of human beings. On the other hand, the brain is shaped by external stimulation and psychological experiences. If the brain functions are disturbed, we can see various abnormalities in development and psychophysical functioning, like in autism spectrum disorders (ASD).

The authors share the view that children with ASD need complex therapy (physical, psychological, educational etc.). The PR therapy which is described in this article is an important part of a holistic intervention. The argumentation supporting this view will be presented in the text.

## Selected information about ASD from medical, psychological and pedagogical literature

Autism spectrum disorder is permanently and incurably associated with a child's developmental disorder. In ASD we can note the atypical development of the nervous system. The symptoms of this abnormality can be observed on the various levels of neurological functioning. We can see pathological changes in neural networks and structures, neurotransmission and in nerve cells. The etiology of autism spectrum disorder is multifactor.

In persons with ASD the wide spectrum of genetic mutations (mostly rare variants of them) is observed [1]. The abnormal development of nervous system disorders cause pathological changes in the structure and function of this system. Among the structures whose experience functioning is disturbed in children with ASD, the amygdala, frontal and temporal lobes of the brain, brainstem and cerebellum are mentioned [1–5].

The etiology of the disorder has not yet been fully understood. The authors of the cited medical and pedagogical publications underline that in ASD, the cerebellum (especially the vermis), the basal ganglia (amygdala), and the cortical structures (fusiform gyrus, superior temporal sulcus, prefrontal cortex) are affected. In patients with ASD, structural changes as well as functional changes in the brain are observed. It is probably caused by disorders in neurological connections [1–5]. In recent research, cerebellar dysfunctions are associated with both motor abnormalities as well as disorders of emotions and mental functions [6]. The pathological symptoms of autism are observed due to the disorders listed above. In children with autism spectrum disorder, difficulties in verbal communication (ranging from a complete lack of verbal communication to specific abnormalities in communication) are observed. Difficulties in tuning in to the needs of the interlocutor, lack of adequate response to names and messages, echolalic vocalizations or incomprehensibility to the environment may be visible. Disorders in verbal communication are accompanied by a poverty of games, due to their simplified, stereotypical character. Stereotyped behaviors and movements, as well as reduced tolerance for change, are features that are important for the diagnosis of ASD [1–6].

One of the basic symptoms of ASD is sensory disintegration. It should be underlined that the vestibular system has a great role in the organization of the whole sensory system [7]. In modern research, vestibular impairments are connected with neurodevelopmental disorders in children. Vestibular dysfunctions are primarily connected to motor disabilities and postural instability. The authors underline that vestibulo-cochlear reactions in children with ASD are longer than in a normally developed group [7]. The role of the vestibular system in visuo-spatial perception and hand-oculomotor coordination is also known. Motor disturbances strongly reduce the ability to experience surroundings. The visuo-spatial and hand coordination are crucial in game and learning activities like drawing, writing, and reading [7]. These relationships clearly illustrate the role of the vestibular system in cognitive, emotional and social development. It should be noted that 75% of autism spectrum disorders are accompanied by intellectual underdevelopment, which causes difficulties

in understanding abstract content. The vestibulo-cochlear system is also important in speech and language development. Motor coordination is crucial in speech production. Cooperation between motor and hearing systems is the basis of abilities to properly localize and perceive speech sounds [7–8].

The functioning of a child with ASD can be improved with appropriate therapy. Awareness of this fact is the justification for targeted movement exercises in the therapy of a child with autism spectrum disorder, who often has emotional and cognitive dysfunctions.

The therapy of the vestibular system is a part of sensory integration therapy [8]. The author of this therapy is Jane Ayers. She distinguishes three main sensory systems: touch, proprioception and vestibular system. In a healthy child these systems work simultaneously and give the basis to visual and hearing perception. This approach underlines the role of vestibular stimulation in therapy. In children with autism spectrum, we can observe hypoactivity or hyperactivity as a result of sensory disintegration. In the sensory integration therapy of mentally disabled children therapists include many types of stimuli movements: excitatory rapid movements, inhibitory slow movements, passive movement and rotations. These forms of intervention give significant improvement in functional activities in 62% of participants [8–9].

Since the essence of autism spectrum disorders is the difficulty in establishing communication with the environment, it is important to improve speech and all forms of communication, including non-verbal, which will allow the child to express their needs and feelings. Without improving communication skills, there is no way for a child to fully develop.

The close links between motor skills, body sensation and between body sensation and sensory integration additionally justify intervention related to motor exercises in children with ASD. The therapy of people with ASD consists, among others, in supporting the child's psychomotor development, eliminating and preventing neurological deficits associated with muscle tone disorders [9–15]. The therapy consists in developing the correct perception and analysis of stimuli provided through the senses.

As it was already mentioned, the aim of the article is to show the therapy using PR and its impact on the development of the CNS in a child diagnosed with ASD.

The goal of PR is general psychomotor improvement, improvement of the nervous system function. Its idea is to include rotation and circumferential movements in the performed exercises [16]. Unlike other forms of classes, the exercises performed during this program are simple and uncomplicated, and you do not need any equipment to perform them. They improve visual perception, preparing the child to learn to read and write. With a large range of rotation, they develop gross motor skills, which, as a stretching exercise, prepares the child to perform more precise hand movements (fine motor skills).

Rotation and circumferential movements are used in the method of proprioceptive neuromuscular facilitation [16], in the programs: Swiss Ball, Pilates, Stretching,

Yoga [17–19], or preventive and corrective exercises. However, they are not the main means of training here. PR is based on positive relations, adapting exercises to the psychophysical condition of the child. A detailed description of the subsequent exercises performed as part of the program is included in the part devoted to the methodology of working with a child.

## 2. Case study

### 2.1. Child's data – before the start of PR (from documentation analysis)

The child was born from a normal pregnancy, after birth he obtained 10 points on the APGAR scale. In infancy, the child's behavior aroused anxiety, he did not fix his gaze on the mother's face, he did not reciprocate emotions (smile), he had slowed down psychomotor reactions. The mother had the opportunity to compare the behavior of the subject with the development of an older child whose development was normal. There was no specialist diagnosis and neurological care in infancy. During the period of attending the nursery, developmental disorders manifested themselves very clearly, the parents consulted specialists (a pedagogue and a psychologist). During this period, the subject used therapies conducted by specialists. From the numerous opinions collected by the mother, the child's behavior can be characterized as follows: attention disorders; delayed speech development; lack of social skills; absence of aggressive and destructive behaviors; non-specific play, typical of autistic children; favorable prognosis as to the future of the child, which indicates the perceived development potential.

In the boy's early development, communication disorders, impaired speech development and its delay, as well as impaired social functioning (in the peer group) were found. Lack of medical documentation, especially neurological.

### 2.2. Child's data – before the start of PR (information from video recordings recorded by parents)

The child's development is highly disharmonious, with clear deficits in the field of motor skills (muscle weakness, reduced ability to manipulate, which causes difficulties in performing precise manual activities. Visual perception is slightly reduced, the decrease concerns mainly spatial orientation. Developmental disorders on the part of the CNS are likely.

## 2.3. Child's data – before the start of PR (interview with the parents)

The parents noticed the child's lack of acquiring age-specific skills, non-specific, generalized reactions to stimuli, and delayed cognitive development. After a short period of despair and resignation, they began to seek specialist help for their son, and they obtained a diagnosis that boils down to the term – autistic syndrome. The boy had practically no verbal contact. The reactions were dominated by vocalizations and an intentionally undifferentiated scream. The boy did not respond to verbal commands addressed to him. The spontaneous reactions were dominated by motor stereotypes (e.g. fluttering hands around the eyes, spinning around one's own axis). In physical activity, the boy showed symptoms of hyperexcitability and motor disorganization – he ran aimlessly around the rooms, he was unable to undertake long-term, orderly activity. The behaviors were dominated by simplified manipulations on objects of a non-specific nature (hitting a toy car on the ground). The boy did not make spontaneous contact with his parents or siblings. He avoided tactile contact, eye contact was very brief. Games in which the character mainly wanted to participate (pushing, running), the child did not take up symbolic and thematic games. Significant difficulties with prolonged deliberate focus on instructions and lack of adequate reactions to attempts to contact from relatives were visible. This description illustrates the generalized cognitive-emotional-executive character of disturbances in contacts with the environment, characteristic of ASD.

## 3. Methodology

Each of the exercises of the Rotation Program fulfilled a specific role and in order to achieve the intended effect, the exercises were performed exactly according to the given rules, which are presented below.

- The condition for the correct performance of the exercise is concentration. Each movement should be performed slowly and precisely, which will reduce the risk of injury.
- Maintain smooth transitions from one exercise to another. The breath should be synchronized with the movement. Breathe evenly and naturally.
- Exercise regularly, at the same time and in the same place.

Perform as many repetitions of a given exercise and as much range of motion as possible without discomfort or pain. You should strive to maintain contact with the child and his motivation to perform further exercises. It is forbidden to act “by force”, against the will of the child. In the event of a clear reluctance, it was recommended to switch to exercises accepted by the child (in studies on the impact

of learning-based therapies on the child, it was warned against using punishments or exercises against the will of children with ASD, pointing to the risk of post-traumatic stress symptoms and the associated escalation of aggression and hyperactivity, and even regress in development) [14].

The program should also include gradual learning to respond to verbal commands. The ability to correctly respond to commands involves both speech understanding functions (based on language learning) and the ability to enter into conscious contact with the interlocutor – focusing attention on the command. The correct execution of a specific movement also trains the previously mentioned coordination and movement skills and body awareness. From a psychological point of view, shaping body awareness is important for building a child's sense of identity and separateness from its environment. A child with autism has difficulties in correctly perceiving the boundaries of his body, interpreting his own and other people's emotions. For this reason, any exercises based on alternating contact and improving body awareness are important. The holistic, systemic work of various brain structures is important in improving motor coordination. Hemispheric integration exercises and procedures stimulate the child's natural development mechanisms. They should be easy to perform and individually developed, taking into account the developmental potential of the child and implemented in three stages.

The first is the implementation of exercises in a passive way, the second is the acquisition of exercise skills by imitation, and the last is performing exercises on verbal command.

### 3.1. Detailed description of the conducted exercises

In the first stage of the program, passive cross exercises were used. During these exercises, the therapist and the child's parents worked simultaneously. Rotation movements were performed, starting from the distal sections of the limbs – fingers and toes, diagonally, then rotational movements were performed within the wrists and ankles, successively through the elbows, knees, hips and shoulder joint, then analogous movements were performed on the opposite side of the body.

Subsequent movements were performed with simultaneous activation of the upper limbs and one lower limb. The therapist activated the upper limbs by adducting and crossing the upper limbs with centripetal and centrifugal rotation in the shoulder joints and wrists, which resulted in alternating opening and closing of the chest and mobilization of respiratory muscles. This type of exercise was aimed at ensuring oxygenation of the body and improving the mechanics of breathing while speaking by mobilizing the muscles of the chest and diaphragm.

The parent and therapist then performed simultaneous movements of both upper and lower limbs. Cross-sectional movements of the upper and lower limbs were performed in all joints with rotation of the distal sections of the upper limbs. The next



step was to repeat the exercises with the activation of both upper and one lower limbs on the previously untrained side. Then cross-sectional movements of all limbs were repeated.

Exercises of cross movements of the upper and lower limbs in the diagonal axis combined with pressure and an attempt to sequentially grasp the foot, ankle, lower leg, knee joint, and thigh with the hand of the opposite upper limb. Each movement was assisted and named by the therapist. Their goal was to improve spatial orientation, motor coordination, sense of balance (stimulation of the kinesthetic sense).

The exercises were carried out with the participation of two people (a parent and a physiotherapist) for a month, every day in the morning. Naming of movements and exercised parts of the body and proprioceptive stimuli associated with pressure on the joints improved sensation and awareness of the body.

After activating exercises, a surface massage was performed with stroking movements, simultaneously on opposite upper and lower limbs. On the upper limb, from the phalanges, through the hand, wrist, elbow, shoulder joint, neck, chest, biceps, inner side of the forearm and ending with the phalanges.

The lower limb was massaged from the outside, starting from the buttock muscles, through the hips, the outer side of the thighs, the knee joint, the shank, the ankle joint, the foot, up to the toes. Then the massage was continued on the inside of the limb upwards ending at the hip joint.

In addition, the abdominal area was gently massaged with a circular motion of varying diameter. This type of exercise was used to calm down and relax after activating exercises.

The exercises ended with the parent's instruction to embrace the child's upper limbs behind the neck and lower limbs behind the trunk. The child, being a participant of the activity, learned the limits of its body and came into contact as closely as possible. Embracing the parent's limbs and trying to make contact gave the child an opportunity to overcome the fear of intimacy and opened them up to controlled contact. These types of exercises are particularly important in working with people with ASD, whose basic deficit is precisely the ability to establish contact with the environment.

After completing the first stage, work with the child began with imitation exercises. In the initial period, each of the exercises described above was initiated by the therapist and the parent. The child was to implement subsequent elements of the program, gradually imitating the movements demonstrated by the parents and the therapist. The therapist and parents remained in close contact with the child all the time, supporting the execution of movements. This type of exercise is of particular importance in the treatment of people with ASD who suffer from deficits in the ability to purposefully imitate. Their echolalic reactions, or echopraxia, take the form of motor automatisms. In therapy, the aim is to extinguish automatisms and activate imitative purposeful reactions. By conducting imitation exercises, it is possible to improve

the attention function and stimulate the child's active participation in social interactions. The ability to imitate is also the basis for the development of speech, which is shaped by deliberate and active imitation of the speech reactions of the environment.

Exercises were carried out three times a week with the participation of two people (parent and physiotherapist), additionally, the child exercised only with parents in the morning for 10 to 15 minutes for a period of two and a half months.

Gradually, the degree of independence of the child was increased, striving for it to perform exercises only after verbal instructions, without demonstration. As in the previous stages, the therapist and parents supported the child in carrying out the exercise program.

An important value of this program is the assumption a priori of flexibility in performing tasks according to the child's abilities. The method of conducting the exercises was always flexibly adapted to the psychophysical state of the child on a given day. If the child was unable to perform any of the exercises on their own, the movements were performed with the help of a therapist. This made it possible to continue the exercises and adapt the methods of stimulation to the reactions in the dysfunctional nervous system and (secondarily) in the musculoskeletal system that changed on a given day. The aim of the active, imitative exercises was to develop the child's communication by understanding and reading the therapist's messages and developing the ability to empathize in parent-child contact. The child exercised with his parents in the morning for 10 to 15 minutes and additionally, the exercises were carried out once a week with the participation of two people (parent and physiotherapist) for a period of three and a half months.

Each subsequent stage of the exercises influenced the development of the child's communication and motor skills and the use of its psychophysical potential.

## 4. Results

### 4.1. Data from the observation of the child after 3.5 months – implementation of the program of rotational movement exercises

Observation carried out in the child's family home in the presence of his parents, siblings and other children. The follow-up was mixed (event samples, participant follow-up).

According to the mother, the currently examined child makes rapid, significant qualitative progress, especially in terms of speech and cognitive functions. Makes contact quickly and easily, follows instructions, understands simple questions. There are situations when he withdraws from the interaction and "shuts in on himself". In contact with parents, he is calm, gives factual answers, is observant, spontaneous.

In the field of verbal communication, he uses an age-appropriate dictionary, correctly builds simple sentences (subject and predicate), uses adjectives (describes the world – this indicates contact with the outside world). During PR, he submits to exercises without signs of reluctance or rebellion. He communicates naturally with his siblings. There is reduced muscle tone and difficulties in fine motor skills.

The description of the child's behavior indicates the positive effects of motor exercises based on both tactile stimulation and coordination exercises. This function is performed by exercises requiring precise touch of specific parts of the body and exercises related to deliberate, rhythmic alternation of movements. The rotational nature of movements, activating the labyrinth and activating eye-hand coordination, is also directly related to the activation of cerebellar structures. The improvement results obtained, indicating the effectiveness of the undertaken exercise program, are scientifically based in the light of the research cited in the introduction, concerning the link between the activity of the cerebellar vermis and cognitive processes, emotions and behavioral control (through neural connections between the cerebellum and the prefrontal cortex).

## 4.2. Data from the observation of the child after 7 months – implementation of the program of rotational movement exercises

Observation carried out in the child's family home in the presence of his parents, siblings and other children. The observation was mixed (samples of events, participant observation). On this day, the subject underwent exercises, and then a joint drawing was performed with the participation of a psychologist. Movement exercises were routine. The child submits to them with pleasure. After them, the child is relaxed. It can be assumed that PR improves the concentration of attention, which is confirmed by a psychologist. Drawing together was aimed at learning the scheme of one's own body. During simple drawing exercises, moderate interest on the part of the subject, understanding and fulfillment of instructions was observed. During one of the tasks, the boy put down the paper without completing the task. The next tasks were started, after a dozen or so minutes, the subject reached for the uncompleted task that had been put aside and completed it correctly (spontaneously). This behavior proves the occurrence of a delayed reaction, which indicates the acquisition of skills at a higher level of thinking and learning, which is a good prognosis.

Another observation also confirms the effectiveness of the applied rotational exercises. Particularly noteworthy is the connection between the improvement of the ability to control behavior and the exercises that activate the structures of the cerebellum. The child began to interact with the environment. Although the reactions are visible after a short delay, the ability to follow orders and complete the activities begins

to become visible. A child's behavioral skills indicate an improvement in attention. The impact of physical exercises on the emotional state of the child was also positive. The boy calmed down and the symptoms of psychomotor hyperactivity decreased. An important positive aspect of the exercises seems to be the combination of elements of surface and deep massage with a deliberately performed rotational movement, which ensures the stimulation of both cerebellar structures and properly stimulates the child's sensory system. Improving the awareness of physical sensations related to the body schema can be a starting point for improving the awareness of one's own emotions, which enables the development of intentional action.

#### **4.3. Data from the observation of the child after 7 months – the implementation of the program of rotational movement exercises (interview with the mother)**

There was a clear improvement in the overall cognitive and motor skills of the child. Intellectual activity improved, spontaneous reactions appeared (oh cool..., that's nice..., that's not allowed...). The boy began to use complex thought structures to describe his own feelings (quote: it's hard for me..., I'm bored..., I'm tired..., it's fun..., it's interesting). The child describes and evaluates what he sees, one can risk saying that the emotional zone has been stimulated. Natural expression (expression of feelings) is triggered. Contact with children during joint play has also improved. There were manifestations of new stimulus-response connections in the child's behavior. During the first stage of PR, where cross-passive exercises were carried out, it was observed that the child had no control over his movements, he was passively subjected to exercises without signs of objection, satisfaction of interest – as if he could not use his own limbs for purposeful activities. However, after 7 months of PR, the boy's awareness of the body increased, the movement became more organized and intentional.

#### **4.4. Data from the observation of the child after 7 months – implementation of the program of rotational movement exercises (psychologist's opinion)**

The inclusion of exercises in the therapy of a 5-year-old child with ASD resulted in a marked improvement in the overall cognitive and motor skills. Intellectual activity improved, better concentration of attention, he began to use complex thought structures to describe the world and his own feelings, the emotional zone was stimulated. Spontaneous expression was released. New stimulus-response connections were observed in the boy's behavior.

## 4.5. Opinion of a special educator/oligophrenopedagogue – important aspects in working with an autistic child

The results of the influence of the social environment on the behavior of a child with ASD were observed in the work. Questions arise. Can such a child function independently in the community? Can accepting and following help reduce the undesirable effects of the condition of people with the spectrum? Could a different state of perception of the world by people from the spectrum be inspiring for the environment and constitute a value and not a problem?

The following levels of child support are important – absolute acceptance, understanding and use of the child's potential, following the child, supporting through stimulation in the form of praise and attention. The child repays this attitude with love, changes the parent's awareness, influences the development of new emotions and feelings. He subconsciously expects friendship, understanding, acceptance and tolerance from his peers. A frequent process of the parent-child relationship is unconsciously lowering its potential and trying to change it by force. Children affected by ASD are guided by innate intuition, they do not understand all artificially established socio-cultural norms and patterns. Very often they are characterized by uncertainty in action, resulting from a high intellectual level or an inharmonious level of development. They are very sensitive to mental and emotional wounds. They want to be in a group, and in the absence of understanding on their part, fear and a sense of loneliness appear. A child with ASD does not feel his body, is unable to create boundaries and apply norms. Through psychomotor development exercises, the awareness of the child's body increases, it begins to create its boundaries and respect the boundaries of other people. Creating positive aspects of the child's development at all levels affects the development of the CNS, causing changes in social, emotional and cognitive development. The above method will not replace other methods of supporting the child's development, therefore, when examining a patient, a multi-specialist diagnosis should be considered in order to take appropriate therapeutic actions.

### 6. Discussion

The article presents the preliminary assessment of the effectiveness of the described therapy. The study confirmed promising results. They clearly justify sharing of this therapy in a bigger group of patients with ASD. The authors are aware that a study based on a bigger group could reinforce scientific assessment of the described therapy. However, the process of collecting scientifically reliable data will probably be long and time-consuming. The research group should be large because the differences between individuals with ASD are significant.

The time of observation in the described study is quite short, but it is caused by the time limitation of the study. However, the authors want to underline, that the results of the PR therapy are stable. Jolanta Grażyna Zuzda has permanent contact with the family of the described child and knows the course of his development.

## 7. Conclusions

- The above program was a clinical experiment and was implemented with one child (case study) in order to improve mental and physical functions. It is important to continue the actions taken and test the functionality of the rotation exercise program on a larger research group.
- Observation of the child's behavior shows the influence of rotational movements on its development.
- Through exercises of motor functions and coordination, as well as sensory stimulation during the massage, the child gains greater awareness of the body, and begins to create its own boundaries and respect the boundaries of other people.
- Conducting imitation exercises and exercises in response to verbal commands in conjunction with naming exercised body parts supports the development of verbal communication by increasing the vocabulary and learning to react to messages from the environment.
- Conducting rotation exercises that activate the muscles of the back and chest as well as respiratory muscles improves the mechanics of breathing, which indirectly supports speech by improving subglottic pressure.
- Creating positive aspects of the child's development at all levels affects the development of the CNS, causing changes in social, emotional and cognitive development.
- It is important to use various forms of therapy for children in cooperation with parents and a team of specialists in various fields (including educators, psychologists, physiotherapists).

From an ethical point of view, it is important to highlight that the author of PR therapy, Jolanta Grażyna Zuzda, took care of the child's well-being in the course of therapeutic intervention. The child's parents gave their assent to implement the described treatment for their son.

### Acknowledgment

The authors thank Barbara Piekarska Abou Hilal, psychologist, Medical Specialist Spółdzielnia Pracy, 15-453 Białystok, Poland, e-mail: [eskulap@eskulap.bialystok.pl](mailto:eskulap@eskulap.bialystok.pl), phone: +48 85 745 00 36, for carrying out the child opinion consultation.

### References

1. Gaurer T. et al. Most genetic risk for autism resides with common variation. *Nature Genetics*, 2014, 46, 881–885.
2. Chojnicka I., de Ines M., Kwasiborska-Dudek J., Zaburzenie ze spektrum autyzmu – kryteria diagnostyczne. Uwarunkowania genetyczne i neurobiologiczne. In: *Diagnoza i terapia logopedyczna małego dziecka z zaburzeniem ze spektrum autyzmu (ASD)*, eds. J. Kwasiborska-Dudek, D. Emiluta-Rozya, Harmonia, Warszawa 2020, 15–32.

3. Bryńska A., W poszukiwaniu przyczyn zaburzeń ze spektrum autyzmu – neuroobrazowanie strukturalne. *Psychiatria Polska*, 2012, 46(6), 1053–1060.
4. Pisula E., Autyzm przyczyny, symptomy, terapia. Harmonia, Gdańsk 2012.
5. Haroon M., ABC of Autism. Wiley-Blackwell, Oxford 2019.
6. Ahmadian N., Van Baarsen K., Van Zandvoort M., Robe P.A., The Cerebellar Cognitive Affective Syndrome – a Meta-analysis. *The Cerebellum*, 2019, 18, 941–950.
7. Van Hecke R. et al., Vestibular function in children with neurodevelopmental disorders: A systematic review. *Journal of Autism and Developmental Disorders*, 2019, 49, 3328–3350.
8. Lane S.J. et al., Neural Foundations of Ayres Sensory Integration®. *Brain Sciences*, 2019, 9(7), 153.
9. Uyanik M., Kayihan H., Bumin G., Sener G., Neurodevelopmental Therapy: Sensory Integration and Vestibular Stimulation Intervention in Mentally Retarded Children. In: International Handbook of Occupational Therapy Interventions, ed. I. Söderback, Springer, New York 2009, 333–343.
10. Choudhery A., Ansari T., A systematic review on the effect of vestibular stimulation in children with autism. *European Journal of Public Health Studies*, 2020, 2(1), 69–82.
11. Suchowierska M., Ostaszewski P., Bąbel P., Terapia behawioralna dzieci z autyzmem. Teoria, badania i praktyka stosowanej analizy zachowania. GWP, Gdańsk 2012.
12. Campos C. et al., Exploring the Role of Physiotherapists in the Care of Children with Autism Spectrum Disorder. *Physical & Occupational Therapy in Pediatrics*, 2019, 39(6), 614–628.
13. Habik N., Metody i zasady fizjoterapii wykorzystywane we wczesnym wspomaganie rozwoju dzieci ze spektrum autyzmu ze szczególnym uwzględnieniem Integracji Sensorycznej. *Niepełnosprawność – Zagadnienia, Problemy, Rozwiązania*, 2017, 3(24), 137–153.
14. Wiczorek M., Sadziak A., Aktywność fizyczna dzieci ze spektrum autyzmu. *Journal of Education, Health and Sport*, 2017, 7(2), 222–238.
15. Raditha C., Handryastuti S., Pusponegoro H.D., Mangunatmadja I., Positive behavioral effect of sensory integration intervention in young children with autism spectrum disorder. *Pediatric Research*, 2023, 93, 1667–1671.
16. Zuzda J.G., Latosiewicz R., Innowacyjny program zajęć rekreacyjnych wykorzystujący ruchy rotacyjne. Politechnika Białostocka, Białystok 2010.
17. Horst R., Trening strategii motorycznych i PNF. TOP School, Kraków 2015.
18. Suk M.L., Hee S.L., Hyo J.B., Myung J.K., Changes of abdominal muscle activity according to trunk stabilization exercises using a Swiss ball. *Physical Therapy Rehabilitation Science*, 2020, 9, 18–24.
19. Coulter H.D., Anatomia Hatha Jogi, IBR Focus Sp. z o.o. Warszawa 2024.

**The authors state that there is no conflict of interest.**

# List of tables

## *Pressure-relieving silicone orthopedic insole made by 3D printing*

Table 1. Type and degree of filling of the orthopedic insole used in the study .....	13
Table 2. Printing parameters for silicones.....	13
Table 3. Comparison of the degree of infill for different types of infill .....	14
Table 4. Averaged maximum and minimum dynamic viscosity values obtained in the test for silicone A and B (source: own elaboration) .....	16
Table 5. Medium Rc values of silicone A for different filling types and their filling grades....	18
Table 6. Medium Rc values of silicone B for different filling types and their filling grades.....	18
Table 7. Magnification of the structures obtained after printing for silicone A .....	19
Table 8. Magnification of the obtained structures after printing for silicone B.....	20

## *System for lung X-Ray image analysis using machine learning algorithms*

Table 1. Dataset dimensions used in the CNN model: Number of samples and image dimensions for training, test, and validation, along with their corresponding class label counts.....	33
Table 2. Summary of the Sequential CNN Model .....	34
Table 3. Convolutional neural network training results .....	35

## *Automatic mechanical diagnostics using deep learning methods*

Table 1. Examples of parameters of extracted image features.....	44
Table 2. Table of model quality coefficients with manual feature extraction.....	46
Table 3. Table of quality coefficients of the model with automatic feature extraction .....	47

## *Application supporting the interpretation of laboratory test results*

Table 1. Blood count reference ranges [1, 2] .....	53
Table 2. Reference ranges and urine properties [1,3].....	53
Table 3. Reference ranges of selected vitamins in the body [4–9].....	54
Table 4. Consequences of deficiency and excess of selected vitamins [4–9].....	54
Table 5. The most common sources of selected vitamins in food [4–10] .....	55
Table 6. Statistics on the age of people testing the application .....	60

## *Utilization of the spin-coating method to produce elastic composites for applications in biomedical engineering*

Table 1. The composition of materials .....	88
Table 2. The density of C and D composites.....	93



<i>Assessment of the wettability of PDMS and denture acrylic polymer by oral gels</i>	
Table 1. Composition of prepared gels.....	108
<i>Mechanical properties of polylactide-based composites with iron powder additions – experimental and numerical evaluation</i>	
Table 1. Tensile test results of the composite materials.....	119
Table 2. Hardness and density values of the tested composite materials .....	119
<i>Design of an ankle joint orthosis for people with extensive sweating.....</i>	125
Table 1. Summary of the obtained parameters of PLA material as a result of monotonic tensile test.....	132
<i>Influence of the femoral neck-shaft and anteversion angles on the loadings acting in the musculoskeletal system during walking</i>	
Table 1. Effect of including deformed femoral bones in the standard model [22] .....	144
Table 2. Statistical analysis for the hip and knee joint reaction force components (P_D – proximal-distal; M_L – medial-lateral; A_P – anterior-posterior) for selected time-points (local extrema) presented in Fig. 1.3 and the level of significance of differences between results obtained for the standard model (SM) and models with modified geometry of the femoral bone (FA_0, FA_40, FNS_100 and FNS_150) (p < 0.05; x – no statistically significant difference) .....	151
<i>Key factors in bone marrow transplant outcomes: statistical insights</i>	
Table 1. Characteristics of variables [10] .....	165
Table 2. Statistical significance for each characteristic of the studied patients.....	167

# List of figures

## *Pressure-relieving silicone orthopedic insole made by 3D printing*

Fig. 1. Schematic of printing using DIW technology [17] .....	11
Fig. 2. 3D model created in SOLIDWORKS CAD .....	12
Fig. 3. Dimensions of an orthopedic insole.....	12
Fig. 4. Orthotics insole area subjected to filling modification with different structures and degrees of filling.....	12
Fig. 5. Layering method for rectilinear infill: (a) first layer; (b) second layer applied at 90°.....	15
Fig. 6. Plot of dynamic viscosity versus shear rate for silicone A.....	16
Fig. 7. Plot of dynamic viscosity versus shear rate for silicone B .....	17
Fig. 8. Stress-strain relationship for similar values of average Rc of silicone A .....	17
Fig. 9. Stress-strain relationship for similar values of average Rc of silicone B.....	18
Fig. 10. Angle measurement for triangular infill .....	20
Fig. 11. Measurement of the width of the obtained layer .....	21
Fig. 12. Orthotic insole printed from silicone A with: a) rectilinear shape fil- ling and 50% degree of infill, b) rectilinear shape filling and 75% degree of infill, c) honeycomb filling and 50% degree of infill, d) honeycomb filling and 75% degree of infill, e) triangular shape filling and 50% degree of infill, f) triangular shape filling and 75% degree of infill .....	22
Fig. 13. Orthotic insole printed from silicone B: a) with triangular shape filling and filling degree of 75%, b) with triangular shape filling and filling degree of 50% .....	23

## *System for lung X-Ray image analysis using machine learning algorithms*

Fig. 1. Sample X-ray image without signs of disease [17] .....	31
Fig. 2. Sample X-ray image of pneumonia [18] .....	32
Fig. 3. Sample X-ray image of COVID-19 [4].....	32
Fig. 4. Accuracy obtained on the training and validation dataset.....	36
Fig. 5. A confusion matrix showing errors and evaluating the performance of the classification model.....	37

<i>Automatic mechanical diagnostics using deep learning methods</i> .....	41
Fig. 1. Diagram of the model with automatic feature extraction.....	46
<i>Application supporting the interpretation of laboratory test results</i> .....	51
Fig. 1. Blood count analysis subpage .....	57
Fig. 2. Example of a blood count analysis result .....	57
Fig. 3. Example of a urine analysis result with an important message .....	58
Fig. 4. Subpage <i>Analysis of vitamin levels</i> .....	58
Fig. 5. Example result of the analysis of vitamin B12 level.....	59
Fig. 6. <i>Vitamins knowledge base</i> subpage .....	59
Fig. 7. Histogram regarding the age of respondents .....	60
Fig. 8. Pie chart regarding the education of respondents.....	61
Fig. 9. Answers to questions regarding application evaluation .....	62
<i>Artificial intelligence in neuroimaging of cerebral aneurysms – theoretical study</i>	
Fig. 1. Four examples of cerebral aneurysm [6].....	66
Fig. 2. Saccular(a) and fusiform (b) aneurysm [16] .....	68
Fig. 3. Head CT (A) demonstrates angioCT (B) showing a 5-mm ruptured aneurysm (arrow) [45] .....	72
Fig. 4. Defective visualization of the aneurysmal sac in real time angioMR [50].....	73
Fig. 5. An unruptured MCA aneurysm was clipped via the traditional pterional approach under the neuroendoscope. (A) Pre-operative CT scan showed no SAH or hematoma in the brain. (B) Pre-operative CTA scan showed a saccular aneurysm at the left MCA bifurcation. (C) A sylvian fissure was sharply dissected under neuroendoscope. (D) Aneurysm and the branches of MCA were exposed under the neuroendoscope. (E) MCA was clipped temporarily. (F) Aneurysm was clipped under the neuroendoscope and temporary clip was removed. (G) Postoperative CT scan showing no hematoma and damage in the brain. (H) Postoperative CTA scan showed that aneurysm was clipped completely and the MCA and its branches were preserved [52] .....	74
Fig. 6. Aneurysm embolization [59].....	75
<i>Utilization of the spin-coating method to produce elastic composites for applications in biomedical engineering</i>	
Fig. 1. Spin-coater with vacuum pumps .....	89
Fig. 2. Liquid composite (a) applied to a Petri dish and (b) composites obtained by using the spin-coating method .....	89
Fig. 3. Contact angle $\Theta$ on the droplet applied to the surface .....	90
Fig. 4. Designated lines of linear roughness measurements (a), and areas of surface roughness measurements (b).....	92
Fig. 5. Contact angle values for composites (a) B, (b) C, and (c) D with varying spin speed and spin time .....	95
Fig. 6. The thickness of the composites containing (a) 10vol% (b) 20vol% $Al_2O_3$ particles.....	97

Fig. 7. Linear roughness of (a) C and (b) D composite materials .....	99
Fig. 8. Surface roughness of (a) C and (b) D composite materials.....	100
<i>Assessment of the wettability of PDMS and denture acrylic polymer by oral gels</i>	
Fig. 1. Contact angle goniometer (Ossila, Sheffield, Great Britain) .....	109
Fig. 2. Contact angle for prepared gels in contact with PDMS material .....	110
Fig. 3. Contact angle for prepared gels in contact with denture acrylic polymer .....	110
<i>Mechanical properties of polylactide-based composites with iron powder additions – experimental and numerical evaluation .....</i>	
Fig. 1. Tensile specimen dimensions .....	117
Fig. 2. Tensile test setup: a) visualization and b) a real test.....	118
Fig. 3. Prepare for numerical tests: a) model with mesh; b) boundary conditions.....	118
Fig. 4. SEM observations of the composite materials .....	120
Fig. 5. Equivalent (von-Mises) stress maps for samples: a) PLA + 10% Fe; b) PLA + 5% Fe; c) PLA + 1% Fe; d) PLA + 1% nanoFe; e) PLA + 0.5% nanoFe; f) PLA + 0.1% nanoFe .....	121
Fig. 6. Stress-strain comparison charts for numerical and experimental study: a) for composites based on PLA with iron powder additions; for composites based on PLA with iron nanopowder additions .....	122
<i>Design of an ankle joint orthosis for people with extensive sweating</i>	
Fig. 1. General structure of the joint [9] .....	127
Fig. 2. Principle of 3D printing process using FDM technique (1 – spool of main filament, 2 – spool of auxiliary filament, 3 – heating table, 4 – component created, 5 – support elements of the component, 6 – auxiliary filament, 7 – main filament, 8 – extruder, 9 – guide rollers, 10 – liquefying guide, 11 – nozzle) [14] .....	129
Fig. 3. 3D printing process.....	130
Fig. 4. Summary of tensile plots of honeycomb-filled PLA specimens with a density of 30%.....	133
Fig. 5. Summary of tensile plots of honeycomb-filled PLA specimens with a density of 50%.....	133
Fig. 6. Summary of tensile plots of PLA samples with honeycomb filling and 30% and 50% density, without exposure in saline solution .....	134
Fig. 7. Summary of tensile plots of PLA samples with honeycomb filling and 30% and 50% density, after 8-week exposure in saline solution .....	134
Fig. 8. Patient leg scan in Autodesk Fusion 360.....	135
Fig. 9. Optimized patient foot grid .....	136
Fig. 10. Developed solid mesh of the ankle orthosis .....	136
Fig. 11. Use of automated modeling functions .....	137
Fig. 12. Final model of ankle and knee joint orthosis .....	137
Fig. 13. Ankle joint orthosis model in PrusaSlicer .....	138

*Influence of the femoral neck-shaft and anteversion angles on the loadings acting in the musculoskeletal system during walking*

Fig. 1. Muscle active force waveforms for 20 muscles. Comparison of the results obtained for models with modified geometry of the femoral bone (FA_0, FA_40, FNS_100 and FNS_150) and the standard model (SM) (mean $\pm$ SD) .....	147
Fig. 2. Mean root-mean-square-differences (RMSD) for the comparison of muscle forces between the standard model (SM) and models with modified geometry of the femoral bone (FA_0, FA_40, FNS_100 and FNS_150). Error bars represent standard deviation .....	149
Fig. 3. Hip and knee joint reaction forces obtained using modified models (FA_0, FA_40, FNS_100, FNS_150) compared to results obtained using the standard model (SM) (mean $\pm$ SD): A) reaction force components (P_D – proximal-distal; M_L – medial-lateral; A_P – anterior-posterior) and B) angles of deviation of the force direction resultant force in the coronal (M_L) and sagittal (A_P) planes. The time-points at which the results were further statistically analysed are marked: 1÷3 .....	152
Fig. 4. Mean root-mean-square-differences (RMSD) for the comparison of joint reaction forces components (P_D – proximal – distal; M_L – medial – lateral; A_P – anterior posterior) between the standard model (SM) and models with modified geometry of the femoral bone (FA_0, FA_40, FNS_100 and FNS_150). Error bars represent standard deviation .....	153

